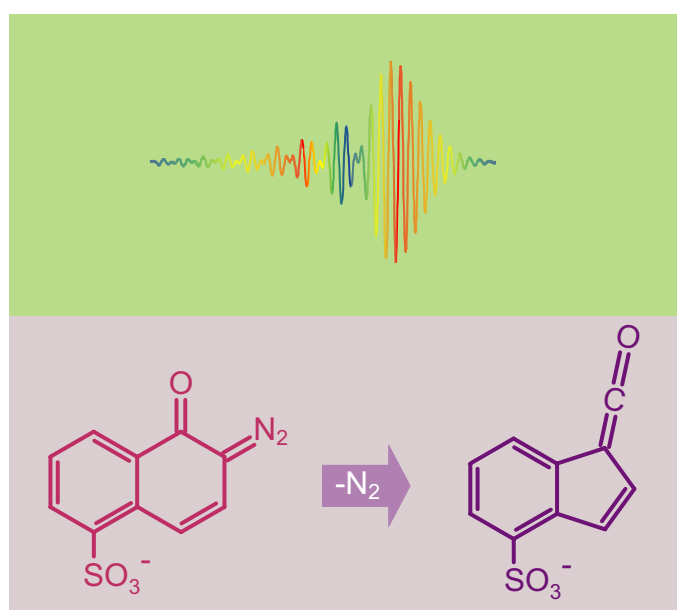


Quantum Control of Photoinduced Chemical Reactions



Dissertation zur Erlangung des
naturwissenschaftlichen Doktorgrades
der Julius-Maximilians-Universität
Würzburg

vorgelegt von
Daniel Wolpert
aus Würzburg

Würzburg 2008

Eingereicht am: 08. Februar 2008
bei der Fakultät für Physik und Astronomie

1. Gutachter: Prof. Dr. G. Gerber
2. Gutachter: Prof. Dr. T. Brixner
der Dissertation

1. Prüfer: Prof. Dr. G. Gerber
2. Prüfer: Prof. Dr. T. Brixner
3. Prüfer: Prof. Dr. H. Hinrichsen
im Promotionskolloquium

Tag des Promotionskolloquiums: 17. März 2008

Doktorurkunde ausgehändigt am: _____

List of Publications

Parts of this work have been published in the following references:

P. Nuernberger, D. Wolpert, H. Weiss, and G. Gerber,
Femtosecond laser-assisted catalytic surface reactions of syngas and their optimization by tailored laser pulses,

In P. Corkum, D. Miller, A.M. Weiner, D. Jonas (Eds.), *Ultrafast Phenomena XV*, volume 88 of *Springer Series in Chemical Physics*, pp. 237–239, Springer, Berlin (2007).

P. Nuernberger, D. Wolpert, H. Weiss, and G. Gerber,
Bond-forming chemical reactions initiated and adaptively controlled by femtosecond laser pulses

to be submitted (2008).

D. Wolpert, M. Schade and T. Brixner,
Femtosecond mid-infrared study of the photoinduced Wolff rearrangement of diazonaphthoquinone

submitted to *J. Chem. Phys.* (2007).

D. Wolpert, M. Schade, G. Gerber, and T. Brixner,
Quantum control of the photoinduced Wolff rearrangement of diazonaphthoquinone in the condensed phase

J. Phys. B: At. Mol. Opt. Phys. 41 (2008) 074025.

Contents

List of Publications	iii
1 Introduction	1
2 Theoretical concepts	3
2.1 Quantum control	3
2.1.1 Single parameter concepts	4
2.1.2 Adaptive quantum control	6
2.2 Mathematical description of femtosecond laser pulses	7
2.2.1 Description in the time and frequency domain	8
2.2.2 Spatial propagation and material dispersion	12
2.2.3 Spatial beam properties	14
2.3 Frequency conversion	15
2.3.1 Nonlinear polarization	16
2.3.2 Phase matching	16
2.3.3 Nonlinear processes	18
2.4 Electronic structure and vibrations of molecules	22
2.4.1 Born-Oppenheimer approximation and potential energy surfaces	22
2.4.2 Vibrations	23
2.5 Ultrafast vibrational spectroscopy	25
2.5.1 Theory of UV pump - IR probe spectroscopy	25
2.5.2 Transient infrared signals	26
2.5.3 Investigated molecular systems and processes	27
3 Experimental methods	29
3.1 Femtosecond laser system	30
3.2 Femtosecond pulse shaping	31
3.3 Pulse characterization methods	34
3.3.1 Autocorrelation and cross-correlation	34
3.3.2 Frequency-resolved optical gating - FROG and XFROG	36
3.4 Detection schemes	37
3.4.1 Harmonic generation	37
3.4.2 Transient absorption	38
3.4.3 Time-of-flight mass spectrometry	39
3.5 Evolutionary algorithm	40

4	Femtosecond mid-infrared spectroscopy setup	43
4.1	The UV pump - MIR probe experiment	43
4.2	Generation of UV pump pulses	44
4.3	Generation of probe pulses in the mid-infrared	44
4.3.1	Optical parametric amplifier	46
4.3.2	Difference frequency generation stage	48
4.4	Pump-probe setup	48
4.4.1	Pump and probe beam paths	48
4.4.2	Spectrally resolved infrared detection	49
4.4.3	Flow cell mount	50
4.5	Characterization of the transient MIR spectrometer	51
4.5.1	Spectral tunability	51
4.5.2	Time resolution	52
4.5.3	Coherent artifact	53
4.5.4	Perturbed free induction decay	54
4.6	Conclusion	56
5	Femtosecond IR study of the photoinduced Wolff rearrangement of DNQ	59
5.1	Introduction	59
5.2	Steady state spectroscopy	61
5.2.1	UV/VIS absorption	61
5.2.2	Infrared absorption	62
5.2.3	Normal mode analysis	65
5.3	Transient absorption spectroscopy in the mid-infrared	66
5.3.1	Normal mode analysis of possible product species	68
5.3.2	Product formation dynamics	69
5.3.3	Reaction model and fit	74
5.4	Conclusion	79
6	Quantum control of the photoreaction of DNQ	81
6.1	Control by chirped pulse excitation	82
6.1.1	Mathematical description of chirped pulses	82
6.1.2	Experimental results	85
6.1.3	Influence of chirped pulse excitation on photoproduct formation	87
6.1.4	Discussion	87
6.2	Double pulse excitation	89
6.2.1	Mathematical description of colored double pulses	89
6.2.2	Experimental results and discussion	92
6.3	Adaptive optimization of the photoproduct formation	96
6.4	Conclusion	98
7	Catalytic surface reactions initiated by femtosecond laser pulses	99
7.1	Catalytic reactions of hydrogen with carbon dioxide	100
7.2	Experimental setup	102
7.3	Study of synthesized surface reaction products	103
7.4	Single parameter variations	105

7.4.1	Reactant molecules	106
7.4.2	Catalyst metal	107
7.4.3	Laser properties	108
7.4.4	Pump-Probe spectroscopy	111
7.5	Discussion of the reaction mechanism	112
7.6	Towards larger molecules	115
7.7	Conclusion	117
8	Adaptive quantum control of catalytic surface reactions	119
8.1	Reduction of carbon monoxide dissociation	119
8.2	Control of competing bond-forming reaction channels	121
8.3	Maximization of DCO ⁺ formation	124
8.4	Analysis of control mechanisms via variation of gas amounts	125
8.5	Conclusion	126
9	Summary	129
	Zusammenfassung	133
	Bibliography	137
	Acknowledgements	163
	Lebenslauf	166

1 Introduction

In analogy to the 20th century that is regarded as the "century of the electron", the 21st century is sometimes called the "century of the photon" [1]. This view is justified because the optical technologies are conquering our every day life in the form of displays, projectors, optical data storage devices to name only a few examples. Especially the laser is gaining more and more importance in medicine and industry as a tool for surgery, and for material processing applications such as cutting and welding.

But light and lasers not only serve as tools, they have also been used to increase our understanding of dynamical molecular processes. Molecular motion has to be studied with a time resolution on the order of 100 femtoseconds (10^{-15} s), the actual time scale of nuclear motion and the making and breaking of chemical bonds. Ultrafast laser sources providing light pulses short enough to resolve these events were developed during the last decades enabling the investigation of fast molecular processes. For his pioneering work in the field of "femtochemistry" on the transition states of chemical reactions using femtosecond spectroscopy Ahmed Zewail was awarded the Nobel Prize in chemistry in 1999 [2]. From the ability to learn about the different steps in the course of chemical reactions it is not very far to desire the control of chemical reactions by using ultrashort laser pulses. However, for advancing from observation to control new methods and ideas had to be developed. In order to selectively manipulate a quantum system to obtain a desired outcome the electric field interacting with the quantum system has to be modulated on the intrinsic time scale of the quantum mechanical processes in a specific way dictated by the quantum system itself. Although almost arbitrarily shaped pulses can be generated by using state of the art optical pulse shaping technology, the main difficulty that one has to solve is which pulse shape is suitable to achieve the intended goal. The large number of possible and accessible pulse shapes makes it impossible to test all of them.

A seminal new approach to solve this problem was proposed by Judson and Rabitz [3] in 1992. Inspired by biological evolution their idea involved a "closed-loop" concept in which direct experimental feedback from the quantum system is fed to a learning algorithm that is used to adaptively optimize the shaped femtosecond pulses until an optimal solution for the initially defined task is obtained. This methodology termed "adaptive femtosecond quantum control" only requires experimental feedback, while a priori knowledge about the molecular Hamiltonian is not necessary. The practicability of this new technique has been demonstrated in many experiments. For instance chemical bonds of molecules in the gas phase were selectively broken and the photoexcitation of molecular systems could be optimized. However, successful control over more complicated rearrangement reactions in a molecular system or the selective formation of chemical bonds has not been reported up to now.

The goal of this thesis is to bring quantum control closer to the realization of the

dream to be able to selectively influence the formation of chemical substances by the use of tailored femtosecond laser pulses. This has been pursued by taking two different approaches. On the one hand, as most preparative chemistry is performed in the condensed phase because high enough particle densities leads to decent product yields, it is necessary to transfer quantum control to the liquid phase. So far only control over photoexcitation [4, 5], -deexcitation [6] and isomerization [7] has been demonstrated by our group. The next step is the selective manipulation of more complicated molecular rearrangement reactions including dissociation leading to photoproducts with an altered atomic composition. Therefore the photo-induced Wolff rearrangement of a diazonaphthoquinone (DNQ) compound has been investigated by the use of shaped femtosecond laser pulses. For this experiment ultrafast vibrational spectroscopy was applied to monitor the outcome of the reaction. On the other hand, the selective laser-induced formation of chemical bonds has not been reported up to now. Starting from atoms and small molecules adsorbed on a metal surface, the formation of molecular bonds by interaction with specifically tailored laser pulses is shown in the second part of this thesis. The organization of this thesis is then as follows.

First of all, the theoretical concepts underlying this thesis are briefly described in Chapter 2, including an introduction to the concepts of quantum control, the mathematical description of femtosecond laser pulses and the nonlinear processes that are exploited at different points of this work. Furthermore, the fundamentals of the electronic structure and vibrations of polyatomic molecules and an introduction into ultrafast vibrational spectroscopy are provided for a better understanding of the spectroscopic signals observed and relevant to this work. Chapter 3 deals with the experimental methods, especially the pulse shaper and spectroscopic means for the detection of the light-matter interaction outcome employed for the realization of quantum control. A setup for the generation of ultrashort pulses in the mid-infrared was built within the scope of this work to perform time-resolved vibrational spectroscopy. Since it is the first time that a pump-probe signal in the mid-infrared is used in the context of quantum control a more detailed description of the experimental setup is provided in Chapter 4. The molecular system chosen for the demonstration of this concept - a diazonaphthoquinone compound, performing a photoinduced Wolff rearrangement which is important for photolithographic applications - is studied in great detail by using visible, steady state and time-resolved infrared spectroscopy together with quantum chemical calculations in Chapter 5. Open-loop and closed-loop control schemes are employed in Chapter 6 with the aim to increase the Wolff rearrangement photoproduct yield of diazonaphthoquinone.

Furthermore it is shown in Chapter 7 that reactions between the small reactant molecules hydrogen and carbon monoxide on a catalyst metal surface can be induced by femtosecond laser pulses providing the energy necessary to form several different product molecules. These reactions are systematically studied by variations of important parameters such as reactant molecules, catalyst metal and laser properties. The outcome of these reactions is then selectively optimized in Chapter 8 by adaptive femtosecond quantum control demonstrating that photoselectivity over different bond-forming reaction channels can be achieved with tailored femtosecond laser pulses. These experiments represent the first application of quantum control to a surface reaction. Finally a summary is given in Chapter 9

2 Theoretical concepts

The subject presented in this thesis is the selective control of photoinduced chemical reactions with femtosecond laser pulses. In this work it will be shown how the outcome of chemical reactions can be steered into a desired direction by the application of suitably shaped electric fields. This concept is called "quantum control", or "coherent control". The fundamental concepts used in quantum control are introduced in Section 2.1. In the following a mathematical description of femtosecond laser pulses, the basic tool for quantum control, is given (Section 2.2). Frequency conversion by utilization of nonlinear effects is important when ultraviolet or infrared wavelengths are needed for exciting or probing molecular dynamics and the outcome of a chemical reaction. The underlying theory is briefly outlined in Section 2.3. The last two sections of this chapter deal with the electronic structure and vibrations of molecular systems (Section 2.4) and the technique of ultrafast infrared spectroscopy (Section 2.5), which is employed in parts of this work to investigate an ultrafast chemical reaction.

2.1 Quantum control

Traditionally, in chemistry the outcome of chemical reactions can be influenced and controlled within certain boundaries by changing the macroscopic variables temperature, concentration and pressure. This aims at shifting the chemical equilibrium between reactants and products towards the desired direction. The use of appropriate catalysts can exploit molecular properties to influence a chemical reaction. However, general control over the microscopic reaction pathways is not achievable by application of these methods.

In conjunction with the above considerations, light can be a new means of starting a chemical reaction and altering the outcome by overcoming barriers leading to new reaction pathways, that otherwise would not be accessible. One of the first approaches was to adjust the spectrally narrow radiation of a laser to a local vibrational mode of a particular chemical bond to selectively excite this mode to achieve dissociation [8, 9]. Unfortunately, for the majority of molecules this concept fails, because the deposited energy does not stay localized in the selected mode. Due to couplings between molecular modes the energy is redistributed to other molecular modes. This process, called intramolecular vibrational energy redistribution (IVR) effectively leads to the loss of selectivity [10–12] and the net effect of the laser excitation is heating the entire molecule. Already for isolated molecules in the gas phase IVR is present, and for molecules in the liquid phase many more redistribution channels due to interaction with other molecules and with the solvent exist.

However, a different approach exploiting the coherence properties of laser radiation

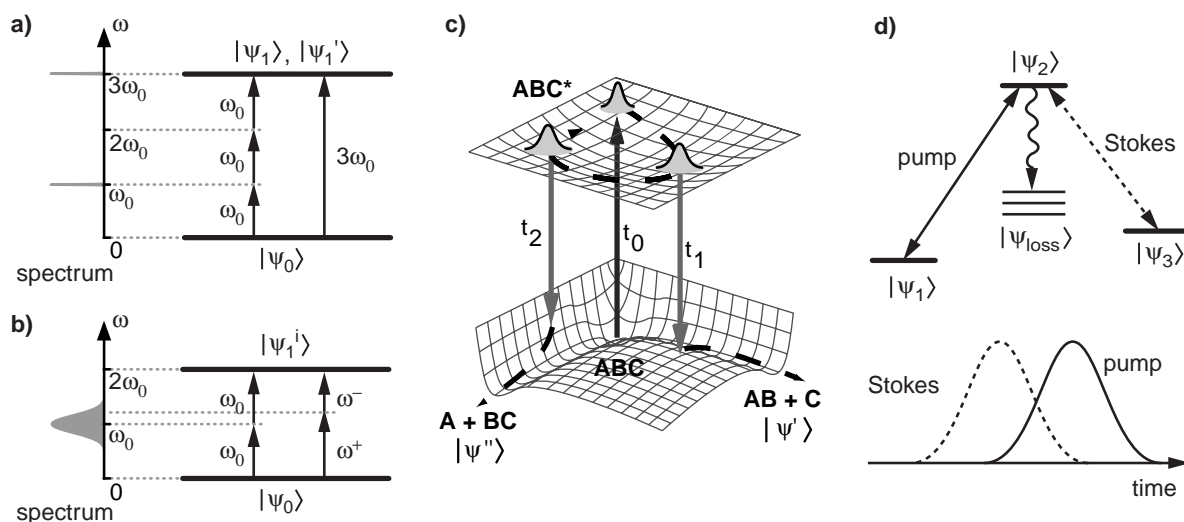


Figure 2.1: Quantum control concepts. a) The Brumer-Shapiro method stresses the quantum mechanical interference between the different pathways connecting the initial state $|\Psi_0\rangle$ to the energetically degenerate final states $|\Psi_1\rangle$ and $|\Psi_1'\rangle$. By changing the relative phase of the lasers at the frequencies ω_0 and $3\omega_0$ control over the final state populations is possible. b) For two-photon excitations with broadband laser pulses, many combinations of frequencies lead to $2\omega_0$. The spectral phase determines how much population ends up in the excited state. c) In the Tannor-Kosloff-Rice pump-dump scheme, the pump pulse initiates wavepacket motion on the excited potential energy surface. A correctly timed dump pulse can transfer the system to the desired final state. d) The STIRAP scheme uses a two-pulse sequence to couple the states of a Λ -type system in such a way, that complete population transfer to the final state $|\Psi_3\rangle$ is achieved.

has led to a variety of control concepts and the emergence of the field of "quantum control" or "coherent control". The goal is to transform a given initial quantum mechanical wavefunction into a desired target wavefunction through the coherent (i.e. phase preserving) interaction of the system with the appropriate electric fields. Control over the reaction product distribution is achieved by using constructive interference and destructive interference between different reaction pathways for obtaining the favored and suppressing unwanted products.

2.1.1 Single parameter concepts

Three different concepts can be distinguished from a historical perspective, although they only look at the quantum control problem from different perspectives, e.g. the frequency-domain or the time-domain, and all of them rely on quantum mechanical interference effects. The scheme that was proposed by Brumer and Shapiro in 1986 [13–17] stresses interference in the frequency domain. In a quantum system the initial state $|\Psi_0\rangle$ and energetically degenerate final states $|\Psi_1\rangle$ and $|\Psi_1'\rangle$ can be coupled via one photon with energy $3\hbar\omega_0$ or three photons with energy $\hbar\omega_0$ (see Fig. 2.1a). The relative phase between the two excitation lasers at frequencies ω_0 and $3\omega_0$ determines the population in the

final states $|\Psi_1\rangle$ and $|\Psi'_1\rangle$ through constructive or destructive interference of the two pathways. Thus, modulation of the relative phase enables control over the final state population. But in addition there has to be a molecular phase lag [18–20] between the two different pathways, a system-inherent property, that is determining the degree of control. For achieving constructive interference for one and destructive or at least partially destructive interference for the other reaction channel both the molecular phase and the relative phase of the laser fields have to be taken into account. The realization of the Brumer-Shapiro control concept was shown in 1990 [21] for atoms and later also for small molecules [22, 23]. Within the broad spectrum of a femtosecond laser pulse many frequency combinations can contribute to multiphoton excitations (Fig. 2.1b) and the interference of these many pathways can be controlled by the manipulation of the spectral phase. The experiments and theoretical calculations of the group of Silberberg on two-photon excitation of Cs atoms demonstrate that certain "dark pulses" can be found, that do not excite the atom at all [24, 25].

A different approach, proposed by Tannor, Kosloff and Rice [26–29] can be more intuitively understood in the time-domain. It is illustrated in Fig. 2.1c. A femtosecond laser pulse (pump pulse) excites a molecular system ABC from the ground state to an electronically excited potential energy surface (PES) ABC* at time t_0 . On this PES a vibrational wavepacket is then created by coherent superposition of the vibrational eigenstates. The wavepacket evolves in time according to the shape of the PES and can reach different molecular configurations at different times t_1 and t_2 , that are connected with different dissociation product channels AB + C or A + BC. An appropriately timed second femtosecond laser pulse (dump pulse) can transfer the population back to the ground state to reach the desired reaction product channel $|\Psi'\rangle$ or $|\Psi''\rangle$. Therefore, this method is called "pump-dump-control". One also has to keep in mind, that not only the delay time between the pump and dump pulses, but also the wavelengths have to be chosen correctly to fit the energy difference between the involved potential energy surfaces of the investigated molecule. The applicability of this technique was first demonstrated in the groups of Gerber and Zewail [30–32] in the early 1990s.

The third control scheme makes use of adiabatic passage techniques [33, 34], which enable complete population transfer in a three-state Λ -type quantum system. In stimulated Raman adiabatic passage (STIRAP), the levels $|\Psi_1\rangle$, $|\Psi_2\rangle$ and $|\Psi_3\rangle$ are coupled by two laser pulses, called pump and Stokes pulse. Complete population transfer can be achieved by slightly overlapping pulses but counterintuitive pulse ordering, meaning the Stokes pulse arrives before the pump pulse (see Fig. 2.1d). Experimentally this pulse sequence can be either realized by time delayed pulses or spatially separated, slightly overlapping cw-laser fields, so that particles crossing the laser beams experience a sequence of two laser fields. It can be shown, that the population in the intermediate state $|\Psi_2\rangle$ remains zero throughout the experiment, which avoids population decay to unwanted channels $|\Psi_{loss}\rangle$.

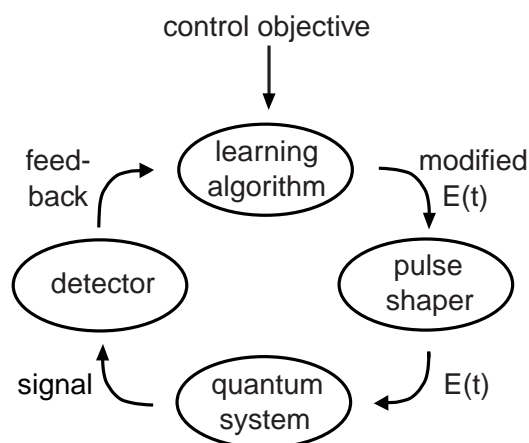
The quantum control schemes discussed so far work with the variation of only a single parameter such as the relative phase of two laser fields or the delay time of two laser pulses. A more general approach would be to include more than one variable in order to achieve better control results. This was already suggested by Tannor and Rice in 1985 [26]. In principle the wavepacket, formed after excitation with an ultrashort laser

pulse could be guided by a specifically shaped pulse all the time during its evolution on the excited state potential energy surface. Thus, the wavepacket would not propagate freely, as governed by the shape of the energy surface, but its motion would constantly be adjusted through the interaction with the light field, leading to an optimized reaction outcome. Higher-lying potential energy surfaces could be included in the process of finding the best pathway. To solve the problem of many-parameter quantum control and finding the appropriate electric fields for the desired goal, the concept of optimal control theory was developed by Rabitz and coworkers [35, 36] as well as Kosloff and coworkers [37] and also other groups [38–40]. Comprehensive introductions to the field, including a mathematical treatment of optimal control theory and other optimization schemes can be found in Refs. [28, 29]. The quantum-mechanical equations of motion form the basis of the optimization schemes in optimal control theory. Therefore, the molecular Hamiltonian and the shape of the PESs have to be known to a sufficiently accurate degree. This is only the case for small molecular systems, where exact calculations can be performed with acceptable accuracy and numerical effort. In larger systems more degrees of freedom are involved and the complexity and dimensionality of the PESs increases, which makes precise theoretical calculations a very difficult task. In addition, it might be difficult to generate the calculated optimal control fields in an experiment due to limitations of the pulse shaping process or the spectral and temporal characteristics of the laser pulses at hand. As a consequence, the approach to calculate the needed control fields and subsequent application in an experiment is in general not feasible. A more general method for the control of complex molecular systems under laboratory conditions is necessary.

2.1.2 Adaptive quantum control

In their pioneering work "Teaching lasers to control molecules" from 1992 Judson and Rabitz [3] suggested a seminal scheme, that circumvents the above discussed problems, concerning the calculation and experimental implementation of optimal electric fields. A closed-loop setup is employed, in which the optimal pulse shape can be obtained by an

Figure 2.2: Closed-loop quantum control. A control objective is assigned to a learning algorithm, which then finds the optimal electric field for the control objective. This is achieved by generation of electric fields $E(t)$ with a computer-controlled pulse shaper and direct detection of the fields' impact on a quantum system. This information is then used as feedback for the algorithm, which iteratively improves the electric field until the optimum is reached.



iterative procedure, where the experimental output is included in the optimization process without the need for a-priori knowledge of the molecular Hamiltonian (Fig. 2.2). A quantum system is excited by a series of differently shaped laser pulses. The experimentally measured outcome (e.g. photoproduct yield) of the photoinduced reaction is then evaluated by a learning algorithm with respect to the defined control objective. Hence, during the optimization the learning algorithm tests other pulse shapes and so the shape of the electric field is improved step by step to achieve the control goal. Common terms for this concept are "adaptive femtosecond quantum control", "optimal control experiment" or "closed loop control". The electric field, that provides the best result for a defined control goal is called the optimal pulse. The optimal control approach is in fact the most general realization of the coherent manipulation of light-matter interaction, as it includes in principle all single parameter scenarios, like pump-dump and others. Many of these effects may be utilized by the learning algorithm during the optimization to find the best pulse shape. As a consequence, in the multi-parameter control scheme the underlying control mechanism is very often not revealed. This is sometimes called the problem of inversion [41] and remains a big challenge for experimentalists and theorists in the field of optimal control.

By now the optimal control concept has found many applications in physics, chemistry and biology. Some of them aim at optimizing the properties of the laser field itself, like the adaptive compression of femtosecond laser pulses [42–47], the subwavelength distribution of nanoscopic optical near-fields [48], the polarization state of ultrashort laser pulses [49, 50] or nonlinear processes like the generation of high harmonics [51–57]. The adaptive optimization of chemical reactions represents the most important application. In the gas phase, molecular photodissociation [41, 58–67], rearrangement [61] and isotope-selective ionization and fragmentation reactions of dimers [68–72], to name only a few were optimized by the application of optimally shaped pulses. In the condensed phase, optimal control was among others applied to processes like fluorescence [5, 73–79], photochemical discrimination of molecules [4] and most recently photoisomerization reactions [6, 7, 80–84]. Many comprehensive reviews exist which deal with different fields of application [51, 85–92].

2.2 Mathematical description of femtosecond laser pulses

The basic tool in ultrafast spectroscopy for investigating fast molecular processes and in the field of optimal control for the control of chemical reactions are femtosecond laser pulses. These pulses consist of many electromagnetic waves with different oscillation frequencies. Superposition of these waves produces a beat pattern at a given point in space only during a short time interval with a duration of typically some tens of femtoseconds. A mathematical description of their spectral and temporal properties will be given in the following section (Section 2.2.1). For every application of ultrashort laser pulses, in addition the spatial properties are of practical relevance. Thus, the spatial propagation through media (Section 2.2.2) and laser beam properties (Section 2.2.3) will be discussed.

The electromagnetic fields $\mathbf{E}(t, \mathbf{r})$ that will be considered in the following have to obey the inhomogeneous wave equation, which in spatially uniform and nonmagnetic media takes the form [93]

$$-\nabla \times (\nabla \times \mathbf{E}(t, \mathbf{r})) - \frac{1}{c^2} \frac{\partial^2}{\partial t^2} \mathbf{E}(t, \mathbf{r}) = \mu_0 \frac{\partial^2}{\partial t^2} \mathbf{P}(t, \mathbf{r}), \quad (2.1)$$

where $c = 1/\sqrt{\varepsilon_0 \mu_0}$ is the vacuum velocity of light, and μ_0 and ε_0 are the magnetic permeability and the permittivity of vacuum, respectively. The induced dielectric polarization $\mathbf{P}(t, \mathbf{r})$ describes the interaction of the external electric field and the medium. Both quantities, the electric field as well as the dielectric polarization depend on space and time. For this thesis, only cases where $\mathbf{E}(t, \mathbf{r})$ can be separated into a function $u^+(\mathbf{r})$ containing the spatial beam profile of the pulse, and a term $\mathbf{E}^+(t, z)$ which describes the temporal structure and the propagation along the z -axis, as well as the polarization state of the electric field will be regarded:

$$\mathbf{E}(t, \mathbf{r}) \propto u^+(\mathbf{r}) \mathbf{E}^+(t, z) + \text{c.c.}, \quad (2.2)$$

where the expression c.c. stands for the complex conjugate of the preceding terms.

2.2.1 Description in the time and frequency domain

For the description of the temporal and spectral properties of ultrashort laser pulses in this section, only the time dependence of the electric field $\mathbf{E}^+(t, z)$ is considered, since the discussion can be limited to a fixed point in space. Also the vectorial properties of the field will be neglected for now. The electric field can be discussed in either the time domain or analogously in the frequency domain, related by the Fourier transformation (denoted by \mathcal{F}):

$$E(\omega) = \frac{1}{\sqrt{2\pi}} \int_{-\infty}^{\infty} E(t) e^{-i\omega t} dt = \mathcal{F}\{E(t)\}. \quad (2.3)$$

The inverse Fourier transform (denoted by \mathcal{F}^{-1})

$$E(t) = \frac{1}{\sqrt{2\pi}} \int_{-\infty}^{\infty} E(\omega) e^{i\omega t} d\omega = \mathcal{F}^{-1}\{E(\omega)\}. \quad (2.4)$$

returns the electric field $E(t)$ in the time domain. Since $E(t)$ is a real-valued quantity, the symmetry relation

$$E(\omega) = E^*(-\omega), \quad (2.5)$$

where the star indicates complex conjugation, is valid for the electric field in the spectral domain. Therefore, a reduced description, which takes only the contributions at positive frequencies into account is sufficient to fully characterize the electric field:

$$E^+(\omega) = \begin{cases} E(\omega) & \text{if } \omega \geq 0, \\ 0 & \text{if } \omega < 0. \end{cases} \quad (2.6)$$

This expression can be separated into a real-valued spectral amplitude (or envelope) function $A(\omega)$ and an exponential term containing the spectral phase function $\Phi(\omega)$:

$$E^+(\omega) = A(\omega) e^{-i\Phi(\omega)} . \quad (2.7)$$

It is often useful to expand the phase into a Taylor series. The spectral amplitude is usually centered around the carrier frequency (center frequency) ω_0 , so the expansion is most conveniently performed according to

$$\Phi(\omega) = \sum_{j=0}^{\infty} \frac{b_j}{j!} (\omega - \omega_0)^j , \quad (2.8)$$

with the spectral phase coefficients

$$b_j = \left. \frac{d^j \Phi(\omega)}{d\omega^j} \right|_{\omega=\omega_0} . \quad (2.9)$$

The zeroth-order coefficient is a constant phase term, called the absolute phase b_0 , while the coefficient of first order is equivalent to a translation of the laser pulse in the time domain. The higher order coefficients are responsible for changes in the temporal structure of the pulse.

The electric field $E^+(\omega)$ is connected to its Fourier counterpart $E^+(t)$ by the relations:

$$E^+(\omega) = \mathcal{F}\{E^+(t)\} , \quad (2.10)$$

$$E^+(t) = \mathcal{F}^{-1}\{E^+(\omega)\} . \quad (2.11)$$

For $E^+(\omega)$ it is therefore sufficient to restrict the temporal electric field $E^+(t)$ to the complex-valued function

$$E^+(t) = A(t) e^{i\Phi(t)} , \quad (2.12)$$

which comprises the real-valued temporal amplitude $A(t)$ (the envelope of the electric field) and the temporal phase function $\Phi(t)$. In the same fashion as for the spectral phase, the temporal phase can be expressed in a Taylor expansion around time zero $t = 0$

$$\Phi(t) = \sum_{j=0}^{\infty} \frac{a_j}{j!} t^j , \quad (2.13)$$

with coefficients a_j defined as

$$a_j = \left. \frac{d^j \Phi(t)}{dt^j} \right|_{t=0} . \quad (2.14)$$

The zero order expansion coefficient a_0 describes a constant phase, also called absolute phase or carrier-envelope phase, and can be understood as the relation of the pulse envelope $A(t)$ with respect to the underlying oscillation. The first order coefficient a_1 is

identical to the carrier frequency ω_0 of the pulse. Therefore this linear oscillation term can be separated from the higher order contributions described by the function

$$\varphi(t) = \Phi(t) - \omega_0 t . \quad (2.15)$$

That leads to an expression for the temporal electric field with a complex amplitude function $\hat{A}(t)$, that can be written as

$$E^+(t) = A(t)e^{i\varphi(t)} \times e^{i\omega_0 t} = \hat{A}(t)e^{i\omega_0 t} . \quad (2.16)$$

This separation into envelope and carrier frequency is often used to simplify calculations of the temporal evolution or spatial propagation, but is only valid as long as the complex amplitude $\hat{A}(t)$ does not change by much within one optical cycle $T=2\pi/\omega_0$. That means, that this so-called slowly-varying-envelope-approximation (SVEA) can be used for all but very short pulses consisting of only a few optical cycles. The SVEA can be applied in all experiments discussed in this thesis.

Another important quantity used in the description of femtosecond laser pulses in the time space is the momentary or instantaneous frequency. It is defined as the derivative of the temporal phase with respect to time [93])

$$\omega_m(t) = \frac{d\Phi(t)}{dt} = \omega_0 + \frac{d\varphi(t)}{dt} . \quad (2.17)$$

It is becoming obvious, that the reduced phase function, obtained with the SVEA describes the deviation of the actual momentary oscillation frequency from the center frequency ω_0 . Pulses for which the momentary frequency $\omega_m(t)$ is constant in time are called unchirped. This is the case, when $a_j = 0$ for all $j \geq 2$ in the Taylor expansion of the temporal phase. If $\omega_m(t)$ is increasing in time (i.e., $d\omega_m(t)/dt > 0$), the pulse is said to be up-chirped, while one speaks of down-chirped pulses if $\omega_m(t)$ is decreasing in time (i.e., $d\omega_m(t)/dt < 0$). The special case of $a_2 \neq 0$ and $a_j = 0$ for all $j \geq 3$, is called linear chirp, because the momentary frequency changes linearly with time.

The connection from the reduced field $E^+(t)$ to the full electric field $E(t)$ can be established by the expression

$$E(t) = 2A(t) \cos(\Phi(t)) = A(t) e^{i\Phi(t)} + \text{c.c.} = E^+(t) + E^-(t) . \quad (2.18)$$

Another important quantity is the temporal intensity $I(t)$. In the time domain it is defined as the average of $E^2(t)$ over one oscillation period

$$I(t) = c_o \varepsilon_0 n \frac{1}{T} \int_{t-T/2}^{t+T/2} E^2(t') dt' = 2c_o \varepsilon_0 n A(t)^2 . \quad (2.19)$$

The above equivalence is only true as long as the SVEA is valid. The spectral intensity can be written in analogy to Eq. (2.19) as

$$I(\omega) = 2c_o \varepsilon_0 n A(\omega)^2 . \quad (2.20)$$

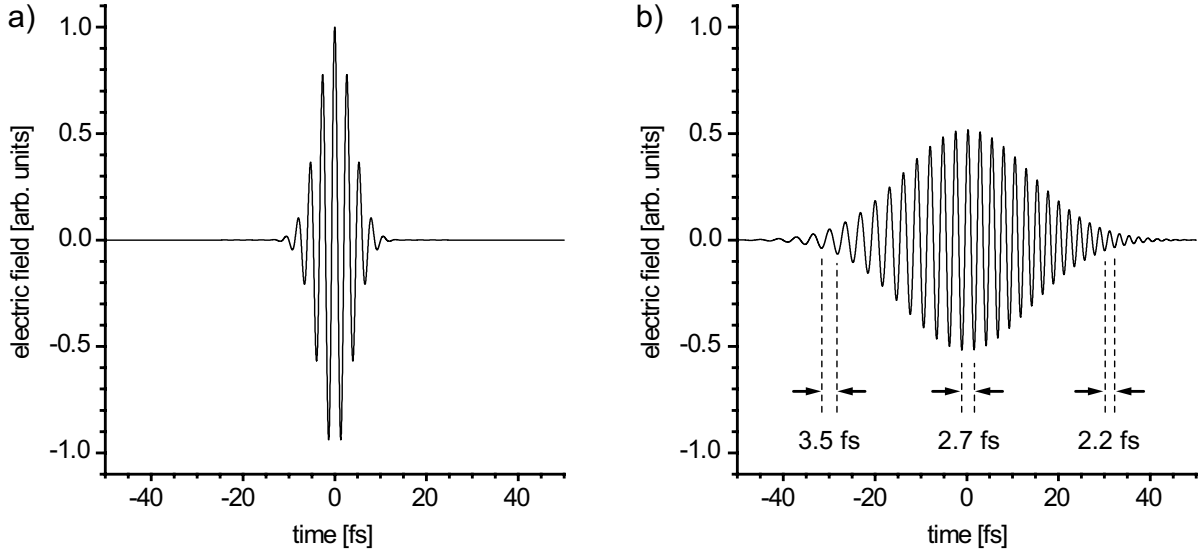


Figure 2.3: Temporal electric field of femtosecond laser pulses with a Gaussian-shaped spectrum centered around 800 nm ($\omega_0=2.35$ rad/fs) with a FWHM of 150 nm ($\Delta\omega=0.445$ rad/fs). a) bandwidth-limited pulse with $\Phi(\omega)=0$. b) up-chirped pulse with $\Phi(\omega) = \frac{1}{2} b_2 (\omega - \omega_0)$ with $b_2=50$ fs². The up-chirp becomes apparent in the decreasing oscillation period of the electric field.

Additional useful parameters in the description of femtosecond laser pulses are the pulse duration Δt and the spectral bandwidth $\Delta\omega$. They are usually defined as the full width at half maximum (FWHM) of the respective intensity distributions

$$\Delta\omega = FWHM\{I(\omega)\}, \quad (2.21)$$

$$\Delta t = FWHM\{I(t)\}. \quad (2.22)$$

Only if the intensity profiles have well defined shapes, such as Gaussian or sech^2 this is meaningful. Both parameters are not independent of each other, because the Fourier transform connects time and frequency space. The product of the pulse duration and spectral bandwidth, as defined in the above Eqs. (2.21) and (2.22) is called the time-bandwidth product $\Delta\omega\Delta t$ and represents a lower limit

$$\Delta\omega\Delta t \geq 2\pi c_B, \quad (2.23)$$

depending on the exact shape of the intensity profiles. The constant c_B is for example $4 \ln(2)/(2\pi) = 0.441$ for a Gaussian spectral distribution, while it is $c_B = 0.315$ for a sech^2 -shaped spectrum. A pulse that exactly reaches this lower limit is called bandwidth-limited, Fourier-limited or transform-limited.

The temporal electric field of a Gaussian-shaped spectral distribution centered around 800 nm ($\omega_0=2.35$ rad/fs) with a FWHM of 150 nm ($\Delta\omega=0.445$ rad/fs) is shown in Fig. 2.3. For zero spectral phase (all b_j are equal to zero) this results in the bandwidth-limited 6.2 fs pulse depicted in Fig. 2.3a. When quadratic spectral phase ($\Phi(\omega) = \frac{1}{2} b_2 (\omega - \omega_0)$ with $b_2=50$ fs²) is applied, a linearly chirped pulse with linearly rising momentary frequency which is elongated in time is obtained (Fig. 2.3b). This is reflected in the decreasing oscillation period of the electric field.

2.2.2 Spatial propagation and material dispersion

While in the last section only the temporal and spectral properties of femtosecond laser pulses were discussed, this section deals exclusively with the propagation properties of femtosecond laser radiation and the implications, when travelling through matter. In general material dispersion leads to the result, that the phase of the pulses is altered by the traversed medium. For now the spatial beam profile $u^+(\mathbf{r})$ in the complete electric field in Eq. (2.2) is again not considered (i.e., a plane wave is assumed), so that the wave equation (2.1) can be written as

$$\left(\frac{\partial^2}{\partial z^2} - \frac{1}{c^2} \frac{\partial^2}{\partial t^2}\right) E(t, z) = \mu_0 \frac{\partial^2}{\partial t^2} P(t, \mathbf{r}) . \quad (2.24)$$

Together with the linear relation between the polarization and the electric field, connected by the dielectric susceptibility $\chi(\omega)$ as known from classical electrodynamics, here written in the spectral domain

$$P(\omega, z) = \varepsilon_0 \chi(\omega) E(\omega, z) , \quad (2.25)$$

and Eq. (2.25) and the Fourier transform of Eq. (2.24) the wave equation can be expressed as

$$\left(\frac{\partial^2}{\partial z^2} + \frac{\omega^2}{c^2} [1 + \chi(\omega)]\right) E(\omega, z) = 0 . \quad (2.26)$$

Solutions for this equation are the traveling waves

$$E(\omega, z) = E^+(\omega, 0) e^{-ik(\omega)z} + \text{c.c.} = E^+(\omega, z) + E^-(\omega, z) , \quad (2.27)$$

in which the wavevector

$$k = \frac{\omega}{c} \tilde{n}(\omega) , \quad (2.28)$$

pointing to the z -direction contains the complex index of refraction

$$\tilde{n}(\omega) = n(\omega) - i\kappa(\omega) = \sqrt{1 + \chi(\omega)} . \quad (2.29)$$

The real part $n(\omega)$ describes refraction and dispersion, and the imaginary part $\kappa(\omega)$ is responsible for loss or gain in the medium.

In resemblance to the time domain, the rapid oscillations in space $\propto e^{-ik_0 z}$ can be factored out by [93]

$$E^+(\omega, z) = E^+(\omega, 0) e^{-ik(\omega)z} = E^+(\omega, 0) e^{-i\delta k z} \times e^{-ik_0 z} , \quad (2.30)$$

with $k_0 = n(\omega_0)\omega_0/c$ and δk given by a Taylor expansion

$$\delta k = \sum_{j=1}^{\infty} \frac{1}{j!} \left. \frac{d^j k}{d\omega^j} \right|_{\omega=\omega_0} (\omega - \omega_0)^j . \quad (2.31)$$

Under the assumption that the SVEA is valid, which means that the envelope of the pulse is not changing significantly while traveling a distance comparable with the wavelength $\lambda_0 = 2\pi/k_0$, the electric field can be described by introducing a complex amplitude function

$$\hat{A}(\omega, z) = E^+(\omega, 0) e^{-i\delta k z} = A(\omega, 0) e^{-i\Phi(\omega, 0)} e^{-i\delta k z} = A(\omega, 0) e^{-i\varphi(\omega, z)} \quad (2.32)$$

that comprises the reduced phase term $\varphi(\omega, z)$.

As a consequence, a pulse traveling through a dispersive medium of length L with index of refraction $n(\omega)$, acquires a spectral phase modulation according to

$$\Phi(\omega, L) = \Phi(\omega, 0) + kL = \Phi(\omega, 0) + \frac{\omega n(\omega) L}{c}. \quad (2.33)$$

The additional contribution due to propagation has to be included in the Taylor expansion (2.8) of the spectral phase, so that the coefficients b_j of Eq. (2.9) become

$$b_j = \left. \frac{d^j \Phi(\omega, L)}{d\omega^j} \right|_{\omega=\omega_0} = \left. \frac{d^j \Phi(\omega, 0)}{d\omega^j} \right|_{\omega=\omega_0} + \frac{L}{c} \left(j \frac{\partial^{j-1} n(\omega)}{\partial \omega^{j-1}} + \omega \frac{\partial^j n(\omega)}{\partial \omega^j} \right) \Big|_{\omega=\omega_0}. \quad (2.34)$$

In vacuum, i.e., $n(\omega)=1$ for all frequencies, only the zero-order and the first-order coefficients would be affected and experience a change by $k_0 L$ and by L/c , respectively. This means, that a constant phase $k_0 L$ is added and the pulse's maximum is temporally shifted by $\Delta t=L/c$ due to propagation from the position $z=0$ to $z=L$.

When propagating in a dispersive medium on the other hand, the first-order coefficient becomes

$$b_1 = \left. \frac{d\Phi(\omega, 0)}{d\omega} \right|_{\omega=\omega_0} + \frac{L}{c} \left(n + \omega \frac{dn(\omega)}{d\omega} \right) \Big|_{\omega=\omega_0} = \left. \frac{d\Phi(\omega, 0)}{d\omega} \right|_{\omega=\omega_0} + \frac{L}{v_g(\omega_0)}, \quad (2.35)$$

where the group velocity

$$v_g(\omega_0) = \left(\left. \frac{dk}{d\omega} \right|_{\omega=\omega_0} \right)^{-1} \quad (2.36)$$

describes the actual velocity of the pulse envelope in the dispersive material, and the group delay

$$\tau_g(\omega_0) = \frac{L}{v_g(\omega_0)} \quad (2.37)$$

is the time it takes the pulse to propagate through the medium.

The second-order coefficient includes the contribution

$$\frac{L}{c} \left(2 \frac{\partial n(\omega)}{\partial \omega} + \omega \frac{\partial^2 n(\omega)}{\partial \omega^2} \right) \Big|_{\omega=\omega_0} = \left. \frac{d\tau_g(\omega)}{d\omega} \right|_{\omega=\omega_0} \quad (2.38)$$

which is termed group-delay dispersion (GDD) and has a linear dependence with respect to the traversed distance in the medium. Therefore, by cancellation of L in Eq. (2.38) a

characteristic property of the dispersive material is obtained, the so-called group-velocity dispersion (GVD) parameter [93]

$$\text{GVD} = \frac{1}{c} \left(2 \frac{\partial n(\omega)}{\partial \omega} + \omega \frac{\partial^2 n(\omega)}{\partial \omega^2} \right) \Big|_{\omega=\omega_0} = \frac{d\left(\frac{1}{v_g(\omega)}\right)}{d\omega} \Big|_{\omega=\omega_0}. \quad (2.39)$$

The discussion in Sec. 2.2.1 showed that a spectral phase coefficient $b_2 \neq 0$ leads to linear chirp. Thus, the GVD parameter is a measure for the amount of linear chirp introduced by a dispersive material. Higher order coefficients are likewise responsible for higher order material dispersion, which results in more complicated distortion of the pulse. In practical applications, especially when working with broadband pulses, material dispersion leading to pulse broadening and phase modulation has to be taken into account.

2.2.3 Spatial beam properties

So far, only plane waves with infinite transverse beam diameter have been regarded as the solution of the wave equation. In reality this is incorrect and physically not meaningful, since such a wave would carry infinite energy. In the paraxial approximation, the transverse beam diameters are small compared to typical beam traveling distances. Solutions to this paraxial wave equation are, among others, Gaussian beams with transverse profiles given in Cartesian coordinates by

$$u^+(\mathbf{r}) = u_0 \frac{1}{\sqrt{1 + z^2/z_0^2}} e^{-i\psi(z)} e^{ik(x^2+y^2)/2R(z)} e^{-(x^2+y^2)/w^2(z)} \quad (2.40)$$

if the beam has a waist of radius w_0 at the position $z=0$. The parameters introduced in Eq. (2.40) are visualized in Fig. 2.4. The quantity

$$z_0 = \frac{\pi w_0^2}{\lambda}, \quad (2.41)$$

is called the Rayleigh range. It is a measure of the length of the waist region, because it describes the propagation interval after which the spot size

$$w(z) = w_0 \sqrt{1 + z^2/z_0^2} \quad (2.42)$$

has increased by a factor of $\sqrt{2}$ with respect to the beam waist w_0 . A beam is called collimated, if the beam diameter does not change significantly over the distances of interest, i.e., if these are smaller than the Rayleigh range.

The first phase term in Eq. (2.40) is called Guoy phase [95, 96]

$$\psi(z) = \arctan(z/z_0). \quad (2.43)$$

It changes only significantly in the vicinity of the beam waist, leading to an additional π phase shift of any beam propagating through a focus. In the second phase term the radius of curvature

$$R(z) = z + z_0^2/z, \quad (2.44)$$

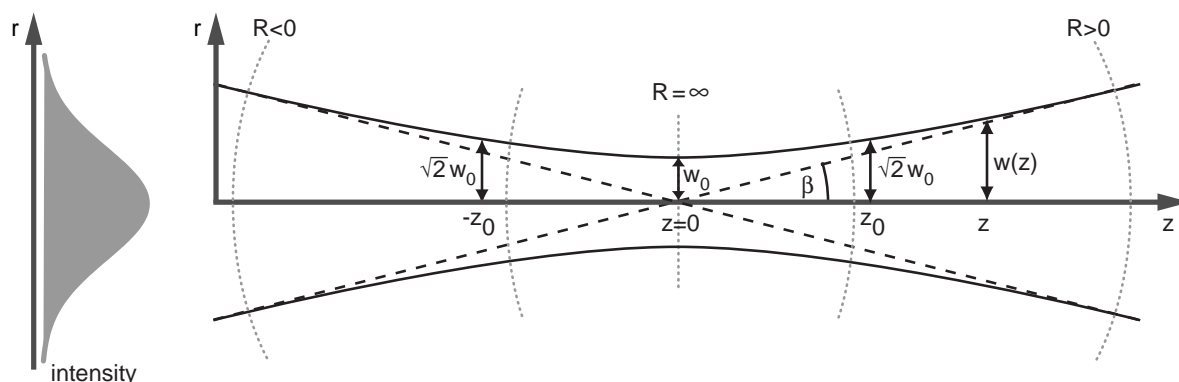


Figure 2.4: Propagation of a Gaussian beam. On the left, the intensity distribution of the lowest-order Gaussian beam is shown (gray solid) as a function of the transverse distance r from the axis. On the right, the propagation of the beam through a waist at $z=0$ is shown. The black hyperbolic lines mark the distances $w(z)$ from the axis where the electric field amplitude has dropped to a factor of $1/e$ with respect to the on-axis value. While at $z=0$, the waist $w(0)=w_0$ is smallest, it has reached a value of $w(z_0)=\sqrt{2}w_0$ at the Rayleigh range z_0 . The wavefront and its radius of curvature $R(z)$ are indicated by the dotted gray lines. In the far-field limit, $R(z)$ is equal to z , and the beam size increases linearly with the travelled distance, as is indicated by the dashed lines, which also denote the divergence angle β [94].

is contained, which is equivalent to the curvature of a spherical wave originating from the spot $z=0$. For large distances from the beam waist it becomes $R(z) \approx z$, and the divergence angle β can be approximated with $\beta \approx w(z)/z$, leading to the expression

$$w(z) \approx \frac{z\lambda}{\pi w_0} \quad (2.45)$$

for the spot size. If the spot size $w(f)$ is known for an incoming collimated beam at the position of a lens, the focal beam waist is

$$w_0 \approx \frac{f\lambda}{\pi w(f)}. \quad (2.46)$$

This rough estimate is very useful for practical applications, when the diameters of overlapping beams have to be matched or adjusted in a specific way. This is often the case in nonlinear frequency mixing processes for laser pulse characterization or for the generation of ultrashort pulses in other frequency regions, which will be discussed in the next section.

2.3 Frequency conversion

Femtosecond laser pulses are commonly generated in the solid state material Titanium-Sapphire (Ti:Sa) and operate in the near-infrared region around 800 nm. However, for many experiments other wavelengths towards the ultraviolet, visible or mid-infrared are required for exciting and probing the molecular system to be studied. This can be

achieved by utilizing nonlinear optical processes (Section 2.3.1). The conditions under which efficient frequency conversion can be achieved are discussed in Section 2.3.2, and examples of frequently used nonlinear processes are given in Section 2.3.3.

2.3.1 Nonlinear polarization

When ultrashort laser pulses, having high enough intensities, propagate through a medium it is not sufficient to describe the response of the medium in the linear regime only, due to the nonlinearity of the electron binding forces within the atoms at high field intensities. The nonlinear dependence of the polarization on the electric field can be expressed as

$$P(\omega) = \varepsilon_0 \sum_{j=1}^{\infty} \chi^{(j)} E(\omega)^j, \quad (2.47)$$

with the dielectric susceptibilities $\chi^{(j)}$ [97–99]. In general the electric field and the polarization are vectorial quantities and therefore each susceptibility $\chi^{(j)}$ of j th order is a tensor of rank $j + 1$. The second-order polarization component pointing into the y -direction can thus be calculated with

$$P_y^{(2)}(\omega_q) = \varepsilon_0 \sum_{jk} \sum_{(nm)} \chi_{yjk}^{(2)}(-\omega_q; \omega_n, \omega_m) E_{1,j}(\omega_n) E_{2,k}(\omega_m), \quad (2.48)$$

where the summation is carried out over all $j, k = x, y, z$, and over all frequencies ω_n and ω_m with the condition $\omega_n + \omega_m = \omega_q$. New frequencies are generated, due to the interaction of the electric fields on the right hand side of Eq. (2.48) with the nonlinear medium. Since the time dependence of the fields $E(\omega_n)$ and $E(\omega_m)$ is associated with the exponential terms $e^{-i\omega_n t}$ and $e^{-i\omega_m t}$ the time dependence of the product of the fields is $e^{-i(\omega_n + \omega_m)t}$, thus the product of the electric fields leads to a contribution to the nonlinear polarization oscillating at the frequency $\omega_n + \omega_m$.

2.3.2 Phase matching

For the frequency conversion process, e.g. in a $\chi^{(2)}$ medium from the frequencies ω_n and ω_m to yield ω_q (Fig. 2.5a) to be highly efficient, both energy conservation and momentum conservation

$$\omega_q = \omega_n + \omega_m \quad (2.49)$$

$$k_q = k_n + k_m, \quad (2.50)$$

where the k_i are the respective wavevectors, has to be fulfilled. Without momentum conservation, there will be only periodically oscillating energy transfer between the initial field and the resulting fields in the nonlinear medium, because the generated wave at some point in space z_0 , having propagated to some other point z_1 will be out of phase with respect to the wave generated at z_1 . This so-called phase mismatch can be described as

$$\Delta k = k_q - k_n - k_m. \quad (2.51)$$

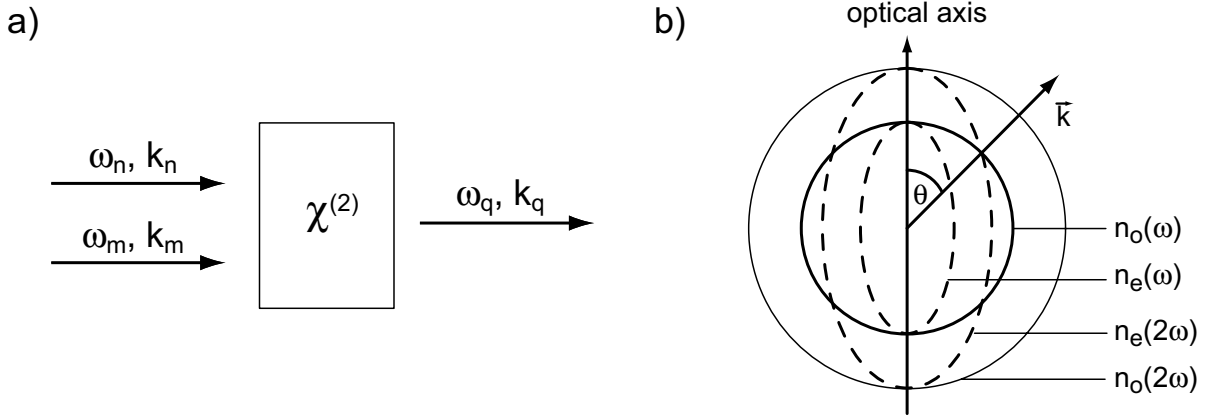


Figure 2.5: a) Frequency conversion in a $\chi^{(2)}$ -process. The incoming fields ω_n and ω_m are mixed in such a way, that the frequency ω_q is generated. b) Phase matching in a negative uniaxial crystal. The circles show the ordinary indices of refraction n_o for a frequency ω and for its second harmonic 2ω , while the ellipses show the corresponding extraordinary indices n_e . The propagation is chosen along the direction of the intersection point, so that $n_o(\omega) = n_e(2\omega)$ and phase matching is achieved.

Under neglect of absorption in the medium and substitution of Eq. (2.28), the energy conservation law can be expressed as

$$\frac{k_q}{n(\omega_q)} = \frac{k_n}{n(\omega_n)} + \frac{k_m}{n(\omega_m)}. \quad (2.52)$$

Usually the three indices of refraction $n(\omega_i)$ are not identical due to material dispersion. Therefore, e.g. uniaxial birefringent crystals are employed, where the existence of ordinary and extraordinary waves with different indices of refraction for a given wavelength enables to overcome this problem. In birefringent crystals, the independent polarization directions in the xy -plane of a wave propagating in the z -direction can have different phase velocities $v_p(\omega) = c/n(\omega)$, depending on the orientation of the crystal. Birefringent materials have at least one axis of anisotropy (optical axis). The polarization component of the electric field perpendicular to the optical axis is called ordinary, while the one parallel to the optical axis is called extraordinary. The crystal orientation and the polarization directions of the fields can be chosen, such that "phase-matching", i.e. $\Delta k = 0$ for a certain wavelength is achieved. Two types of phase matching geometries are commonly used. In Type I both incoming waves are ordinary and the resulting wave has orthogonal polarization, while in Type II the incoming waves have orthogonal polarization. The extraordinary index of refraction can be altered by changing the angle θ between the optical axis and the direction of propagation of the waves to match the desired value:

$$n_e(\omega, \theta) = \frac{n_o(\omega) n_e(\omega)}{\sqrt{n_o(\omega)^2 \sin^2 \theta + n_e(\omega)^2 \cos^2 \theta}}. \quad (2.53)$$

As illustrated in Fig. 2.5b, the extraordinary index can adopt values between $n_e(\omega, 0) = n_o(\omega)$ and $n_e(\omega, 90^\circ) = n_e(\omega)$ by tuning the angle θ . In the case of second-harmonic

generation for instance the extraordinary index can be chosen to be $n_o(\omega)=n_e(2\omega)$ to fulfill the phase-matching condition.

2.3.3 Nonlinear processes

This section intends to give a short overview of the different nonlinear processes [97–99], that are exploited within the scope of this thesis. In Fig. 2.6a-d these processes and the involved frequencies together with the required order of nonlinearity ($\chi^{(2)}$, $\chi^{(3)}$) are illustrated.

Sum-frequency / Difference-frequency generation

For sum-frequency generation (SFG) in a type I phase-matched process, the wave with the highest frequency is the extraordinary wave and polarized in the y -direction. In this case Eq. (2.48) simplifies to

$$P_y^{(2)}(\omega_q) = \varepsilon_0 \sum_{(nm)} \chi_{yxx}^{(2)}(-\omega_q; \omega_n, \omega_m) E_{1,x}(\omega_n) E_{2,x}(\omega_m) . \quad (2.54)$$

For femtosecond pulses, which have a broad spectrum, one has to remember that phase matching can only be achieved for one wavelength. Under the assumption, that the appropriate experimental conditions for efficient phase-matching for all accessible frequencies can be chosen and that the susceptibilities can be assumed to be independent of frequency, after Fourier transformation an expression for the electric field in the time domain can be derived:

$$E_q^{(2)}(t) = \varepsilon_0 \chi^{(2)} E_1(t) E_2(t) . \quad (2.55)$$

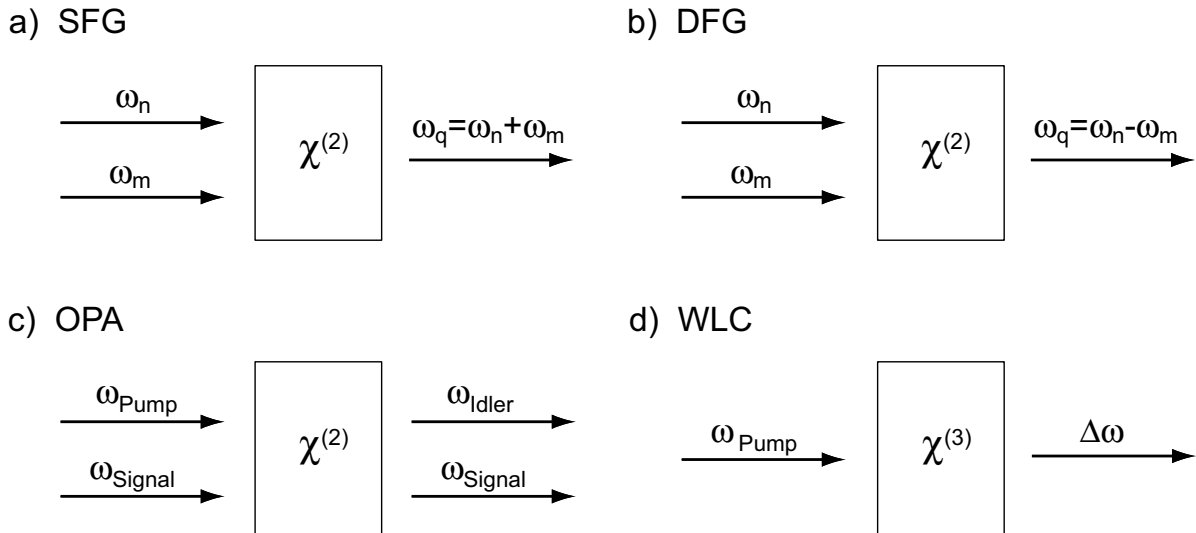


Figure 2.6: Examples of nonlinear processes. a) Sum-frequency generation (SFG). b) Difference-frequency generation (DFG). c) Optical parametric amplification. d) Supercontinuum or white-light-continuum (WLC) generation in a $\chi^{(3)}$ process.

This relation is valid for both, sum-frequency generation and difference-frequency generation (DFG), depending on the polarizations of the incoming waves. Thus, either the SFG or DFG process is phase-matched for a specific situation. The intensity of the generated fields, $E_q^{SFG}(t)$ or $E_q^{DFG}(t)$ is proportional to the product $I_1(t)I_2(t)$. The signal, that can be detected by a photodiode is the time integral

$$S^{SFG/DFG} \propto \int_{-\infty}^{\infty} |E_q^{SFG/DFG}(t)|^2 dt \propto \int_{-\infty}^{\infty} I_1(t)I_2(t) dt . \quad (2.56)$$

A special case is the one of second-harmonic generation (SHG), in which the fields $E_1(t)=E_2(t)$ are identical. Therefore, the overall second-harmonic yield depends quadratically on the intensity of the fundamental field.

Optical parametric amplification

The optical nonlinearity responsible for SFG, DFG or SHG can also be used to amplify weak optical signals [98, 99]. The basic configuration (Fig. 2.6c) involves a weak seed wave at frequency ω_S called "Signal", that is incident on a nonlinear optical crystal together with an intense Pump wave at ω_P . The amplification of the Signal wave at ω_S is accompanied by the generation of the so-called "Idler" wave at $\omega_I = \omega_P - \omega_S$. Power is transferred from the intense Pump wave to the weaker Signal and Idler waves. This process is similar to DFG, with the difference that parametric amplification is considered to be initiated by a single pump beam, while DFG is initiated by two pump beams of more or less the same intensities.

Starting from the nonlinear wave equation (2.1), a system of coupled differential equations for the electric fields E_j describing the interaction of the three waves can be derived

$$\frac{dE_S}{dz} = \frac{8\pi i \omega_S^2 d_{eff}}{k_S c^2} E_I^* E_P e^{-i\Delta k z} \quad (2.57)$$

$$\frac{dE_I}{dz} = \frac{8\pi i \omega_I^2 d_{eff}}{k_I c^2} E_P E_S^* e^{+i\Delta k z} \quad (2.58)$$

$$\frac{dE_P}{dz} = \frac{8\pi i \omega_P^2 d_{eff}}{k_P c^2} E_S E_I e^{-i\Delta k z} . \quad (2.59)$$

In these equations, d_{eff} represents the effective nonlinear coefficient, that depends on the type of phase-matching and the specific nonlinear crystal used. It comprises the relevant contributions of the susceptibility tensor $\chi_{ijk}^{(2)}$ for the proper polarization directions. Under the assumption of a non-depleted Pump wave, i.e. the conversion efficiency is very small and therefore the ω_P Pump wave remains essentially constant, we can take $E_P(z) = E_P(0)$. Furthermore, perfect phase-matching $\Delta k=0$ shall be assumed. Then, by differentiation of Eq. (2.58) with respect to z and introducing the complex conjugate of Eq. (2.59) one obtains

$$\frac{d^2 E_I}{dz^2} = \frac{64\pi^2 \omega_S^2 \omega_I^2 d_{eff}^2}{k_S k_I c^4} E_I^* E_P E_P^* \equiv \kappa^2 E_I , \quad (2.60)$$

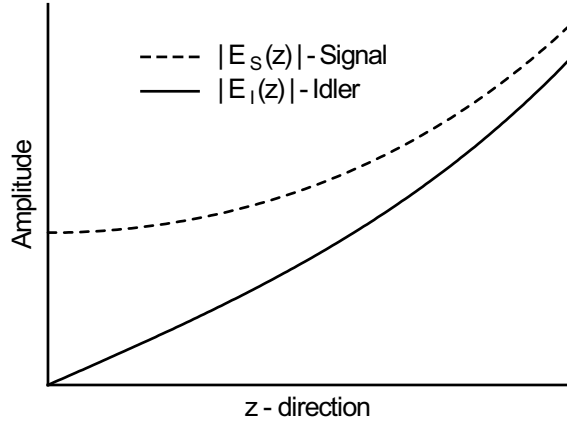


Figure 2.7: Spatial evolution of the Signal and Idler waves $|E_S(z)|$ and $|E_I(z)|$ in the nonlinear medium in a non-depleted optical parametric process under the additional assumption of perfect phase-matching $\Delta k=0$ according to Eq. (2.61) and (2.62) .

with the coupling constant κ . The general solution to this equation is a linear combination of $\sinh \kappa z$ and $\cosh \kappa z$. In the OPA the Idler is initially not present ($E_I(0) = 0$), whereas the signal field starts with the small value $E_S(0)$ of the seed wave. The solutions to Eq. (2.58) and Eq. (2.59) are then given by

$$E_S(z) = E_S(0) \cosh \kappa z \quad (2.61)$$

$$E_I(z) = i \sqrt{\frac{n_S \omega_I}{n_I \omega_S}} \frac{E_P}{|E_P|} E_S^*(0) \sinh \kappa z . \quad (2.62)$$

The spatial behaviour of these solutions is illustrated in Fig. 2.7 . Both field amplitudes $|E_S(z)|$ and $|E_I(z)|$ experience monotonic growth and approach a function proportional to $e^{\kappa z}$ asymptotically for ($\kappa z \gg 1$). This implies, that by increasing the crystal thickness one could obtain huge conversion efficiencies. However, in reality for Gaussian laser pulses with femtosecond duration the field amplitudes do not show monotonic growth because effects such as spatial walk-off due to birefringence or temporal walk-off due to group-velocity dispersion have to be taken into account. As a consequence an optimal crystal thickness exists for every specific situation, i.e. Signal, Idler and Pump wavelengths, in combination with the nonlinear medium.

Supercontinuum generation

When intense laser pulses interact with transparent media, spectral broadening ranging over an extended spectral region from ultraviolet to the infrared can be achieved. This process is called supercontinuum or white-light continuum (WLC) generation and was first observed by Alfano and Shapiro in 1970 [100]. While the WLC has many applications, including time-resolved broadband pump-supercontinuum probe spectroscopy [101] and the use as a broadband seed wave for optical parametric amplification [102], the physical mechanism of WLC generation is not completely understood. It is widely believed [103, 104] , that several nonlinear processes, e.g. self-focusing, Raman-like processes and self-phase modulation contribute to WLC generation.

The optical characteristics of the supercontinuum comprise different aspects. The spectral range depends on the medium in which the WLC is generated, it has a modu-

lated spectrum and the polarization points into the same direction as that of the generating pulse. The spatial beam profile consists of a red outer ring, which is called conical emission, that is explained by a Cerenkov-based effect [105], and the inner white disk, that is the actual white-light part.

As self-phase modulation is thought to play an important role in WLC generation, as well as in other processes, e.g. the "coherent artifact" in pump-probe spectroscopy (see Chapter 4) a brief introduction shall be given. Self-phase modulation is based on the third order susceptibility $\chi^{(3)}$, that is in general present in most media. A contribution

$$E_q^{(3)}(t) = \varepsilon_0 \chi^{(3)} E_1(t) E_2(t) E_3(t) \quad (2.63)$$

to the electric field due to the third-order polarization of the medium can be derived. In the case of identical fields the expression

$$P(t) = \varepsilon_0 \left[\chi^{(1)} + \frac{3\chi^{(3)}}{2c\varepsilon_0 n} I(t) \right] E^+(t) + \text{c.c.} \quad (2.64)$$

for the polarization, including the intensity (2.19) of the incoming wave can be found. By using Eq. (2.29), that defines the linear index of refraction as $n_0 = \sqrt{1 + \chi^{(1)}}$, then the complete index of refraction

$$\begin{aligned} n &= \sqrt{1 + \chi^{(1)} + \frac{3\chi^{(3)}}{2c\varepsilon_0 n_0} I(t)} = n_0 \sqrt{1 + \frac{3\chi^{(3)}}{2c\varepsilon_0 n_0^3} I(t)} \\ &\approx n_0 + \frac{3\chi^{(3)}}{4c\varepsilon_0 n_0^2} I(t) := n_0 + n_2 I(t) \end{aligned} \quad (2.65)$$

also acquires an intensity-dependence. For the approximation in Eq. (2.65) the relation $n_0 \gg n_2 I(t)$ has been used, where n_2 is the nonlinear index coefficient that describes the coupling strength between the index of refraction and the electric field [93]. Due to this intensity dependence of the refractive index, a pulse propagating in a medium with sufficiently large $\chi^{(3)}$ will experience temporal phase modulation, leading to spectral broadening. This can be illustrated by taking the complete temporal phase

$$\Phi(t, z_0) = \varphi(t, 0) + \omega_0 t - k_0 z_f \quad (2.66)$$

of the electric field in a fixed point z_f in space [106]. Together with the relation (2.28) for the wave vector, Eq. (2.66) can be written as

$$\Phi(t, z_f) = \varphi(t, 0) + \omega_0 t - \frac{n\omega_0}{c} z_f = \varphi(t, 0) + \omega_0 t - \frac{\omega_0 z_f}{c} [n_0 + n_2 I(t)] , \quad (2.67)$$

and therefore the associated momentary frequency (2.17) becomes

$$\omega_m(t, z_f) = \frac{d\varphi(t, 0)}{dt} + \omega_0 - \frac{\omega_0 n_2 z_f}{c} \frac{dI(t)}{dt} . \quad (2.68)$$

By performing the Fourier transform (2.3) it can be shown, that the temporal phase modulation effects the spectral profile of the pulse, by creating red shifted frequencies at the leading edge ($dI(t)/dt > 0$) of the pulse and blue shifted frequencies at the trailing edge ($dI(t)/dt < 0$) of the pulse. This also implies, that the WLC is up-chirped, since the red frequencies arrive before the blue frequencies in the pulse.

2.4 Electronic structure and vibrations of molecules

In this section the basic concepts important for the treatment of photophysical and photochemical processes in molecules, such as potential energy surfaces, electronic structure and vibrations shall be given.

2.4.1 Born-Oppenheimer approximation and potential energy surfaces

The full Hamiltonian [28, 107]

$$\mathcal{H}(\mathbf{r}, \mathbf{R}) = \mathcal{T}_N + \mathcal{T}_e + \mathcal{V} , \quad (2.69)$$

of a molecular system comprising at least two atoms, consists of the kinetic energies of the nuclei \mathcal{T}_N and of the electrons \mathcal{T}_e and the potential

$$\mathcal{V} = \mathcal{V}_{eN} + \mathcal{V}_e + \mathcal{V}_N , \quad (2.70)$$

with contributions from the Coulomb interaction between the electrons and nuclei, between the electrons themselves and between the nuclei. The coordinates \mathbf{R} and \mathbf{r} correspond to the nuclei and the electrons respectively. The time-independent Schrödinger equation

$$\mathcal{H}(\mathbf{r}, \mathbf{R})|\Psi_{mol}(\mathbf{r}, \mathbf{R})\rangle = E|\Psi_{mol}(\mathbf{r}, \mathbf{R})\rangle , \quad (2.71)$$

where E represents the energy, can be solved by introducing an approximation. Contributions due to spin and rotational motion of the molecule are neglected in this discussion.

As the nuclear motion is very slow compared with the motion of the electrons due to the mass ratio of about three orders of magnitude, the time-independent Schrödinger equation can be considered for the electrons only at a fixed internuclear geometry \mathbf{R} . In the Born-Oppenheimer approximation the total wave function

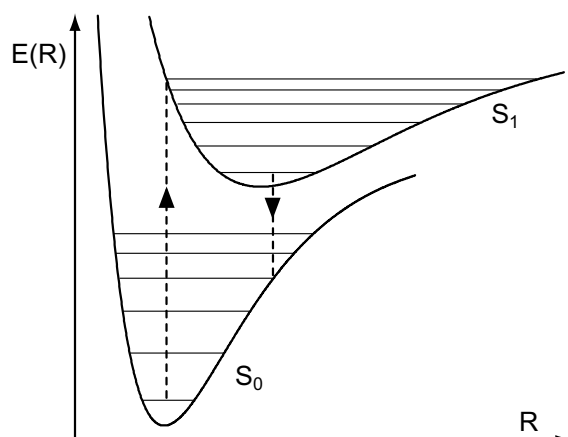
$$|\Psi_{mol}(\mathbf{r}, \mathbf{R})\rangle = |\Psi_e(\mathbf{r}, \mathbf{R})\rangle |\Psi_N(\mathbf{R})\rangle \quad (2.72)$$

can be separated into the electronic wave function $|\Psi_e(\mathbf{r}, \mathbf{R})\rangle$, that depends on the electron coordinates \mathbf{r} and the internuclear geometry \mathbf{R} , and the nuclear wave function $|\Psi_N(\mathbf{R})\rangle$. The eigenvalues and the wave functions of the electrons depend parametrically only on the magnitude of the nuclear position vector \mathbf{R} . The Schrödinger equation for the electrons alone has to be solved for every value of \mathbf{R} to obtain the eigenvalues $E(\mathbf{R})$. The electronic eigenvalues $E(\mathbf{R})$ as a function of \mathbf{R} are called potential energy curves. The sum of the nuclear potential \mathcal{V}_N and $E(\mathbf{R})$ plays the role of an effective potential under which the nuclei move. Therefore, the Schrödinger equation for the nuclei can be written as

$$\mathcal{H}(\mathbf{r}, \mathbf{R})|\Psi_N(\mathbf{R})\rangle = [\mathcal{T}_N + E(\mathbf{R}) + \mathcal{V}_N(\mathbf{R})]|\Psi_N(\mathbf{R})\rangle = E|\Psi_N(\mathbf{R})\rangle . \quad (2.73)$$

This leads to the picture, illustrated in Fig. 2.8 in which the vibrational states are considered on top of the electronic levels represented by the potential energy curves $E(\mathbf{R})$.

Figure 2.8: Electronic transitions between the S_0 and S_1 potential energy curves to i) illustrate vertical vibronic transitions (Franck-Condon principle) and ii) to give an example of the spacing of vibrational energy levels in anharmonic potentials. The energy distance between neighboring levels is decreasing with increasing quantum number.



For polyatomic molecules, the number of coordinates, that are necessary to describe nuclear motion is increasing with the size of the molecule. Thus, the electronic states are described by multi-dimensional potential energy surfaces.

Transitions between electronic states can be considered as taking place almost instantaneously with respect to the time scale of molecular vibrations (Franck-Condon principle). The heavy nuclei do not change their position during the electronic transition. Thus, a vibronic transition is represented by a vertical line in the energy diagram. The transition probability from an initial to a final state is proportional to the absolute square of the dipole matrix element

$$M_{if} = \left[-e \sum_j \langle \Psi_f^e | \mathbf{r}_j | \Psi_i^e \rangle \right] \times \langle \Psi_f^n | \Psi_i^n \rangle . \quad (2.74)$$

The first factor is the electric dipole transition moment, due to the redistribution of the electrons, while the second factor is known as the Franck-Condon factor. It describes the overlap of the vibrational wave functions $|\Psi^n\rangle$ in the initial and final states.

2.4.2 Vibrations

To describe the motion of a polyatomic molecule, consisting of N atoms, $3N$ coordinates are necessary. From these $3N$ degrees of freedom, three can be attributed to translation and three (or two in the case of a linear molecule) originate from rotations. Thus, the remaining number of degrees of freedom for molecular vibrations is $3N - 6$ (or $3N - 5$ for a linear molecule). The potential energy as a function of the vibrational amplitudes Q can be expanded in the Taylor series

$$V(Q) = V_0 + \sum_i \left(\frac{\partial V}{\partial Q_i} \right) Q_i + \frac{1}{2} \sum_{i,j} \left(\frac{\partial^2 V}{\partial Q_i \partial Q_j} \right) Q_i Q_j + \dots \quad (2.75)$$

around the equilibrium position $Q=0$. The partial derivatives are the force constants. In the harmonic approximation only terms up to the second order are included. The equations of motion for the molecule consisting of $3N$ atoms comprise $3N$ linear differential equations, that can be disentangled by coordinate transformation leading to $3N - 6$

uncoupled normal mode equations. Any motion of the molecule can be represented as a superposition of the normal modes of vibration, where all atoms oscillate with the same frequency and have a fixed phase. In this case, the Schrödinger equation resolves into independent equations for each normal mode, and the total vibrational eigenfunction is the product of the harmonic oscillator eigenfunctions of the different normal modes. The total vibrational energy is then given by

$$E = \sum_i \hbar \omega_i (v_i + 1/2) . \quad (2.76)$$

If the force constants, defining the harmonic potential are known, the normal modes of vibration can be determined. However, in general it is necessary to include cubic, quartic and possibly higher order terms into the expression for the potential energy to achieve a better description of the molecular system. This implies that the energy is no longer a sum of independent terms corresponding to the normal modes of vibration. Anharmonic correction terms, that involve the quantum number of two or more normal vibrations, have to be taken into account [108]. A formalism can be derived, in which the molecular system is still described in the harmonic approximation using the normal modes, while the anharmonicity is treated by perturbation theory. The vibrational energy states of a molecule can then be expressed as [108, 109]

$$E/\hbar = \sum_i \omega_i (v_i + 1/2) + \sum_{i \leq j} x_{ij} (v_i + 1/2)(v_j + 1/2) , \quad (2.77)$$

where ω_i is the harmonic frequency of the i th vibrational mode, v_i is the vibrational quantum number of the mode and the x_{ij} are the anharmonic constants, that can be related to the cubic and quartic force constants in a normal coordinate basis. The transition frequency of a specific mode k coupled to the bath of all other modes $i \neq k$ is given by

$$\omega(v_k \rightarrow v_{k+1}) = \omega_k + 2x_{kk}v_k + \sum_{i \neq k} x_{ik}v_i , \quad (2.78)$$

where the first term is the anharmonic correction of the $v_k=0 \rightarrow v_k=1$ transition in the vibrational ground state

$$\omega_k = \omega_k^0 + 2x_{kk} + \sum_{i \neq k} x_{ik}/2 . \quad (2.79)$$

Two types of anharmonicity can be distinguished. The second term in Eq. (2.78) describes the "diagonal" anharmonic shift of an excited vibrational mode k . The transitions in the vibrational ladder are successively shifted to lower frequencies. The decrease in the vibrational energy difference with increasing quantum number, illustrated in Fig. 2.8, is an example of "diagonal" anharmonicity. The third term describes the "off-diagonal" frequency shifts due to coupling between the mode k and the remaining modes. When other modes i are highly excited (high quantum number v_i indicates that the molecule is hot, i.e. it has a large internal vibrational energy), the mode k exhibits a red-shifted transition frequency, even for the fundamental $v_k=0 \rightarrow v_k=1$ transition.

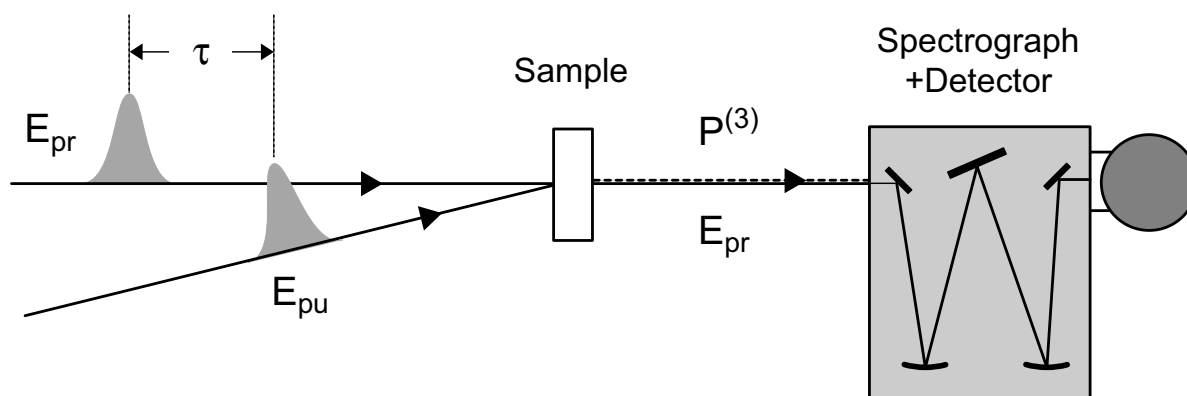


Figure 2.9: Experimental configuration for ultrafast infrared spectroscopy with frequency-resolved detection. Adapted from Ref. [110].

2.5 Ultrafast vibrational spectroscopy

Time-resolved vibrational spectroscopy has the potential to elucidate the structural evolution of a molecular system during ultrafast chemical reactions. Infrared transitions can often be clearly associated with certain groups in the reactant and product molecules, which makes infrared spectroscopy ideally suited for the investigation of chemical and photophysical reactions providing direct insight into the structural dynamics on a microscopic level.

After a brief discussion of the theoretical basis of UV pump - IR probe spectroscopy in Section 2.5.1, the different transient infrared signals, that can be observed will be explained (Section 2.5.2). Section 2.5.3 attempts to present an overview of the many different classes of molecules and molecular processes, that have been studied so far using time-resolved infrared spectroscopy.

2.5.1 Theory of UV pump - IR probe spectroscopy

Ultrafast spectroscopy in the infrared spectral region is based on the same methods as the more conventional studies, where electronic transitions are used to probe dynamical processes in molecules. An intense pump pulse excites the molecule to a higher excited state, which can trigger a photoreaction. Instead of following the time evolution of the system by using a time-delayed probe pulse in the ultraviolet or visible regime, infrared pulses are employed. The absorption change of the molecular sample due to excitation and photoreaction is monitored via weak infrared probe pulses, which experience a transmission change when passing the sample. The pump-probe experiments in this thesis have been performed with frequency-resolved detection (Fig. 2.9), where a polychromator is employed to spectrally disperse the infrared probe pulses after transmission through the sample.

Pump - probe spectroscopy is a third order nonlinear technique, in which a third order polarization $P^{(3)}$ is generated in the sample by two interactions with the pump and one interaction with the probe field [111]. The polarization represents a source

term in the wave equation (Eq. 2.1), which can be solved in the slowly varying envelope approximation and in the small signal limit. The wave equation is then given by

$$\frac{\partial E(t)}{\partial z} = \frac{i\omega_{pr}}{\epsilon_0 c} P^{(3)}(t) \quad (2.80)$$

connecting the polarization with the electric field. In the small signal limit the solution is

$$E_{pr,total}(t) = E_{pr}(t) + E_{gen}(t), \quad E_{gen}(t) = \frac{i\omega_{pr}L}{\epsilon_0 c} P^{(3)}(t), \quad (2.81)$$

where L is the optical path length in the sample. The polarization of the sample generates a new pulsed field $E_{gen}(t)$, that interferes with the original probe field $E_{pr}(t)$. Depending on whether the generated field is in-phase or out-of-phase with the probe field, transient absorption or gain will be observed. The photodetector, that records the optical signal is slow compared to the pulse duration, thus the total signal detected is proportional to the time integral

$$\int_{-\infty}^{\infty} dt |E_{pr,total}(t)|^2 = \int_{-\infty}^{\infty} dt [|E_{pr}(t)|^2 + |E_{gen}(t)|^2 + 2\text{Re}E_{pr}(t)E_{gen}(t)] . \quad (2.82)$$

The first term in this expression is constant and corresponds to the "unpumped" signal, i.e. the signal that would be measured if the pump pulse was not present. It can be subtracted off in an experiment by proper normalization (for technical details see Section 3.4.2), so that only the difference signal is measured. The second term can be neglected in the small signal limit, while the third term is responsible for the modulation (absorption or gain) of the measured signal. Ref.[111] gives a detailed description of the underlying theory of UV pump - IR probe experiments. In addition calculations of transient infrared absorption spectra for different cases, such as the destruction of a molecule by a visible laser pulse, transients in a two-level system and transients in a three-level system are provided.

2.5.2 Transient infrared signals

The transient signals observed in time-resolved infrared spectroscopy have various origins. The absorption change can either be positive or negative. Negative absorption change occurs at spectral positions, where the ground state absorption bands of the molecular system are located and the transient absorption spectra reflect the ground state absorption spectrum. Due to photoexcitation of the molecule with the pump pulse, population is transferred to an excited electronic state. Hence, the ground state $S_0(v_0 \rightarrow v_1)$ vibrational transition is bleached, i.e. less molecules absorb at the specific wavelength. Depending on the dynamics of the molecule the bleach can recover fully or only partially after a certain time. Full recovery is observed, when the excited state population entirely relaxes back to the ground state. When an irreversible photoreaction is involved, the ground state will only partially recover, and the residual bleach is

a measure of the quantum yield of the reaction. The rise of new absorption bands can have several reasons. Besides the appearance of a band belonging to a reaction intermediate or final photoproduct, excited state absorption from a vibrational transition in the electronic excited state, e.g. $S_1(v_0 \rightarrow v_1)$ is also possible and has also to be taken into account. Spectral shifts of transient bands are frequently observed. As explained in the previous section, anharmonicity leads to shifting of vibrational energy levels. Initially red-shifted bands can be observed, when species with a large amount of internal vibrational energy (hot ground state of the reactant or hot ground state of products) are created. During vibrational relaxation processes energy dissipation to the solvent (cooling) occurs, which translates into a blue-shifting behavior of the positions of the vibrational modes back to the frequency position observable in the vibrational ground state.

2.5.3 Investigated molecular systems and processes

By using time-resolved infrared spectroscopy one can gain information about the dynamics of structural changes during photoinduced processes in molecules. In addition vibrational relaxation dynamics and anharmonic couplings between vibrational modes can be studied [109, 112–114]. A comprehensive review of the field is, e.g. Ref. [115]. Dissociation, bond activation and rearrangement in organometallic compounds [116–119] was intensively investigated. Another field of application lies in the study of photoisomerization in photoactive proteins, such as bacteriorhodopsin and related proteins [120–124], green fluorescent protein (GFP) [125] or photoactive yellow protein (PYP) [126–128] and also the dissociation dynamics of CO from heme proteins [129, 130]. Other processes, such as ring-opening and ring-closure in photochromic switches [131–135], hydrogen bond dynamics [110, 136] and hydrogen transfer [137–140] in solutions, as well as more complicated chemical reactions [141, 142] have also been studied.

3 Experimental methods

After introducing the basic concepts and ideas behind quantum control and the theoretical formalism for describing femtosecond laser pulses in the previous chapter, this chapter deals with the combination of these concepts and the techniques necessary for the experimental realization of open-loop and closed-loop quantum control.

In Fig. 3.1 the interplay of the different components of the employed quantum control setup is shown schematically. The amplified titanium:sapphire (Ti:Sa) laser system (see Section 3.1) on the left hand side is the starting point for all experiments. It delivers the femtosecond pulses, that are used to influence and monitor the time evolution of the investigated molecular system. The ultrashort time scale allows for the resolution of molecular dynamics and the large spectral bandwidth of the pulses can lead to the creation of a vibrational wavepacket by coherent excitation of vibrational modes in the electronic excited state of the investigated system.

The dynamics of the system can be influenced by altering the properties of the applied laser pulses. This can be realized by manipulating single parameters, like the energy, the polarization or the wavelength of the employed pulses. In addition a second pulse can be introduced and the temporal delay between the two pulses represents a further control parameter. A many-parameter scenario, where the spectral phase of the pulses is modulated by means of a pulse shaper (details in Section 3.2) is a more general and flexible concept, since very complex pulse shapes can be generated. The methods necessary for the characterization of the structure of the shaped pulses are discussed in Section 3.3.

The laser pulses are used to investigate and control different effects in several quantum systems. Depending on the quantum system different detection schemes are required. For purely optical processes, like the generation of the second harmonic in a nonlinear crystal, a simple measurement of the intensity of the generated signal can be sufficient, while for complicated molecular systems in different environments more sophisticated techniques have to be applied. In the case of organic molecules in solution, the measurement of transient absorption changes, that enables to follow the temporal evolution of the molecular system, is an appropriate method to characterize intermediate steps or the outcome of a photochemical process. In the experiments dealing with the surface reactions of hydrogen and carbon monoxide in Chapter 7 and 8 a totally different approach has to be chosen. The detection of generated product species is performed with time-of-flight (TOF) mass spectrometry (Section 3.4.3)

The category on the right hand side concerns the type of control. In open-loop experiments the experimental outcome is recorded as a function of only one or two specific parameters, that characterize the laser field, e.g. linear chirp or the delay time between two pulses. In this case the applied laser pulse shapes are varied in a systematic way, and they are limited to a subset of all pulse shapes that can in principle be generated with

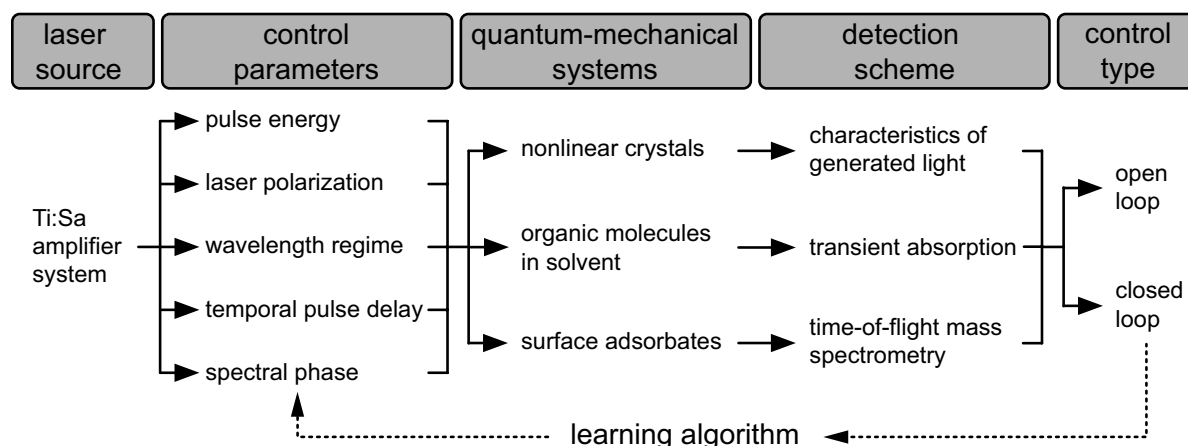


Figure 3.1: Schematic overview of the experimental setup. It can be divided into five categories. Femtosecond laser pulses are provided by a titanium:sapphire (Ti:Sa) laser system. The pulses are modified according to different control parameters and are then applied to control certain processes in quantum systems. Appropriate detection schemes are used to evaluate the experimental outcome in either open-loop or closed-loop configuration, where a learning algorithm iteratively optimizes the shape of the laser pulse.

the pulse shaper. In the closed-loop quantum control scheme the change of the experimental observable is evaluated by a learning algorithm (Section 3.5), that is iteratively improving the control field until the optimal solution is found.

3.1 Femtosecond laser system

The main components of the femtosecond laser system are schematically shown in Fig. 3.2. The starting point is a home-built titanium:sapphire (Ti:Sa) oscillator, pumped by a continuous-wave ND:YVO₄ laser (Coherent Verdi V6) operating at 532 nm. It delivers pulses with 60 fs duration at a repetition rate of 90 MHz which have a central wavelength of $\lambda_0=800$ nm and a pulse energy of 3 nJ. In order to achieve higher pulse energies, the oscillator pulses are sent into an amplifier setup based on the chirped-pulse amplification (CPA) method [143], that involves several steps. First, the oscillator pulses enter an “Öffner-type stretcher” in which they are elongated in time by applying large linear chirp with a suitable combination of a grating and concentric reflective optics [144–146]. The stretched pulses have a duration of 120 ps and therefore low peak intensity, and thus damage of the optical components in the following amplifier setup is avoided. The pulses then serve as seed pulses for a regenerative amplifier which is pumped by a Nd:YLF laser (Coherent Evolution 15), having a wavelength of 527 nm and a repetition rate of 1 kHz. Finally, a folded “Treacy-type compressor” [144, 145, 147] setup consisting of only a grating and plane reflective optics is employed to compensate for the phase introduced by the stretcher and amplifier components without misaligning the entire amplifier system. The duration of the amplified and compressed pulses is 80 fs and a pulse energy of up to 1 mJ at a repetition rate of 1 kHz can be reached. They

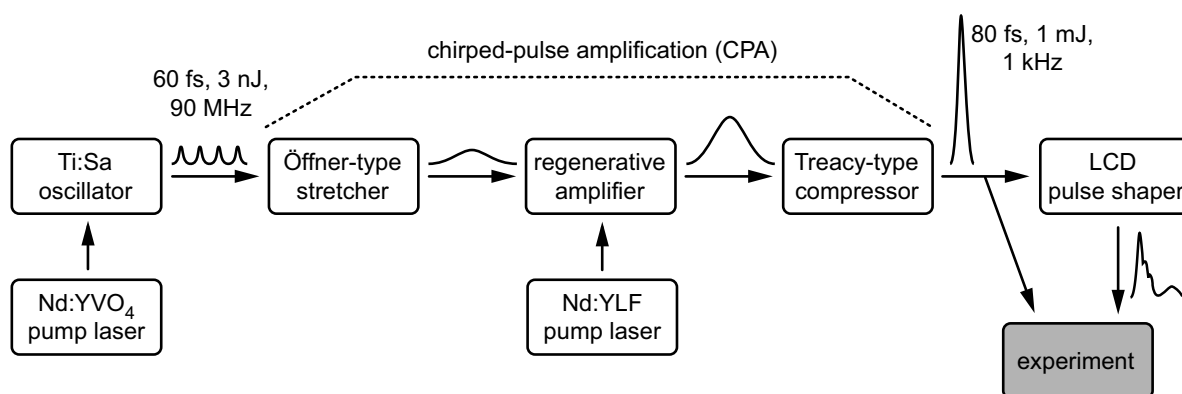


Figure 3.2: Femtosecond laser system. Femtosecond pulses are first generated at a high repetition rate but low pulse energy by a titanium:sapphire (Ti:Sa) oscillator. In a chirped-pulse amplification (CPA) scheme, they are subsequently temporally stretched, amplified, and temporally recompressed again, yielding pulses at a lower repetition rate but with a pulse energy increased by more than five orders of magnitude. The amplified laser pulses can be directly used for an experiment, or they are first modulated in a pulse shaper.

can either be used directly in an experiment, or they may also be sent to a pulse shaper, for further fine adjustment of the pulse compression and also the generation of complex pulse shapes.

3.2 Femtosecond pulse shaping

The complex shaped laser fields necessary for performing open-loop as well as closed-loop quantum control experiments are obtained by using a pulse shaper setup which will be described in this section. For this purpose a number of different methods exist. In general it is possible to modulate phase, amplitude and polarization of femtosecond laser pulses with an appropriately chosen setup. Shaping of ultrashort laser pulses can in principle be achieved in either in the time domain or in the frequency domain, as they can be described in either the frequency or the time domain connected via Fourier transformations. In this section phase-only pulse shaping in the frequency domain with a liquid-crystal display (LCD) pulse shaper will be discussed, since this is the pulse shaper used in the experiments of this thesis.

The femtosecond pulse shaper used here is based on a $4f$ -geometry that allows for modulation of laser pulses in the frequency domain [88, 148]. It basically consists of a "zero-dispersion-compressor" [149, 150] in which the incoming beam is dispersed and collimated again by a symmetrically arranged grating and lens pair without introducing any additional phase, i.e. the pulses leave this configuration with the same temporal structure they possessed when they entered. In this setup (Fig. 3.3) the laser beam is angularly dispersed by a grating and collimated by a cylindrical lens that is placed after the grating at the distance of the focal length. This way all the different frequencies contained in the beam are propagating parallel after the lens and are focused individually and spatially displaced in the so-called "Fourier plane". A second lens and grating pair

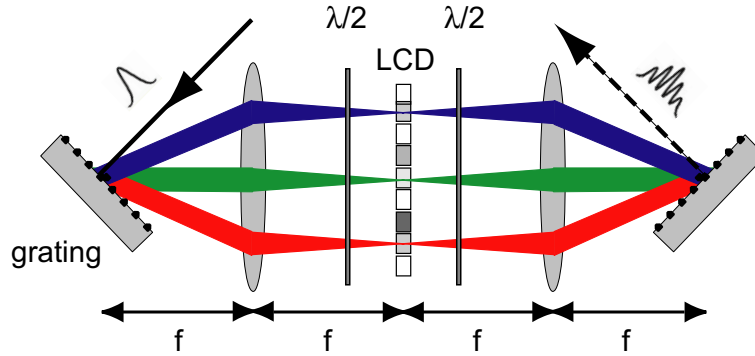


Figure 3.3: Femtosecond pulse shaper. A zero-dispersion compressor in $4f$ configuration is used to spatially disperse the frequency components contained in the pulse by a grating. The lens is used for collimation of the beam and focuses each frequency component into the Fourier plane, where pulse shaping with a liquid crystal display (LCD) occurs. A second lens and grating pair recombines the spectral components.

in a symmetric configuration to this plane recollimates the beam and recombines the different spectral components. All optical components involved are spaced one focal length apart. In the Fourier plane, the symmetry plane of the setup, maximal frequency resolution is achieved. Therefore, manipulation of the spectral phase of the pulse is taking place in the Fourier plane, by inserting a spatial light modulator (SLM) at this position.

The spatial light modulator used is a liquid-crystal display (LCD) [148, 151, 152] (see Fig. 3.4a) with 128 independently addressable pixels. It consists of two glass plates at distance d , coated on the inner surface with thin rectangular areas of transparent and electrically conducting indium tin oxide (ITO). Opposing areas form the two electrodes of a pixel, which has a height of $y_p=2$ mm and is $x_p=97$ μ m wide. An electric voltage can be applied to each individual pixel. The space between the glass plates is filled with long-stretched liquid-crystal molecules in the nematic phase, i.e. the long symmetry axes are aligned with respect to each other showing in the z -direction according to Fig. 3.4b. By application of a suitable voltage U_i to the ITO electrodes of pixel i ($i=1,\dots,128$), the liquid-crystal molecules are reoriented along the electric field lines and are tilted in the $y-z$ plane (Fig. 3.4c), while the amount of tilt is a monotonous function of U_i . Thus, the molecular electric dipole moment projected along the y -axis is altered, leading to a change in the index of refraction $n_y(U_i)$ along the y -direction. This in turn results for light polarized in the y direction in an additional phase retardation

$$\Delta\Phi(U_i, \omega_i) = \frac{[n_y(U_i) - n_y(0)] \omega_i d}{c} \quad (3.1)$$

relative to the phase retardation imposed without any voltage applied. This is why half wave plates ($\lambda/2$) are used before and after the LCD (see Fig. 3.3) to rotate the initially p-polarized electric light field (pointing in x -direction) by 90° to pointing along the y -direction. Since different voltages can be applied independently to each of the 128 pixels, 128 individual frequency components, lined up next to each other along the x -direction

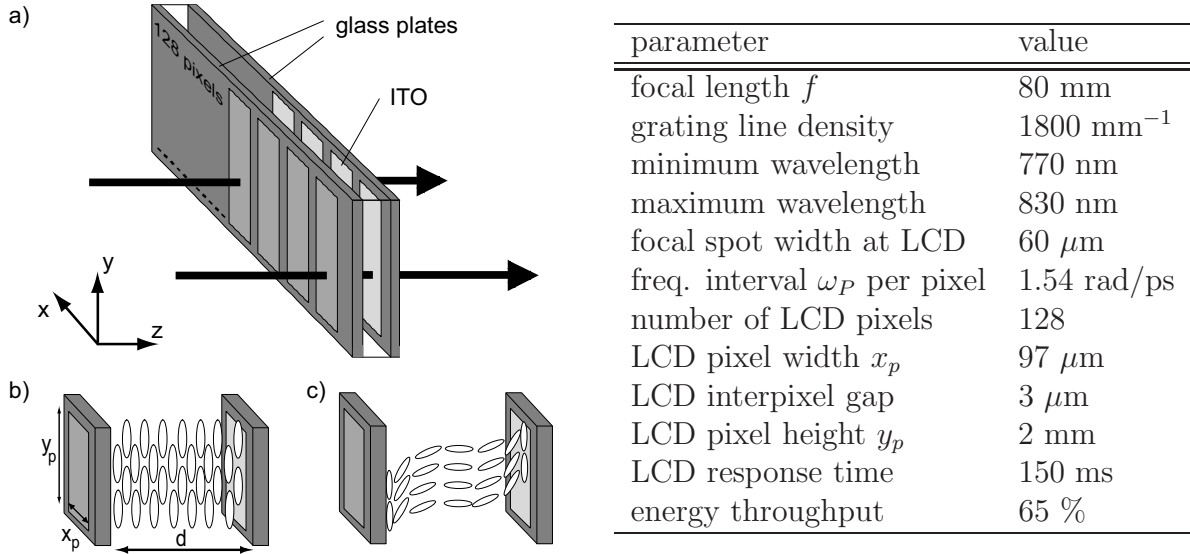


Figure 3.4: The liquid-crystal display (LCD) spatial light modulator located in the Fourier plane of the pulse shaper. a) The LCD consists of two glass plates whose inside surfaces are coated with 128 indium-tin-oxide (ITO) electrodes. The space between the glass plates is filled with long-stretched liquid-crystal molecules. b) An individual pixel shown for the case where the voltage between the electrodes of the pixel is off. c) When a voltage is applied, the crystals reorient themselves along the direction of the electric field, leading to a refractive index change for light polarized along the y -axis. Each of the frequency components passing through the different pixels can be retarded independently. The table on the right side summarizes the technical parameters of the LCD pulse shaper setup.

in the Fourier plane, can be retarded independently. As a consequence almost arbitrary shaped spectral phase functions $\Phi(\omega)$ can be obtained. For the generation of specific phase modulations $\Delta\Phi(U_i, \omega_i)$ an experimental calibration is necessary, to both assign the spatial position x (or the pixel number) to the frequency component and the applied voltage at the respective pixel to the introduced phase retardation. This can be done by a procedure described in Ref. [153].

LCD-based pulse shapers also have limitations and unwanted effects can occur, that one has to be aware of when using the pulse shaper in an experiment. The shortest temporal feature of the shaped femtosecond pulse is determined by the bandwidth limit of the incoming unshaped pulse. Therefore the fastest change in the intensity profile can not be shorter than the duration of the transform-limited pulse. An LCD pixel can cover only a limited amount of phase retardation, due to the maximum tilt of the liquid-crystal molecules. However, it is sufficient for a phase of $\Delta\Phi(U_i, \omega_i) \in [0, 2\pi]$ for all frequency components ω_i . For phases exceeding this range, the phases $\Phi(\omega)$ are applied modulo 2π , leading to phase jumps among neighboring pixels of about 2π (“phase wraps”). The steplike phase function applied with an LCD-SLM effects the output pulse shape. With the help of the Fourier transform (2.4) relation it can be shown, that pre- and postpulses appear in addition to the main laser pulse. Their temporal separation from the main pulse is $2\pi/\omega_P = 4.1 \text{ ps}$, where ω_P is the frequency interval that falls on

one pixel [154]. Within this temporal "pulse shaping window" the pulses can be shaped without the need to take interference with the pre- and postpulses into account. Another effect that should not be forgotten is that temporal shaping is also coupled to spatial effects. The spatial structure of the LDC mask may cause varying diffraction effects for the individual frequency components which can lead to "spatial chirp" after the pulse shaper. This means that the different spectral components travel at different distances from the center of the spatial beam profile [154–156]. If the focal spot size in the Fourier plane is reduced to a width smaller than the pixel width x_p , this effect is minimized, which is the case in our setup. The technical parameters of the LCD can be found in the table on the right side of Fig. 3.4.

3.3 Pulse characterization methods

The complex pulses generated with the pulse shaper have to be characterized with suitable experimental methods. The techniques that were used in this work are described in this section. Intensity autocorrelation and cross-correlation can be employed, when it is sufficient to know the temporal profile of the pulse, whereas for the characterization of the complete electric field the frequency-resolved versions of intensity autocorrelation and cross-correlation, FROG and XFROG, are necessary.

3.3.1 Autocorrelation and cross-correlation

A widely used technique for the characterization of ultrashort laser pulses is second-order autocorrelation. The basic idea is to characterize the short pulse with an identical replica of itself in a nonlinear process. The employed setup is shown in Fig. 3.5a. In a Mach-Zehnder-type interferometer the laser beam is split into two copies of the same pulse. The path length of one of the arms of the interferometer is adjustable by movement of a motorized delay stage. The two beams are recombined non-collinearly in a suitable nonlinear crystal, phase-matched for the generation of the second harmonic. Each of the pulses alone is creating light at the second harmonic. In addition, if the two pulses are temporally overlapped in the crystal a cooperative SHG signal is measured. As it is pointing in the direction of the sum of the k -vectors of the individual beams, it can be separated by an iris. The cooperative SHG signal, recorded by a photodetector as a function of the temporal delay τ of the pulses, is called "Intensity Autocorrelation" and is given by

$$A_{IAC}(\tau) \propto \int_{-\infty}^{\infty} I(t)I(t - \tau)dt . \quad (3.2)$$

The FWHM Δt_{IAC} of the autocorrelation is an approximate measure for the pulse duration. For a Gaussian intensity profile $I(t)$ the relation between autocorrelation width and the FWHM of the temporal pulse profile is given by $\Delta t_{IAC} = \sqrt{2}\Delta t$. Information about the complete electric field, including phase and amplitude cannot be obtained unambiguously with autocorrelation measurements. An obvious ambiguity is time reversal to $I(-t)$, which leaves the autocorrelation signal $A_{IAC}(\tau)$ unchanged. Besides

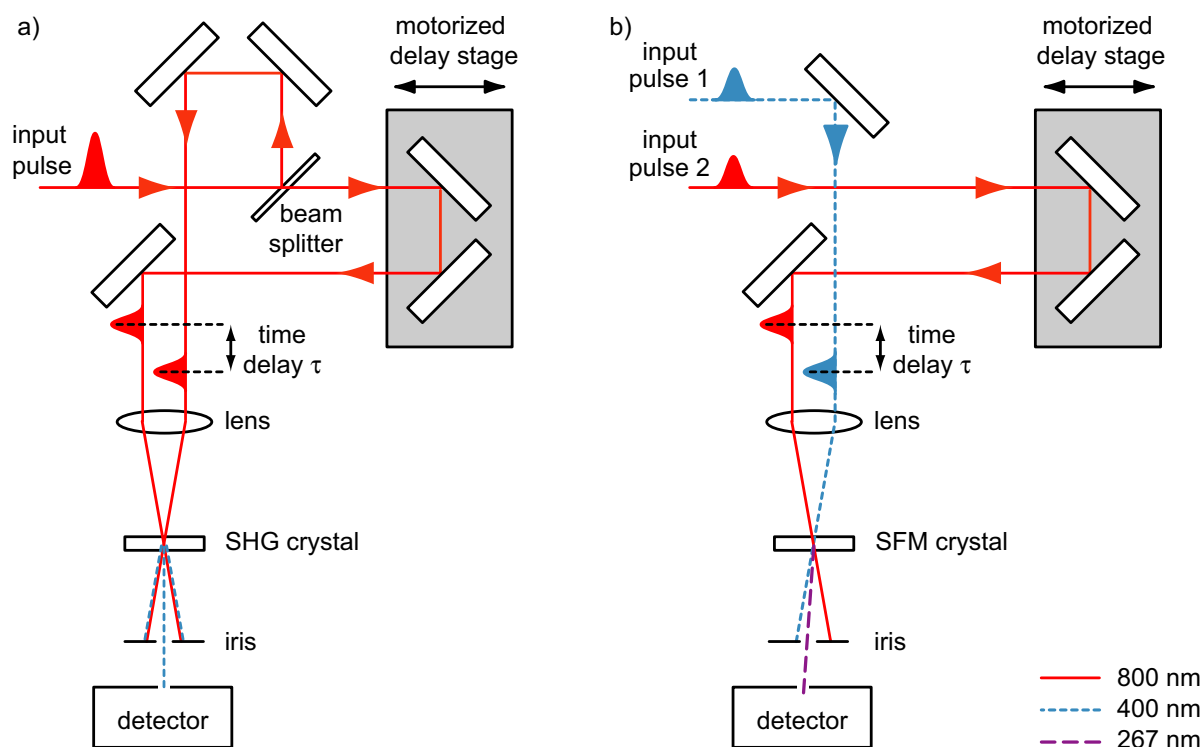


Figure 3.5: Schematic setups for the measurement of a) an intensity autocorrelation; b) an SFM intensity cross-correlation between a fundamental pulse at 800 nm and its second harmonic at 400 nm. The detector records the total signal as a function of the time delay τ which is adjustable with a computer-controlled motorized delay stage. If the detector is replaced by a spectrometer, FROG traces can be recorded.

this "self-referencing technique", in which a replica of the same pulse is used for its characterization, a "cross-referencing technique" that takes a known reference pulse for characterization is a possibility to gain more information about the unknown pulse.

Other nonlinear effects besides SHG, e.g. SFG or DFG (Section 2.3.3) can be exploited to record a cross-correlation of two different pulses (Fig. 3.5b), that may have different frequencies or temporal profiles. However, the duration Δt_1 of one of the pulses has to be known in order to gain information about the other pulse. Then the second-order intensity cross-correlation (ICC)

$$A_{ICC}(\tau) \propto \int_{-\infty}^{\infty} I_1(t)I_2(t - \tau)dt \quad (3.3)$$

between the two pulses with intensity profiles $I_1(t)$ and $I_2(t)$ can give an estimate for the other via the relation

$$\Delta t_{ICC} = \sqrt{\Delta t_1^2 + \Delta t_2^2}. \quad (3.4)$$

The cross-correlation is not ambiguous with respect to the time direction, since the two involved laser pulses generally have different intensity profiles. In contrast to the

autocorrelation, in which complex pulse shapes are not directly reflected due to the fact that the pulse is correlated with itself, the cross-correlation directly reveals the temporal structure of the unknown pulse.

3.3.2 Frequency-resolved optical gating - FROG and XFROG

More sophisticated techniques have to be employed for the complete characterization of ultrashort laser pulses. This can be achieved by measuring a spectrally resolved autocorrelation. The photodetector in Fig. 3.5a is then replaced by a spectrometer. This technique is called frequency-resolved optical gating (FROG) [157, 158] and was developed by Trebino and coworkers. It can be realized in different geometries and with different degrees of nonlinearity [159–164] and is applicable in a wide frequency range from the ultraviolet to the mid-infrared. There is also a cross-referencing version called cross-correlation frequency-resolved optical gating (XFROG) [165–167], which can be useful for the characterization of weak ultrashort pulses. In the experiments of this work, SHG-FROG and SFG-XFROG are applied for the characterization of pulses at 800 nm and 400 nm respectively. The unmodulated fundamental pulse was taken as the reference pulse for the SFG-XFROG.

The recorded signal (the "FROG-trace") is a function of frequency ω and the corresponding time delay τ of the two input pulses. Thus, the two-dimensional FROG signal is

$$S_{FROG}(\tau, \omega) \propto \left| \int_{-\infty}^{\infty} E_{sig}(\tau, t) e^{-i\omega t} dt \right|^2, \quad (3.5)$$

with the signal field $E_{sig}(\tau, t)$ which depends on the two input fields and the time delay τ between them. In the cases of SHG-FROG and SFG-XFROG the signal fields take the form

$$E_{sig}^{SHG}(\tau, t) = E^+(t)E^+(t - \tau) \quad (3.6)$$

$$E_{sig}^{SFG}(\tau, t) = E^+(t)E_{ref}^+(t - \tau), \quad (3.7)$$

respectively.

The retrieval of the complete electric field from the FROG or XFROG traces is not an analytically solvable problem. A numerical algorithm has to be used to extract the correct electric field in an iterative procedure. The reconstruction of the complete electric field from the two-dimensional FROG-trace, unlike in the case of a one-dimensional quantity, is possible by an iterative Fourier transform phase-retrieval algorithm [157]. For this purpose the signal field $E_{sig}(\tau, t)$ is Fourier-transformed with respect to τ

$$E_{sig}(\Omega, t) = \frac{1}{\sqrt{2\pi}} \int_{-\infty}^{\infty} E_{sig}(t, \tau) e^{-i\Omega\tau} d\tau. \quad (3.8)$$

With the inverse Fourier transform of Eq. (3.8) the measured FROG trace (3.5) can be rewritten in terms of the two-dimensional Fourier transform

$$S_{FROG}(\tau, \omega) = \left| \int_{-\infty}^{\infty} \int_{-\infty}^{\infty} E_{sig}(t, \Omega) e^{-i\omega t + i\Omega\tau} dt d\Omega \right|^2. \quad (3.9)$$

Since the signal field is connected to the electric field $E^+(t)$, the task for the algorithm is to find the correct signal field that corresponds to the measured FROG-trace. Therefore, starting from an initial guess for the electric field, the algorithm determines the two-dimensional signal field (3.8) and subsequently attempts to minimize the deviations of the calculated FROG signal (3.9) from the measured one. When the two-dimensional signal field is found, the complete electric field $E^+(t)$ can be obtained from it by setting $\Omega=0$. In the case of SHG-FROG, the function is represented by

$$E_{sig}(\Omega = 0, t) = \frac{1}{\sqrt{2\pi}} \int_{-\infty}^{\infty} E_{sig}(t, \tau) d\tau = \frac{1}{\sqrt{2\pi}} E^+(t) \int_{-\infty}^{\infty} E^+(t - \tau) d\tau. \quad (3.10)$$

After the substitution $\tau \rightarrow \tau' = t - \tau$ it reduces to the linear dependence

$$E_{sig}(\Omega = 0, t) = \frac{1}{\sqrt{2\pi}} E^+(t) \int_{-\infty}^{\infty} E^+(\tau') d\tau' = \text{const } E^+(t). \quad (3.11)$$

Using this procedure, the full electric field information can be obtained, apart from trivial ambiguities like the absolute phase, the direction of time in SHG-FROG due to delay time inversion symmetry or relative phases of well-separated frequency components [167].

For the FROG and XFROG traces of this work, the commercial software FROG 3.2 (Femtisoft Technologies) is used for a retrieval of the electric field.

3.4 Detection schemes

As different quantum systems in different environments are the subject of the quantum control experiments performed in this work, suitable detection techniques have to be applied to monitor the interaction of the light field and the investigated quantum system. In the following, these methods, especially technical details not mentioned in other parts of this work, will be discussed. The generation of the second harmonic serves as a prototype nonlinear process for an optical implementation of quantum control (Section 3.4.1). In the liquid phase, transient absorption spectroscopy (Section 3.4.2) is a valuable detection scheme, while for the experiments performed on adsorbate molecules on a metal surface time-of-flight mass spectrometry is employed (Section 3.4.3).

3.4.1 Harmonic generation

Frequency conversion processes in nonlinear crystals were introduced in Section 2.3. Under the condition that the SHG efficiency is constant for all involved spectral components (sufficient acceptance bandwidth of the crystal), the second harmonic signal

can be considered as a measure for the duration and peak intensity of the generating pulse. Thus, a transform-limited pulse will yield the maximal SHG signal. This can be exploited for adaptive pulse compression experiments [94], in which a pulse shaper is used to compensate for spectral phase distortions originating from the laser system itself or optical components in the path to the experiment. The laser pulse is sent through a pulse shaper and subsequently into a SHG crystal where second-harmonic radiation is generated. Suitable filters block the fundamental and the temporally integrated overall SHG yield is finally measured by a detector whose response is linearly depending on the energy of the light impinging upon it, e.g. a photodiode or a photomultiplier tube, and a boxcar averager. The SHG signal serves as feedback for a learning algorithm that iteratively compensates the phase distortions through maximizing the second-harmonic signal. This procedure is also called an SHG optimization and provides the shortest possible laser pulse [42–47, 168–173]. This "cleaned" spectral phase is taken as the starting point for performing spectroscopy or pulse shaping experiments.

3.4.2 Transient absorption

The general theory of transient absorption has already been presented in Section 2.5.1. This section deals with the technical aspects of transient absorption spectroscopy. The effect of the pump pulse, that excites the molecular system is investigated with a time delayed second pulse. Due to photoexcitation and dynamical evolution of the molecular sample, the probe pulse experiences different absorption by the sample. The difference in absorption compared with an unpumped sample volume recorded as a function of the delay time τ can provide information about the temporal evolution of the system. The Lambert-Beer law

$$I(\lambda, \tau) = I_0(\lambda) e^{-\sigma(\lambda)N(\tau)d} , \quad (3.12)$$

where $I_0(\lambda)$ is the intensity of the probe beam at wavelength λ before passing the sample, d is the sample thickness, $\sigma(\lambda)$ is the wavelength-dependent absorption cross section, and $N(\tau)$ is the number of molecules which absorb at wavelength λ , describes the intensity of the probe beam at this wavelength after passing the sample. The Lambert-Beer law can also be written in terms of the absorbance or 'optical density', defined as

$$OD(\lambda, \tau) = -\log_{10} \left[\frac{I(\lambda, \tau)}{I_0(\lambda)} \right] = \frac{1}{\ln(10)} \sigma(\lambda)N(\tau)d . \quad (3.13)$$

The probe beam intensity in absence of the pump pulse (for an unpumped sample volume) can be taken as the reference value already described in Eq. (2.82)

$$I_{ref}(\lambda) = I_0(\lambda) e^{-\sigma(\lambda)N_0d} . \quad (3.14)$$

This leads to the definition of the differential optical density, which is the change in absorbance seen by the probe pulse in the presence of the pump pulse

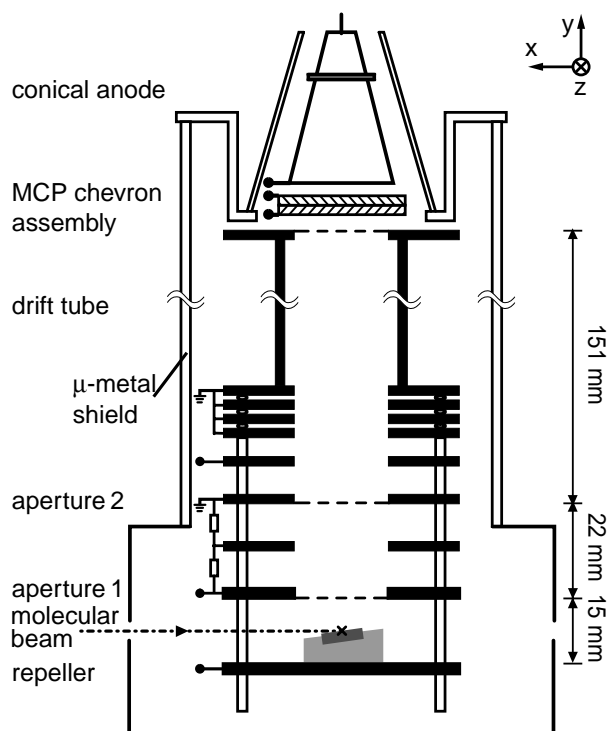
$$\Delta OD(\lambda, \tau) = -\log_{10} \left[\frac{I(\lambda, \tau)}{I_{ref}(\lambda)} \right] = \frac{1}{\ln(10)} \sigma(\lambda)[N(\tau) - N_0]d . \quad (3.15)$$

Usually a mechanical chopper blocking every other laser pulse is employed to measure the absorption change on a shot-to-shot basis. This greatly enhances the signal to noise ratio, because only short term shot to shot energy fluctuations limit the signal quality and long term drift of the pulse energy is not a major problem.

3.4.3 Time-of-flight mass spectrometry

In the experiments dealing with catalytic surface reactions on a metal surface in Chapter 7 and 8, ions are generated due to the interaction of the laser field and the adsorbed molecules on the metal surface. Time-of-flight (TOF) mass spectrometry is employed for the detection of the created ions. The TOF mass spectrometer is a modified version [174, 175] of a device based on the conventional Wiley-McLaren design [176]. It is incorporated in a high vacuum system consisting of two chambers, a main and a collateral vacuum chamber that are evacuated by a turbomolecular pump (Pfeiffer TPU330) and a diffusion pump (Varian VHS-6), respectively, both backed by a rotary vane pump (Leybold D65BCS). In addition a liquid nitrogen trap is connected to the back side of the main chamber to remove condensable gases. With this arrangement a base pressure of 10^{-6} torr in the main chamber can be attained. The adsorbate molecules are applied to the metal surface via a stream of gas. The gas molecules are entering the collateral chamber through a nozzle, directing them to a skimmer that represents the only connection between the two vacuum chambers. The skimmer forms a gas beam in the main chamber which hits the metal surface. Almost parallel to the surface normal and perpendicular to the gas beam, there is a time-of-flight (TOF) mass spectrometer as

Figure 3.6: Time-of-flight mass spectrometer. In the interaction region (marked by a cross), the molecular beam (dot-dashed) is crossed by the laser beam propagating in the yz -plane under an angle of 15° relative to the z -axis. Generated photoproduct cations are extracted by static electric fields, applied to repeller and apertures, and reach the detector, which consists of a micro-channel plate (MCP) pair in chevron geometry and a conical anode, after a drift time which is related to their ion mass. The repeller is modified so that a stub (light gray) holds a tilted metallic single crystal (dark gray) whose surface is in the interaction region.



depicted in Fig. 3.6. The molecular ions produced in the interaction region by the laser beam are accelerated towards the detector with a system of electrodes to which suitable extraction voltages are applied, where they generate a voltage signal on a conical anode behind a chevron-stacked micro-channel plate (MCP) assembly [177]. Discrimination of the different ions with respect to their mass-to-charge ratio is performed by measuring the flight time of the different ionic species from the interaction region on the metal surface to the detector. The ions which are instantaneously generated by the femtosecond laser pulse compared with the flight time to the detector, get accelerated to the same kinetic energy $mv^2/2 = qU$, where U is the accelerating voltage. Then their flight times $t(m, q)$ are directly related to their specific mass m/q via

$$t(m, q) \propto \sqrt{\frac{m}{q}}, \quad (3.16)$$

where m and q are the mass and the charge of the ions, respectively. The ion signals are measured either directly via a digital oscilloscope (LeCroy LC574A) or via a Time-to-Digital-Converter (FastComTec p7886) after a fast preamplifier (Ortec 9301), and are subsequently recorded by a computer.

For the surface experiments the TOF mass spectrometer has been modified in such a way that the repeller electrode serves as a mount for the single crystal surface. For this purpose a copper stub with a hollow is added to the repeller electrode. The gas beam hits the metallic single crystal, placed in the hollow under an angle of about 5° . A voltage of +200 V is applied to the crystal, and several subsequent grounded electrodes and a double μ -metal shield ensure a field-free drift region, while at the detector itself the back and front plates of the MCP assembly are set to -100 V and +1800 V, respectively, followed by the conical anode at 0 V. The temperature of the crystal is measured at the backside which is in contact with a type K thermocouple (Thermocoax DIN IEC 584) that is read out by a PID temperature controller (Eurotherm 2132). The whole repeller assembly including the single crystal can be cooled with a cryogenic system (CTI Cryogenics, refrigerator model 22 and compressor 8200) allowing a drop of temperature down to several tens of Kelvin. The cold finger of the cryogenic cooling system is connected to the repeller via thick copper wires. In order to guarantee electric isolation from the repeller and good heat conduction at the same time a ceramic aluminum nitride disk is inserted between repeller and the copper wires connected to the cooling system. With this configuration temperatures of 150 K at the metal surface can be obtained. The pressures are measured via glass-tubulated Bayard-Alpert ion gauges (Huntington IK-150-SF) connected to a vacuum gauge controller (Granville-Phillips 270).

3.5 Evolutionary algorithm

The concept of closed-loop quantum control was already presented in Section 2.1.2. In an iterative procedure a learning algorithm evaluates the performance of the applied pulse shapes with respect to a certain control objective using a feedback signal from the experiment. One of the ingredients of this concept is the learning algorithm which will be discussed in this section. In the experiments described within this thesis an

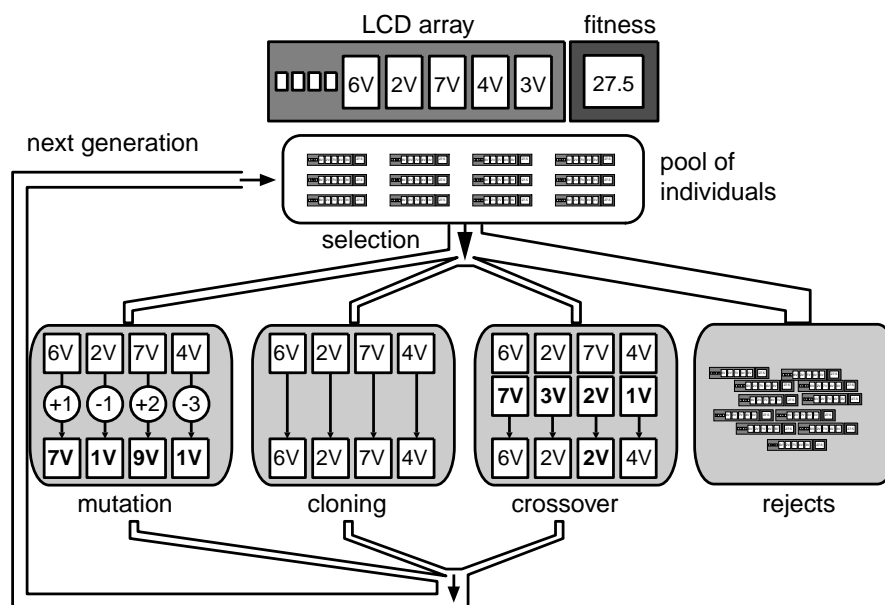


Figure 3.7: Evolutionary algorithm. The sketch schematically shows one generation. Each individual laser pulse is characterized by its genetic code (i.e. LCD pixel voltages), 60 of them (pool of individuals) are tested per generation. Depending on their fitness value, an individual is either rejected or survives and is used in the mutation, cloning, and crossover procedure for the evaluation of the pool of individuals of the next generation. The optimal pulse shape is found by iterative repetition of this loop.

evolutionary algorithm was employed for the adaptive optimization of femtosecond laser pulse shapes.

Evolutionary algorithms [178, 179] are optimization methods inspired by biological evolution. They are based on the idea of the "survival of the fittest", which means that certain genetic qualities that define an individual decide over the chances of survival leading to a natural selection. As a consequence, individuals with genetic patterns that are well adapted to environmental conditions will survive and pass their genetic code to the following generation, while the others will eventually become extinct.

In the context of using evolutionary algorithms for quantum control, the control goal must be defined prior to an optimization. This is usually the maximization of the so-called "fitness function" which includes one or more experimental observables. Mostly it takes the form of the ratio of two experimental observables X and Y according to

$$F = \frac{X}{\max(Y, Y_0)}, \quad (3.17)$$

where the quantity Y_0 in the denominator is a constant threshold value (discriminator), which is determined by the signal-to-noise ratio of the experiment and is used to keep the algorithm from finding unphysical solutions which originate from very small denominators in the fitness function.

Each pulse shape is represented by a genetic code containing 128 voltage values as they are applied to the 128 pixels of the LCD (Fig. 3.7). When the optimization is

started, the voltages are randomly initialized and then tested in the experiment. During one generation a pool of e.g. 60 individuals is tested and the fitness values are determined. A certain percentage of individuals with the highest fitness values is selected for reproduction and a new pool of individuals is generated by mutation, crossover and cloning, while the other individuals are rejected.

In the crossover procedure, four new individuals are created per survivor, by randomly pairing two of the survivors, which interchange the voltage values corresponding to a randomly selected LCD pixel. This provides two new complementary individuals created from two of the survivors. In the mutation procedure, each pixel voltage is changed by a certain amount as determined by a random number generator. The mutation leap is based on a Gaussian probability distribution with a width proportional to the last mutation leap in this pixel, effecting self-optimizing mutation leaps [94].

The search space that has to be explored by the algorithm is determined by the number of individual pulse shapes that can be generated with the LCD pulse shaper. A 12 bit voltage corresponds to $(2^{12})^{128}=10^{462}$ pulse-shaper settings (some of which deliver equivalent pulses). Since testing all these pulse shapes is definitely an impossible task, the evolutionary algorithm allows an iterative determination of the best pulse shape for a given optimization task available under the experimental conditions.

4 Femtosecond mid-infrared spectroscopy setup

Ultrafast vibrational spectroscopy requires the generation of usually ultraviolet (UV) pump and mid-infrared (MIR) probe pulses. The generation of tunable ultrashort mid-infrared pulses is based on nonlinear optical frequency mixing techniques, such as optical parametric amplification and difference frequency generation, that have already been covered in Section 2.3.3. The experimental setup of the transient femtosecond mid-infrared spectrometer, that was constructed within the scope of this work is described in this chapter. All the experiments, discussed in Chapter 5 and Chapter 6 in this work, were performed with this setup. After a general introduction to the complete pump-probe setup (Section 4.1), a detailed discussion of the generation of UV pump and MIR probe pulses (Section 4.2 and 4.3) is given. The actual pump-probe setup, including the sample mount is specified in more detail in Section 4.4. The transient MIR spectrometer is characterized in terms of tunability, time resolution and stability in Section 4.5. Here is further given a short introduction into coherent effects which have to be taken into account in femtosecond vibrational spectroscopy.

4.1 The UV pump - MIR probe experiment

A schematic overview of the experimental setup is shown in Fig. 4.1. It is based on the 1 kHz Ti:Sapphire CPA laser system, described in Chapter 3.1. The pulses with a central wavelength of about 800 nm and a pulse energy of about 0.6 mJ are split in two equal parts, using a 50:50 beamsplitter to create pump and probe pulses at the desired wavelengths by frequency conversion stages further on in the setup. The part for the pump pulse is sent to the pulse shaper, to correct for remaining higher-order dispersion causing temporal distortions of the 800 nm pulses that could not be compensated for by the compressor of the CPA system. The pulse shaper will also be used to create different excitation pulse shapes for the control experiments, that are discussed in Chapter 6. The time delay between pump and probe pulses is scanned by a computer controlled delay stage. Frequency doubling in a BBO crystal creates pulses with a central wavelength around 400 nm, which are used for the excitation of the molecular sample. The probe pulses are generated in a two stage process. Difference-frequency mixing of the Signal and Idler pulses from an optical parametric amplifier (OPA) produces probe pulses in the mid-infrared. After the sample, the MIR pulses are spectrally dispersed in a grating spectrometer and detected by a mercury cadmium telluride (MCT) photoconductive detector. Data processing was performed after analog to digital conversion (ADC) by a personal computer (PC).

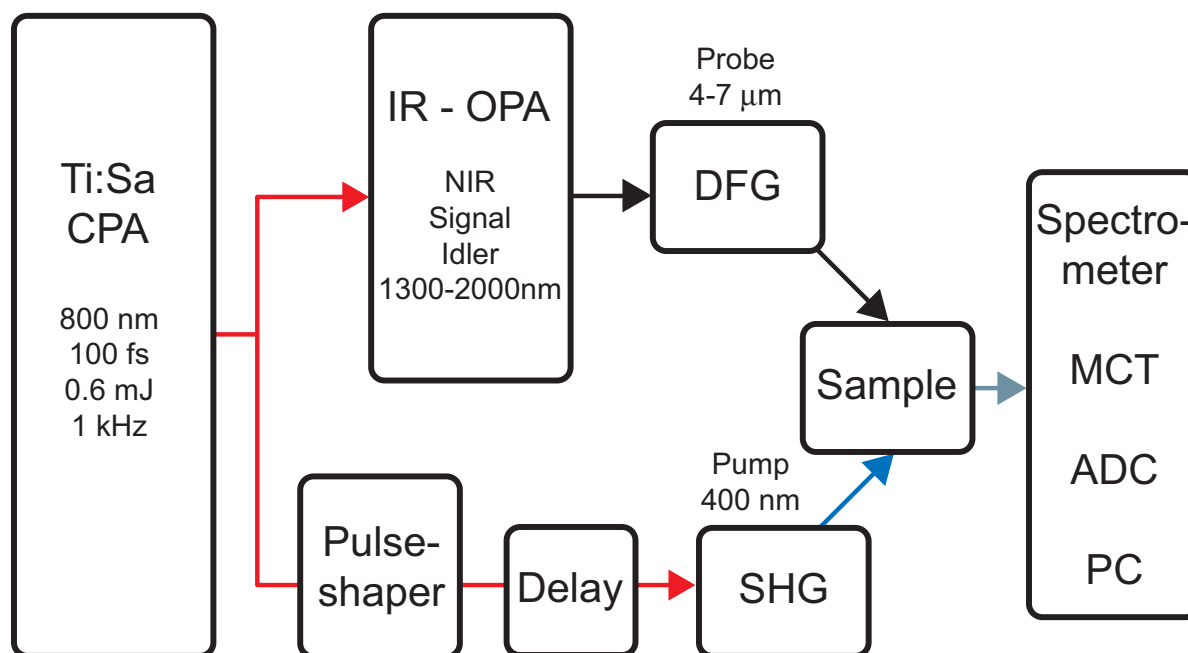


Figure 4.1: Setup for UV pump - MIR probe transient vibrational spectroscopy. The UV pump pulses are generated by second harmonic generation (SHG) in a BBO crystal and can be shaped by means of a pulse shaper. The MIR probe pulses are obtained after optical parametric amplification (OPA) and subsequent difference frequency mixing (DFG) of the generated near-infrared (NIR) Signal and Idler pulses. The transient spectra are detected with a spectrometer and are processed by a PC.

4.2 Generation of UV pump pulses

The excitation pulses are generated by second-harmonic-generation (SHG) of the fundamental 800 nm pulses from the CPA in a type I beta barium borate (BBO) crystal, cut under 29.1° with $100 \mu\text{m}$ thickness. For transient absorption spectroscopy the pulse shaper was used for an adaptive maximization of the second harmonic yield (SHG optimization) by adjusting the spectral phase of the fundamental pulse. This results in temporally clean and short pump pulses, leading to the best time resolution possible. After the pulse shaper a 1:2 telescope reduces the beam diameter and the adjustment of the beam diameter at the position of the sample is facilitated. The 800 nm pulses of about $250 \mu\text{J}$ pulse energy before the pulse shaper, can be converted into 400 nm pulses of up to $10 \mu\text{J}$.

4.3 Generation of probe pulses in the mid-infrared

Ultrashort tunable mid-infrared pulses are routinely generated by difference-frequency generation from the Signal and Idler pulses of an 800 nm pumped optical parametric amplifier (OPA) [102]. The most commonly used crystal for DFG is silverthiogallate (AgGaS_2), which allows for tuning in the range of $3\text{-}12 \mu\text{m}$ [180]. Depending on the pump

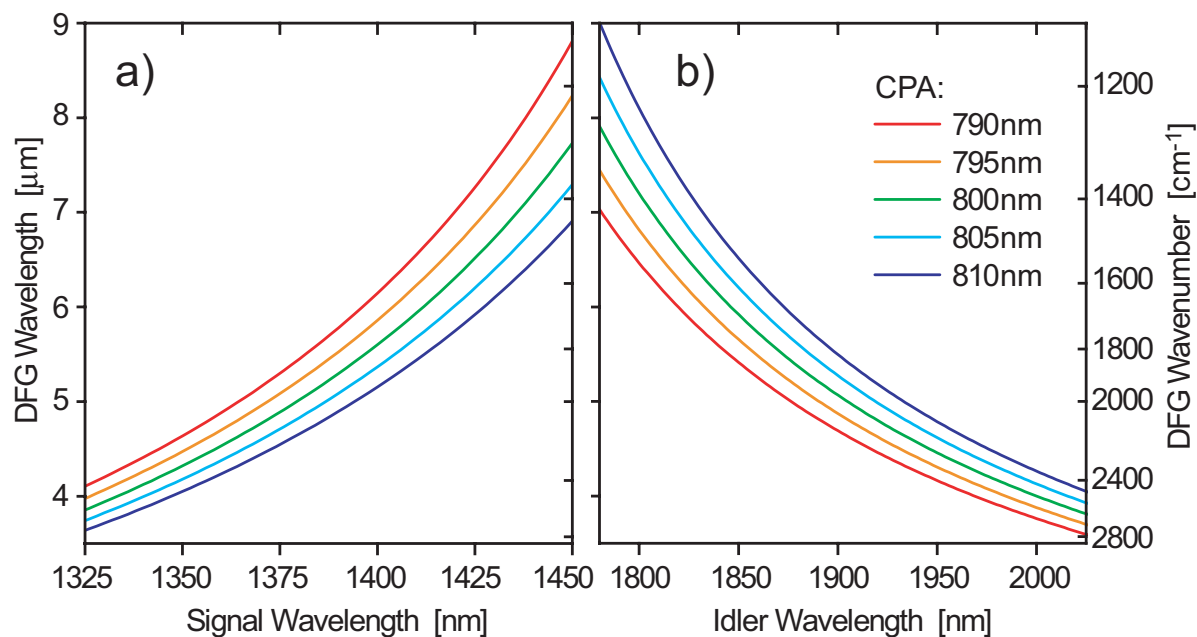


Figure 4.2: a) Dependence of the DFG wavenumber (right scale) and wavelength (left scale) on the Signal wavelength and b) on the Idler wavelength for different Ti:Sa CPA central wavelengths around 800 nm. Calculated according to Eqs. (4.2) and (4.3).

pulse energy, mid-infrared pulses with energies in the microjoule regime are obtained. Although during the last decade different designs of this principle were realized, a design first introduced by P. Hamm [181] has established itself due to its easy implementation and high stability [182]. Many other groups, working in the field of transient vibrational spectroscopy, 2D-IR spectroscopy [183] or MIR pulse shaping [184–186] are referring to this design. Therefore, it was also chosen to be the one to be constructed for this work.

Different nonlinear processes are involved in the subsequent stages of this scheme. The starting point is the generation of a seed pulse, created by white light continuum (WLC) generation. The near-infrared part of the WLC is then amplified in an OPA process in the first stage. The Signal pulse from the first amplification stage is further amplified in the second OPA stage, to produce intense Signal and Idler pulses. The mid-infrared pulses are then generated by difference-frequency generation (DFG) from Signal and Idler.

For practical purposes it is useful to determine the wavenumbers $\bar{\nu}$ (in cm^{-1}) of Signal and Idler, that are necessary to obtain the desired central wavenumber of the mid-infrared pulses for a given central wavelength of the CPA pump pulses. They can be calculated by the following equations:

$$\bar{\nu}_{CPA} = \bar{\nu}_{Signal} + \bar{\nu}_{Idler} \quad (4.1)$$

$$\bar{\nu}_{DFG} = 2\bar{\nu}_{Signal} - \bar{\nu}_{CPA} \quad (4.2)$$

$$\bar{\nu}_{DFG} = \bar{\nu}_{CPA} - 2\bar{\nu}_{Idler} \quad (4.3)$$

These relations are visualized in Fig. 4.2 for different CPA central wavelengths in the region around 800 nm.

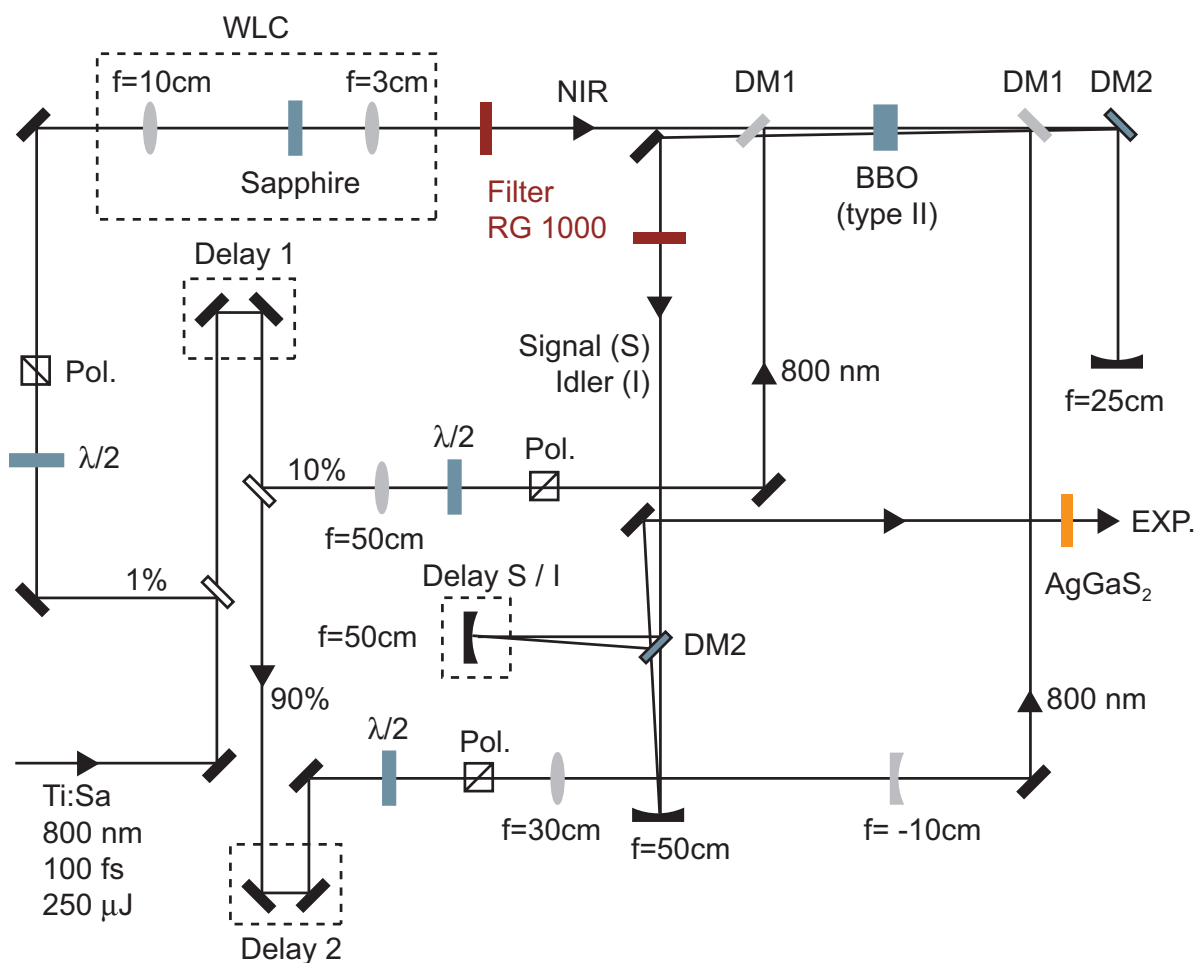


Figure 4.3: Complete experimental setup for the generation of tunable mid-infrared pulses. Ti:Sa laser pulses are converted to the mid-infrared in a home-built two stage near-infrared (NIR) optical parametric amplifier followed by difference-frequency mixing of the Signal and Idler pulses in a silverthiogallate (AgGaS_2) crystal. A detailed description is given in the text.

4.3.1 Optical parametric amplifier

The complete setup for the generation of mid-infrared pulses is shown in Fig. 4.3. In the following the different frequency conversion and amplification stages are discussed in detail.

White light continuum generation

The OPA is pumped with p-polarized, 100 fs, 250 μJ pulses from the Ti:Sa CPA at 800 nm and 1 kHz. The seed pulse for the first stage of the OPA is created by single-filament white light continuum (WLC) generation in a sapphire crystal (see upper left hand side in Fig. 4.3). In contrast to other techniques to generate the seed pulses like superfluorescence, WLC seed pulses are much more stable, so that the resulting mid-infrared pulses exhibit very low pulse to pulse energy fluctuations. A weak fraction of

about $2 \mu\text{J}$ is split off of the incoming beam by using a thin BK7 glass window (back side is anti-reflection coated). Using a lens with 10 cm focal length, the reflected portion of the beam is focused in a 4 mm thick sapphire plate, that is cut perpendicular to the c-axis for efficient white light generation. The intensity of the focused beam can be controlled by a combination consisting of a half-wave plate and a polarizer. It is also used to rotate the polarization by 90° , because the OPA process in the first stage requires s-polarized seed pulses, due to the phase matching condition (see first OPA stage). The intensity has to be adjusted very carefully, so that the formation of multiple filaments in the sapphire disk is prevented. That would lead to very unstable and strongly fluctuating seed pulse energies. After the sapphire plate the white light continuum is recollimated and focused into the BBO crystal with a 3 cm lens. The visible as well as part of the NIR ($<1000 \text{ nm}$) is blocked by a RG 1000 glass filter, so that only the near-infrared part of the WLC arrives at the BBO.

1st OPA stage

For the first OPA stage, the s-polarized seed pulses from the white light continuum and p-polarized 800 nm pump pulses (another fraction of about 10% of the Ti:Sa pulses) have to be collinearly combined in a type II phase matching, 4 mm thick, BBO crystal by means of the dichroic mirror DM1 (high transmission for 1200-2200 nm, s-polarization; high reflection for 750-850 nm, p-polarization). The crystal is cut under $\theta = 27^\circ$ and $\phi = 30^\circ$ for optimal type II phase matching of the OPA process. The pump pulses are tightly focussed by a 50 cm lens into the BBO. Their beam waist is much smaller than the beam waist of the seed pulses, so that excellent spatial properties of the generated beams are obtained. The intensity of the 800 nm pump pulses is adjusted by a combination consisting of a half wave plate and a polarizer so that it is close to the white light generation threshold in the BBO crystal. Temporal overlap of the seed and pump pulses is obtained by adjustment of a delay stage (Delay 1).

2nd OPA stage

The amplified Signal pulses are sent over the dichroic mirror DM2 (high transmission for 1650-2500 nm, p-polarization; high reflection for 1200-1550 nm, s-polarization), so that the Idler pulse is removed. The remaining Signal pulse is collimated by a concave gold mirror and directed back to the BBO crystal in the same vertical plane (same phase-matching angle as in first OPA stage), but about 3 mm below the beam in the first OPA stage. With this double pass configuration the same BBO crystal can be used again for parametric amplification in the second stage. The pump pulses for the second OPA stage are the remaining fraction (about 90%) of the Ti:Sa pulses. After the delay stage (Delay 2), where the temporal overlap in the second stage is optimized, the beam waist of the pump beam is reduced by a 1:3 telescope, to match the beam waists of the collimated Signal beam from the first stage and the pump beam of the second stage. The pulse energies of Signal and Idler after the second OPA stage are up to $20 \mu\text{J}$, depending on the wavelengths of Signal and Idler.

4.3.2 Difference frequency generation stage

The Signal and Idler pulses generated by the OPA have perpendicular polarization (Signal: s-pol., Idler: p-pol.) according to the phasematching condition in the BBO crystal. This is required for the following DFG process. The RG 1000 filter after the OPA is used to remove contributions from 800 nm Pump light and not phasematched sum-frequency generation light originating from interaction of the Pump wave with Signal and Idler (Signal+Pump:green, Idler+Pump:yellow). Signal and Idler leave the OPA more or less collinearly depending on the alignment and in addition slightly displaced in time due to group-velocity-dispersion in the BBO crystal. Thus, for the precise adjustment of the temporal and spatial overlap of Signal and Idler in the DFG process, the pulses are divided by the dichroic mirror DM2. The Signal pulses are sent over a delay stage (Delay S/I) and are collinearly recombined with the Idler pulses in the same dichroic mirror. Both, Signal and Idler are focused with spherical gold mirrors ($f=50$ cm) into a 1 mm thick, type I silverthiogallate (AgGaS_2) crystal, cut under $\theta = 39^\circ$ and $\phi = 45^\circ$ for difference-frequency generation. Depending on the wavelength region of the mid-infrared pulses, pulse energies of up to 350 nJ were achieved.

4.4 Pump-probe setup

In this section the pump-probe setup, consisting of the beam paths for the pump and probe pulses, the spectrometer, the IR-detector, the signal processing electronics as well as the the sample mounting, is described in detail. The optics part is shown in Fig. 4.4.

4.4.1 Pump and probe beam paths

After blocking the residual Signal and Idler beams with a long wave pass (LWP) filter (high transmission for $\lambda > 2.6 \mu\text{m}$), the MIR probe pulses are collimated by a spherical gold mirror ($f=50$ cm). A 2:1 telescope, consisting of spherical gold mirrors with $f=5$ cm and $f=10$ cm, increases the beam diameter by a factor of two. Thus, when focusing the beam on the sample, the obtainable beam waist is reduced by this factor (see Section 2.2.3). Spherical gold mirrors ($f=15$ cm) are used to focus the probe beam on the sample and to recollimate the beam. It is then sent to the spectrometer. In front of the sample and the spectrometer, attenuators can be placed to adjust the intensity of the probe pulses, so that about 10 nJ arrive at the sample and that the IR-detector is below the saturation regime. For attenuation, materials with high refractive index for high reflection losses, but low absorption in the MIR, like silicon, germanium (both $\sim 50\%$ transmission) or zinc telluride ($\sim 75\%$ transmission) are used.

The 400 nm pump pulses are focused by a 30 cm lens into the sample. A pickoff (1%) of this beam before the sample is directed on photodiode PD1 and after the sample the pump beam is focused on a second photodiode PD2 for monitoring purposes. As already explained in Sec. 3.4.2 a mechanical chopper is employed to block every other laser shot. Whether a laser shot is blocked or not is determined by PD1. This serves to decide about the sign of the change in optical density. The sample can be replaced by a knife edge, which can be scanned perpendicular to the direction of beam propagation,

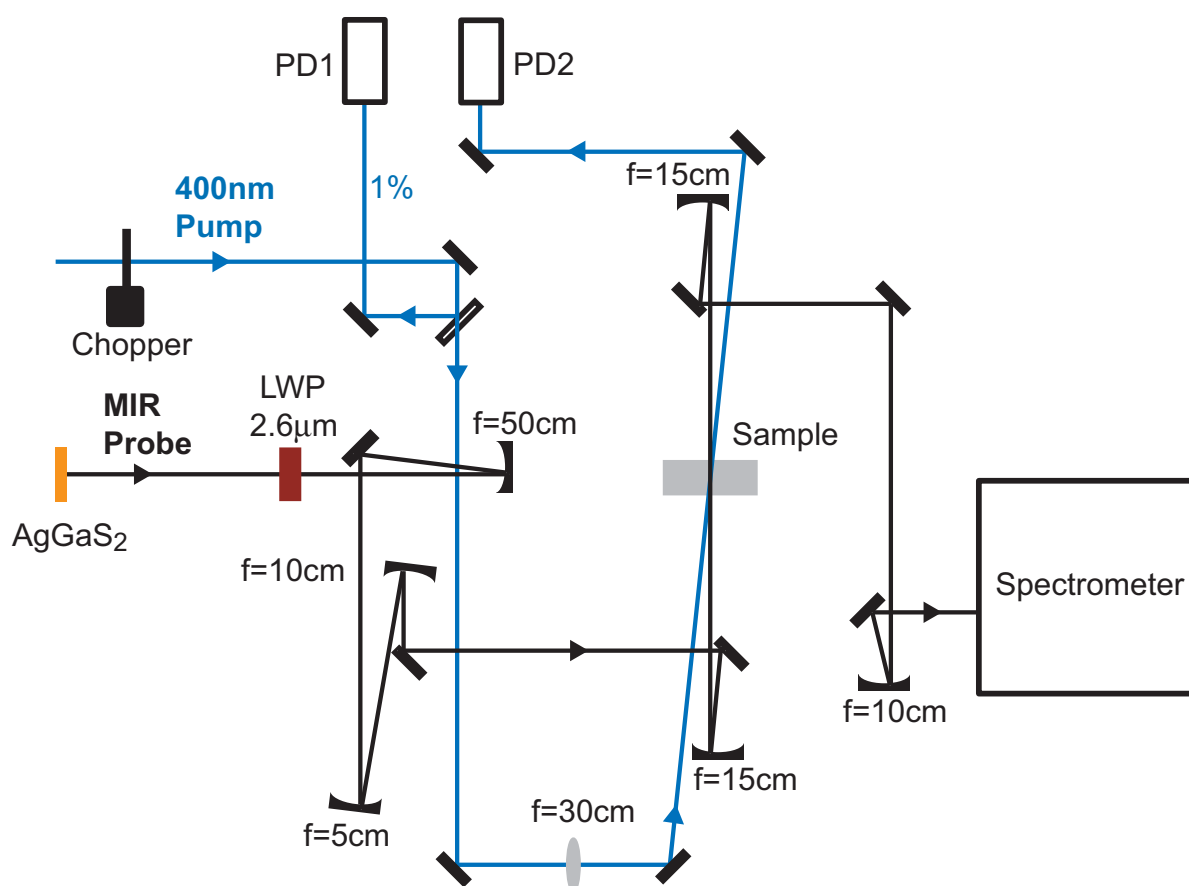


Figure 4.4: Setup for the 400 nm pump - mid-infrared probe experiment. The MIR probe beam coming from the AgGaS_2 crystal is collimated and sent over a 2:1 telescope ($f=5\text{cm}$, $f=10\text{cm}$ concave mirrors) before being focused into the sample. After the sample the MIR beam is directed to the spectrometer. A small fraction (1%) of the 400 nm pump beam is split off by a pickoff before the sample in order to monitor with a photodiode (PD1) if the beam is blocked by the chopper. The major fraction of the pump beam is focused into the sample. The pump beam diameter at the sample position can be determined by a knife edge scan using PD2 after the sample. With this arrangement of PD1 and PD2 one could in principle also measure the absorption of the pump beam in the sample.

so that the beam diameter exactly at the place of the sample can be determined. As a function of the knife edge position the unblocked beam intensity is measured by PD2. In principle this arrangement of PD1 and PD2 before and after the sample could also be employed to measure the absorption of the pump pulses in the sample.

4.4.2 Spectrally resolved infrared detection

In the spectrometer (Chromex 250 is/sm spectrograph/monochromator), the MIR pulses are dispersed by a 150 l/mm reflective grating. They are detected by a 32-element mercury cadmium telluride (MCT) photoconductive detector array (Infrared Associates, Inc.). The resolution depends on the central wavelength of the MIR pulses, and ranges

from $2\text{-}6\text{ cm}^{-1}$ per pixel. The signal of each detector-element is amplified by a 32-channel preamplifier (Infrared Systems Development Corporation MCT-3200). Further signal processing takes place in a home-built 32-channel boxcar array, where the signal is further amplified, integrated and send to a analog to digital converter (National Instruments PCI-6033E).

4.4.3 Flow cell mount

The sample is pumped through a flow cell with CaF_2 windows by means of a peristaltic pump (Cole Parmer, Masterflex L/S), so that the sample volume is completely exchanged for each consecutive pump-probe pulse pair. The sample thickness was usually $100\text{ }\mu\text{m}$. The flow cell is mounted on a base, that can be moved in the directions of the probe beam propagation (z-direction) and perpendicular (x-direction) by linear translation stages. The movement in x-direction can be controlled by a step motor (Zaber). For different purposes, the flow cell mount can be taken off the movable base and be replaced by a pinhole to ensure spatial overlap of pump and probe, a thin germanium plate for adjustment of the temporal overlap (see Section 4.5), another flow cell for measuring the solvent only, or a knife edge. By performing a knife edge scan, the beam diameters of pump and probe are determined, and can be matched by adjusting the optical elements before. The pump beam diameter has to be larger than the probe beam diameter, so that molecules in the entire probe volume are excited, which maximizes the transient absorption signal. For the experiments in the following, the mid-infrared probe beam diameter was $260\text{ }\mu\text{m}$, and the pump beam diameter was $340\text{ }\mu\text{m}$.

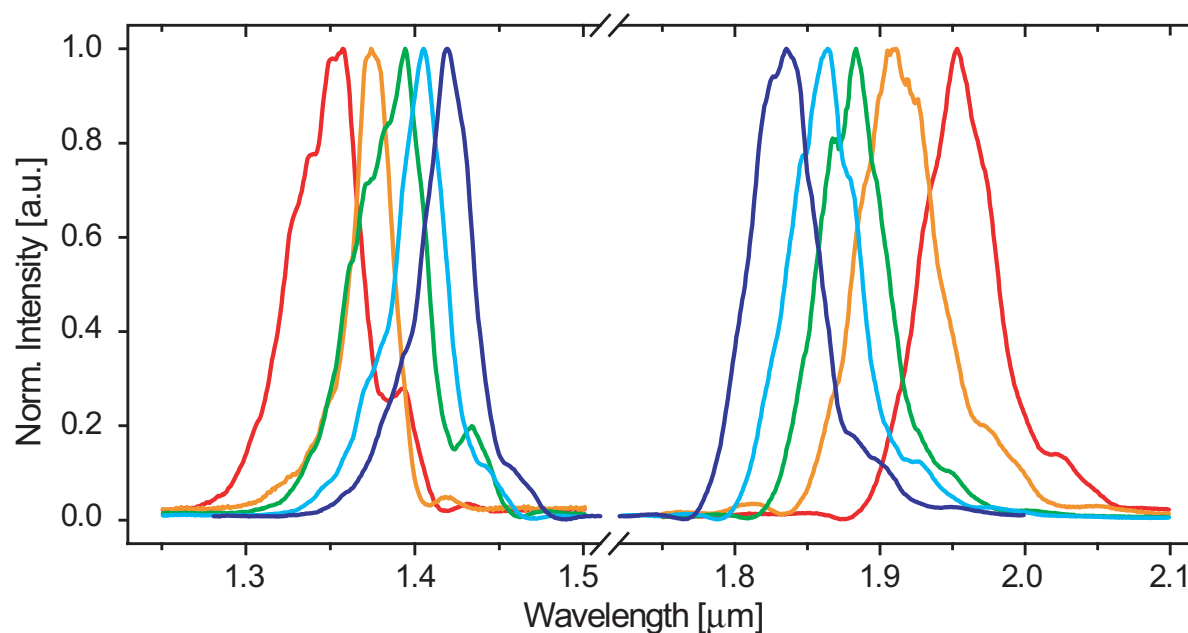


Figure 4.5: Normalized spectra of the Signal and Idler pulses, that show the wide tunability of the home-built OPA.

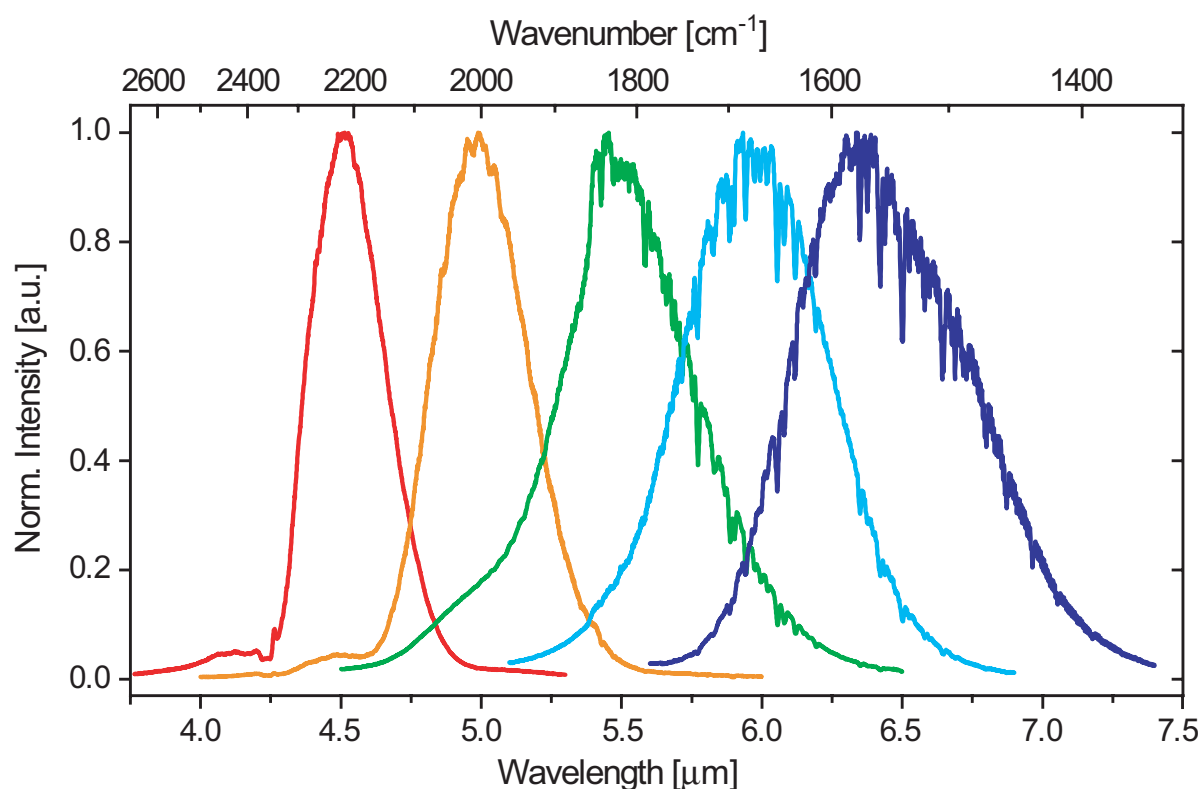


Figure 4.6: Normalized spectra of the MIR probe pulses, that show the wide tunability from 4.3-7.0 μm of the home-built OPA/DFG system. The distortions in the spectra from 5.5 μm on are due to the absorption of residual water vapor in the MIR beam path.

4.5 Characterization of the transient MIR spectrometer

4.5.1 Spectral tunability

The spectral tunability of the mid-infrared probe pulses is demonstrated in this section. Fig. 4.5 shows normalized spectra of Signal and Idler pulses, indicating the wavelength range, that is accessible by tuning the OPA via the phase-matching angle of the BBO crystal. The Signal pulses lead to spectra from 1300-1450 nm and the Idler pulses to spectra from 1800-2000 nm. The respective spectra (same color code) of the MIR pulses generated by difference-frequency mixing of Signal and Idler can be seen in Fig. 4.6. Tunability from 4.3-7.0 μm (2300-1450 cm^{-1}) is shown here. In the region around 6.0 μm water vapor in the MIR beam path heavily distorts the spectra. The bending vibration mode of H_2O is responsible for the strong absorption in this spectral region. Therefore the whole setup has to be purged with dried air or nitrogen gas, when performing transient absorption experiments in this region. Some residual absorption is still visible in the spectra from 5.5 μm on.

The lower wavelength region, down to 3 μm can easily be reached, but this was not necessary for this work, since none of the studied molecules in the following chapters have vibrational bands in this region. Wavelengths above 7 μm should be feasible by using

another AgGaS₂ crystal with the appropriate phase-matching angle for this wavelength region. But since these regions were not required for this thesis, that was not attempted.

4.5.2 Time resolution

The time-resolution of a UV pump - MIR probe experiment can be determined by a cross-correlation measurement of pump and probe pulses in a semiconductor sample [187], e.g. Si, Ge or ZnSe. UV radiation with photon energies, that exceed the band gap of the semiconductor material, generates free carriers in the conduction band (CB) almost instantaneously compared with the pulse durations. These free carriers can populate a continuum of states in the conduction band (see Fig. 4.7a). Therefore MIR radiation can be absorbed as long as the free carriers have not relaxed back to the valence band (VB). Using this method the zero delay point of UV-pump and MIR-probe pulses can easily be determined. By scanning the delay time Δt between pump and probe a step-like curve as shown in Fig. 4.7b can be recorded. At negative delay times no difference in absorption can be measured, since no free carriers exist in the conduction band. The small difference of about 50 fs in the zero delay point for pixels at the two ends of the detector array, means that the MIR pulses are slightly chirped, since different wavelengths arrive at different times at the semiconductor sample. The time resolution in this and in other measurements was determined to be in the range of 200-300 fs.

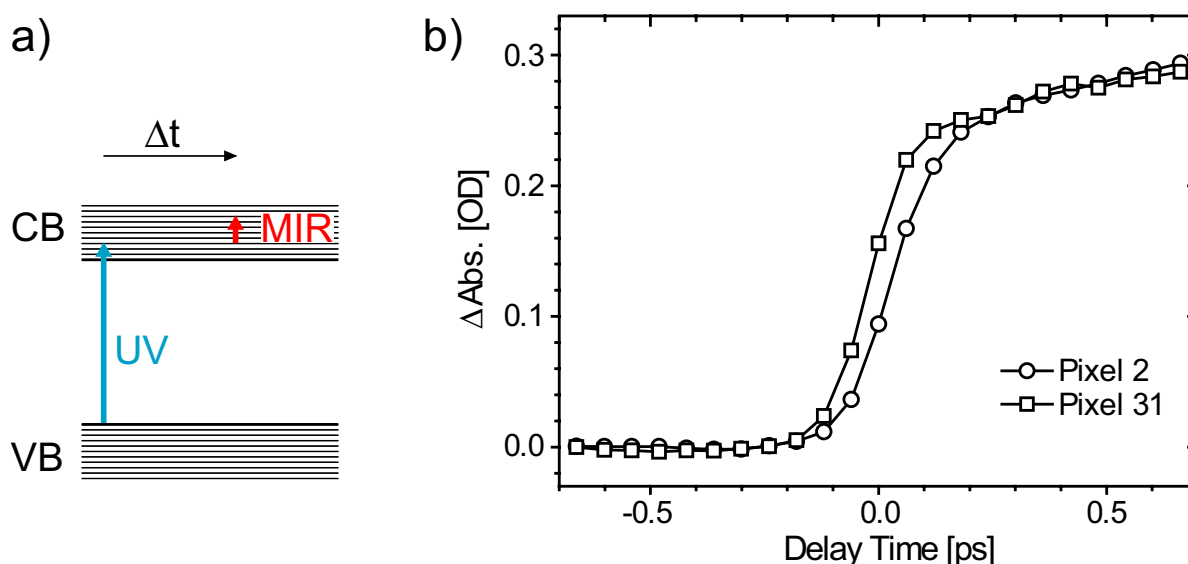


Figure 4.7: a) Free carriers are excited by the UV pump pulse from the valence band (VB) to the conduction band (CB). The time delayed MIR probe pulse can then be absorbed by the CB electrons. b) Transient absorption measurement in Ge with 400 nm excitation. The small difference in zero delay point of 50 fs between pixel 2 (2146 cm⁻¹) and pixel 31 (2020 cm⁻¹) indicates that the MIR pulses are slightly chirped.

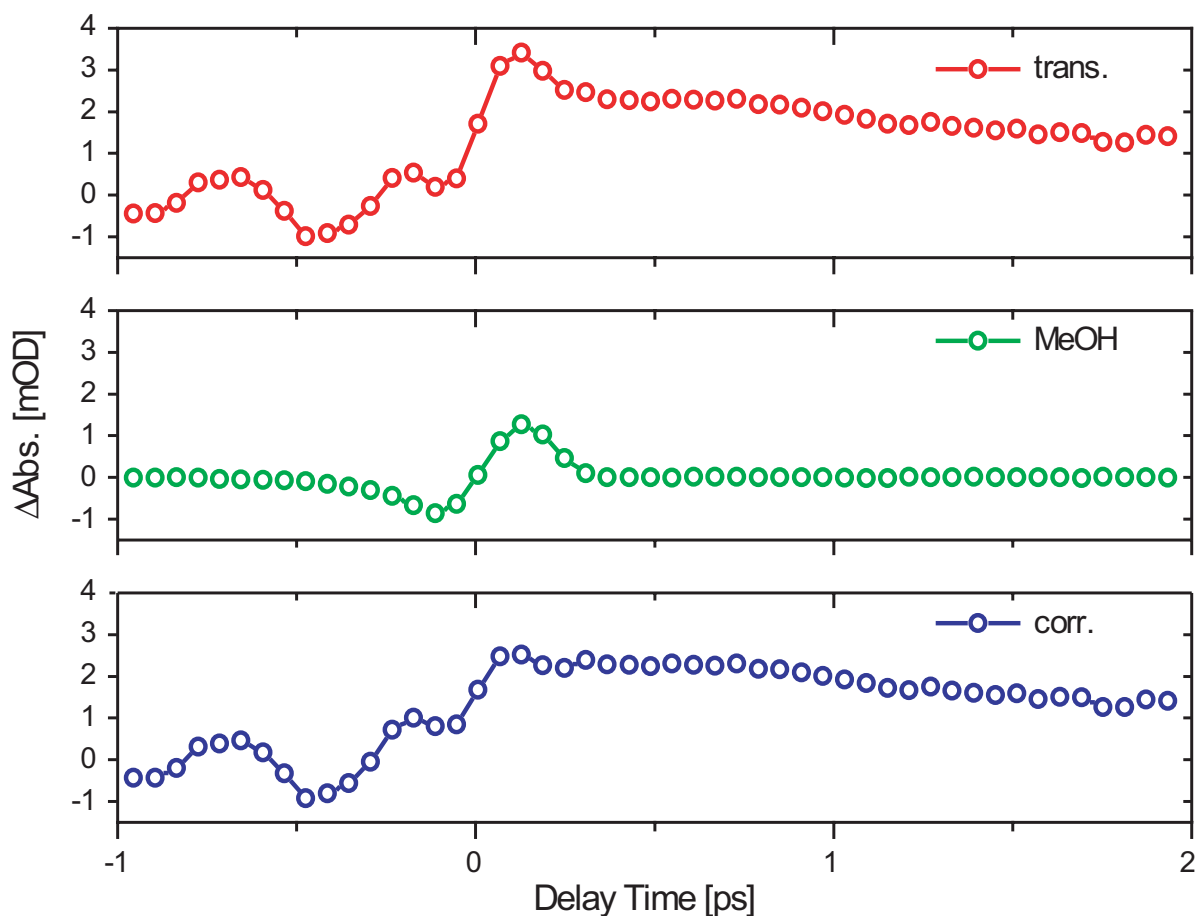


Figure 4.8: Coherent artifact from cross-phase modulation (XPM) in transient absorption spectroscopy. The upper curve (red) shows a transient in which the coherent artifact is visible as the peak around time zero. An independent measurement of the solvent only (green curve) under the same experimental conditions reveals the contribution of the XPM effect. The corrected transient (blue) is shown in the lower graph.

4.5.3 Coherent artifact

The coherent artifact is an unwanted nonlinear effect in liquid phase femtosecond transient absorption spectroscopy. It originates in the nonlinear interaction, called cross-phase modulation (XPM), of the intense pump pulse with the solvent and the window material of the flow cell [188, 189]. It has nothing to do with the dynamics of the molecule or system that is investigated. During the interaction, the real part of the refractive index $n(t)$ of the optical medium is modulated according to

$$n(t) = n_0 + n_2 |E(t)|^2, \quad (4.4)$$

where $|E(t)|^2$ is the temporal envelope of the pump pulse. That leads to time-dependent modulation of the phase and spectral redistribution in the probe pulse. This affects the spectrally resolved probe pulse and gives rise to a signal around the zero

delay point, where pump and probe overlap in time, and interferes with the evaluation of the time-resolved data at very short delay times. It depends on the material of the cell windows, the solvent, pulse intensity and duration, and on the chirp of the probe pulse.

An example is given in Fig. 4.8, where a measured transient from -1 to 2 ps is shown, which is obscured by the coherent artifact (upper curve - red). The same measurement can be performed again with the solvent only in the flow cell (middle curve - green), and so the contribution of the XPM effect to the transient in the upper red curve is visualized. Ideally one should be able to correct for the XPM by subtracting the two measurements from each other. But in reality this constitutes a difficult task, since the experimental conditions have to be exactly identical for both measurements. When the sample absorbs at the excitation wavelength a scaling factor has to be included [189]. In transient vibrational spectroscopy a second artifact, the perturbed free induction decay (see next Section) also has to be taken into account. It manifests itself as e.g. oscillatory features at short negative delay times, that are clearly visible in the red transient in Fig. 4.8. Then differentiating between molecular dynamics and artifacts becomes even harder. Therefore the lower curve (blue) in Fig. 4.8, which is corrected for the XPM effect (with an appropriate scaling factor), still exhibits a small dip right after the zero delay point.

4.5.4 Perturbed free induction decay

In addition to the coherent artifact, an effect called perturbed free induction decay is observed in ultrafast vibrational spectroscopy. It originates from the interaction between the decaying vibrational coherence created by the infrared probing pulse with the pump pulse. This interaction is possible, because the accessible time resolution in femtosecond infrared spectroscopy is shorter than typical dephasing times of vibrational coherences.

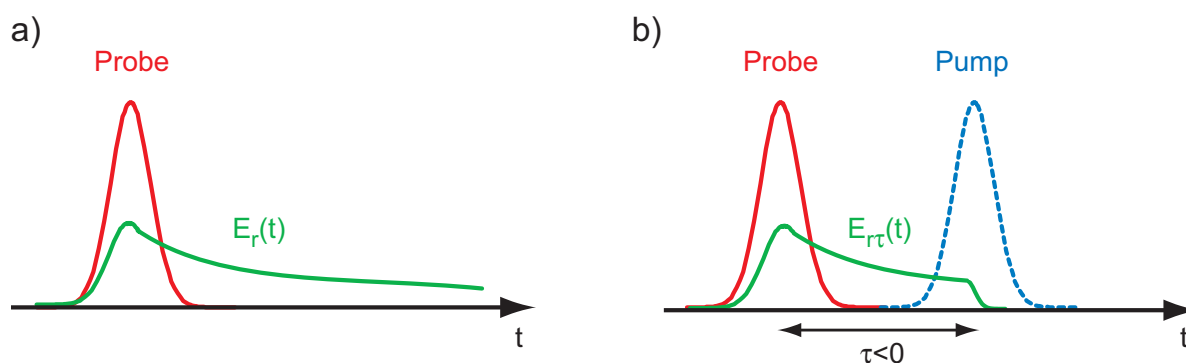


Figure 4.9: a) Free induction decay: The infrared probe pulse in resonance with a vibrational transition of a molecular sample generates a coherent polarization which radiates the free induction decay field $E_r(t)$. b) Perturbed free induction decay: The pump pulse arriving after the probe pulse (negative delay time $\tau < 0$) perturbs the free induction decay light field which disappears upon electronic excitation ($E_{rr}(t)$). This results in a measured change of absorbance. Illustration according to [190].

For electronic transitions of molecules in solution the spectral linewidth is typically on the order of 100-1000 cm^{-1} . In the case of electronic homogeneous broadening, the full width half maximum (FWHM) of the absorption line (in cm^{-1}), is related to the dephasing time T_2 , by $T_2 = 1/(100c\pi\Delta\nu_{FWHM})$. Although electronic transitions may have a significant inhomogeneous broadening component, it can still be deduced, that the characteristic time for dephasing is on the order of 10 to 100 fs. In contrast to that, for vibrational transitions line widths of only 5-25 cm^{-1} are common. That leads to a phase relaxation time of up to 1000 fs, which is longer than the duration of an infrared probing pulse of some 100 fs.

The appearance of the perturbed free induction decay (PFID) effect in ultrafast vibrational spectroscopy can be explained as follows [111, 190]: In UV pump - MIR probe experiments, an intense pump pulse is used to induce a photoreaction. The response of the sample is probed by monitoring the change in absorbance with a weaker probe pulse as a function of temporal delay between pump and probe. Therefore an absorbance change is expected only at positive delay times (when the pump arrives at the sample before the probe). However, the infrared probing pulse can resonantly create a vibrational coherence (coherent polarization), which decays with its characteristic dephasing time T_2 . This coherent polarization acts as a source of radiation (the so-called free induction decay) which decays with the dephasing time constant T_2 illustrated in Fig. 4.9a as the field $E_r(t)$. When the excitation pulse reaches the sample after the probing pulse, it can not influence the intensity of the probing pulse itself. However it may influence the temporal or spectral properties of the free induction decay signal of the sample (Fig. 4.9b), whenever the electronic excitation process modifies the strength or position of the absorption line. As a consequence, in the case of spectrally resolved detection, the IR-detector will record a difference signal, which decays towards negative delay times with time constant T_2 .

The temporal behavior of the perturbed free induction decay signal $\Delta T(\omega, \tau)$ can be calculated with the following equations:

$$\Delta T(\omega, \tau) \propto \begin{cases} -e^{\tau/T_2} \frac{\cos[(\omega - \omega_a)\tau]/T_2 + (\omega - \omega_a) \sin[(\omega - \omega_a)\tau]}{(\omega - \omega_a)^2 + (\tau/T_2)^2} & \text{for } \tau < 0 \\ 1 & \\ -\frac{1}{(\omega - \omega_a)^2 + (\tau/T_2)^2} & \text{for } \tau > 0, \end{cases} \quad (4.5)$$

where ω_a is the frequency of the vibrational line center, T_2 the dephasing time, ω the detection frequency and τ the delay time. This behavior is depicted in Fig. 4.10 for a vibrational transition with central wavenumber at 2117 cm^{-1} and FWHM line width of 23 cm^{-1} , corresponding to a phase relaxation time of 460 fs. The PFID signal is not only present at the line center but also at frequencies close to it where characteristic oscillations in the PFID signal are observed. The above equation is valid for δ -shaped excitation and probing infrared pulses. Finite pulse duration can also be included to the calculation, which leads to qualitatively similar PFID signal, with smoothing of the signal changes at the zero delay point and more pronounced oscillations at the spectral wings of the absorption line. In the case of infinite time resolution for δ -shaped pulses,

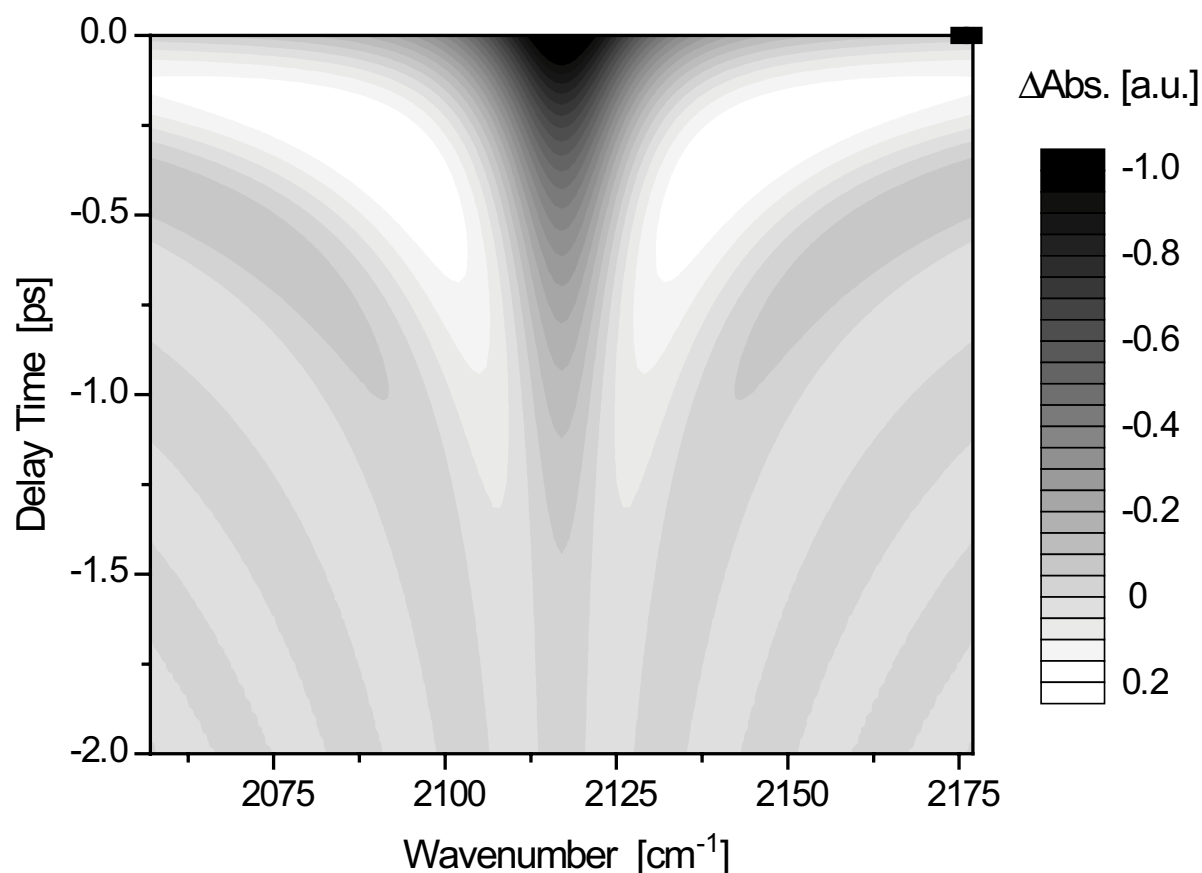


Figure 4.10: Perturbed free induction decay signal simulated according to Eq. 4.5, for a central wavenumber of 2117 cm^{-1} and a FWHM linewidth of 23 cm^{-1} . It is exponentially decaying towards negative delay times at the line center while in the wings of the absorption line oscillations are observed.

perturbed free induction decay is observed only at negative delay times ($\tau < 0$), while the reaction or relaxation dynamics of the sample occurs after the zero delay point at $\tau > 0$. In an experiment with finite time resolution, a mixture of all these processes takes place within the cross correlation time of the pump and the probe pulse. Thus, the observation of fast molecular reactions is strongly hindered by perturbed free induction decay.

4.6 Conclusion

For the purpose of investigating ultrafast structural changes in photoreactions, a pump-probe setup for femtosecond transient absorption spectroscopy in the mid-infrared was constructed. It consists of a Ti:Sa pumped optical parametric amplifier with a subsequent difference frequency mixing stage, where subpicosecond infrared probe pulses, tunable in the region from at least $4\text{-}7 \mu\text{m}$ are generated. Typically the pulse to pulse energy fluctuations of the mid-infrared probe pulses are about 0.5% and this leads to detectable absorption changes on the order of 0.1 mOD with reasonable averaging time.

With spectrally resolved detection, a wavenumber range of 80-150 cm^{-1} , depending on the spectral region of the mid-infrared pulses can be recorded in a single measurement. The pump pulses are created by frequency doubling of the Ti:Sa fundamental to obtain pulses at 400 nm. The instrumental response time, and thus the time resolution of the experimental setup is 200-300 fs. In addition to the pulse generation, a flexible mount for the flow cell in which the sample solution is pumped by a peristaltic pump, was designed and built. It enables fast and easy alignment of the spatial and temporal pump-probe overlap, beam diameter measurements as well as easy exchange of the sample.

5 Femtosecond IR study of the photoinduced Wolff rearrangement of DNQ

5.1 Introduction

Diazonaphthoquinone (DNQ) derivatives are the photoactive compounds of photoresist materials, used in lithography for the production of integrated electronic circuits. Novolak-DNQ mixtures are currently involved in the fabrication of more than 80 % of the worlds integrated circuits [192]. A possible example of the photolithographic process is schematically depicted in Fig. 5.1a. On top of a silicon oxide layer on a silicon substrate, the photoresist is applied. Irradiation through a structured mask leads to

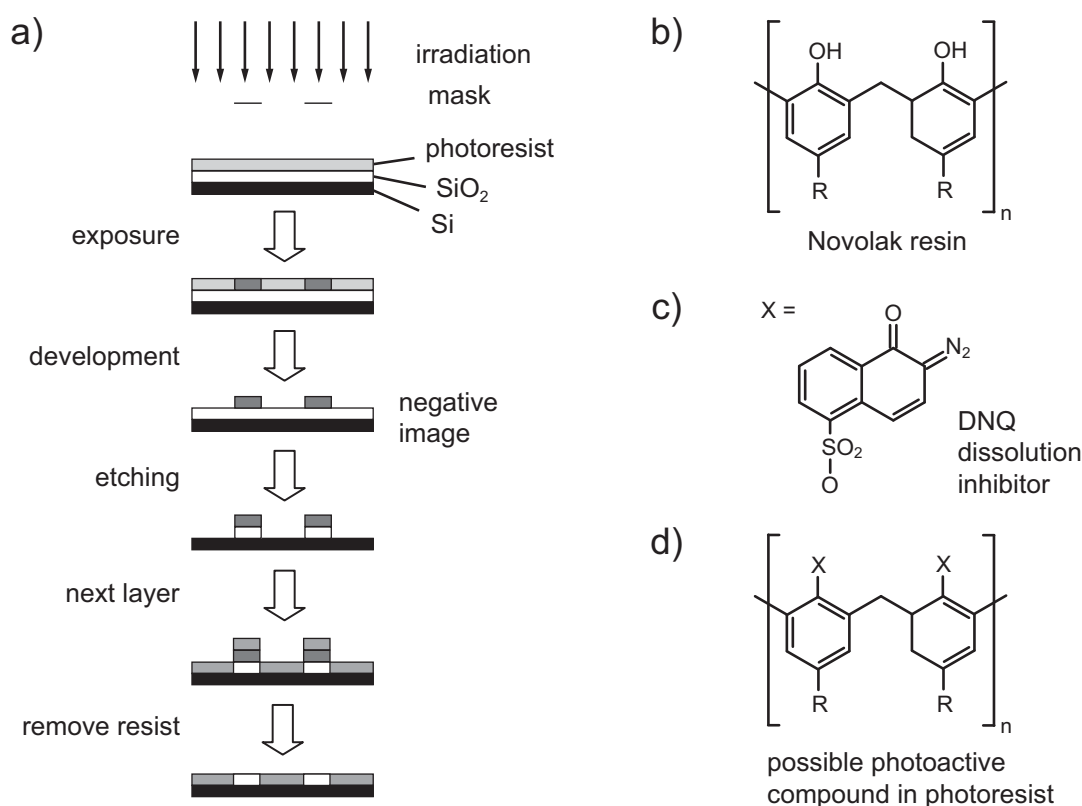


Figure 5.1: a) The process of photolithography. b) Novolak resin. c) The dissolution inhibitor DNQ. d) Possible combination of Novolak and DNQ.

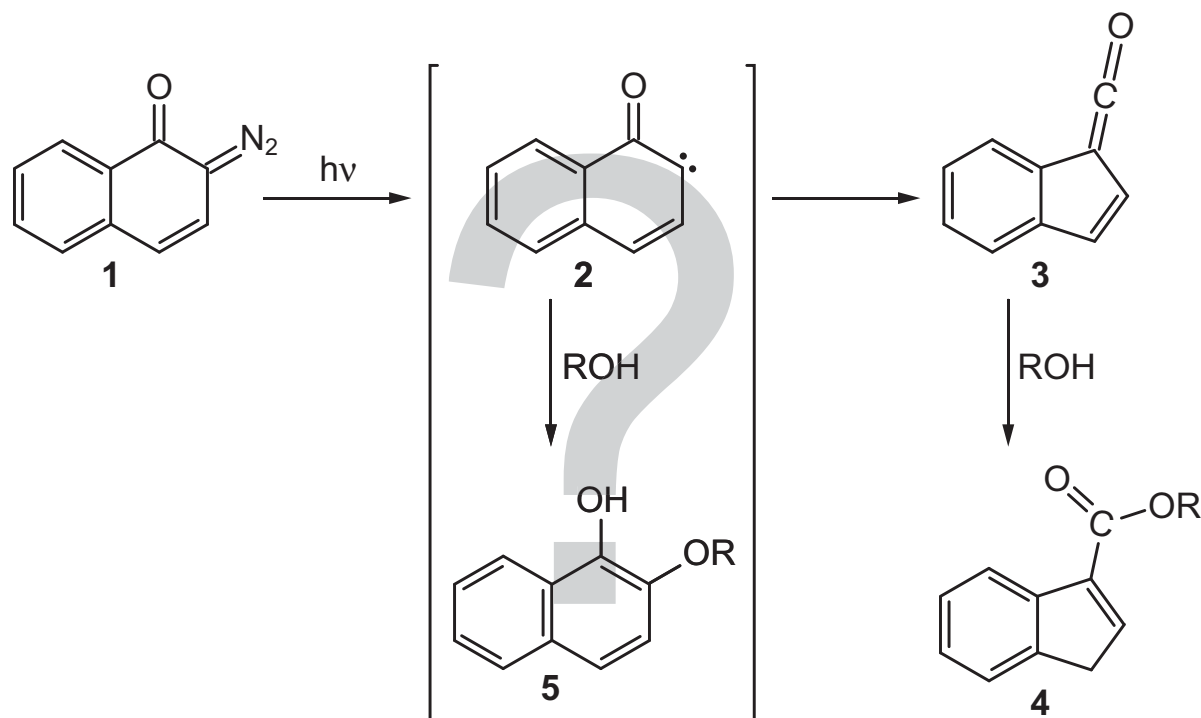


Figure 5.2: Scheme of the photoreaction of 2-diazo-1-naphthoquinones (1) according to Vlegaar et.al. [191]. After diazo separation the still disputed carbene intermediate (2) is followed by a ketene (3). Further reactions with the solvent ROH (e.g. water or methanol) lead to indene carboxylic acid methyl ester (4) and, if the carbene exists 1-hydroxy-2-alkoxy-naphthalene (5).

photoinduced changes of the properties of the photoresist material. In the development step the exposed regions of the photoresist can be removed by use of an appropriate solvent to produce the negative image. In these regions the unprotected silicon oxide layer is removed by etching. Then another layer of material, e.g. metal is evaporated on the structured silicon oxide layer.

Photoresist materials consist of three compounds, an organic solvent, the Novolak resin and DNQ. The Novolak resin is a phenol-formaldehyde condensation polymer (Fig. 5.1b), which is responsible for the film forming properties of the photoresist [193]. Films of Novolak dissolve in aqueous alkali, but when small concentrations of DNQ (Fig. 5.1c) are added the rate of dissolution is dramatically reduced. When irradiated with UV light however the dissolution is even faster than for pure Novolak films, which makes Novolak-DNQ mixtures ideal for the use as photoresist material in lithographic applications. In Fig. 5.1d an example of the combination of DNQ and Novolak is shown. Another interesting application is the potential use as phototrigger for the release of drug molecules encapsulated in a micellar system [194, 195] initiated by two-photon excitation of DNQ [196].

The photoreaction of DNQ is an intramolecular rearrangement reaction known as the Wolff rearrangement [197, 198]. After the loss of the diazo group a ketene is finally formed. As shown in Fig. 5.2 the first step is the separation of the diazo group. This reaction step has been studied for other diazo compounds, like in the case of an α -diazoester [199] where a carbene is formed from the excited diazo compound within hundreds of femtoseconds, while subsequent ketene formation is very slow. Additionally ab initio calculations have located a variety of conical intersections for electronically excited diazomethane that could give rise to rapid N_2 loss [200]. However, for DNQ the mechanism for the formation of the ketene intermediate (3) is still under discussion [201]. Two different mechanisms have been proposed. Some authors favor a concerted reaction, where the ketene is formed directly. In this case the nitrogen molecule is released from the diazonaphthoquinone synchronously with the ring contraction [202]. Other groups support a stepwise reaction which includes the intermediacy of a carbene (2) [191, 203, 204].

However, all these former investigations performed via Laser Flash Photolysis (LFP) had two shortcomings. They only have access to time-resolved spectra in the UV/VIS spectral region, which makes it quite hard to assign transient features to reaction products, as no structural information can be deduced. In addition most of these studies were constrained to the nanosecond scale. The best time-resolution to date (8 ps) was obtained by Vlegaar et al. [191].

In this work the first femtosecond spectroscopy experiments on DNQ are performed in order to gain more insight into the reaction dynamics of the photoinduced Wolff rearrangement reaction. The reaction is studied with mid-infrared transient absorption spectroscopy with subpicosecond time resolution. The DNQ sample is characterized not only in the UV/VIS spectral region, but also in the infrared. The assignment of features in the vibrational spectra is confirmed by density functional theory (DFT) calculations and normal mode analysis.

5.2 Steady state spectroscopy

5.2.1 UV/VIS absorption

The DNQ sample was purchased from Sigma Aldrich (Fluka, CAS: 2657-00-3) as 2-Diazo-1-naphthol-5-sulfonic acid sodium salt hydrate. The structure of this diazonaphthoquinone derivative is shown in Fig. 5.3a. In all of the following experiments it was used without further purification. Steady state absorption spectra in the UV/VIS spectral region were recorded at room temperature with the commercial Hitachi-2000 photospectrometer. Around 400 nm DNQ has a strong absorption due to the S_0 to S_1 electronic transition. Fig. 5.3b shows the absorption spectrum of DNQ dissolved in methanol, which exhibits two broad bands, one around 320 nm and the other around 400 nm. Almost exactly the same spectrum is observed for DNQ dissolved in water (not shown here). Therefore, the excitation wavelength of the pump pulse in the time-resolved experiments (see Section 5.3) was chosen to be 400 nm.

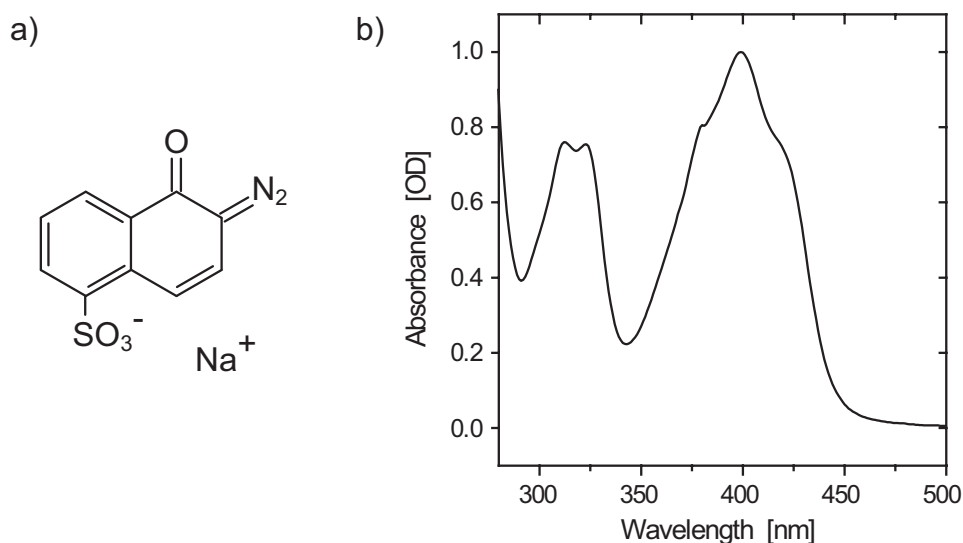


Figure 5.3: a) Molecular structure of 2-Diazo-1-naphthol-5-sulfonic acid sodium salt hydrate. b) Steady state absorption spectrum of DNQ dissolved in methanol. It shows strong absorption around 400 nm due to the S_0 to S_1 electronic transition.

5.2.2 Infrared absorption

Steady state infrared absorption measurements of DNQ were carried out in methanol solution and in a solid form in a potassium bromide (KBr) pellet. In the latter case the sample together with KBr is pressed to a pellet under high pressure. This makes a solvent-free measurement of the sample possible. Although there are interactions of the sample with KBr, this technique is well suited for qualitative measurements. The infrared spectra were recorded with a standard Fourier-Transform (FTIR) spectrometer (JASCO Corp., FT/IR-410) with a resolution of 1 cm^{-1} . The measured spectrum in Fig. 5.6 shows already the expected features. The $\text{C}=\text{N}=\text{N}$ diazo stretching vibration around 2100 cm^{-1} , as well as the CO stretch vibration bands from $1500\text{--}1700 \text{ cm}^{-1}$ of DNQ can be identified. These findings coincide quite well with infrared spectra of DNQ-Novolak photoresists [205]. In these experiments on substituted ortho-naphthoquinonediazides the splitting of the diazo stretching vibration into three overlapping bands and the five bands in the CO stretching region are also present.

For the measurements in methanol and water, the dissolved DNQ sample was filled in an IR transmission cell with CaF_2 windows. The sample thickness was $50 \mu\text{m}$. The absorption spectrum from $1100\text{--}2300 \text{ cm}^{-1}$ in methanol is shown in Fig. 5.4a and a closer view on the diazo stretching vibration is given in Fig. 5.4b. In Fig. 5.5a and b the measurement in water is shown. In some frequency regions strong absorption of the used solvents prevent the analysis of the spectra. This is indicated by the grey regions in the graphs. Spectra for DNQ in the solvent (red line) and the solvent only (black line) were recorded, so that the vibrational spectrum could be corrected for the solvent absorption (blue line). Overall the spectra in methanol and water are quite similar to the spectrum recorded with DNQ incorporated in the KBr pellet, although the amplitudes and frequencies of the vibrational bands are slightly different.

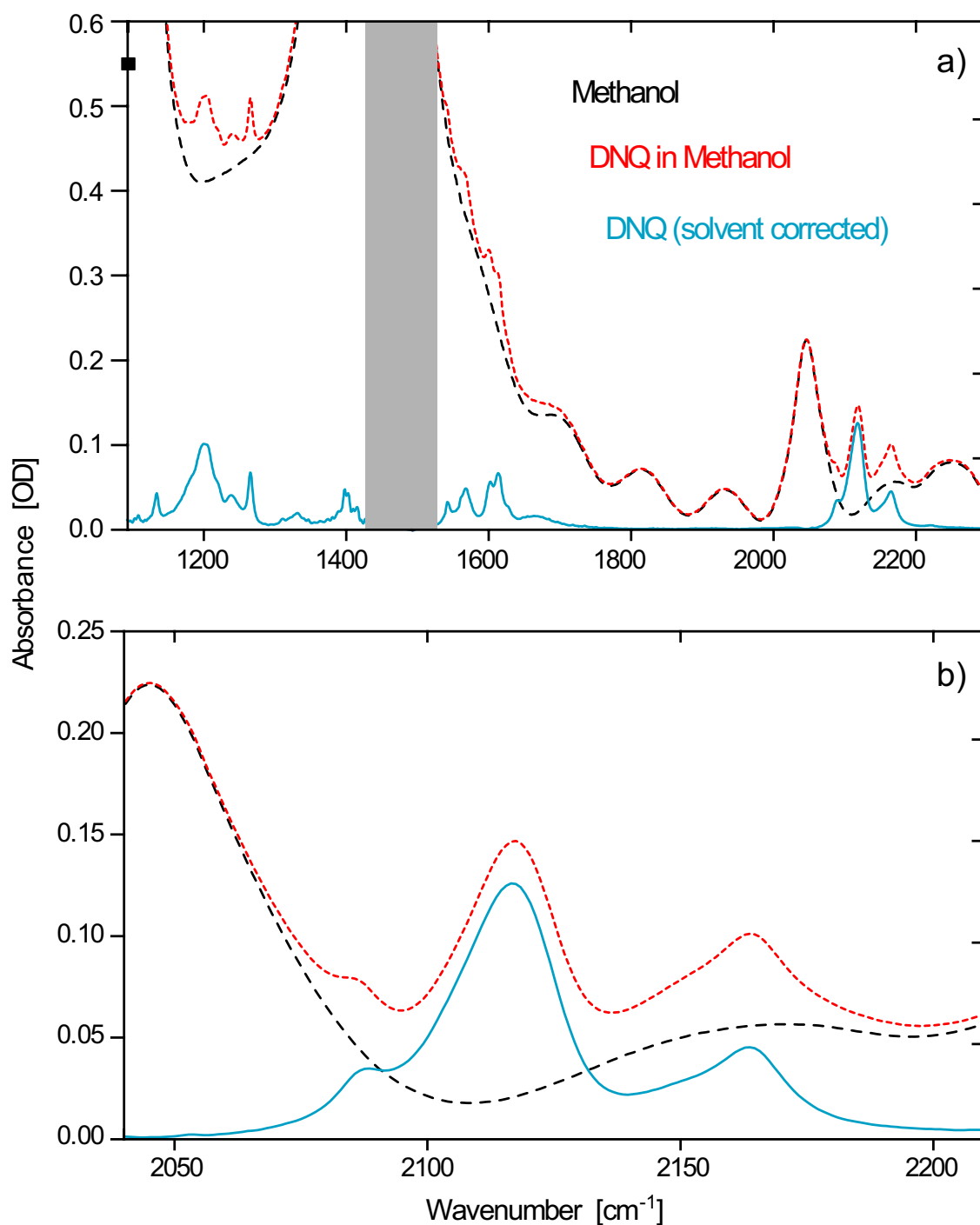


Figure 5.4: a) Infrared absorption spectra of methanol only (black), DNQ in methanol (red) and DNQ corrected for the solvent contribution (blue). The grey bar indicates regions, where the solvent absorption is too strong preventing the evaluation of the spectra. b) Closer view on the C=N=N stretching region around 2100 cm⁻¹.

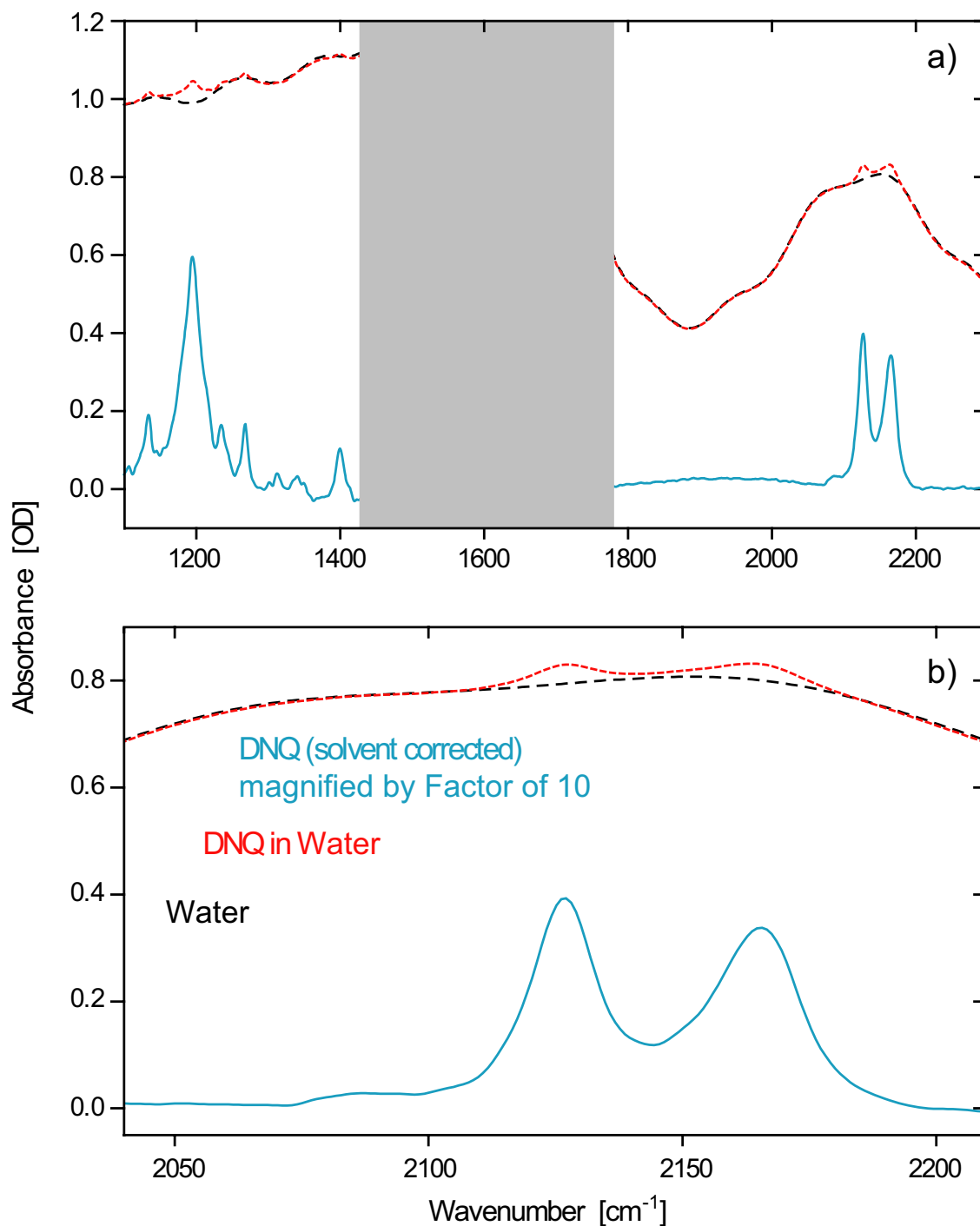


Figure 5.5: a) Infrared absorption spectra of water only (black), DNQ in water (red) and DNQ corrected for the solvent contribution (blue). The grey bar indicates regions, where the solvent absorption is too strong preventing the evaluation of the spectra. b) Closer view on the C=N=N stretching region around 2100 cm^{-1} .

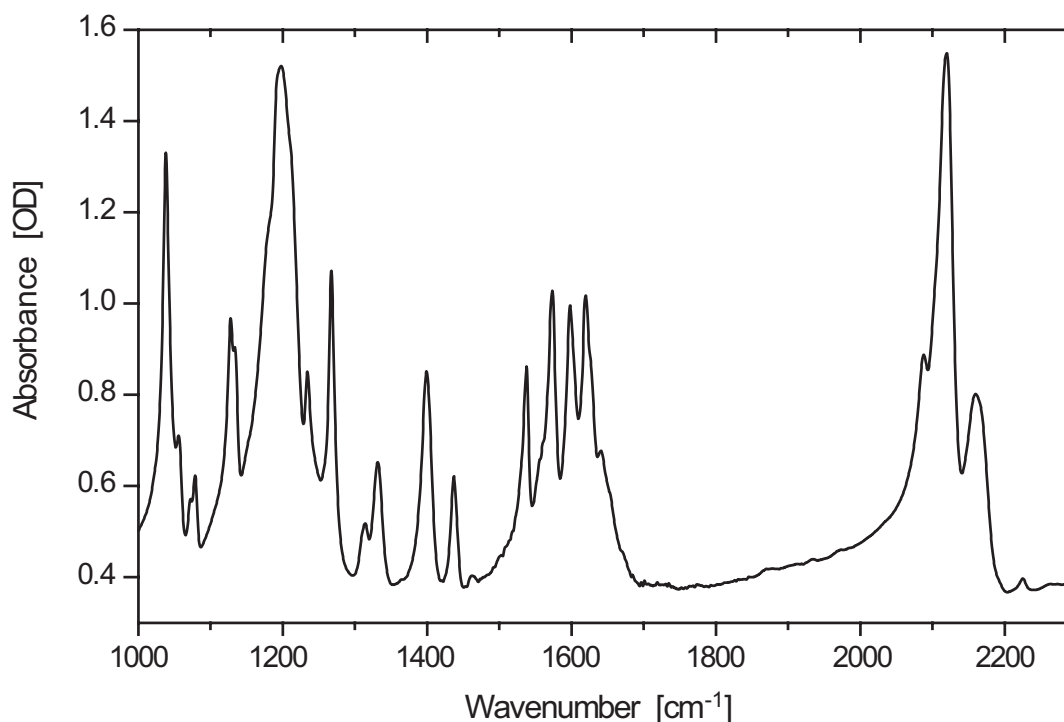


Figure 5.6: Steady state infrared absorption spectrum of DNQ pressed in a KBr pellet.

5.2.3 Normal mode analysis

Quantum chemical density-functional calculations of the normal modes of DNQ with the software package Gaussian 03 [206] provide the frequencies and intensities of the vibrational bands in the ground state of the molecule. The calculations were carried out for DNQ in vacuum for reasons of simplicity, as the inclusion of the solvent environment often leads to numerical problems. The differences should be negligible. This calculation helps to assign the observed absorption bands in the infrared spectra to the normal modes of vibration. When this calculation is also performed for the products of DNQ, that are expected during the course of the reaction, the appropriate vibrational modes for monitoring the structural dynamics of the molecule can be chosen. The agreement of the calculated and experimentally measured spectra usually is not perfect, but still quite good, so that the spectral regions of interest can be identified.

In our calculations the density functional Becke three-parameter hybrid method [207, 208] in combination with the Lee–Yang–Parr correlation functional (B3LYP) [209] was used. The molecular geometry was optimized using this functional with the 6-31G* basis set. The calculations for the normal modes, and their amplitudes were carried out at the 6-311+G** level. The result for DNQ in vacuum is shown in Fig. 5.7. The obtained line spectrum is convoluted with Lorentzian peak functions with 5 cm^{-1} FWHM in order to illustrate the spectra in a more realistic way. The frequencies of the most prominent modes and their assignment are given in Tab. 5.1. The comparison of the calculated and the experimentally measured frequencies show quite good agreement. The, by far strongest and most characteristic mode for DNQ is located around 2120 cm^{-1} , which

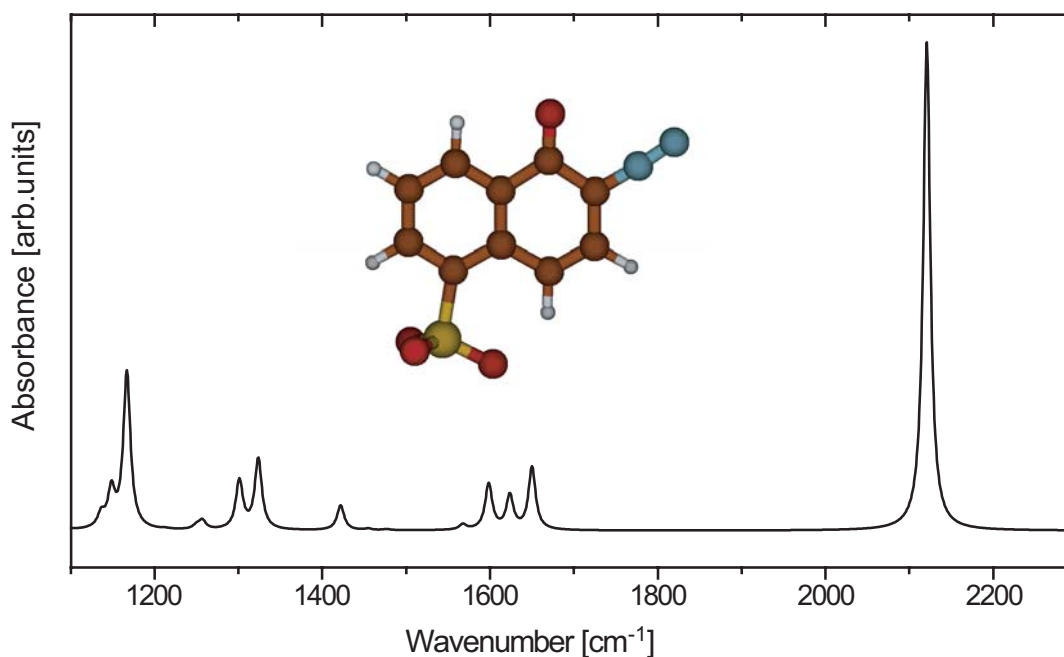


Figure 5.7: Quantum chemical DFT calculation of the vibrational normal modes of DNQ in vacuum as obtained from DFT calculations using the (B3LYP) correlation functional with the 6-311+G** basis set. The line spectrum is convoluted with Lorentzian peak functions with 5 cm^{-1} FWHM. The molecular structure shown is obtained by the geometry optimization in Gaussian 03.

can be attributed to the C=N=N stretching vibration (no.2 in Tab. 5.1). Between $1500\text{--}1700\text{ cm}^{-1}$, where vibrations of the C=O group are expected, four weaker bands are found, that can be assigned to combinations of C=O stretching and naphthalene deformation modes (no.4–7 in Tab. 5.1) Other modes towards the lower frequency region of the spectrum also exist, and are assigned to deformational modes of the naphthalene rings and to contributions of the SO₃-group. The nomenclature of the naphthalene ring modes is according to [210], and $\nu(\dots)$ denotes stretching modes of the respective groups.

5.3 Transient absorption spectroscopy in the mid-infrared

The initial steps of the Wolff rearrangement of DNQ are investigated in two different solvent environments, methanol and water. For this purpose transient femtosecond vibrational spectroscopy is employed in order to monitor the structural dynamics during the photoreaction. Prior to that a normal mode analysis of possible intermediate and product species is performed (Section 5.3.1). The transient absorption measurements are presented in Section 5.3.2. Based on these results a reaction scheme will be established and the dynamics of the product formation will be analyzed with a suitable fit model (Section 5.3.3).

Table 5.1: Spectral positions and assignment of calculated (DNQ in vacuum) and by FTIR absorption spectroscopy experimentally measured (DNQ in methanol, see Fig. 5.4a; DNQ in water, see Fig. 5.5a) most prominent vibrational modes in units of cm^{-1} . $\nu(\dots)$ denotes the stretching mode of the respective group and the numbers indicate the naphthalene ring modes according to Ref. [210].

no.	calc.	MeOH	H ₂ O	assignment
1	—	2164	2165	—
2	2121	2116	2127	$\nu(\text{C}=\text{N}=\text{N})$
3	—	2088	2087	—
4	1650	1612	—	$3 + \nu(\text{C}=\text{O})$
5	1624	1602	—	$39 + \nu(\text{C}=\text{O})$
6	1598	1567	—	$19 + \nu(\text{C}=\text{O})$
7	1568	1541	—	32
8	1422	1397	1400	4
9	1324	1264	1268	5
10	1301	1240	1234	$20 + \nu(\text{C}=\text{N})$
11	1167	1199	1195	$42 + \nu(\text{S}-\text{O})$
12	1149	1133	1133	$6 + \nu(\text{S}-\text{O}) + \nu(\text{C}-\text{S})$

Table 5.2: Spectral positions and assignment of the most important calculated vibrational modes in units of cm^{-1} of possible intermediate species during the photoreaction of DNQ. The data in this table is from calculations, performed in vacuum. The numbering of the modes of DNQ, and the nomenclature of the assignment is the same as in Tab. 5.1 . ν : stretching mode, S: symmetric, As: antisymmetric, o.o.p.: out of plane.

species	no.	calc.	assignment(character)
carbene	1	1612	$39 + \nu\text{S}(\text{C}=\text{O})$
	2	1575	$39 + \nu\text{As}(\text{C}=\text{O})$
	3	1323	5
	4	1268	21
	5	1229	41
	6	1172	$42 + \nu(\text{S}-\text{O})$
	7	1150	$22 + \nu(\text{C}-\text{S})$
ketene	1	2117	$\nu(\text{C}=\text{C}=\text{O})$
	2	1162	o.o.p.(C-S)

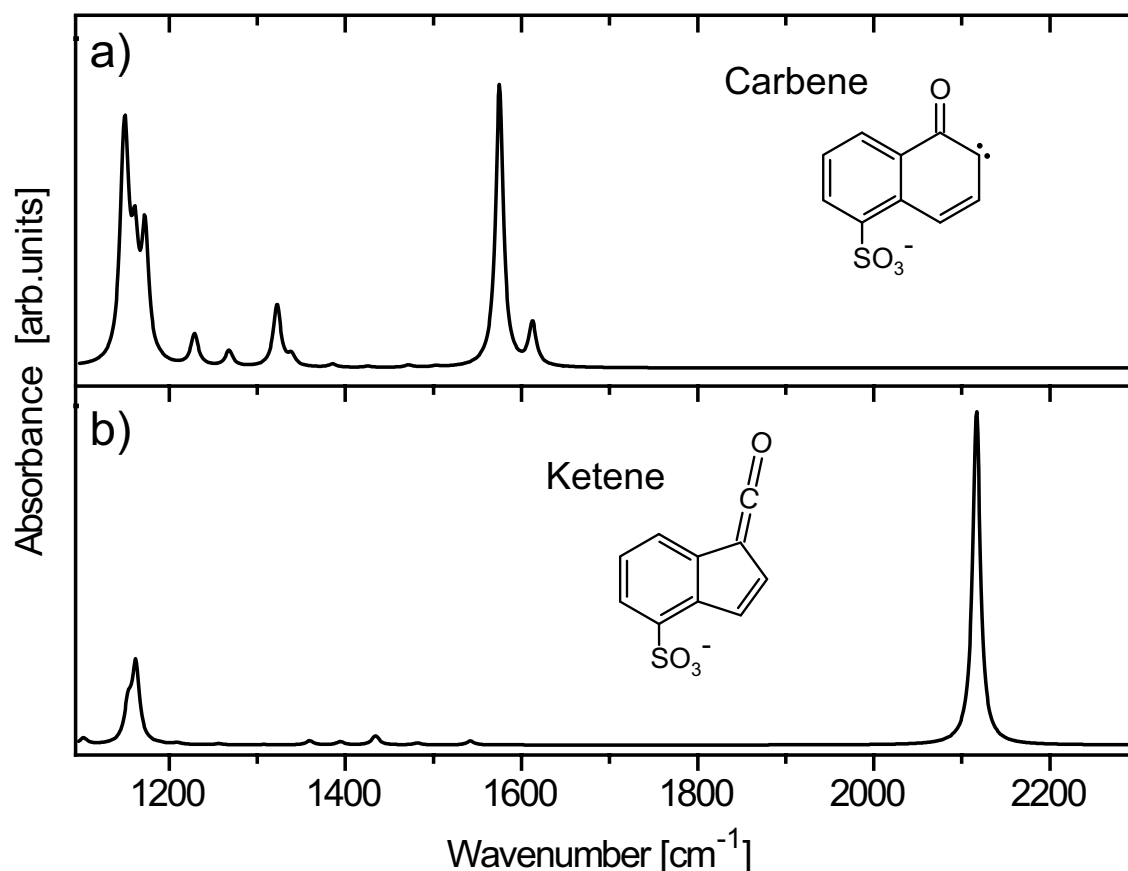


Figure 5.8: DFT calculation of the normal modes of possible intermediate species of the Wolff rearrangement reaction of DNQ. a) carbene, b) ketene. All calculations were performed under the assumption of isolated molecules. The normal mode spectra were convoluted with Lorentzian peak functions with 5 cm^{-1} FWHM.

5.3.1 Normal mode analysis of possible product species

For the time-resolved mid-infrared study of the photoinduced Wolff rearrangement of DNQ, it is useful to know the spectral regions of vibrational modes for intermediate species, that are possibly formed. According to the publications, dealing with the photoreaction of DNQ [191, 201–204], carbene and ketene species are expected to occur after the loss of N_2 . Therefore, the equilibrium geometry and the normal modes for the carbene and ketene species were also calculated using Gaussian 03 (for details see previous section). The calculations were again performed for isolated molecules. The resulting spectra are displayed in Fig. 5.8 and the calculated band positions and assignments are listed in Tab. 5.2. From the calculated spectra, it can be deduced that the ketene can be identified due to its $\text{C}=\text{C}=\text{O}$ stretching mode with its characteristic absorption band at 2117 cm^{-1} (no. 1 in Tab. 5.2). This result agrees very well with low temperature matrix isolation experiments performed by Pacansky et al. [205] where the corresponding ketene band was observed at 2130 cm^{-1} . From the calculated spectra, the interesting spectral regions were identified to lie around 2100 cm^{-1} , where not only the diazo ($\text{C}=\text{N}=\text{N}$)

band of DNQ but also the C=C=O stretching vibration (2117 cm^{-1}) of the ketene intermediate should be found. So both the bleaching dynamics of the reactant molecule (DNQ) and the ketene formation should be observable in this region. Another important spectral region is around 1600 cm^{-1} , where the C=O stretching modes of DNQ and the carbene, if it exists, will be present.

5.3.2 Product formation dynamics

The initial steps of the photoreaction of DNQ are investigated with femtosecond vibrational spectroscopy concentrating on the spectral region around 2100 cm^{-1} , where absorption from both DNQ and the ketene intermediate will be observed. DNQ is dissolved in methanol and pumped through a flow cell with $100\text{ }\mu\text{m}$ thickness. The optical density of the sample solution is adjusted to about 1 OD at 400 nm, and the sample is excited by the frequency doubled Ti:Sa pulses at a central wavelength of 400 nm. In all experiments the pump pulses are focused to a beam diameter of $170\text{ }\mu\text{m}$ and their energy is between 2 and $8\text{ }\mu\text{J}$. The wavelength of the infrared probe pulses is tuned to the desired spectral region between 1500 and 2200 cm^{-1} and their energy is adjusted to about 10 nJ by means of appropriate reflective filters. Absorption of water vapor in the spectral region around 1600 cm^{-1} , due to the ν_2 bending vibration of H_2O is strongly reduced by purging the setup and the spectrometer with dried air and nitrogen gas when performing measurements in this region.

Experimental results

The transient spectral evolution of DNQ after excitation with frequency-doubled Ti:Sa pulses at a wavelength of 400 nm are displayed in Fig. 5.9a (methanol) and in Fig. 5.9b (water). The change of absorbance in mOD is plotted as a function of probe wavenumber and delay time for the spectral region from 2020 cm^{-1} to 2198 cm^{-1} for the measurement in methanol and from 2070 cm^{-1} to 2203 cm^{-1} for the measurement in water, respectively, and the delay times are ranging from -5 ps to 30 ps . In this two-dimensional contour representation two important features can be distinguished and qualitatively described as follows. First of all, a decrease in absorption at several spectral positions, for DNQ in methanol at 2165 cm^{-1} , 2117 cm^{-1} and 2084 cm^{-1} and for DNQ in water at 2165 cm^{-1} and 2127 cm^{-1} (the bleach at 2087 cm^{-1} is very weak but present) are observed as expected, corresponding to bleaching of the C=N=N stretching vibration of DNQ in the electronic ground state upon photoexcitation (see infrared spectra in Fig. 5.4b and Fig. 5.5b). In addition, a rising positive absorption is appearing in the lower wavenumber region (at 2050 cm^{-1} in methanol and at 2070 cm^{-1} in water) right after zero delay time and shifts and increases in strength towards higher wavenumbers within about 10 ps in methanol and 3 ps in water. This strong new absorption band located at 2128 cm^{-1} (methanol) and 2136 cm^{-1} (water) shows no further development after about 20 ps for both solvents. As the positive absorption shifts from lower to higher wavenumbers, the bleached bands are passed, and after the time evolution of this band, some overlap of the bleached 2117 cm^{-1} band and the product band at 2128 cm^{-1} remains. The absorbance change at negative delay times is caused by perturbed free

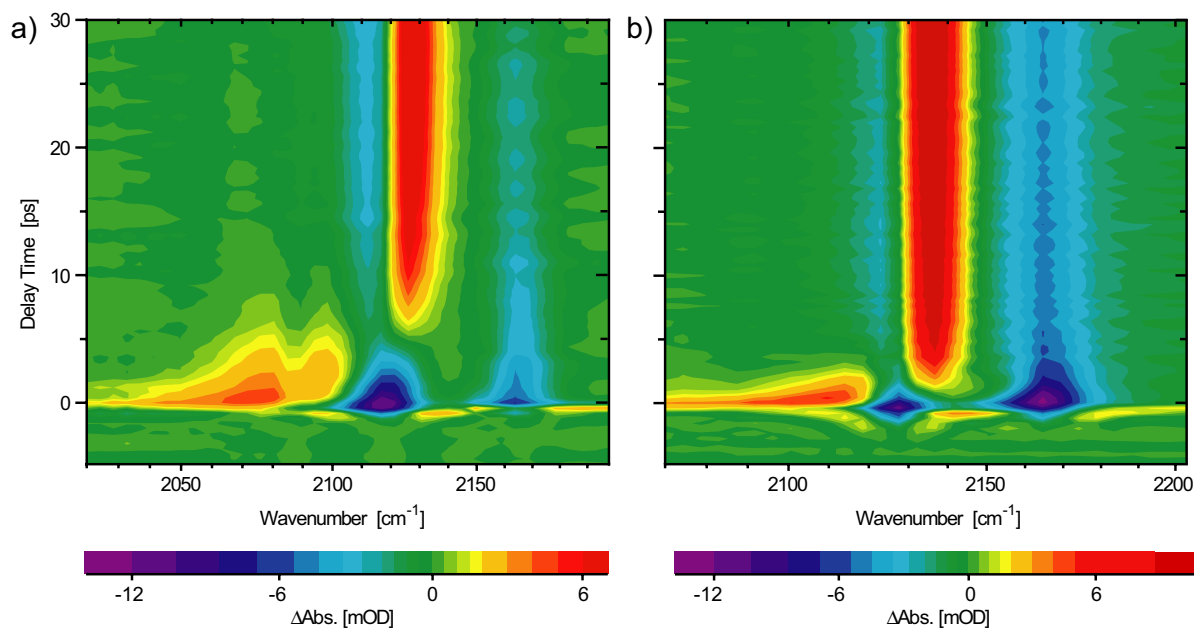


Figure 5.9: Two dimensional contour plot of the spectrally and temporally resolved transient absorption signals of DNQ dissolved in a) methanol and b) water. The data shows bleaching (negative changes in optical density) of the ground state vibrational modes of DNQ after photoexcitation with 400 nm femtosecond pulses. A new band appears in the lower wavenumber region and shifts in a) to 2128 cm^{-1} (methanol) within about 10 ps and b) to 2135 cm^{-1} (water) within about 3 ps. Note the nonlinear color scale in both graphs.

induction decay and is not due to molecular dynamics [111, 190].

The time evolution can be further illustrated by cuts along the frequency axis (Fig. 5.10a and Fig. 5.10b) of the two-dimensional contour representation in Fig. 5.9a and Fig. 5.9b together with the mid-infrared absorption spectra. The transient spectra at fixed delay times show again, the bleached ground state vibration and that the broad new positive absorption shifts to higher wavenumbers. According to the DFT calculations and especially the experiments by Pacansky et al. [205] where the corresponding ketene band was observed at 2130 cm^{-1} , this band can be assigned to the ketene intermediate, because it is located in the same spectral region (close to 2117 cm^{-1} and 2130 cm^{-1}), where the characteristic ketene $\text{C}=\text{C}=\text{O}$ stretching mode is expected. After 50 ps no further changes in the transient spectra are observed.

Discussion and suggested reaction scheme

Based on the collected data, a model for the photoinduced Wolff rearrangement of DNQ shown in Fig. 5.11 can be deduced. After photoexcitation to the S_1 electronic state of DNQ, the excited state population can return back to a vibrationally hot electronic ground state S_0 of DNQ ($v > 0$) with a certain probability. This is followed by vibrational relaxation to the vibrational ground state ($v = 0$). In the transient absorption data this is indicated by the partial recovery of the bleach contributions after a few ten picoseconds. This part of the excited population does not contribute to the photoproduct formation.

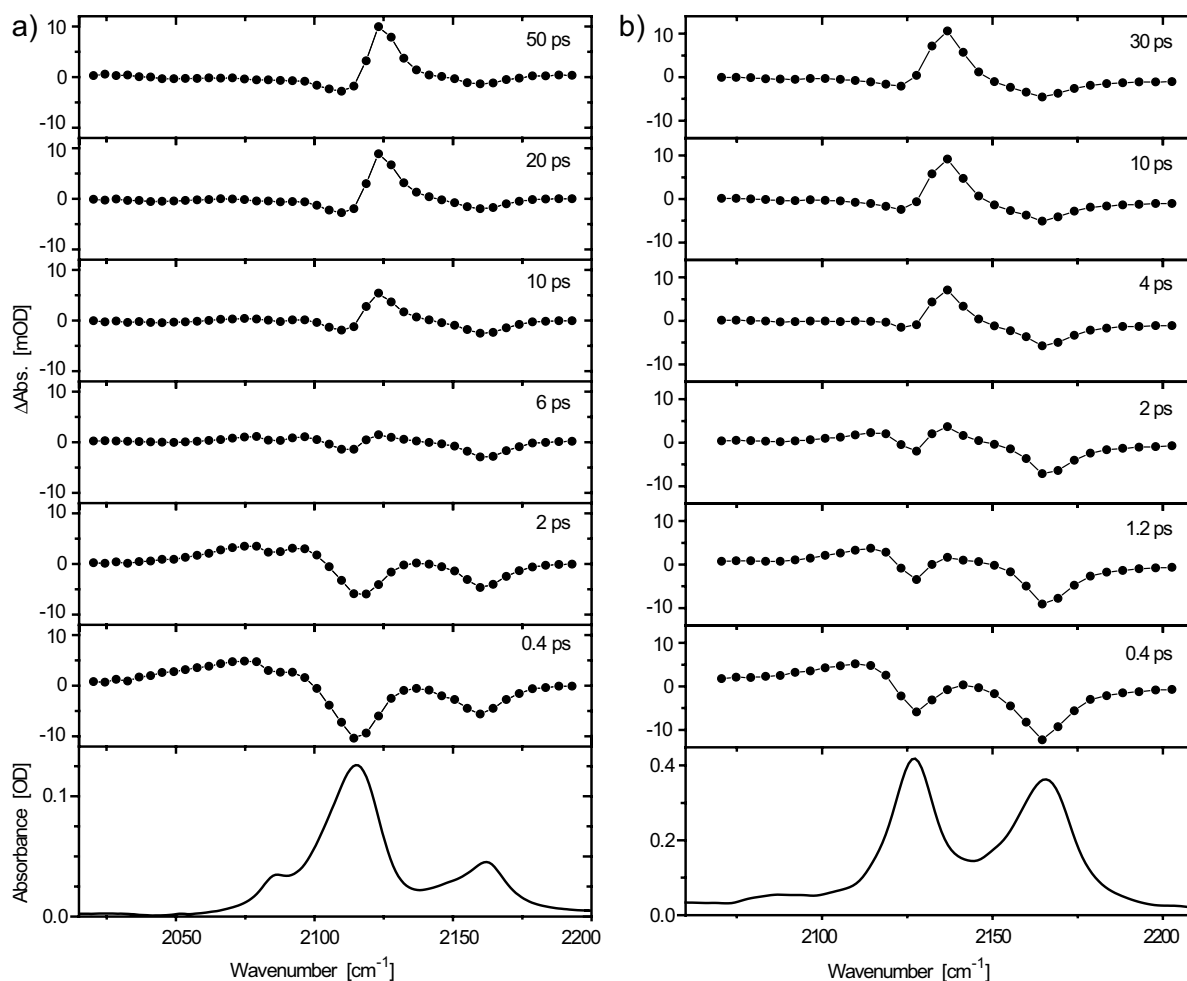


Figure 5.10: Transient infrared spectra of DNQ in a) methanol and b) water recorded at different delay times from 0.4 ps to 50 ps, showing the bleached vibrational bands of the educt DNQ and the rising and shifting positive absorption originating from the ketene intermediate from lower to higher wavenumbers. Steady state infrared spectra are displayed at the bottom.

The other possibility for the excited state population is to undergo Wolff-rearrangement, which leads to formation of the ketene intermediate. The ketene is formed with an excess of vibrational energy in a highly excited vibrational state denoted with $v=v_{max}$, which relaxes over several intermediate vibrational states ($v_{max} > v > 0$) to the vibrational ground state ($v=0$) of the ketene. The strong shift of the vibrational band, assigned to the ketene, from lower to higher wavenumbers during relaxation to the $v=0$ vibrational ground state is a very strong indication for the validity of this model, since the energy difference between neighboring vibrational states is increasing due to anharmonicity. A similar behaviour was observed by Laimgruber et.al. [141] in their study of the ketene formation of ortho-nitrobenzaldehyde. There the strong shift of the ketene band was explained by vibrational cooling.

Admittedly, the appearance of the ketene vibration in the lower frequency regime (at 2050 cm^{-1} in methanol and at 2070 cm^{-1} in water) right after zero time-delay is surpris-

ingly fast. However, for the appearance of this new absorption band other reasons than an initially hot ketene photoproduct are very unlikely. Certainly, it does not belong to a carbene since it has no vibrational bands in the wavelength regime above 1650 cm^{-1} (see Fig. 5.8). Although DFT calculations can never simulate real spectra with absolute correctness a deviation of more than 400 cm^{-1} can be excluded. An alternative explanation for the positive contribution in the transient spectra could be excited state absorption of the DNQ S_1 state. Often the electronic excited state has vibrational absorption lines in a similar spectral region as the ground state. If so, the transient spectra would solely show the excitation process of the reactant, namely bleaching due to depletion of the DNQ S_0 ground state and an absorption increase related to population transfer to the DNQ S_1 excited state followed by vibrational cooling. However, this scenario cannot be brought into accordance with the present data. The positive absorption corresponding to the vibrationally relaxed state does not show any further dynamics on the accessible time scale. That would mean, upon photoexcitation into the excited state, the population undergoes vibrational cooling and then stays in the $S_1(v=0)$ state on the timescale of nanoseconds without decaying to S_0 . This model is obviously wrong since the ground state bleach recovers meanwhile, which implicates that population definitely returns to

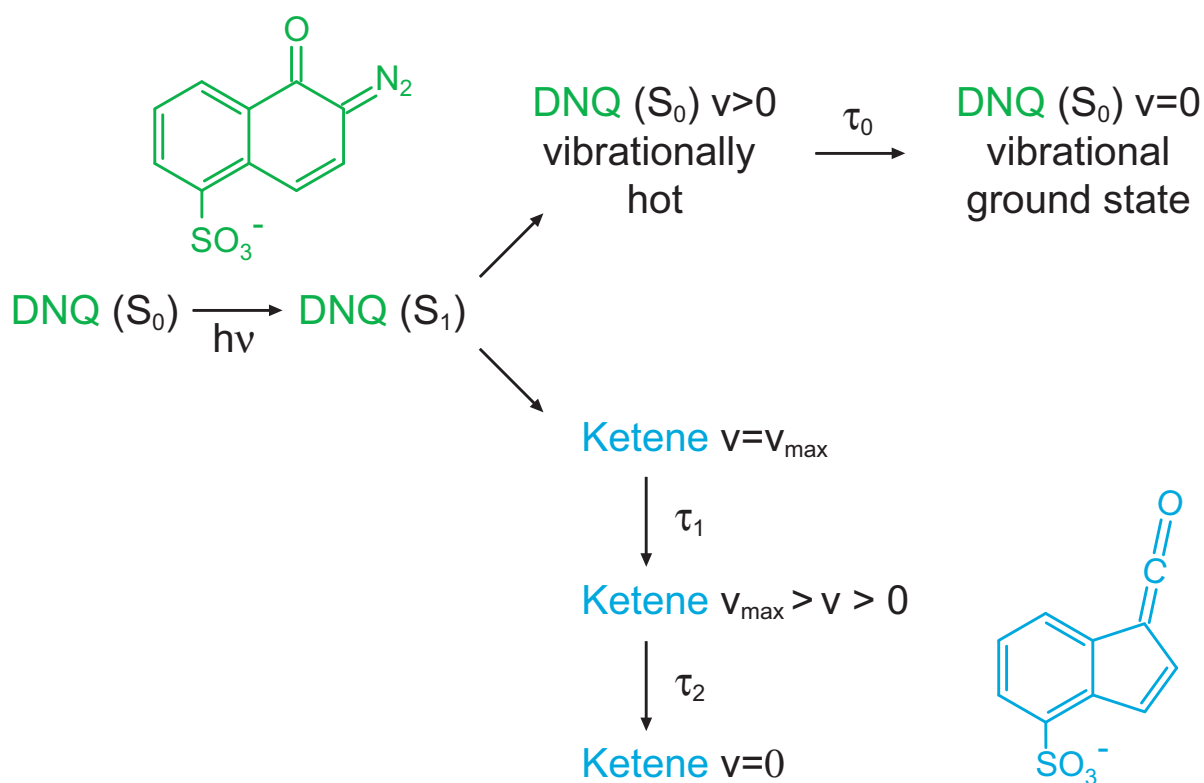


Figure 5.11: Model for the photoinduced Wolff-rearrangement of DNQ in methanol on the basis of the collected transient absorption data. After photoexcitation the population in the S_1 excited state of DNQ can either return to the S_0 ground state or go the vibrationally excited state ($v > 0$) of the ketene photoproduct. Relaxation to the vibrational ground state $v=0$ of the ketene takes about 10 ps.

$S_0(v=0)$. The energy distance between the $S_0(v=0)$ and the $S_0(v=1)$ state is at least 0.2 eV which is much larger than the thermal energy kT at room temperature or the bandwidth $\Delta\nu$ of the employed laser. Hence, vibrationally excited states ($v > 0$) in the DNQ S_0 state can neither be populated thermally nor in a pump-dump like process so that they initially must have been empty. Thus, the only possibility for refill of the $S_0(v=1)$ is repopulation from the S_1 state through internal conversion associated with a synchronous decay of the corresponding absorption. Further, fluorescence should be expected in this case at wavelengths larger than the excitation wavelength of 400 nm. However, Vleggaar et al. [191] report that no fluorescence can be observed upon photoexcitation of DNQ in the wavelength regime between 450 nm and 700 nm. Finally, if the argument is that molecules in excited states have vibrational lines in the vicinity of their ground state bands a comparable positive S_1 absorption should appear for the four C=O lines around 1600 cm^{-1} , which is not the case. On the basis of these facts the newly-appearing absorption band is attributed to the ketene photoproduct. A detailed discussion can also be found in [211, 212].

Ketene formation

In the transient absorption contour plots (Fig. 5.9a and Fig. 5.9b) the rise of the absorption band at lower wavenumbers (around 2050 cm^{-1} in methanol and 2070 cm^{-1} in water), that is assigned to the ketene photoproduct, appears to be very fast. Therefore, in order to deduce a rise time for the photoproduct formation, measurements at early delay times with finer delay time steps have to be performed. This has been done at suitable wavenumbers, namely at 2055 cm^{-1} in methanol and 2079 cm^{-1} in water. The results are shown in Fig. 5.12. At negative delay times all transients exhibit a strong contribution from perturbed free induction decay originating from the bleached absorption band of the DNQ educt in the vibrational ground state in the vicinity. This effect is causing oscillations in the signal (see discussion in Section 4.5.4). Around zero delay time possibly also a contribution from a coherent artifact (details in Section 4.5.3) is present. For this reason, it is not possible to extract a rise time from the transients by a data fitting procedure. However, since no delayed peak is observed in the transients, one can conclude, that the rise time must be very short. As an upper estimate for the formation time of the ketene, the experimental time resolution, the instrument response time can be taken instead. In a separate measurement it was determined to be about 300 fs (see Section 4.5.2). This means that the ketene photoproduct is formed from DNQ within this time interval. If a carbene intermediate does or does not exist can not be revealed with the time resolution of our transient mid-infrared spectrometer, but an upper limit could be determined. Further measurements in the spectral region around 1600 cm^{-1} (only possible in methanol but not in water due to solvent absorption) were performed to cross-check for a positive absorption change related to a carbene intermediate leading to a negative result. Only bleaching of the C=O bands corresponding to DNQ as well as small positive contributions shifting and coalescing into the bleach bands which are attributed to a vibrationally hot DNQ ground state could be observed.

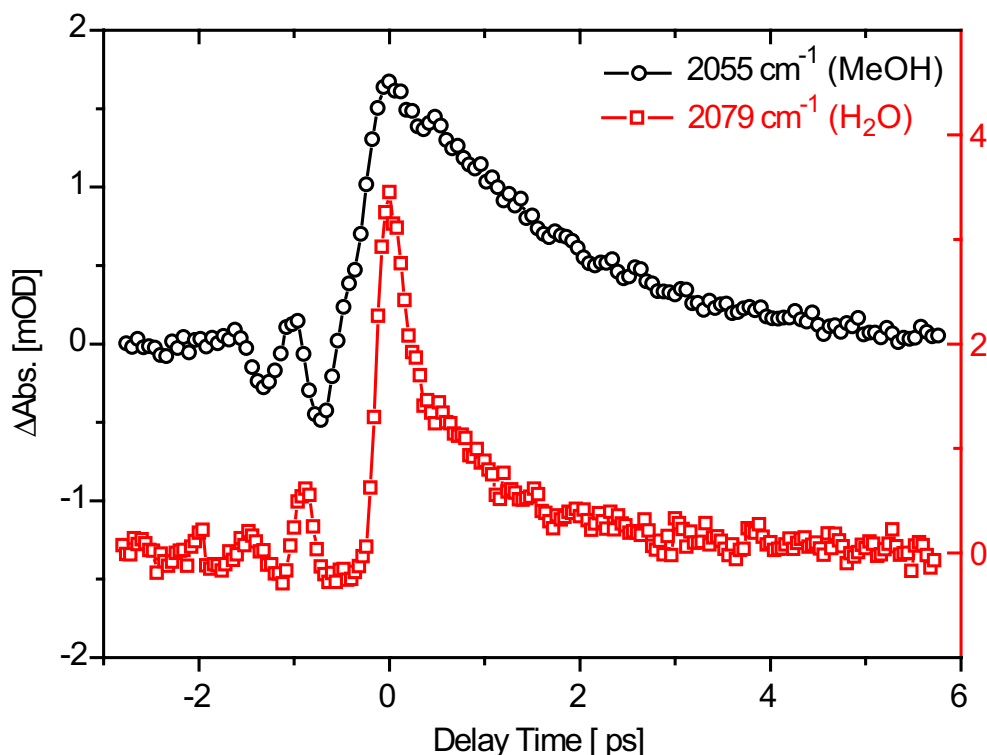


Figure 5.12: Transients in the ketene formation region at early delay times, recorded at 2055 cm^{-1} in methanol (black circles) and at 2079 cm^{-1} in water (red squares) showing immediate rise of the ketene absorption band within the time resolution of the experiment. The oscillatory features at negative delay times are due to perturbed free induction decay originating from the neighboring bleached vibrational band belonging to DNQ.

5.3.3 Reaction model and fit

For a quantitative analysis of the transient absorption data, the fit model derived from the schematic reaction model discussed above is depicted in Fig 5.13. It is assumed, that the excitation process, the $S_1 \rightarrow S_0$ transition in DNQ, and the formation of the ketene photoproduct occurs instantaneously, which is reasonable, since the measurements indicate a formation time faster than 300 fs, what is small compared to all other time scales of the photoreaction. In the data fit the instrument response is taken into account by convolution with a Gaussian with full width half maximum (FWHM) of 300 fs, while the contributions around zero delay time due to a coherent artifact and perturbed free induction decay have been omitted in the data fits. The quantum yield of a photo-induced process is the number of times that a defined event (usually a chemical reaction step) occurs per photon absorbed by the system. Thus, the quantum yield is a measure of the efficiency with which absorbed light produces some effect. Therefore the probability for Wolff-rearrangement and ketene formation is denoted with the quantum yield Q , while $1 - Q$ is the probability for population transfer back to the DNQ S_0 electronic ground state. The initial excited state population in S_1 is N_{S_1} . The time evolution of the population can be described by a set of rate equations with appropriate initial conditions.

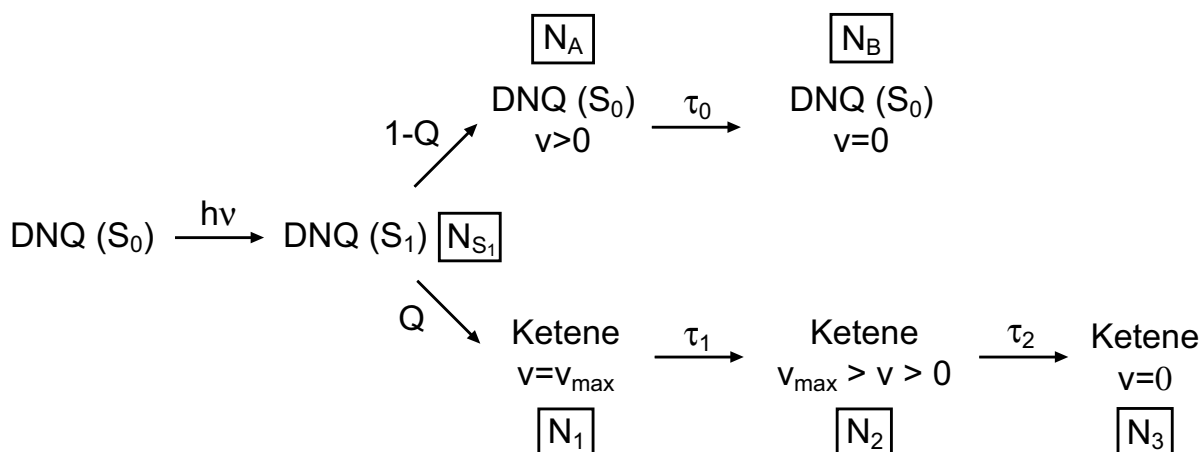


Figure 5.13: Model for the photoinduced Wolff rearrangement of DNQ in methanol on the basis of the collected transient absorption data. N_{S_1} is related to the excited state population, N_A the fraction of the population returning to a hot ground state and N_B the population that has refilled the S_0 vibrational ground state of DNQ. N_1 , N_2 and N_3 are the populations in the ketene hot ground states $v=v_{max}$, $v_{max} > v > 0$ and the vibrational ground state $v=0$ respectively.

The labeling of the fit model parameters, such as populations N_i and the respective time constants τ_i (or decay constants λ_i , which are $1/\tau_i$) is according to Fig 5.13. The time evolution of the population can be described by a set of rate equations with appropriate initial conditions

$$\begin{aligned}
 \frac{dN_A(t)}{dt} &= -\lambda_0 N_A, & N_A(0) &= (1 - Q) N_{S_1} \\
 \frac{dN_B(t)}{dt} &= \lambda_0 N_A, & N_B(0) &= 0 \\
 \frac{dN_1(t)}{dt} &= -\lambda_1 N_1, & N_1(0) &= Q N_{S_1} \\
 \frac{dN_2(t)}{dt} &= \lambda_1 N_1 - \lambda_2 N_2, & N_2(0) &= 0 \\
 \frac{dN_3(t)}{dt} &= \lambda_2 N_2, & N_3(0) &= 0.
 \end{aligned}
 \tag{5.1}$$

Thus, the partial recovery of the bleach contributions, meaning the partial refilling of $v=0$ during vibrational relaxation in the DNQ electronic ground state S_0 is described by

$$N_A(t) = (1 - Q) N_{S_1} \exp(-t/\tau_0) \tag{5.2}$$

$$N_B(t) = (1 - Q) N_{S_1} [1 - \exp(-t/\tau_0)]. \tag{5.3}$$

Consequently the bleach dynamics of the ground state vibrations of DNQ is modelled by

$$\text{DNQ}(t) = -\sigma_B [N_{S_1} - N_B(t)], \tag{5.4}$$

where σ_B is a factor proportional to the absorption cross section of the respective bleached vibrational band. At $t=0$ the bleach signal is proportional to the amount of population, that left the S_0 ($v=0$) ground state and is excited to S_1 . After the re-filling of the S_0 ($v=0$) vibrational ground state, the bleach signal is a measure for the quantum yield of the reaction by being proportional to $-QN_{S_1}$. Under the conditions of our experiments it is determined to be 0.32 in both methanol and water as obtained from the respective transients at 2165 cm^{-1} . At other excitation wavelengths the quantum yield might be different.

The population dynamics during vibrational relaxation of the ketene photoproduct, including the vibrationally hot ($v=v_{max}$) state, the intermediate vibrational states ($v_{max} > v > 0$) and the vibrational ground state ($v=0$) are described by

$$N_1(t) = Q N_{S_1} \exp(-t/\tau_1) \quad (5.5)$$

$$N_2(t) = Q N_{S_1} \frac{\tau_2}{\tau_1 - \tau_2} [\exp(-t/\tau_1) - \exp(-t/\tau_2)] \quad (5.6)$$

$$N_3(t) = Q N_{S_1} \left[\frac{\tau_1}{\tau_2 - \tau_1} \exp(-t/\tau_1) - \frac{\tau_2}{\tau_2 - \tau_1} \exp(-t/\tau_2) + 1 \right], \quad (5.7)$$

where τ_1 is the filling time and τ_2 the depletion time of the intermediate vibrational levels for the respective frequency interval. Hence, the transient absorption signals for the ketene photoproduct formation are modelled by

$$\text{Ketene}(t) = \begin{cases} \sigma_1 N_1(t) & \text{for } v = v_{max} \\ \sigma_2 N_2(t) & \text{for } v_{max} > v > 0 \\ \sigma_3 N_3(t) & \text{for } v = 0 \end{cases} . \quad (5.8)$$

including again suitable σ_i factors proportional to the absorption cross sections of the respective vibrational transitions. This effective description of the transient passage of vibrational levels is similar to Ref. [131]. Note that the measured signals are the net difference between absorption from $v \rightarrow v+1$ and stimulated emission from $v+1 \rightarrow v$.

The results of the data fits for DNQ in methanol are displayed in Fig. 5.14 (DNQ in water in Fig. 5.15), where the different contributions (DNQ bleach in green, ketene absorption in blue) and the overall results (red curves) are shown. The resulting time constants for the measurements in both solvents methanol and water are listed in Tab. 5.3. The fitting procedure leading to these results was as follows. At 2165 cm^{-1} there is only bleach of the absorption band of DNQ in the electronic ground state and therefore a fit by using Eq. 5.4 provides the quantum yield Q of the reaction, which is used for all other fits. In all other transients, contributions from bleach and from the appearing ketene photoproduct have to be taken into account. Depending on the wavenumber, $N_2(t)$ (for intermediate vibrational levels) or $N_3(t)$ (only for the vibrational ground state of the ketene, i.e. for 2123 cm^{-1} and 2128 cm^{-1}) has to be chosen for the data fit. Since the bleach contribution in all transients originate from the same vibration, the time constants τ_0 are assumed to be the same.

The relatively simple model introduced above, with only two contributions to the transient absorption, bleach of the C=N=N stretch vibration of DNQ and the appearance of the C=C=O stretch vibration of the ketene photoproduct, fits the experimental data very well. The solvent dependence of the vibrational cooling time constant for the

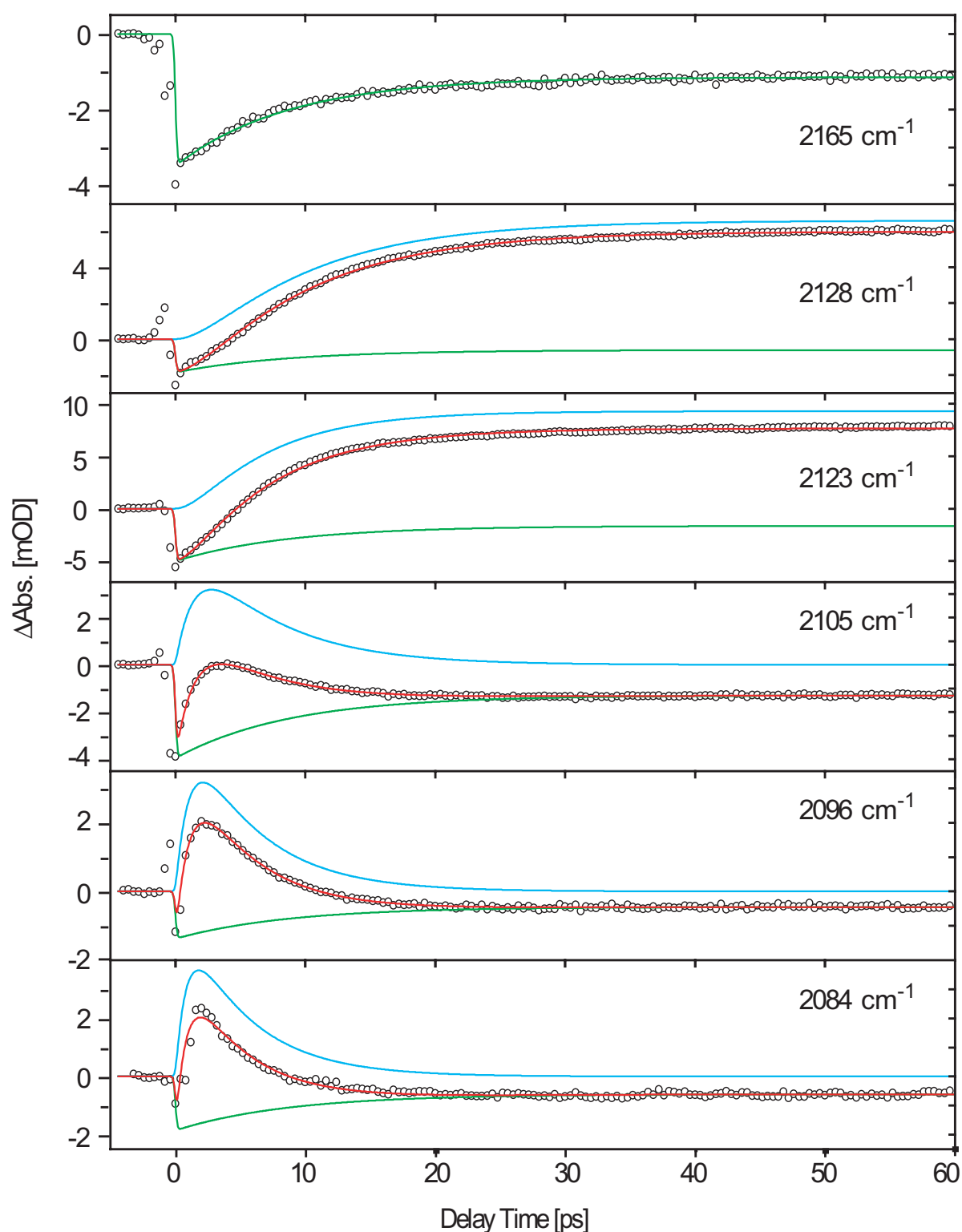


Figure 5.14: Temporal evolution of the absorption changes at fixed spectral positions for DNQ in methanol. Bleach contributions in all transients are related to the DNQ educt bands in the ground state. The new absorption band and its shift to higher wavenumbers can be observed in the transients from 2084 cm^{-1} to 2128 cm^{-1} . The green curve represents the DNQ bleach contribution according to Eq. (5.4), the blue curve the ketene contribution ($N_3(t)$ for 2128 cm^{-1} and 2123 cm^{-1} and N_2 for the other transients) the red curve the sum of both.

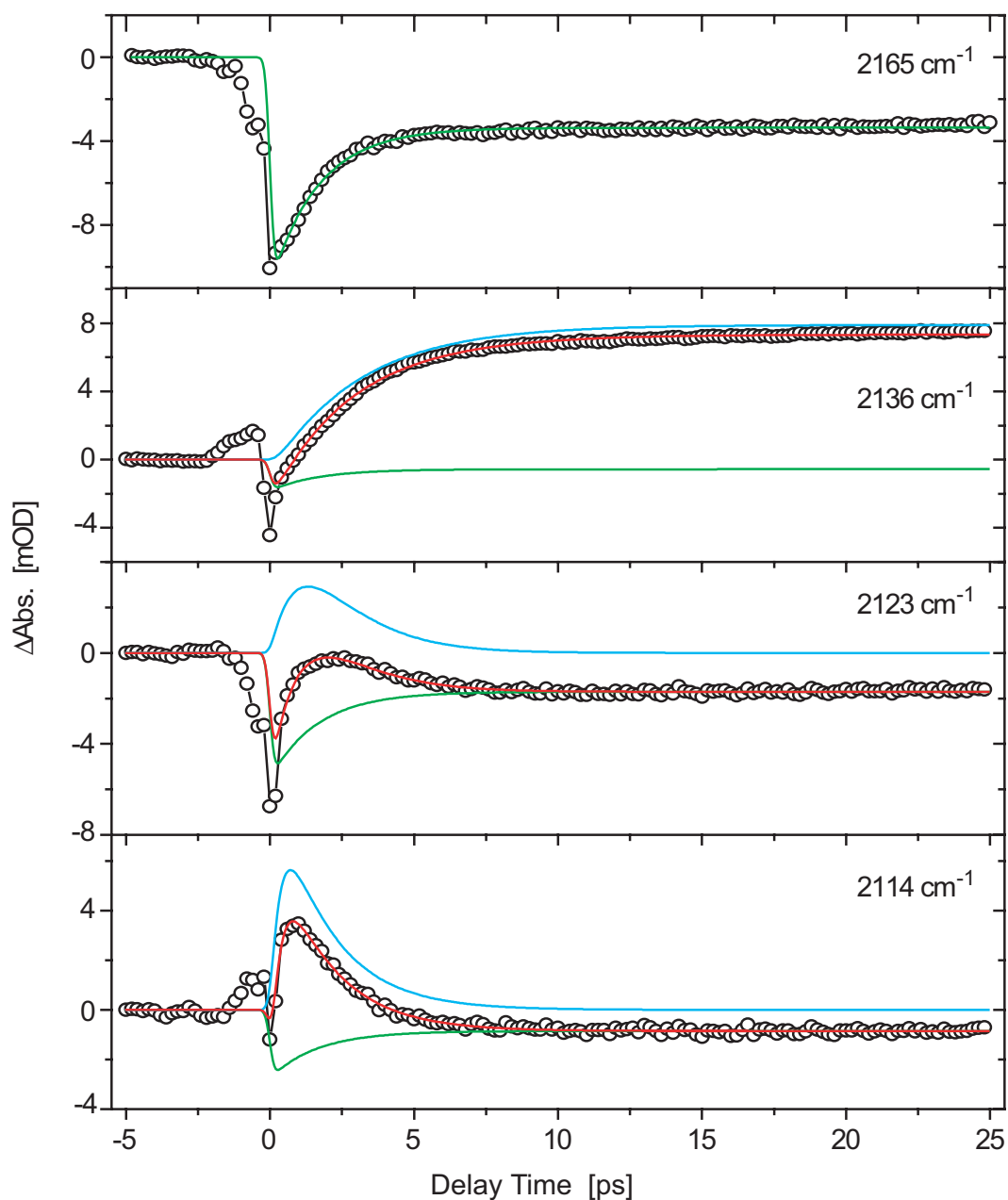


Figure 5.15: Temporal evolution of the absorption changes at fixed spectral positions for DNQ in water. Bleach contributions in all transients are related to the DNQ educt bands in the ground state. The new absorption band and its shift to higher wavenumbers can be observed in the transients from 2114 cm^{-1} to 2136 cm^{-1} . The green curve represents the DNQ bleach contribution, the blue curve the ketene contribution and the red curve the sum of both.

Table 5.3: Quantitative results of the data fit of the measured transients for DNQ in methanol (MeOH) displayed in Fig. 5.14 and of the corresponding measurement in water (H₂O) shown in Fig. 5.15.

	ν [cm ⁻¹]	τ_0 [ps]	τ_1 [ps]	τ_2 [ps]
MeOH	2165	8.7±0.2	—	—
	2128	8.7±0.2	2.3±0.1	9.1±0.2
	2123	8.7±0.2	1.6±0.1	6.3±0.1
	2105	8.7±0.2	1.4±0.1	6.3±0.1
	2096	8.7±0.2	1.0±0.1	5.3±0.1
	2084	8.7±0.2	0.8±0.1	4.9±0.1
H ₂ O	2165	1.7±0.1	—	—
	2136	1.7±0.1	0.3±0.1	3.1±0.1
	2123	1.7±0.1	1.1±0.2	1.5±0.3
	2114	1.7±0.1	0.3±0.1	1.8±0.1

ketene intermediate (10 ps in methanol and 3 ps in water) can be explained in terms of solvent properties. Since excess vibrational energy is transferred from the hot solute to the surrounding solvent, hydrogen bonding with the solvent and among the solvent molecules themselves as well as the overlap of the vibrational spectrum of solute and solvent [213, 214] can play an important role for the efficiency of energy transport away from the solute molecule. Also of importance might be the dissipation of energy in the solvent that can be described by the conduction of heat. The thermal diffusivity [215, 216] represents the most important material parameter for this case. It is defined as $\kappa = \lambda M / C \rho$, where λ is the thermal conductivity, M the molecular weight, C the specific heat and ρ the density of the solvent. The higher thermal diffusivity of water ($\kappa_{H_2O} = 14.4 \cdot 10^{-8} \text{ m}^2/\text{s}$, $\kappa_{MeOH} = 10.2 \cdot 10^{-8} \text{ m}^2/\text{s}$) and stronger hydrogen bonding possibly results in faster vibrational cooling compared to methanol.

5.4 Conclusion

In this chapter, the photoinduced Wolff-rearrangement reaction of 2-diazo-1-naphthoquinone (DNQ) has been investigated. Steady state absorption measurements in the mid-infrared in combination with quantum chemical DFT calculations revealed the characteristic vibrational bands of DNQ. The C=N=N stretching vibration around 2116 cm⁻¹ turned out to be the most prominent feature. For the expected photoproducts (e.g. ketene), the calculations predict the spectral positions of the absorption bands which are suspected to appear. A transient absorption study is performed, to illuminate the structural dynamics of the ultrafast rearrangement reaction of DNQ, the formed photoproducts, intermediates and the characteristic time scales of the reaction steps.

The experimental observations indicate that the initial steps of the Wolff rearrange-

ment reaction of DNQ are very fast. The separation of the diazo-group, subsequent ring opening, rearrangement and closure of the ring to form the ketene occurs within 300 fs, which is the time resolution of our experiment. This finding shows that no statement on the possible existence of a carbene intermediate, as proposed in recent experiments [191, 203, 204] can be given. If a carbene intermediate exists, it must have a very small lifetime.

From the time-resolved data a model for the relaxation dynamics of the ketene photoproduct and DNQ after photoexcitation can be deduced. Population in the excited state of DNQ is either performing the Wolff-rearrangement reaction or is returning to the ground state. From the partial recovery of the ground state bleach of DNQ the quantum yield of the reaction is determined to be about 0.32 for both solvents. The ketene right after its formation has an excess of vibrational energy and the relaxation can be monitored by the shifting absorption band of the C=C=O vibration of the ketene. The vibrational relaxation dynamics in methanol with a time constant of about 10 ps, is much slower than in water (3 ps).

6 Quantum control of the photoreaction of DNQ

After the remarkable success of control over molecular fragmentation processes in the gas phase, control of liquid or condensed phase processes became a fascinating field for the application of femtosecond quantum control. So far only control and optimization or deoptimization of relatively simple condensed phase processes, like the efficiency of photoexcitation and isomerization, using single parameter as well as adaptive approaches have been demonstrated ([85] and references therein). Selective control over the population of different dissociation channels or more complex molecular rearrangement reactions than isomerization, has not been demonstrated yet.

For control experiments in the condensed phase, different techniques for monitoring and visualizing the time evolution of the quantum system, or the outcome of a chemical reaction can be employed. Most of these techniques are optical spectroscopy methods, such as emission spectroscopy or transient absorption spectroscopy. Usually these signals lie in the visible wavelength region of the electromagnetic spectrum. Therefore they offer only limited information about the structural changes during more complex photoreactions. In addition it is not easy to find spectral regions, that can be unambiguously assigned to specific products or intermediates during the reaction, because electronic transitions (absorption bands) in the condensed phase are quite broad and usually cover a range on the order of 1000 cm^{-1} . This means that for an experiment, where the goal is to control more complex photoreactions, which include structural changes of the molecule under study, one has to come up with a spectroscopic technique that is appropriate for this task. In contrast to electronic transitions, vibrational transitions in the mid-infrared spectral region provide structural information and the probability of bands overlapping with each other is much less, due to narrow transitions on the order of 10 cm^{-1} . Thus, using transient absorption spectroscopy in the mid-infrared offers the possibility to find appropriate spectroscopic signals, that are specific for different molecular configurations, as they would occur in rearrangement or dissociation reactions. For this reason, infrared detection will be applied to monitor the outcome of the photoreaction of DNQ (for details refer to Chapter 5) upon excitation with shaped femtosecond laser pulses. The ketene intermediate after Wolff rearrangement of DNQ dissolved in methanol will be the objective of all the following quantum control experiments. The spectroscopic signature is the transient absorption signal of the appearing vibrational band assigned to the ketene at 2128 cm^{-1} and 50 ps delay time (see Fig. 5.14), where vibrational relaxation of the initially hot ketene is already over.

At first, single parameter quantum control schemes will be employed, using the linear chirp (Section 6.1) and colored double pulse (Section 6.2) parametrizations. Then an adaptive multiparameter control concept using a closed learning loop is applied and

adaptive optimizations that seek to enhance the ketene formation during the photoreaction of DNQ are performed (Section 6.3).

6.1 Control by chirped pulse excitation

Linearly chirped pulses are employed to study the response of the photo-induced Wolff rearrangement reaction of DNQ on the chirp parameter. The chirped pulses are created by applying a quadratic spectral phase to femtosecond pulses with a Gaussian spectrum. The instantaneous frequency is therefore changing linearly with time. Depending on the sign of the quadratic spectral phase, one can obtain "up-chirped" (positively chirped) pulses, where the lower frequencies precede the higher frequencies, or "down-chirped" (negatively chirped) pulses, where the momentary frequency is decreasing with time.

6.1.1 Mathematical description of chirped pulses

For a pulse with a Gaussian spectrum of FWHM $\Delta\omega$ and a second-order spectral phase modulation, i.e. all Taylor coefficients b_j are equal to zero except for b_2 in Eq. (2.8), the electric field in the spectral domain becomes

$$E^+(\omega) = c_\omega \exp\left(-\frac{2 \ln(2) (\omega - \omega_0)^2}{\Delta\omega^2}\right) \exp\left(-i\frac{b_2}{2} (\omega - \omega_0)^2\right), \quad (6.1)$$

which after inverse Fourier transform (2.4) leads to the temporal electric field

$$E^+(t) = c_t \exp\left(-\frac{2 \ln(2) \Delta\omega^2 t^2}{[4 \ln(2)]^2 + b_2^2 \Delta\omega^4}\right) \exp\left(i\omega_0 t + i\frac{b_2 t^2}{2[4 \ln(2)]^2 / \Delta\omega^4 + 2b_2^2}\right), \quad (6.2)$$

where the quantities c_ω and c_t are constants. From the properties of the Fourier transform it follows for a Gaussian spectrum, that the shortest pulse duration Δt_0 obtainable with a spectral width $\Delta\omega$ is determined by the minimal time-bandwidth product (2.23)

$$\Delta t_0 = \frac{4 \ln(2)}{\Delta\omega}. \quad (6.3)$$

This can be plugged into Eq. (6.2) and the amplitude function $A(t)$ can be rewritten as

$$A(t) = \exp\left(-\frac{2 \ln(2) \Delta\omega^2 t^2}{[4 \ln(2)]^2 + b_2^2 \Delta\omega^4}\right) = \exp\left(-\frac{2 \ln(2) \Delta t_0^2 t^2}{\Delta t_0^4 + [4 \ln(2)]^2 b_2^2}\right). \quad (6.4)$$

This envelope function of $E^+(t)$, and therefore $I(t)$, is also a Gaussian. However, for $b_2 \neq 0$, $I(t)$ is stretched in time, leading to the new temporal FWHM $\Delta t(b_2)$

$$\Delta t(b_2) = \sqrt{\Delta t_0^2 + \frac{[4 \ln(2)]^2 b_2^2}{\Delta t_0^2}} = \sqrt{\Delta t_0^2 + b_2^2 \Delta\omega^2}, \quad (6.5)$$

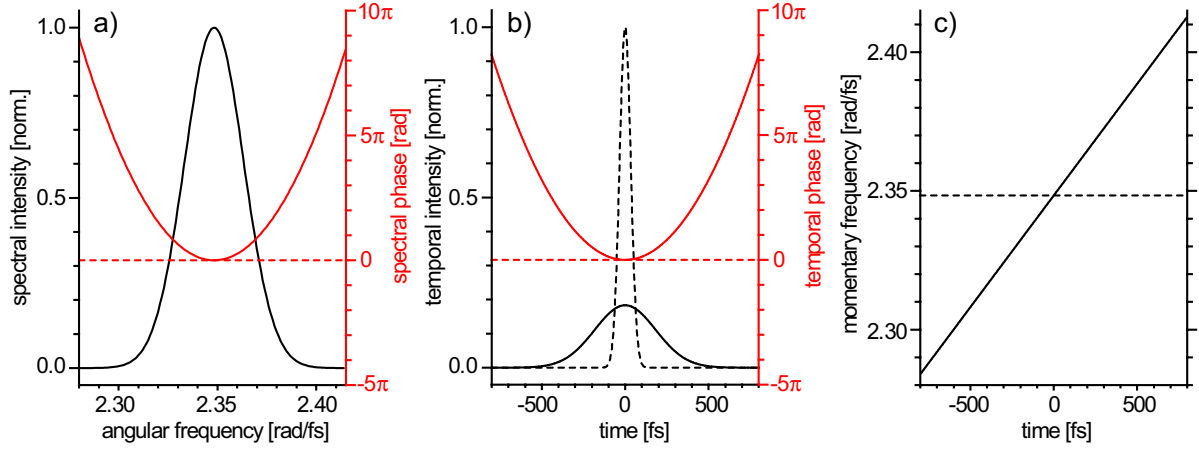


Figure 6.1: Linearly chirped laser pulses. a) Spectral intensity (black line) of a femtosecond laser pulse around a center wavelength of 800 nm with spectral width of 12 nm and spectral phases of a transform limited pulse (zero phase, red dashed line) and the quadratic phase (red line) corresponding to an up-chirped pulse with $b_2=12000 \text{ fs}^2$. b) Temporal intensity of the transform-limited pulse (black dashed line) and the up-chirped pulse (black line) and corresponding temporal phases. c) momentary frequencies of the transform-limited pulse (black dashed line) and the up-chirped pulse (black line).

which in the case of $b_2 = 0$ reduces to the minimal temporal width Δt_0 , while the pulse is elongated in time for all $b_2 \neq 0$. The momentary frequency $\omega_m(t)$ reveals that the pulses are actually linearly chirped, i.e. that $\omega_m(t)$ changes linearly with time:

$$\omega_m(t) = \frac{d}{dt} \left(\omega_0 t + \frac{b_2 t^2}{2[4 \ln(2)]^2 / \Delta\omega^4 + 2b_2^2} \right) = \omega_0 + \frac{b_2}{[4 \ln(2)]^2 / \Delta\omega^4 + b_2^2} t. \quad (6.6)$$

The sign of the linear slope

$$a(b_2) = \frac{b_2}{[4 \ln(2)]^2 / \Delta\omega^4 + b_2^2}, \quad (6.7)$$

describes whether lower frequencies precede higher ones (up-chirped pulse, $b_2 > 0$) or vice versa. With Eq. (6.7) the expression for the momentary frequency (6.6) becomes

$$\omega_m(t) = \omega_0 + a(b_2) t. \quad (6.8)$$

An illustrating example is shown in Fig. 6.1a-c. The spectral intensity of a laser pulse centered around 800 nm with a FWHM of 12 nm is depicted in Fig. 6.1a (black line) together with the spectral phases of a bandwidth-limited (dashed red line) and an up-chirped (red line) pulse with $b_2=12000 \text{ fs}^2$. These values are chosen such that they resemble the laser pulses delivered by our laser system. The resulting temporal intensities according to the square of Eq. (6.4) and the temporal phases are given in Fig. 6.1b. The corresponding momentary frequency $\omega_m(t)$ from Eq. (6.6) is displayed in Fig. 6.1c and as one can see it rises linearly for the up-chirped pulse. The bandwidth-limited pulse has a duration of 79 fs, while the chirped pulse is stretched to 430 fs according to Eq. (6.5).

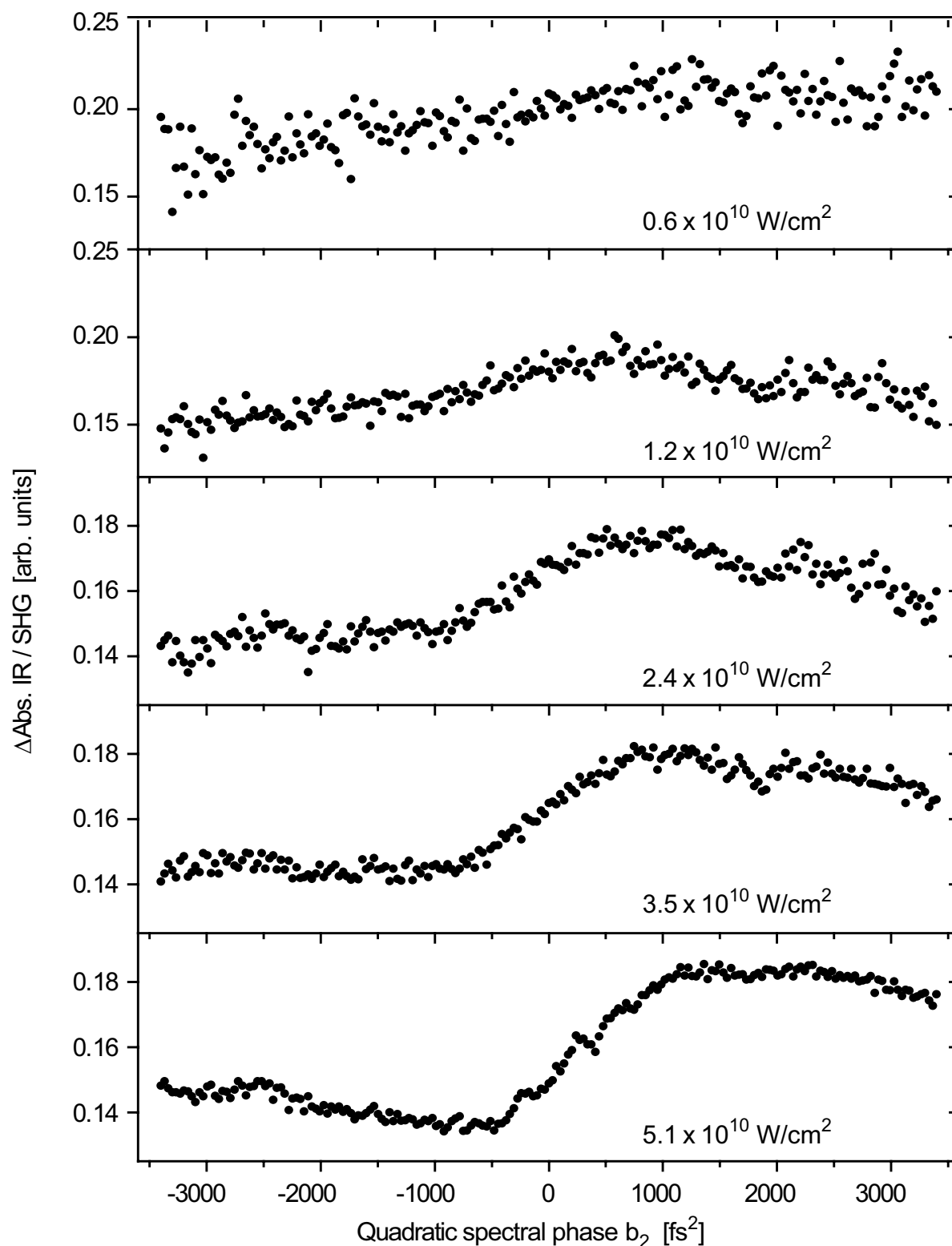


Figure 6.2: Chirped pulse excitation of DNQ at 400 nm. Variation of the quadratic spectral phase (linear chirp) of the excitation pulses as a function of pulse energy (intensity at the sample position). The transient absorption signal of the ketene photoproduct at 2128 cm^{-1} after 50 ps, divided by the energy (SHG) of the 400 nm pulses is the measured quantity. For higher pulse intensities the chirp dependence of the signal is much stronger.

6.1.2 Experimental results

The setup for this experiment is the pump - probe setup shown in Fig. 4.1 that was already used for the time-resolved mid-infrared absorption study of DNQ in chapter 5. The linearly chirped excitation pulses were obtained by applying a quadratic spectral phase on the pulses from the Ti:Sa amplifier system at the fundamental wavelength of 800 nm. Subsequent frequency doubling in a 100 μm thick BBO crystal leads to chirped second harmonic pulses with a central wavelength around 400 nm. In general, frequency doubling of phase-modulated pulses results in phase and amplitude shaped second harmonic pulses [217], but for the case of linear chirp no amplitude modulation occurs [218, 219]. For Gaussian shaped or similarly smooth spectra with only quadratic spectral phase, the phase maps proportionally over to the second harmonic spectrum. The Taylor coefficients of the spectral phase are connected by $b_2(400 \text{ nm})=1/2 b_2(800 \text{ nm})$. However, the absolute amplitude of the generated second harmonic pulses depends on the chirp of the fundamental pulses, since SHG is a nonlinear process, which strongly depends on the intensity of the applied pulses. Therefore all the transient absorption signals recorded with shaped second harmonic pulses have to be normalized by the second harmonic pulse energy to be able to compare the effect of the frequency ordering of differently chirped pulses. Otherwise the dominating effect would be the difference in intensity. This normalization is done by simultaneously detecting a pickoff from a glass plate, that is inserted in the excitation beam path before the sample flow cell (see Fig. 4.4) by a reference photodiode. This signal is proportional to the pulse energy of the 400 nm pulses, and division of the infrared absorption change by this signal leads to the relative photoproduct yield per pulse energy. Before the chirp parameter scan and all other experiments with shaped pulses, the 800 nm pulses are adaptively compressed, using the learning algorithm (Sec. 3.5) to maximize the second harmonic yield [42–47]. The resulting optimal phase pattern is then used as an offset for the following experiments.

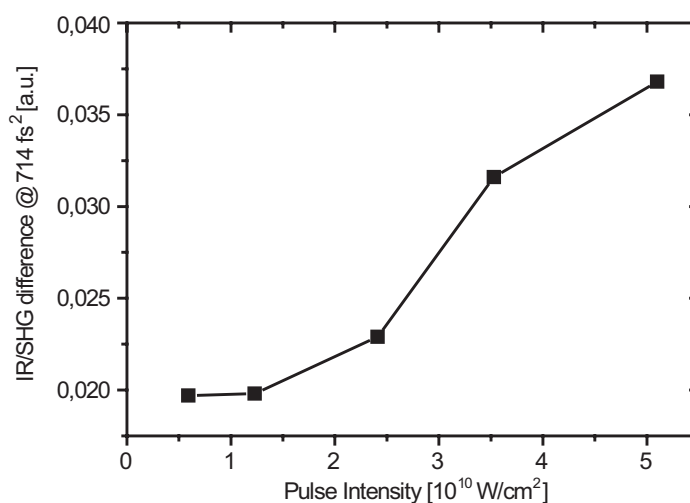


Figure 6.3: Chirp dependence as a function of excitation pulse intensity. Difference of infrared absorption (ketene photoproduct at 2128 cm^{-1} after 50 ps) normalized by SHG yield for linear chirp with different sign at $\pm 714 \text{ fs}^2$.

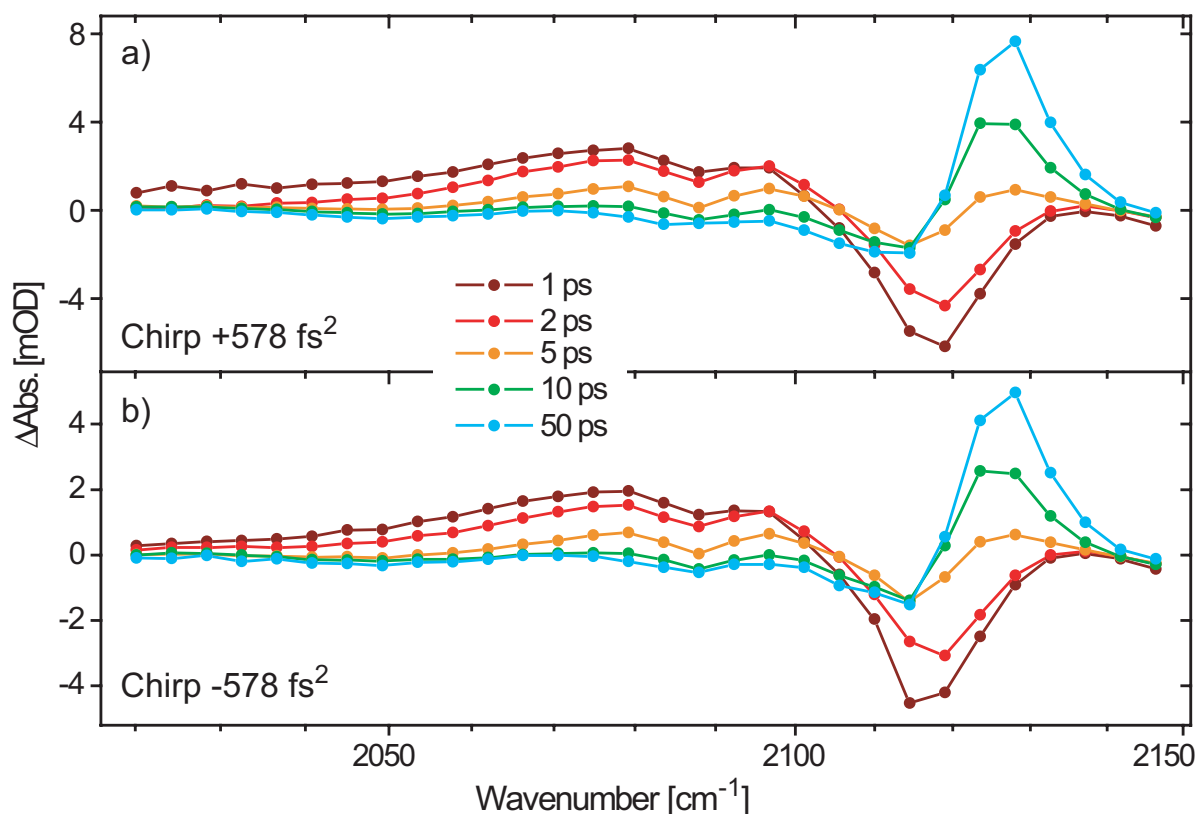


Figure 6.4: Transient absorption spectra in the region of 2150–2020 cm^{-1} from 1–50 ps for a) up-chirped and b) down-chirped excitation pulses. No difference except the overall magnitude of absorption change due to the chirp sign is observed.

The results of the chirp parameter variation are shown in Fig. 6.2. The quadratic spectral phase, leading to linearly chirped excitation pulses around 400 nm is scanned and the transient absorption signal of the appearing ketene intermediate after Wolff-rearrangement of DNQ, at 2128 cm^{-1} and 50 ps delay time, divided by the energy (SHG) of the 400 nm pulses is measured for different excitation pulse intensities. For small excitation intensities, starting with $0.6 \times 10^{10} \text{ W/cm}^2$ ($E_P = 1.2 \mu\text{J}$, $w_0 = 180 \mu\text{m}$, $\Delta t = 200 \text{ fs}$) almost no dependence on the linear chirp is observed and the signal-to-noise ratio is quite low. But when the pulse intensity is increased, the chirp dependence of the signal is becoming stronger, until at the highest pulse intensity employed the chirp dependence is very distinct. The curve corresponding to $5.1 \times 10^{10} \text{ W/cm}^2$ shows a minimum at negative quadratic spectral phase around -700 fs^2 , meaning that a slightly down-chirped pulse leads to less photoproduct formation than the transform limited pulse at zero quadratic spectral phase at $b_2 = 0$. At the same chirp with positive sign ($+700 \text{ fs}^2$) much more photoproduct is formed. This is additionally visualized in Fig. 6.3 by plotting the difference in photoproduct yield for different chirp signs (at $\pm 714 \text{ fs}^2$) as a function of the excitation pulse intensity.

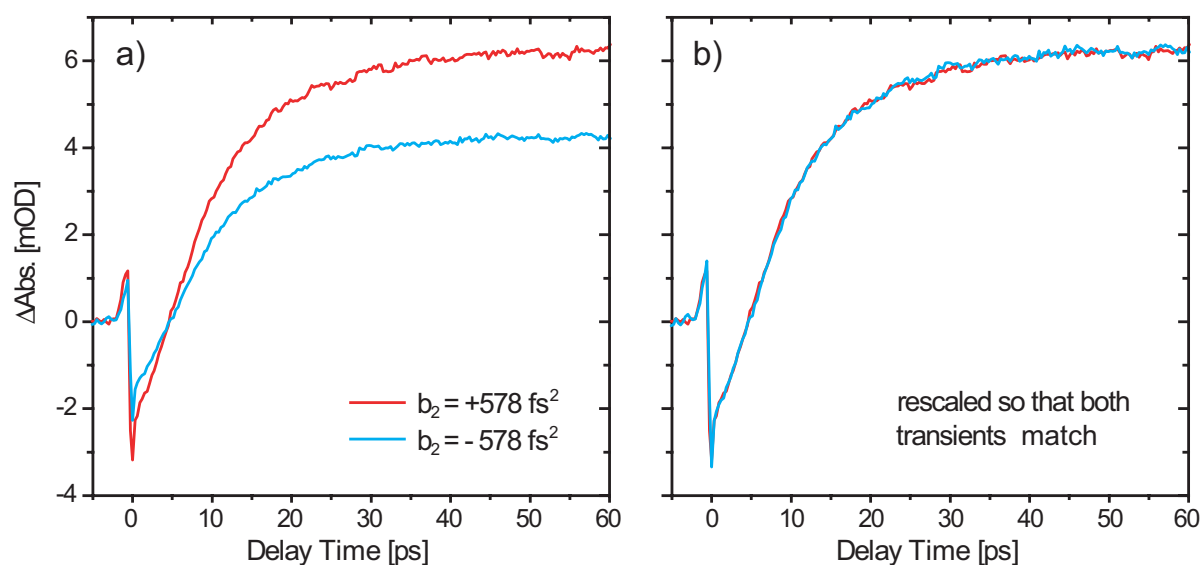


Figure 6.5: a) Transients at 2123 cm^{-1} for up-chirped (red curve) and down-chirped (blue curve) excitation pulses reflecting the result of the chirp parameter scan. b) Rescaled transients show the same time dependence, which means that variation of the chirp parameter does not influence the temporal dynamics of the photoreaction.

6.1.3 Influence of chirped pulse excitation on photoproduct formation

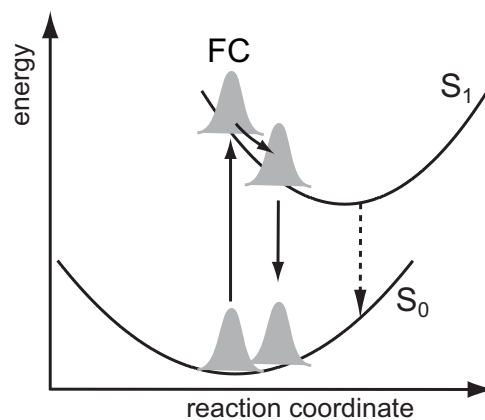
In this section the question, whether chirped pulse excitation also influences the photoproduct formation dynamics of the Wolff-rearrangement reaction of DNQ, is addressed. Therefore, transient absorption spectra like in Sec. 5.3 are recorded for chirped excitation pulses with different signs of the quadratic spectral phase. The absolute value of the applied chirp is chosen to be close to the position of the minimum at negative chirp in the chirp parameter scan shown in Fig. 6.2. The resulting transient spectra for the up-chirped and down-chirped pulses of the same duration and energy are displayed in Fig. 6.4. At all delay times they show no difference concerning the dynamics, except their absolute magnitude, which reflects the result already obtained in the chirp parameter scan. For positive linear chirp a higher amount of the ketene photoproduct is formed.

Additionally, for different chirp signs the transients at 2128 cm^{-1} as a function of delay time, depicted in Fig. 6.5a exhibit the same behavior. The transients can be rescaled by a suitable factor, so that both transients perfectly match (see Fig. 6.5b). This means, that the chirp parameter has no influence on the dynamics of the photoreaction, following the excitation of DNQ from the S_0 to the excited potential energy surface S_1 .

6.1.4 Discussion

The results of the experiments described in the previous section can be summarized as follows. Slightly negatively chirped pulses lead to less photoproduct formation and this

Figure 6.6: Intrapulse dumping mechanism. The excited-state wave packet is initially created by an excitation pulse in the Franck-Condon (FC) region of the S_1 PES. Within this laser pulse, population can also be transferred back to the S_0 PES again. The efficiency of the overall photoexcitation depends on the laser pulse shape and can be monitored by a suitable signal, e.g. by stimulated emission (dashed arrow) with a probe pulse after the interaction of the system with the excitation pulse or as here with a mid-infrared transient absorption signal (adapted from Ref. [220]).



effect is more pronounced for higher excitation intensities. The dynamics of the photoreaction is not influenced by the linear chirp (see Fig. 6.5). This allows the conclusion, that the reduction / enhancement of photoproduct yield for down- / up-chirp is due to an intrapulse dumping mechanism (see Fig. 6.6). This is a well-known mechanism and has been studied many times experimentally and theoretically [220–223]. The amount of excited molecules significantly depends on the chirp imposed on the laser pulse. Pulses with down-chirp, where high frequencies precede lower frequencies excite less molecules than pulses with up-chirp of the same energy. The first part of the laser pulse forms a wavepacket on the excited state potential energy surface. Wavepacket evolution along the reaction coordinate is usually accompanied by a reduced potential energy gap between S_0 and S_1 , so that lower frequency photons in the second part of the laser pulse can transfer population back down to the S_0 ground state. For negative chirp ($b_2 < 0$) the momentary frequency is decreasing, and so the shrinking S_0 - S_1 energy gap can be matched. Thus, population is efficiently brought back to the S_0 ground state, and less molecules remain in the S_1 excited state. As a consequence also less photoproduct is formed in consecutive reaction steps. For positively chirped pulses, intrapulse dumping is successfully prevented or at least minimized by exhibiting an increasing momentary frequency and hence more molecules are excited than with transform limited or negatively chirped pulses. Intrapulse dumping needs two interactions within the same laser pulse, therefore it is strongly depending on the intensity of the laser pulse. That is exactly what we observe in our experiment. Also the fact, that the following dynamics of the photoreaction is not influenced by the chirp is explained by the intrapulse dumping scenario, since it affects only the excitation to the S_1 potential energy surface.

The knowledge of this mechanism can be used generate a higher photoproduct yield. In this case when up-chirped pulses are employed a much higher ketene yield is obtained compared to an unshaped pulse.

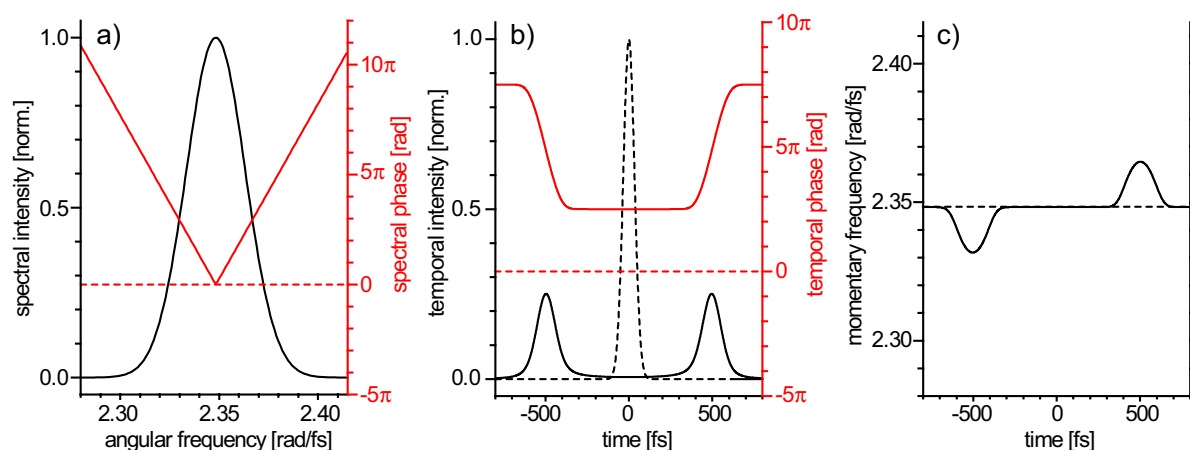


Figure 6.7: Colored double pulses. a) Spectral intensity (black line) of a femtosecond laser pulse around a center wavelength of 800 nm with spectral width of 12 nm (same parameters as in Fig. 6.1) and spectral phases of a transform limited pulse (zero phase, red dashed line) and the triangular phase (red line) corresponding to a colored double pulse with $\frac{\Delta\tau}{2}=500$ fs leading to a pulse separation of 1000 fs. b) Temporal intensities of the transform-limited pulse (black dashed line) and the colored double pulse (black line) and corresponding temporal phases. c) momentary frequencies of the transform-limited pulse (black dashed line) and the colored double pulse (black line).

6.2 Double pulse excitation

Another pulse parametrization besides linear chirp has also been employed for the investigation of the intrapulse dumping mechanism [81, 82, 224]. In this systematic study the two time domain parametrizations, linear chirp and colored double pulses have been compared and the question whether their influence on the excitation of a molecular system is equivalent was addressed. Therefore it is quite natural to also apply colored double pulses to the photoreaction of DNQ. This could provide additional insights because two separated pulses are employed. With such a scheme a pump-dump mechanism can be exploited for the control of a reaction.

After introduction of the colored double pulse parametrization (Sec. 6.2.1) the impact of colored double pulses on the ketene formation of DNQ is analyzed and related to chirped pulse excitation (Sec. 6.2.2).

6.2.1 Mathematical description of colored double pulses

First-order spectral phase modulation with the coefficient $b_1 \neq 0$ (2.8) leads to a temporal shift of the laser pulse. Therefore, the envelope of the temporal electric field is not changed by an additional $b_1 \neq 0$, but only shifts it in time. Thus, by applying different b_1 values to certain spectral regions of the laser pulse spectrum one can create pulse sequences. In the literature, this procedure has already been described [224, 225] and has been applied several times [224–230]. Colored double pulses can be generated by a

triangular spectral phase modulation

$$\phi(\omega) = \frac{\Delta\tau}{2} (\omega - (\omega_0 + \delta\omega)) \operatorname{sgn}(\omega - (\omega_0 + \delta\omega)) , \quad (6.9)$$

where $\Delta\tau$ is the separation of the double-pulse (“double triangular phase slope”) and $\omega_0 + \delta\omega$ is the so-called “spectral break point”, i.e. the frequency where the sign of this linear spectral phase slope is flipped. With this spectral phase modulation, the electric field in the spectral domain is given by

$$E(\omega) = c_\omega \exp\left(-\frac{2\ln(2)(\omega - \omega_0)^2}{\Delta\omega^2}\right) \begin{cases} \exp\left(+i\frac{\Delta\tau}{2}(\omega - \omega_0 - \delta\omega)\right) & \text{for } \omega < \omega_0 + \delta\omega \\ \exp\left(-i\frac{\Delta\tau}{2}(\omega - \omega_0 - \delta\omega)\right) & \text{for } \omega > \omega_0 + \delta\omega \end{cases} . \quad (6.10)$$

The inverse Fourier-transform (2.4) takes the form

$$\begin{aligned} \mathcal{F}^{-1}\{E^+(\omega)\} &\propto \exp\left(-i\frac{\Delta\tau}{2}(\omega_0 + \delta\omega)\right) \int_{-\infty}^{\omega_0 + \delta\omega} \exp\left(-\frac{2\ln(2)(\omega - \omega_0)^2}{\Delta\omega^2}\right) \exp\left(i\omega\left(t + \frac{\Delta\tau}{2}\right)\right) d\omega \\ &\quad + \exp\left(i\frac{\Delta\tau}{2}(\omega_0 + \delta\omega)\right) \int_{\omega_0 + \delta\omega}^{+\infty} \exp\left(-\frac{2\ln(2)(\omega - \omega_0)^2}{\Delta\omega^2}\right) \exp\left(i\omega\left(t - \frac{\Delta\tau}{2}\right)\right) d\omega \end{aligned} \quad (6.11)$$

and finally leads to the temporal electric field

$$\begin{aligned} E^+(t) &\propto \Delta\omega \exp(i\omega_0 t) \left\{ \exp\left(-i\frac{\Delta\tau}{2}\delta\omega - \frac{\Delta\omega^2(t + \frac{\Delta\tau}{2})^2}{8\ln(2)}\right) \left[1 - \operatorname{erf}\left(i\frac{\Delta\omega(t + \frac{\Delta\tau}{2})}{2\sqrt{2\ln(2)}} - \frac{\delta\omega\sqrt{2\ln(2)}}{\Delta\omega}\right)\right] \right. \\ &\quad \left. + \exp\left(i\frac{\Delta\tau}{2}\delta\omega - \frac{\Delta\omega^2(t - \frac{\Delta\tau}{2})^2}{8\ln(2)}\right) \left[1 + \operatorname{erf}\left(i\frac{\Delta\omega(t - \frac{\Delta\tau}{2})}{2\sqrt{2\ln(2)}} - \frac{\delta\omega\sqrt{2\ln(2)}}{\Delta\omega}\right)\right] \right\}, \end{aligned} \quad (6.12)$$

with the error function $\operatorname{erf}(x) = 2/\sqrt{\pi} \int_0^x \exp(-y^2) dy$.

The example in Fig. 6.7 shows a symmetrically divided spectrum ($\delta\omega = 0$) centered around a wavelength of 800 nm with a spectral width of 12 nm leading to two subpulses with equal intensity. The momentary frequency $\omega_m(t)$ deviates by the same amount from ω_0 at the two moments in time with maximal intensity (Fig. 6.7c). In contrast, for $\delta\omega \neq 0$, the two subpulses would differ in amplitude, and also $\omega_m(t)$ would be asymmetric with respect to $t=0$ since the portions of the spectral intensity shifted forward and backward in time are not equal.

The envelopes of the two subpulses at $t = \pm\Delta\tau/2$ consist of a Gaussian envelope with the same temporal width as an unchirped laser pulse, but there is an additional distortion by the error function, which leads to an elongation [225] of the subpulse, accounting for the reduced width of the spectral contributions of each subpulse.

In the special case of a symmetrically divided spectrum (i.e. $\delta\omega = 0$, depicted in Fig. 6.7, where each of the two subpulses comprises half the pulse energy, the error-function terms are purely imaginary, and with the imaginary error function $\operatorname{erfi}(x) =$

$-i \operatorname{erf}(ix)$, Eq. (6.12) becomes

$$E^+(t) \propto \Delta\omega \exp(i\omega_0 t) \left\{ \exp\left(-\frac{\Delta\omega^2 (t + \frac{\Delta\tau}{2})^2}{8 \ln(2)}\right) \left[1 - i \operatorname{erfi}\left(\frac{\Delta\omega (t + \frac{\Delta\tau}{2})}{2\sqrt{2 \ln(2)}}\right)\right] + \exp\left(-\frac{\Delta\omega^2 (t - \frac{\Delta\tau}{2})^2}{8 \ln(2)}\right) \left[1 + i \operatorname{erfi}\left(\frac{\Delta\omega (t - \frac{\Delta\tau}{2})}{2\sqrt{2 \ln(2)}}\right)\right] \right\}. \quad (6.13)$$

The latter expression (6.13) can be rewritten [225] with the help of

$$\alpha_{1,2} = \Delta\omega \exp\left(-\frac{\Delta\omega^2 (t \pm \frac{\Delta\tau}{2})^2}{8 \ln(2)}\right) \quad (6.14)$$

$$\gamma_{1,2} = \operatorname{erfi}\left(\frac{\Delta\omega (t \pm \frac{\Delta\tau}{2})}{2\sqrt{2 \ln(2)}}\right), \quad (6.15)$$

so that it simplifies to

$$E^+(t) \propto \exp(i\omega_0 t) [(\alpha_1 + \alpha_2) + i(\alpha_2 \gamma_2 - \alpha_1 \gamma_1)]. \quad (6.16)$$

Using Eq. (6.16), the temporal phase $\Phi(t)$ can be calculated and takes the form

$$\Phi(t) = \omega_0 t + \arctan\left(\frac{\alpha_2 \gamma_2 - \alpha_1 \gamma_1}{\alpha_1 + \alpha_2}\right). \quad (6.17)$$

The momentary angular frequency $\omega_m(t)$ is again given by the derivative of this formula. The two momentary angular frequencies at $t = \pm \Delta\tau/2$, the moments of maximal intensity, are of special interest, because they are the effective central frequencies of the two subpulses.

In the case that $\Delta\tau$ is positive and $\Delta\tau/2 \gg \Delta t$, so that the parameter α_1 from Eq. (6.14) can be neglected at $t = \Delta\tau/2$ in a first approximation, the spectral phase (6.17) simplifies to

$$\Phi(t) \approx \omega_0 t + \arctan(\gamma_2) = \omega_0 t + \arctan\left[\operatorname{erfi}\left(\frac{\Delta\omega (t - \frac{\Delta\tau}{2})}{2\sqrt{2 \ln 2}}\right)\right], \quad (6.18)$$

and the momentary frequency at $t = \Delta\tau/2$ is thus

$$\omega_m(\Delta\tau/2) = \left. \frac{d\Phi(t)}{dt} \right|_{t=\Delta\tau/2} = \omega_0 + \frac{\Delta\omega}{\sqrt{2\pi \ln 2}}. \quad (6.19)$$

In Eq. (6.18), the influence of the second subpulse has been neglected in order to obtain expression (6.19) for the momentary frequency of the subpulses. The result can be easily understood if one thinks of a pulse with a spectrum consisting of half a Gaussian, e.g. $A(\omega) = 0$ for $\omega < \omega_0$. In such a case, the central frequency $\bar{\omega}$ can be calculated by

$$\bar{\omega} = \frac{\int_{\omega_0}^{\infty} \omega A(\omega) d\omega}{\int_{\omega_0}^{\infty} A(\omega) d\omega} = \frac{\int_{\omega_0}^{\infty} \omega \exp\left(-\frac{2 \ln(2) (\omega - \omega_0)^2}{\Delta\omega^2}\right) d\omega}{\int_{\omega_0}^{\infty} \exp\left(-\frac{2 \ln(2) (\omega - \omega_0)^2}{\Delta\omega^2}\right) d\omega} = \omega_0 + \frac{\Delta\omega}{\sqrt{2\pi \ln(2)}}, \quad (6.20)$$

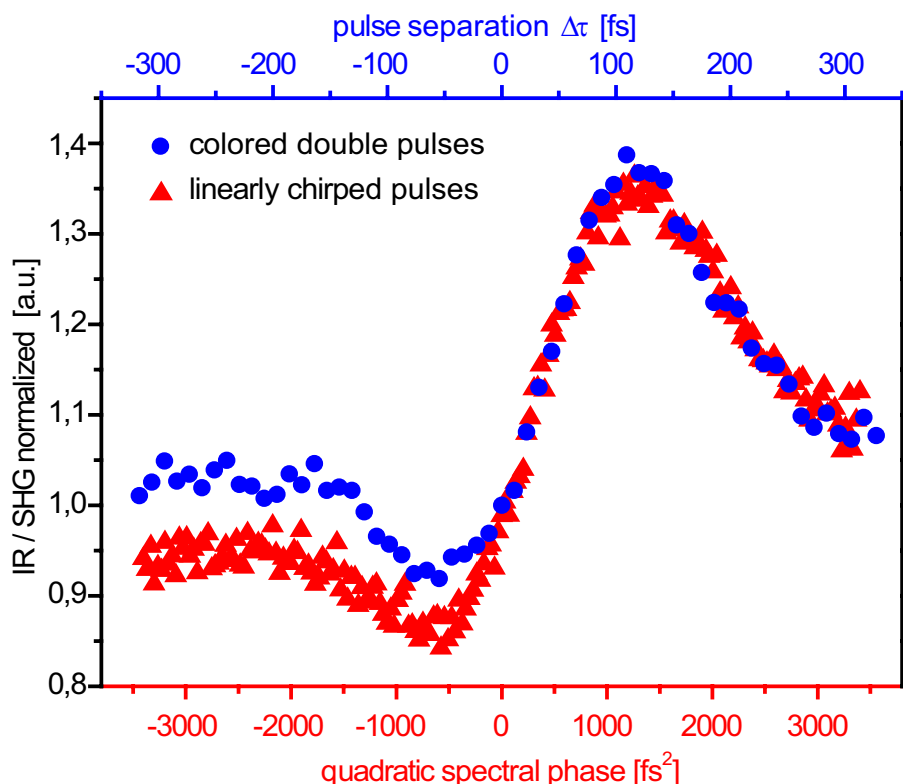


Figure 6.8: Colored double pulse (blue dots) vs. chirped pulse (red triangles) excitation of DNQ. The mid-infrared absorption of the ketene intermediate at 2128 cm^{-1} at 50 ps delay time divided by the SHG intensity normalized to the value at zero quadratic spectral phase as a function of colored double pulse separation $\Delta\tau$ and quadratic spectral phase of the 400 nm excitation pulses. The interrelation between the abscissas is determined as explained in the text.

in accordance with Eq. (6.19). Thus, a triangular spectral phase pattern leads to two sub-pulses with different effective central angular frequencies separated by $\Delta\omega\sqrt{2}/(\pi\ln 2)$. Depending on the sign of $\Delta\tau$, the first pulse at $t = -|\Delta\tau|/2$ is shifted more to the red (for $\Delta\tau > 0$) or to the blue ($\Delta\tau < 0$) in comparison to the second pulse at $t = +|\Delta\tau|/2$.

6.2.2 Experimental results and discussion

Under identical conditions as the chirp parameter scans, already described in Sec. 6.1.2, DNQ dissolved in methanol is excited with frequency-doubled linearly chirped pulses and colored double pulses at the highest possible 400 nm pulse energy leading to a peak intensity at the sample position of about $5\times 10^{10}\text{ W/cm}^2$. The chirp parameter scan is performed in the same fashion as before. In the double pulse scan only the linear slope of the colored double pulses is varied, while the spectral breakpoint where the sign of the linear slope changes is kept fixed at the center frequency of the pulse. Hence, each subpulse has the same intensity and only the separation of the two pulses is changed. The recorded signal is again the mid-infrared absorption of the ketene

intermediate at 2128 cm^{-1} at 50 ps delay time divided by the SHG intensity. The two scan parameters, quadratic spectral phase b_2 and linear double pulse slope $\Delta\tau$ can be related by the respective momentary frequencies $\omega_m(t)$ [81, 82, 224]. As derived in the previous sections, the momentary frequency of linearly chirped pulses changes linearly with time, while the temporal envelope is an elongated Gaussian. In contrast, triangular double pulses have a temporal envelope consisting of two intense peaks which have different effective central frequencies.

Momentary frequencies $\omega_0 - \omega_f$ at time $t = -t_f$ and $\omega_0 + \omega_f$ at $t = +t_f$ can be achieved according to Eq. (6.19) by a triangular double pulse whose spectrum has a FWHM $\Delta\omega = \sqrt{2\pi \ln(2)} |\omega_f|$, and the pulse separation is adjusted to $\Delta\tau = 2t_f \text{sgn}(\omega_f)$. If one wants to achieve the same momentary frequencies at those times by employing linearly chirped pulses instead, the necessary second-order spectral phase modulation for the given $\Delta\omega$ can be calculated from Eq. (6.7) and simply is $b_2(a = \omega_f/t_f)$. For large enough double pulse separations ($\Delta\tau \gg \Delta t_0$) compared to the pulse duration t_0 , b_2 can be approximated by the linear relation

$$b_2(\omega_f/t_f) \Big|_{\Delta\tau \gg \Delta t_0} \approx \frac{\Delta\tau \sqrt{2\pi \ln(2)}}{2\Delta\omega}, \quad (6.21)$$

connecting the two pulse parametrizations.

The above sketched procedure holds for the comparison of linearly chirped pulses and colored double pulses at the fundamental at 800 nm. For the frequency doubled shaped 800 nm pulses in our experiment however, this has to be slightly refined. In order to obtain the momentary frequency of the colored double pulses centered around 400 nm, the temporal phase of the frequency-doubled pulse for a certain value of $\Delta\tau$ is simulated, taking into account the real experimentally measured spectrum of the fundamental pulse. This leads to the momentary frequency $\omega_m(t)$ by taking the derivative with respect to the time according to Eq. (2.17). This can now be compared with the momentary frequency of the linearly chirped 400 nm pulse. This results in linked abscissas as depicted in Fig. 6.8, where the results of the colored double pulse and linear chirp parameter scans are compared. The common ordinate is normalized to the ketene/SHG yield of the transform-limited pulse ($b_2=0$ or $\Delta\tau=0$). Although the temporal profiles of the two pulse parametrizations are very different the scan curves show almost identical behavior. For negative double pulse separation $\Delta\tau$, where the first subpulse is blue shifted and the second subpulse is redshifted, less ketene photoproduct / SHG yield is obtained as for a transform-limited pulse, whereas the same pulse separation with reversed frequency ordering produces much more photoproduct. Thus, the effect seen in the double pulse scan can also be explained by intrapulse dumping. Similar to the linear chirp scan, the first subpulse containing higher frequencies creates an excited state wave-packet and the second subpulse of lower frequency matches the decreasing potential energy difference upon wave-packet propagation. For positive $\Delta\tau$ the frequency ordering is reversed and intrapulse dumping is efficiently reduced leading to increased ketene photoproduct / SHG yield.

However, in the special case of the photoinduced Wolff rearrangement of DNQ, where the photoreaction is extremely fast and already over after about 300 fs (see Sec. 5.3.2 for details) there is only a small time window for intrapulse dumping. Excited state

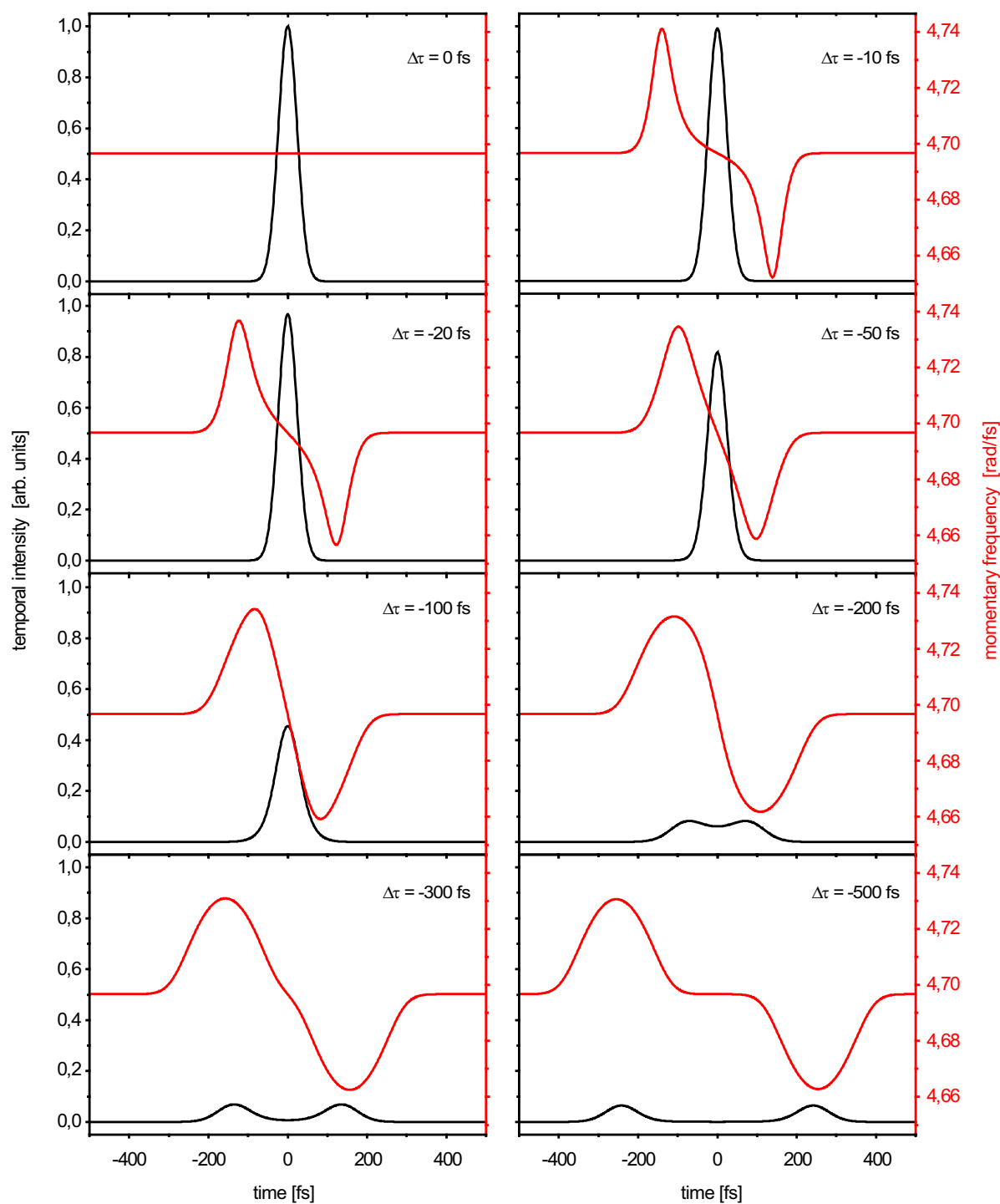


Figure 6.9: Colored double pulses with small triangular slopes $\Delta\tau$ from 0 to -500 fs are frequency doubled to yield double pulses centered around 400 nm. The temporal intensities (black) and the momentary frequencies (red) of the pulses (same starting parameters as in Fig. 6.7) are depicted. For small values of the triangular slope $\Delta\tau$ the pulses are not separated from each other and they are linearly chirped as the linear momentary frequency shows.

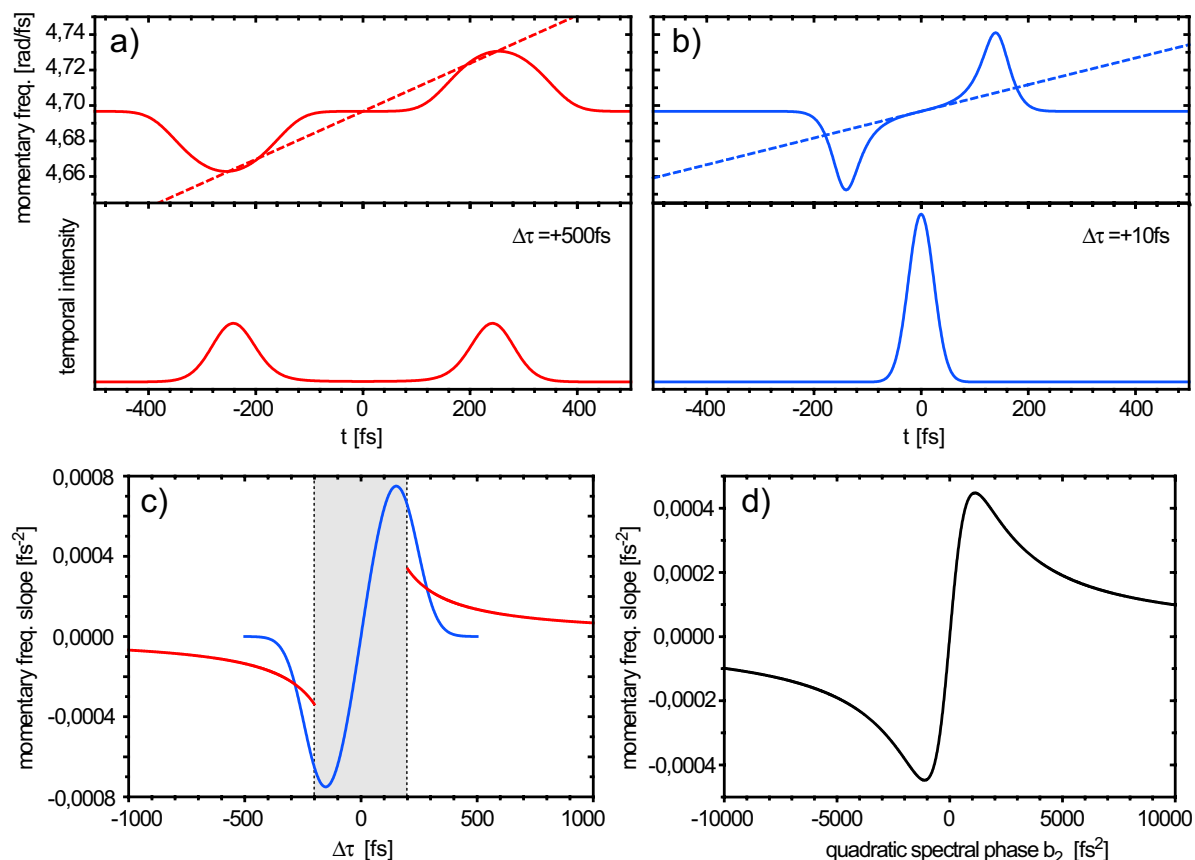


Figure 6.10: Comparison of colored double pulses and linear chirped pulses for small values of the triangular slope $\Delta\tau$. Two regimes can be identified. a) The subpulses are fully separated in time ($\Delta\tau=+500$ fs). Then the momentary frequencies at the maxima of the two subpulses can be compared with the linearly rising momentary frequency of a linearly chirped pulse (dashed line). b) The subpulses are not separated in time ($\Delta\tau=+10$ fs). The momentary frequency in this case can be approximated with a linearly rising momentary frequency having the same slope at $t=0$ (dashed line). c) Slope of the momentary frequency as a function of triangular slope $\Delta\tau$ for both regimes. The blue curve represents the slope for small $\Delta\tau$ (also indicated by the grey region) as obtained by $\frac{d^2\Phi}{dt^2}$ from Eq. (6.18), while the red curve shows the slope for larger $\Delta\tau$ where the subpulses are separated. d) Momentary frequency slope for linearly chirped pulses as a function of the quadratic spectral phase.

population that can be dumped back to the electronic ground state is only present for a very short time interval after photoexcitation. Within this time interval the colored double pulses are not really separated in time, as the simulation in Fig. 6.9 illustrates. The temporal intensities and momentary frequencies as a function of time are calculated for frequency-doubled fundamental pulses with slight triangular phases yielding colored double pulses centered around 400 nm as they are created in the experiment. Moreover, the pulses rather exhibit linear chirp as the linear momentary frequency $\omega_m(t)$ around time zero depicted in Fig. 6.9 indicates. Only the temporal intensities and momentary frequencies for negative triangular phase slopes ($\Delta\tau < 0$) are shown because for positive

$\Delta\tau$ the behaviour of the intensities and phases is symmetric, only the frequency ordering is reversed. Starting from $\Delta\tau=0$ going to slightly negative values the slope of the momentary frequency $\omega_m(t)$ around $t=0$ decreases meaning that the pulses are increasingly down-chirped. From about $\Delta\tau=200$ fs on the slope of $\omega_m(t)$ is slightly increasing until the two subpulses are fully separated. The momentary frequency shows complex behaviour making it very difficult to compare it to linearly chirped pulses for small values of the triangular slope. Two regimes can be identified as depicted in Fig. 6.10. If the two subpulses are fully separated in time as shown in Fig. 6.10a for $\Delta\tau=+500$ fs (red lines), the momentary frequencies at the maxima of the two subpulses can be compared with the linearly rising momentary frequency of a linearly chirped pulse (dashed line). In this fashion colored double pulses were related to linearly chirped pulses up to now [81, 82, 224]. Close to $\Delta\tau=0$ when the subpulses are still overlapping in time this procedure is no longer exact. But in this case the momentary frequency can be approximated with a linearly rising momentary frequency having the same slope at $t=0$. This is shown for $\Delta\tau=+10$ fs in Fig. 6.10b. An illustrative quantity is the slope of the momentary frequency as a function of triangular slope $\Delta\tau$ which is shown for both regimes in Fig. 6.10c. The blue curve represents the slope for small $\Delta\tau$ at $t=0$ (also indicated by the grey region), while the red curve shows the slope (as defined in Fig. 6.10a) for larger $\Delta\tau$ where the subpulses are separated. In Fig. 6.10d the momentary frequency slope for linearly chirped pulses as a function of the quadratic spectral phase is depicted for comparison. As one can see the behaviour is qualitatively similar but not identical.

To conclude, for small values of the triangular phase slope $\Delta\tau$ colored double pulses are not yet separated in time and are approximately linearly chirped, whereas for large double pulse separation one can only speak of an effective linear chirp in the sense of matching momentary frequencies at certain points in time.

6.3 Adaptive optimization of the photoproduct formation

The next logical step after performing systematic parameter scans is to investigate the controllability of the photoreaction of DNQ dissolved in methanol by an adaptive optimization with a suitably defined control goal in order to explore whether more degrees of freedom lead to improved control. In our case this would be the maximization of the ketene photoproduct / SHG yield ratio. As already explained in detail in Sec. 3.5 the evolutionary algorithm requires the definition of a fitness function that is to be maximized. When the fitness takes the form of the ratio of two experimental observables, a discriminator which is determined by the signal-to-noise ratio of the experiment has to be included to keep the algorithm from finding unphysical solutions which originate from very small denominators in the fitness function. Therefore the fitness function is defined as

$$\text{Fitness} = \frac{\text{Ketene MIR Absorption}}{\max(\text{SHG yield}, D)}, \quad (6.22)$$

where the quantity D is the appropriately chosen discriminator. The technical details

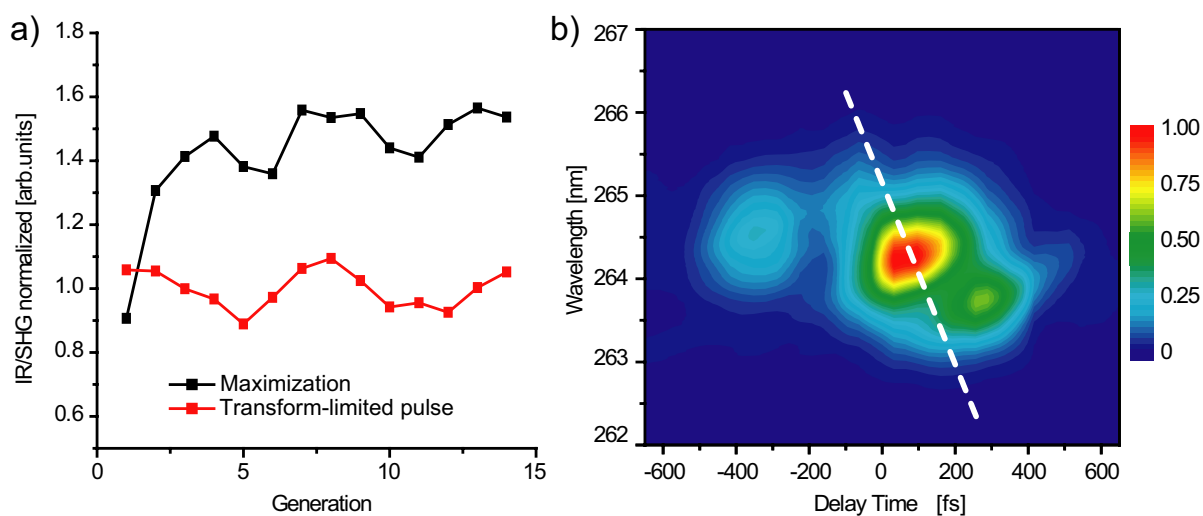


Figure 6.11: Adaptive maximization of the ketene photoproduct normalized by the intensity of the second harmonic excitation pulse at 400 nm. a) Evolution of the best 10% of the individuals per generation (black) together with the result obtained by a transform-limited pulse (red) which serves as a reference. b) XFROG trace of the optimal pulse directly showing the frequency distribution over time. The white dashed line represents the momentary frequency of the up-chirped pulse (around $+1000 \text{ fs}^2$) from the chirp scan in Fig. 6.8.

of these optimization experiments are slightly different from the description in Sec. 3.5. Due to the small absorption cross-section for vibrational transitions, extensive signal averaging is necessary to achieve acceptable signal-to-noise ratios. Therefore the averaging time was set to 3 s, i.e. 1500 pump-probe pulse pairs (see definition of absorption change in Sec. 3.4.2) are averaged. The number of individuals was reduced to 40 per generation and only 16 genes (not 128) were defined and interpolation determined the complete phase function introduced by the 128-pixel LCD in the pulse shaper. Otherwise the search space would have been too large so that the algorithm would have needed too much time for finding the optimal pulse shape. In this case long term drift of the laser system (pulse duration and pulse energy) would have disturbed the optimization. But with these parameters the overall time required for an adaptive optimization run was limited to the order of an hour.

Many optimization runs were performed which lead to more or less similar results, although the starting conditions for the different runs were not exactly identical. The maximal achievable 400 nm excitation pulse energy for instance was different from day to day. However, most of the times the fitness value obtained by the transform-limited pulse was exceeded by the optimal pulse. In the optimization run shown in Fig. 6.11 the discriminator was set to 10% of the SHG yield obtained with the transform-limited reference pulse to allow a certain degree of structure in the optimal pulse found by the learning algorithm. Due to the long time required for a single optimization a systematic study of the impact of the discriminator was not possible. Nevertheless it was found that for higher values of the discriminator the optimal pulses exhibited less structure and were close to transform-limited. This is intuitive since a higher discriminator rejects more

structured pulses because they generate less second harmonic photons. In this case the best pulse is able to increase the fitness by 50 percent compared to the transform-limited pulse (Fig. 6.11a). The optimal pulse is characterized with cross-correlation frequency-resolved optical gating (XFROG) as was already introduced in Sec. 3.3.2. The XFROG trace is shown in Fig. 6.11b. As one can see, from the center peak around $t=50$ fs to the second strongest peak around $t=300$ fs the frequency within the structured multi-pulse is rising. For comparison the white dashed line shows the change in momentary frequency for the up-chirped pulse (around $+1000$ fs²) from the chirp scan in Fig. 6.8. The frequency ordering of the optimal pulse and the up-chirped pulse matches and thus intrapulse dumping seems to contribute to the optimization effect by a huge amount.

6.4 Conclusion

The experiments in this chapter showed that the ketene formation after Wolff rearrangement of DNQ is very sensitive to the shape of the applied excitation laser pulses. Both the linear chirp and colored double pulse single parameter variations lead to the conclusion that the well known intrapulse dumping mechanism is responsible for the impact of the frequency ordering within the excitation pulse on the photoproduct yield. Due to the shrinking energy gap between the S_0 and S_1 states, down-chirped excitation pulses with decreasing momentary frequency efficiently dump population back to the electronic ground state, while pulses with up-chirp reduce this effect and therefore more population remains in the excited state leading to an increased product yield. Adaptive optimizations using a closed learning loop basically lead to the same result, since the optimal pulse for the maximization of the ketene yield exhibits a similar frequency ordering, where lower frequencies precede higher frequencies.

7 Catalytic surface reactions initiated by femtosecond laser pulses

For the synthesis of molecules bimolecular reactions in which two or more reactant molecules interact by e.g. collisions are necessary. The condensed phase has a high relevance for synthetic chemistry, because there, bimolecular reactions are very efficient due to the high particle density. With the advent of femtosecond laser technology, time-resolved studies of laser-induced bond cleavage within bimolecular reactions have become possible. This way to form new molecules has been investigated in the gas phase as well as in the condensed phase.

In the gas phase harpooning type bimolecular reactions, e.g. $I_2 + Xe \rightarrow I + XeI$ [32, 231] have been studied. In the group of Zewail it was even shown that it is possible to influence the reaction outcome with the help of a pump–repump scheme [32]. Also liquid phase harpooning reactions such as the formation of $XeCl$ from molecular Cl_2 dissolved in Xe [232, 233] are possible. Other reactions start from a weakly bound van-der-Waals precursor, e.g. $HI-CO_2$ in [234–237]. There a reaction is initiated by photodissociation of HI and the hydrogen atom attacks the carbon dioxide to form HO and CO . Therefore the reaction taking place is formally written as $H + CO_2 \rightarrow HO + CO$.

Another possibility is bond activation in liquid phase reactions, where after dissociation of a compound, different excited transition states can be populated and bond formation with a solvent molecule originating from the solvent shell around the dissolved compound can finally be realized [238–248].

But also initially unbound reaction partners have experimentally proven to be able to perform a photoassociation process by photoexcitation of a free-to-bound transition to e.g. induce the formation of the Hg_2 excimer from Hg atoms [249–251]. Photoassociation experiments can also be performed in cold traps employing laser-cooling techniques. Both theoretical [252–255] and first experimental studies [256–258] using shaped laser pulses in a cold trap have been performed recently.

Despite the extensive work dealing with the time-resolved observation of bond formation, optical control of bimolecular reaction products in the condensed phase could not be demonstrated yet, and there are also only very few experiments concerning quantum control of bimolecular reactions in the gas-phase such as the example from the Zewail group [32] already mentioned above. Therefore, controlling this type of reaction is generally a challenging task.

In the experiments of this and the following chapter, the approach is totally different: small molecules are adsorbed on a surface where they interact with the laser. A previously unobserved catalytic surface reaction between carbon monoxide and hydrogen induced by femtosecond lasers is reported. Previous investigations on these systems are summarized and the feasibility of these reactions is motivated in Section 7.1. The

experimental concept for the realization of such a scheme is introduced in Section 7.2. The successful demonstration of the synthesis of product molecules on a catalyst metal surface is presented in Section 7.3, and their formation is analyzed by systematically varying single parameters of the system (Section 7.4). Possible scenarios responsible for the underlying reaction mechanism are discussed in Section 7.5, and an outlook for the experimental synthesis of even larger molecules is presented in Section 7.6. At the end, the performed experiments are summarized in Section 7.7.

7.1 Catalytic reactions of hydrogen with carbon dioxide

Very soon after the availability of reliable femtosecond laser sources scientists have also employed femtosecond laser spectroscopy to explore processes on metal surfaces. Other types of lasers have been used earlier for this purpose, but starting from the first demonstration of intact desorption of NO molecules from a Pd(111) single crystal induced by femtosecond laser pulses [259], a complete new field of ultrafast laser spectroscopy on metal surfaces has emerged among the diversity of surface chemistry techniques [260–262]. Already in the first time-resolved experiments [263–265] the unique new reaction pathways accessible by the short pulses and the corresponding nonequilibrium excitation of the substrate’s electronic system became apparent and revealed that femtosecond laser desorption is not only due to a phonon-assisted heating effect.

Besides desorption experiments femtosecond lasers have soon been introduced to investigate reactions on single crystal surfaces. The most prominent among them is the oxidation of carbon monoxide in the presence of oxygen on various metal surfaces [266–268]. The pioneering work by Ertl and coworkers [268] beautifully demonstrated that femtosecond lasers can be used as a powerful tool in surface chemistry and revealed the underlying mechanism via hot substrate electrons. As the same group showed, this mechanism also accounts for the recombinative desorption of hydrogen under femtosecond laser irradiation which is clearly different from thermal excitation [269]. However, only very few surface reactions could be observed or assisted by femtosecond lasers, while complex catalytic reactions have been completely inaccessible up to now.

For this reason, we have chosen to study the reaction of hydrogen and carbon monoxide (the so-called syngas mixture) adsorbed on a single crystal metal surface with unshaped femtosecond laser pulses. Catalytic reactions from syngas to hydrocarbons have been realized under extreme conditions with both high pressures and temperatures, the most famous being the Fischer-Tropsch synthesis (see e.g. Refs. [270, 271]), in which syngas is converted to liquid hydrocarbons. Other catalytic reaction schemes towards hydrogenation of the CO instead of methanation are also known, but they likewise have the disadvantage of being high-pressure processes. A transition metal that proved to be well suited for the purpose is palladium, which is able to catalyze methanol and methane under thermodynamically favorable conditions (at a temperature of about 550 K and at pressures of several tens of bars) [272, 273]. Thus, a Pd(100) single crystal is utilized in the experiments of this chapter, which are conducted in a high vacuum chamber with pressures in the low 10^{-6} mbar regime without and up to 10^{-4} mbar with a stream of syngas. This is in contrast to the majority of surface experiments that is carried out

in the UHV regime with surfaces that are frequently cleansed, but this allows a modelation of the high-pressure experiments and enables a detection of a decent amount of molecules.

The adsorption of CO [274, 275] and of H₂ [276] on Pd(100) have been described in detail in the literature. In the first layer, CO does not decompose and adsorbs bridge-bonded with the C atom binding to the metal. If the bond is broken (e.g. by electron bombardment [274]) the remaining C atoms can stay on the surface as bulk carbon which lowers the adsorption energy for further CO adsorption [275]. H₂ already adsorbs dissociatively at very low coverages on Pd and subsequently penetrates into the bulk where it is dissolved [276]. As the maxima for thermal desorption of hydrogen and CO are 360 K [276] and 490 K [275], respectively, all experiments presented in this work have been performed at 290 K, so that adsorbed species stick well to the surface and their mobility is still quite high.

Recently, Rupprechter and coworkers [277, 278] have investigated the coadsorption of hydrogen and carbon monoxide on Pd(111) over a wide pressure range from the UHV up to the mbar regime. It has been found that high-pressure CO structures are identical to high-coverage structures in UHV at low temperature and a pressure of 1000 mbar is necessary at 300 K to saturate the crystal surface with CO. This result gives rise to two conjectures: first, although extrapolating results from UHV and low temperature studies to the experimental conditions employed in this chapter might generally be wrong, basic insights can be transferred; second, the surface is not saturated, so that higher yields might be possible under higher pressure.

Another finding in [278] has been that exposing the surface to a 1:1 mixture of syngas at temperatures above 150 K leads to an active situation in which CO replaces adsorbed hydrogen that is transferred deeper into the Pd bulk. Site-blocking, i.e. the ability of a surface adsorbate species to prevent adsorption of impinging gas molecules was also observed in either direction. Hydrogen as well as carbon monoxide may block the adsorption of the other species depending of the surface temperature. At higher pressures (up to 55 mbar in their experiments), indications for surface roughening or a dynamic and not perfectly ordered CO adsorbate structure have been found, and the authors conjecture that this may facilitate CO hydrogenation. However, despite diverse syngas mixtures, reaction products were not observed under any of the applied conditions, probably because the energy barriers are too high.

The basic idea for the experiments presented in this and the following chapter is the contemplation that the energy necessary for a reaction to overcome the energy barriers can be provided by a femtosecond laser pulse. Moreover, specially shaped laser pulses might be able to improve the result even more, or steer the reaction outcome into a desired direction. Studies by Petek and coworkers [279], and Matsumoto and coworkers [280, 281] have pointed out the possibility of quantum control of surface photochemical reactions. Matsumoto and coworkers have very recently shown that in the case of caesium adsorbed on a platinum surface, the phonons in platinum and vibrational modes of the caesium-platinum bond can be selectively excited by chirped pulses or pulse trains with varied temporal pulse separation. Hence, also the possibility of initiating and even controlling a laser-assisted surface reaction with adequate femtosecond laser pulses is very plausible.

7.2 Experimental setup

The setup used in all experiments is sketched in Fig. 7.1. The laser beam is sent through the pulse shaper, with which it can be phase modulated, as it will be done in the experiments of the following chapter. The beam is then focused by a lens with 40 cm focal length through a window into the interaction region of the TOF mass spectrometer located in the main chamber of the vacuum system (see Section 3.4.3 for details). There, it hits the Pd(100) single crystal under an angle of about 15° with respect to the surface. Only a few percent of the laser energy is employed and the intensity on the surface is about 10^{12} W/cm². The beam is reflected by the crystal and leaves the vacuum chamber again through another window.

The two employed gases H₂ and CO have been purchased with purities of at least 99.999% (Messer Griesheim) and 99.997% (Tyczka), respectively, and are used as-is. Two mass flow controllers (Advanced Energy) especially calibrated for the two gases are used to accurately dose the amount of gas that is allowed to enter the system, as is sketched in Fig. 7.1. The two gas pipes are combined in front of the nozzle through which the gas mixture enters the collateral vacuum chamber, where it hits the skimmer and results in a gas beam in the main vacuum chamber and onto the Pd(100) single crystal (diameter 10 mm, thickness 1 mm; Mateck, used as-is). The base pressure in the main chamber, without exposure to the two gases, is 10^{-6} torr, while up to 10^{-4} torr are reached with the highest gas amounts employed in the experiments.

The interaction of the femtosecond laser pulses and the surface adsorbate consisting of hydrogen and carbon monoxide leads to the formation of ions whose signal is measured, processed and subsequently recorded by a computer (for details, see Section 3.4.3).

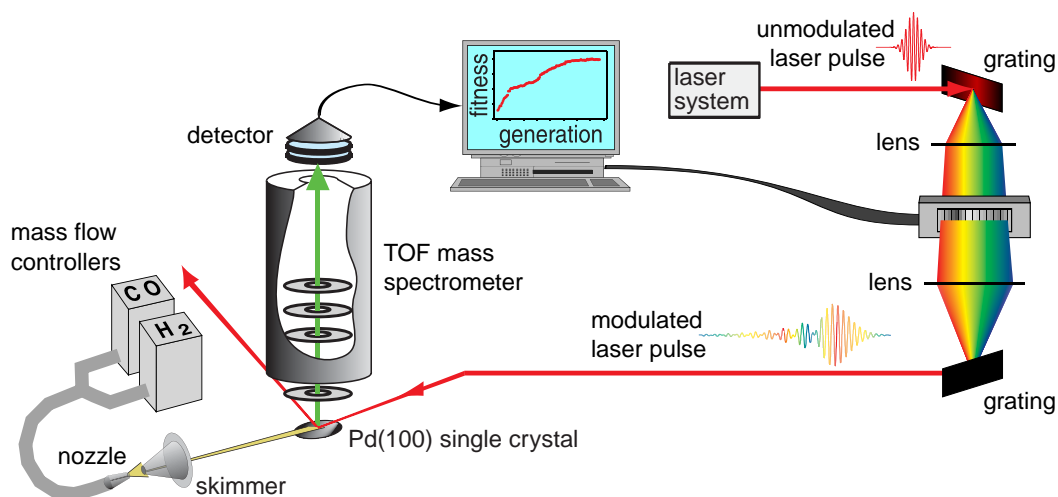


Figure 7.1: Experimental setup. The femtosecond laser pulses pass the pulse shaper before they are focused onto a Pd(100) single crystal surface located in the interaction region of a TOF mass spectrometer. The syngas mixture can be dosed with two mass flow controllers and streams via a nozzle and a skimmer onto the surface. The experimental data from the time-of-flight (TOF) mass spectrometer is measured by a computer. This signal is recorded to yield the mass spectra presented in this chapter, or it can be further used by an evolutionary algorithm to modify the pulse shapes so that eventually they are optimal for a desired task.

7.3 Study of synthesized surface reaction products

When the laser beam is not hitting the surface, no ions are produced and hence no signal is detected. Initially when the surface is exposed to laser light without syngas flow onto the surface, several ion peaks of still remaining syngas and residual gas in the vacuum chamber show up. After several minutes, an equilibrium is reached where there are practically no ion peaks left, except some very small contributions mainly of bulk hydrogen still dissolved in the metal.

When hydrogen is sent into the main vacuum chamber and onto the surface, three huge peaks arise, that can be attributed to H^+ , H_2^+ and H_3^+ , the first being the most intense and the latter being the weakest (black curve in Fig. 7.2). The triatomic hydrogen molecule is unstable in the electronic ground state, but excited and ionized states are long-lived and play an important role in molecular spectroscopy [282–287] as well as in astronomy [287, 288]. Furthermore, also reports on the successful generation of larger hydrogen species can be found in the literature, e.g. clusters up to H_{23}^+ in ion traps [286]. It has been suggested that one way for the formation of H_3^+ is the reaction between a H_2^+ molecule and H_2 adsorbed on a surface [283]. Due to this and because the electronic ground state of H_3 is unstable, one can conclude that both the surface and the laser play decisive roles during this reaction.

A totally different mass spectrum can be detected if only carbon monoxide enters the chamber. There are three peaks at masses 12, 16, and 28 amu which can be assigned to C^+ , O^+ , and CO^+ , respectively. The peak heights and the amount of gas introduced into the chamber are directly correlated, and turning off the CO supply results in the disappearance of these peaks. No other peak except a tiny contribution from bulk hydrogen is found. The signals corresponding to C^+ , O^+ , and CO^+ that originate from carbon monoxide are not present if only hydrogen is entering the chamber as was shown before (see Fig. 7.2).

Additional ion mass peaks appear when a mixture of CO and H_2 is streamed onto the surface. Not only the peaks of the respective single mass spectra change, but also new peaks arise (green to gray lines in Fig. 7.2), where the CO gas flow is set to the constant value of 4.0 sccm (standard cubic centimeters per minute), while the amount of additional hydrogen is increased from 0 to 10.0 sccm. In this measurement, depending on the hydrogen concentration, new peaks at 13, 17 and 29 amu show up first, followed by peaks at 14, 15, 18, and 19 amu. These peaks clearly indicate the formation of the ions CH^+ , CH_2^+ , CH_3^+ , OH^+ , H_2O^+ , H_3O^+ , and HCO^+ (methylidene, methylene, methyl, hydroxyl, water, hydronium, and formyl cations, respectively). As a putative methane ion with a mass of 16 amu would coincide with the O^+ peak, no statement on this molecule can be given. Furthermore a detailed analysis of the latter peak also allows the identification of a contribution of H_2CO^+ (formaldehyde cation), which is shown by an adequate modellation of this multipeak at the end of this section.

Comparison between the different mass spectra in Fig. 7.2 show that the water peak emerges at the expense of the O^+ signal and is not due to residual water. The interaction of the laser with the adsorbed gas molecules leads to the formation of hydroxyl, water, and hydronium cations. In contrast to a shrinking O^+ signal with increased hydrogen amounts, the production of methylidene, methylene, and methyl cations does not lead to

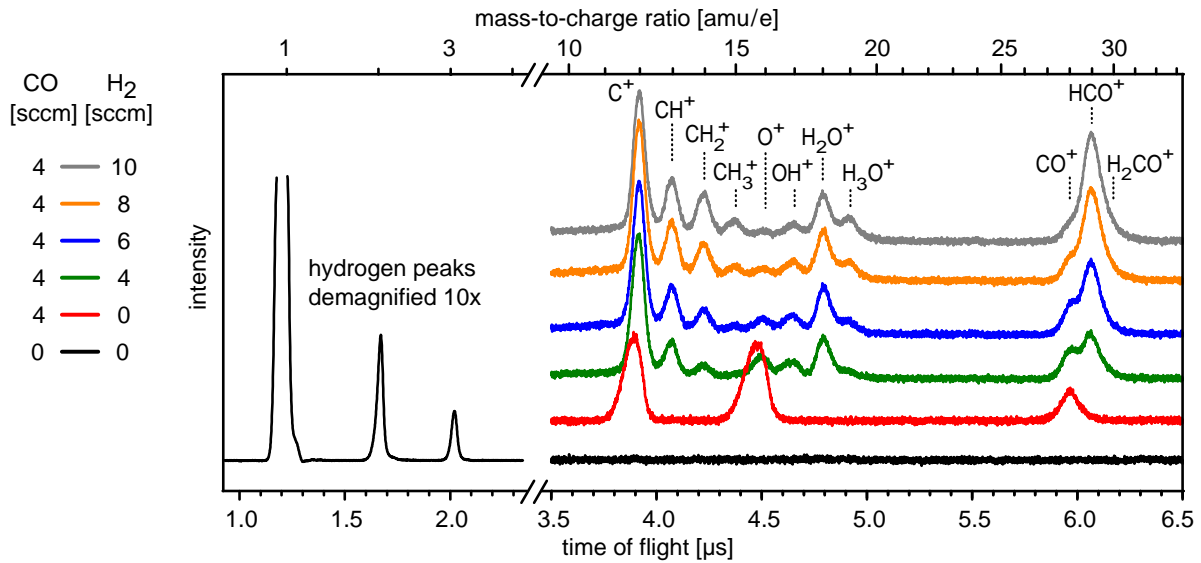


Figure 7.2: Ion spectra (vertically offset for clarity) with different amounts of carbon monoxide and hydrogen streamed onto the Pd(100) single crystal. Gas amounts are given in sccm (standard cubic centimeters per minute). Spectra with H₂ only (black), CO only (red), a stoichiometric mixture of CO and H₂ (green), and an increasing excess of H₂ (blue, orange and gray curve) are shown. For all curves except the black one, the amount of CO is held constant at 4 sccm. The signal for short flight times is just shown for the H₂-only measurement, and is demagnified by a factor of 10 to give an impression of the hydrogen ion peaks. The lower abscissa shows the time-of-flight of the ions, while the upper abscissa gives the mass-to-charge ratio m/q as determined by a mass calibration.

a decrease of the C⁺ signal, which actually grows with increasing hydrogen concentration. This behavior for C⁺ is comparable to observations by Denzler et al. [269], who found that laser desorption of D₂ from a ruthenium surface is enhanced in the presence of H₂. They attributed this effect to the faster excitation of the lighter isotope (hydrogen compared with deuterium) and the resulting impact on other adsorbed species. In our case, no deuterium is present, but the carbon monoxide is adsorbed with the carbon binding to the surface. The behavior of the C⁺ signal resembles the situation of D₂ desorption in Denzlers experiment, with the difference that the loosening of the carbon instead of the deuterium adsorption is facilitated by additional hydrogen. Thus, this observation can be interpreted as an evidence for the surface being involved in the catalytic process.

In order to explore the composition of the hydrogenated CO⁺ species emerging under hydrogen supply, a suitable data set with a relative CO to H₂ ratio of 2:1 is analyzed, which clearly shows a double peak structure and also foretells a third feature at longer time of flight. From the mass spectra in Fig. 7.2, it is already evident by eye that the peaks resemble a Gaussian shape. This is further confirmed by comparing fits assuming Gaussian and Lorentzian peak shapes, with the only restriction that the peak widths w for the three subpeaks are identical. The fit models are

$$y_0 + \sum_{i=1}^3 \frac{A_i}{w^2 + (t - t_{0i})^2} \quad (7.1)$$

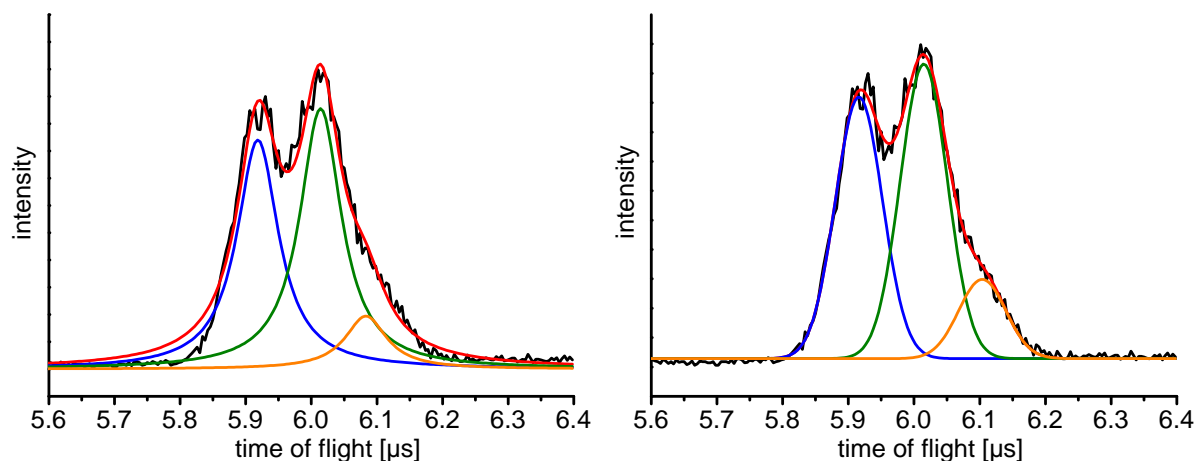


Figure 7.3: Extract from an ion spectrum with 4.0 sccm CO and 2.0 sccm H₂ streamed onto the Pd(100) single crystal. The data (black) indicates the existence of three peaks. Fitting the data under the assumption of Lorentzian (left) and Gaussian (right) peak shapes results in curves with different levels of accuracy. The best fit is shown in red, while the three contributing substructures are plotted in blue, olive and orange for clarification.

for the Lorentzian shape and

$$y_0 + \sum_{i=1}^3 A_i \exp\left(-\frac{(t - t_{0i})^2}{w^2}\right) \quad (7.2)$$

for the Gaussian shape, where t_{0i} is the central position of the i th peak, while A_i corresponds to the amplitude.

As can be seen in Fig. 7.3, using Lorentzian shapes leads to deviations at the rising edge of the feature, and the three t_{0i} do not match the mass calibration adequately. A totally different picture arises if Gaussian shapes are assumed. The agreement of the fitted curve with the data is much better, furthermore the positions of the peaks coincide very well with the mass calibration.

The problem of peak shape assignment often is of major importance in TOF mass spectrometry in order to correctly identify certain species which are not obvious at first glance. In the literature, it can be found that TOF mass peaks have approximately Gaussian appearance, while aberrations such as MCP detector ringing follow a Lorentzian distribution [289]. Thus, the modelling of the observed features in Fig. 7.3 using Gaussian-shaped peaks should reveal the contributing mass peaks correctly.

7.4 Single parameter variations

Even without the application of surface spectroscopic techniques and experiments under UHV conditions it is possible to gain basic insight into the surface reactions to some degree. Thus, in order to explore the observed chemical reactions, selected aspects of the macroscopic experimental conditions have been changed. Hence, additional information about the underlying mechanisms and the role of the reactant molecules, the metal surface, and the laser characteristics is provided.

7.4.1 Reactant molecules

When replacing the reactant gas molecules that are streamed onto the metal surface, modifications in the overall ion spectrum are expected. In a first experiment hydrogen is replaced by deuterium. Since D_2 exhibits different potential energy surfaces, adsorption properties and another surface mobility compared to H_2 differences in the measured ion spectrum are observed. In addition, the assignment of the observed product ions is verified as the heavier isotope should lead to a shifted time-of-flight of the identified ions due to the additional neutron mass.

As expected, the peaks in the ion spectrum (Fig. 7.4) are separated by two atomic mass units, so that e.g. the heavy water ion D_2O^+ appears at 20 amu instead of the position of 18 amu for H_2O^+ . It can also be deduced that the bond-forming reactions are less efficient with respect to H_2 as reactant gas, as can e.g. be seen by the weak CD_3^+ signal and the complete absence of D_2CO^+ even for the strongest D_2 excesses employed (Fig. 7.4, gray line). This behavior can be interpreted as an indication for the reduced mobility of the heavier isotope on the surface and thus reactions in which more than two particles have to be involved occur with much lower probability.

In another experiment with exchanged reactant gases, carbon monoxide is replaced by carbon dioxide. Neither C^+ , O^+ , CO^+ , nor CO_2^+ are observed for all provided amounts of CO_2 and all applied laser intensities. This confirms that CO_2 does not adsorb at all on the Pd surface at room temperature or at least not in such a way that it could be detected by laser ionization as CO , and hence reflects the importance of the surface and the adsorption process in the chemical reactions observed with carbon monoxide.

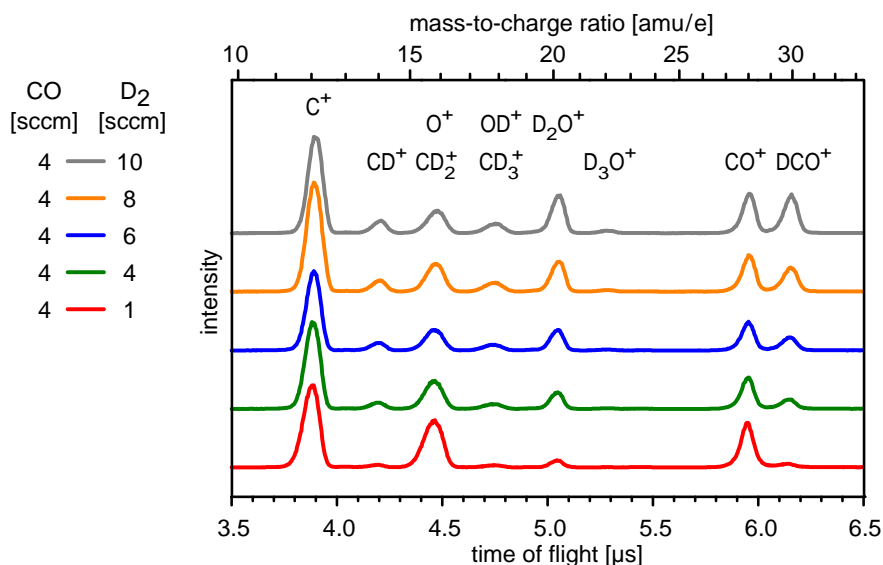


Figure 7.4: Ion spectra (vertically offset for clarity) with different amounts of carbon monoxide and deuterium streamed onto the Pd(100) single crystal. The gas amounts are given in sccm (standard cubic centimeters per minute). For all curves, the amount of CO is held constant at 4 sccm. Spectra with little D_2 (red), a stoichiometric mixture of CO and D_2 (green), and an increasing excess of D_2 (blue, orange and gray curve) are shown. The lower abscissa shows the time-of-flight of the ions, while the upper abscissa gives the mass-to-charge ratio m/q as determined by a mass calibration.

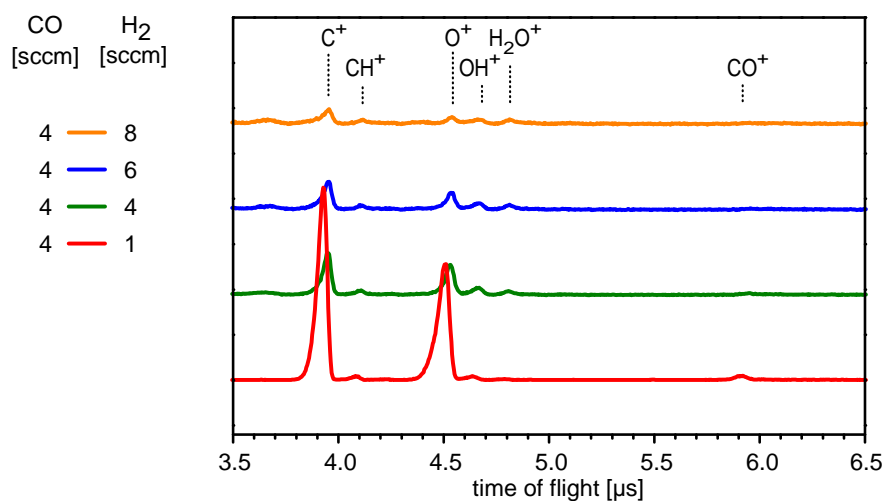


Figure 7.5: Ion spectra (vertically offset for clarity) with different amounts of carbon monoxide and hydrogen streamed onto a Pt(100) single crystal. Gas amounts are given in units of sccm (standard cubic centimeters per minute). For all curves, the amount of CO is held constant at 4 sccm. Mass spectra with little H₂ (red), a stoichiometric mixture of CO and H₂ (green), and an increasing excess of H₂ (blue and orange curve) are shown.

7.4.2 Catalyst metal

The influence of the metal surface on the observed ion signals is further studied by exchanging the Pd(100) single crystal with a Pt(100) single crystal. The platinum crystal has the same dimensions as the palladium crystal and is mounted at the same position in the chamber, while no other condition is changed relative to the experiments from Sec. 7.3.

With the platinum surface, the total ion signal observable is lower by almost an order of magnitude compared to the palladium surface, but the recorded ion spectra (Fig. 7.5) clearly exhibit the non-hydrogenated peaks C⁺, O⁺, and (only very weakly) CO⁺. Moreover, also additional weak product peaks are observable, namely CH⁺, OH⁺, and H₂O⁺, but neither ions are detected which bear three hydrogen atoms, nor those corresponding to a hydrogenated form of non-dissociated CO. This is a pronounced difference compared to the experiment where the palladium surface is employed.

Further differences with respect to the experiments on the palladium surface have attracted attention, for instance an asymmetric peak shape and an overall increase in background noise. Most remarkable, the complete ion spectrum is decreasing when more hydrogen is added to the gas beam. This could be an indication that CO adsorption on the platinum surface is inhibited by excessive hydrogen amounts and hence, the reaction proceeds even less efficiently. Site-blocking effects like this are not unusual and have been observed in surface experiments before [278]. The experiments with a platinum surface therefore demonstrate that the surface material plays an important role in the reaction mechanism, which leads to increased reaction product formation in case of a palladium surface.

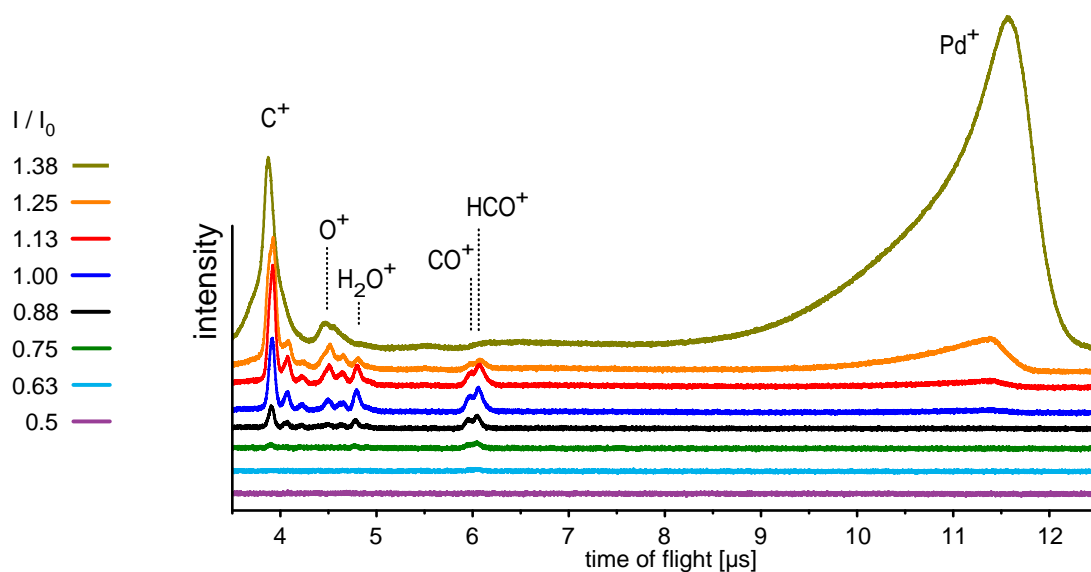


Figure 7.6: Ion spectra (vertically offset for clarity) with both 4 sccm carbon monoxide and 4 sccm hydrogen streamed onto a Pd(100) single crystal as a function of laser intensity. The effect is highly nonlinear, and too high intensities lead to the formation of palladium ions which both impede the formation of product ions and obscure their detection.

7.4.3 Laser properties

Laser intensity

It has been found that the overall ion spectrum is very sensitive to the laser intensity, which is explained by the high nonlinearity of the laser-induced process. According to reference data [290], for the observed ions in the time of flight mass spectra, if created from isolated neutral species with the same nuclear composition, energies in the range of 8–14 eV are necessary. Thus, with the employed laser wavelength (800 nm = 1.55 eV) they could all be created by absorption of six to nine photons. In this estimate the influence of the surface, the reaction step and the desorption is not even included. Loy and coworkers [291] have shown that femtosecond laser desorption (not ionization) of CO from Pt(111) surfaces also already necessitates eight photons.

In the experiments shown here, the analysis of recorded ion spectra for different intensities has given an estimate for the intensity dependence of about nine photons. However, this dependence cannot be determined easily. In Fig. 7.6 the change of the spectrum is shown as a function of intensity, which provides an indication of how the ion spectrum changes with intensity. The intensity values are normalized to the intensity I_0 with which the spectra of Fig. 7.2 have been recorded. A reasonable time of flight mass spectrum can only be recorded in a relatively small intensity interval. While reducing the laser power by a factor of two makes the ion spectrum practically disappear because too few ions are produced, an increase very soon leads to too high laser powers which can even lead to surface ablation and causes the creation of palladium ions. The assignment of the huge peak arising at high intensities to palladium is not only confirmed by the mass calibration, but also by the corresponding experiments with the platinum surface, where also platinum ions can be formed. The Pt^+ ions have a longer time-of-flight due to the

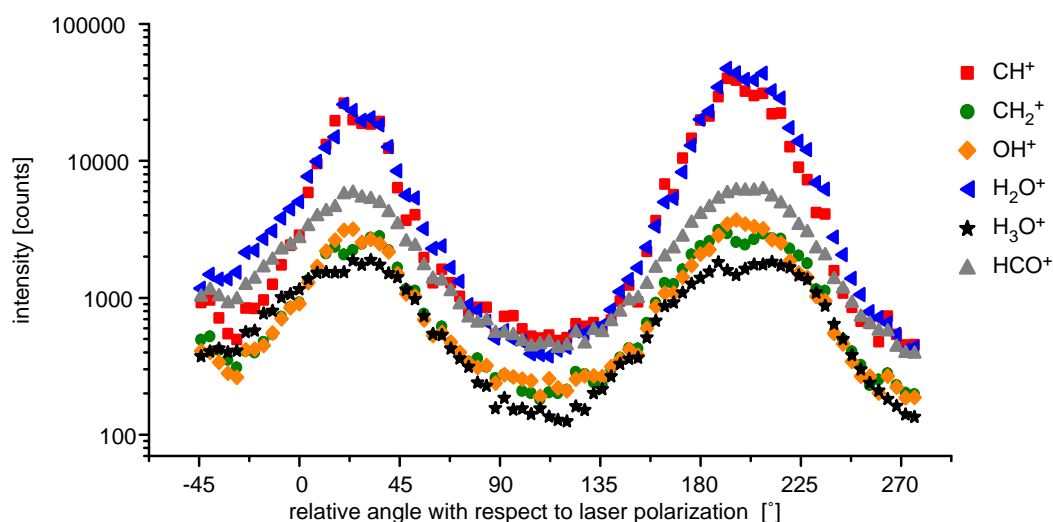


Figure 7.7: Integrated signal of the product peaks as a function of linear polarization. 0° corresponds to vertical laser polarization at the mirror in front of the vacuum chamber. Due to the relative geometry of the laser beam and the Pd surface, the maximum of the signal is not at 0° , but rather at polarization angles where the p -polarization component at the palladium surface is maximal. Note the logarithmic ordinate.

larger atomic mass (195 amu for Pt compared to 106 amu for Pd). The asymmetric shape of the palladium peak can at least partially be related to the fact that five stable isotopes exist whose probability distribution is similar to the peak shape. For very high intensities, however, other effects like space charge lead to a severely deformed ion spectrum. While the main ion peaks are deformed, it is interesting to note that also the formation of products apparently is impeded when palladium ions are produced.

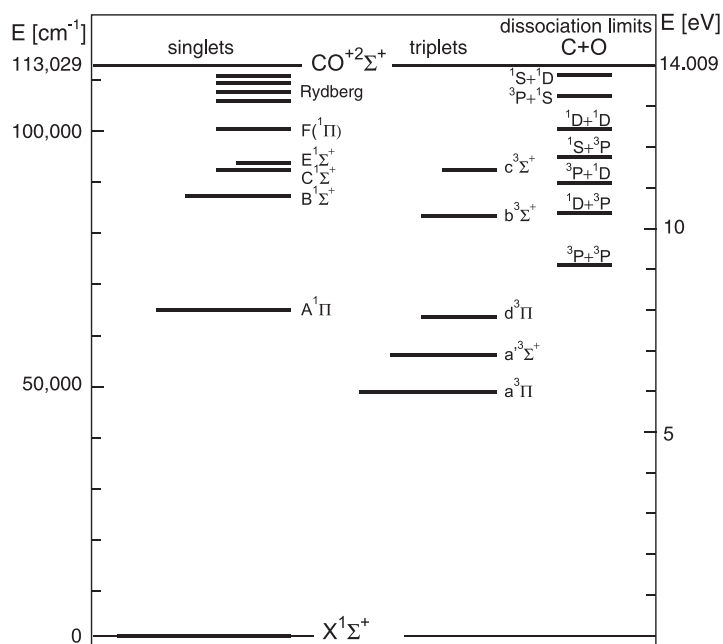
Laser polarization

The polarization of the laser beam irradiated on the metal surface also has been proven to be a very critical property for the signal magnitude of the experiment. This is in accordance with observed polarization sensitivities in laser surface spectroscopy [260]. When the component of the laser polarization parallel to the surface normal is maximal, i.e. at p -polarization relative to the surface, the recorded signal for all ion peaks is maximal. According to our observation, utilizing s -polarized light leads to a signal decrease of two orders of magnitude (Fig. 7.7) for all peaks.

Laser wavelength

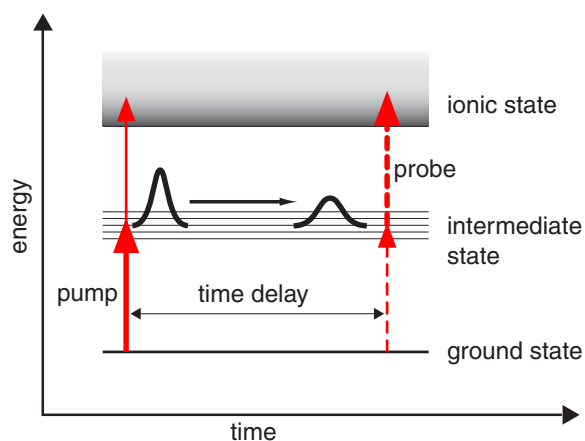
In a subsequent experiment, the excitation wavelength was changed to 400 nm by frequency-doubling of the fundamental using a SHG crystal. A filter that is transmittive only for 400 nm is placed in front of the vacuum chamber. In principle one could expect that the signal magnitude should increase because less photons are formally necessary for the reaction, since the signal exhibits a highly nonlinear dependence on the incoming laser fluence. However, no ion peaks could be observed at all with pulse wavelength centered around 400 nm at comparable fluence and with all possible linear laser polarizations.

Figure 7.8: Energy level diagram of the carbon monoxide molecule, adapted from Ref. [292] (see there for a detailed discussion).



A possible explanation for this finding could be that a resonance at odd multiples of 800 nm is involved in the reaction process. This could be the reason why no ion signal at all was detected with the second-harmonic. The energy level diagram of carbon monoxide in the gas phase is depicted in Fig. 7.8. It shows that from the ground state a resonance is not directly accessible for both 800 nm or 400 nm pulses. While for the lowest singlet resonance (≈ 8 eV) from the ground state five 800 nm (5×1.55 eV = 7.75 eV) photons would be the closest possible transition, the energy discrepancy with 400 nm (3.1 eV) laser pulses is much larger. This implies that the lowest singlet transition might be of relevance in the multiphoton ionization of the CO molecule in the performed experiments. What also has to be taken into account is the fact that the surface influences the energy levels and the selection rules for the adsorbed CO compared to isolated CO molecules in the gas-phase. It is thus possible that the levels are shifted further towards

Figure 7.9: Sketch of the pump-probe scheme. The energies of the pump (solid red arrows) and the probe (dashed red arrows) pulse are adjusted so that no ions are generated in the absence of the other pulse, i.e. the major contribution to the signal is given by a combined pathway indicated by the thick red arrows. If the intermediate state is accessed by the pump pulse, the probe pulse can subsequently ionize the species. The sketched wave packets indicate the temporal evolution of the intermediate state after the initial excitation.



energies in resonance with an odd multiple of 800 nm photons.

An energetic shift could also be caused by field enhancement or Stark shifting. This effect has already been exploited in gas-phase experiments in order to manipulate the outcome of a reaction [293, 294]. This would be in agreement with the optimization results in Fig. 8.6, where a decrease of the optimization effect is observed upon variation of the laser intensity. The field strength and therefore the energetic shift might have been adjusted in such a way that the desired reaction is supported.

7.4.4 Pump-Probe spectroscopy

In order to further study the catalytic process, pump-probe experiments with two identical pulses at a central wavelength of 800 nm have been performed. The two pulse replicas are generated in a Mach-Zehnder type interferometer where a computer-controlled delay stage is introduced into one arm to allow for variation of the relative time delay between them. No signal could be measured with the two beams polarized perpendicularly, so that the experiments were done with identical polarizations.

The pump-probe scheme is shown in Fig. 7.9. The intensities of the two employed laser pulses are adjusted so that none of them generates ions apart from hydrogen in

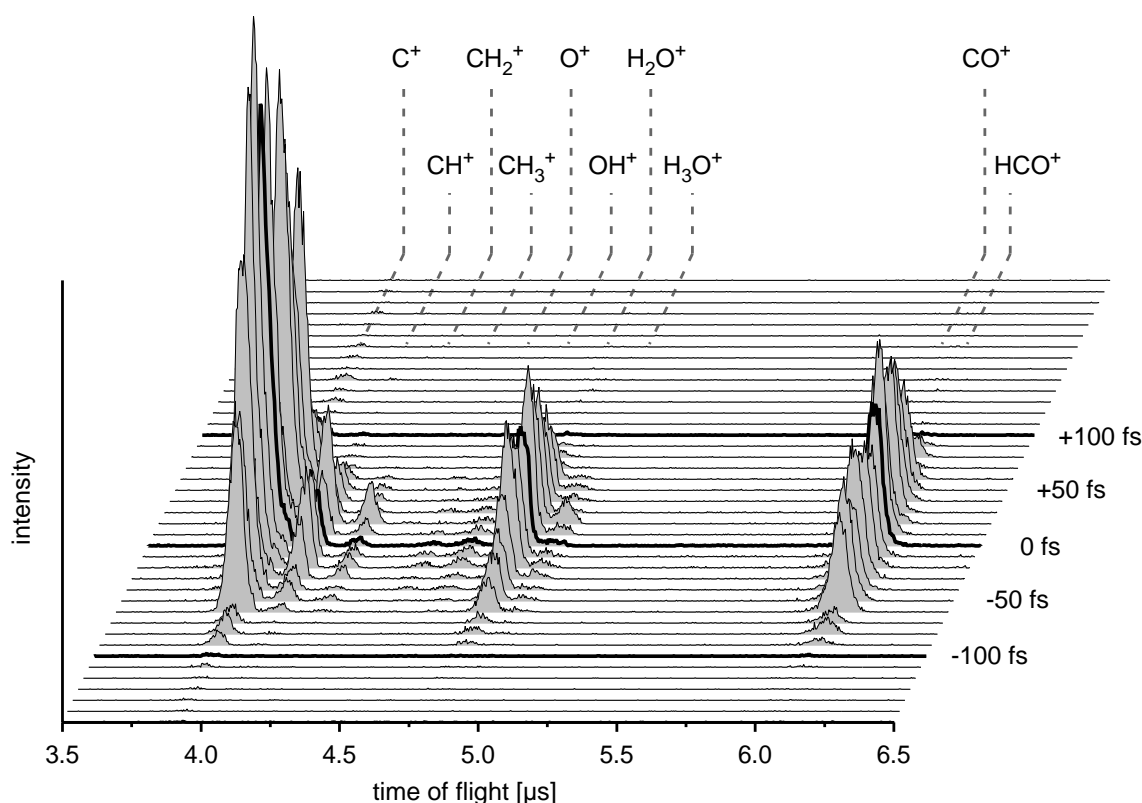


Figure 7.10: Ion spectra obtained with the Pd(100) surface for a 1:1 mixture of CO and H₂ as a function of the pump-probe delay between two identical 800 nm pulses. The ion species corresponding to the peaks are indicated, grey dotted lines are drawn to guide the eye.

the absence of the other pulse. This means that the pump pulse (indicated by the solid red arrows in Fig. 7.9) or the probe pulse (indicated by the dashed red arrows in Fig. 7.9) alone are not sufficient to ionize the respective molecular species on the surface. However, if one pulse initiates an excitation or reaction in or on the surface without creating ions, i.e. an intermediate state is accessed, which lasts clearly longer than the pulse duration, then a subsequent pulse should be able to "complete" this reaction and ionize the species, thus leading to a transient behavior. This is visualized in Fig. 7.9 by an excitation to the intermediate state with the pump pulse (thick solid red arrow), which evolves in time (indicated by a spreading wave packet) and is finally ionized by the time delayed probe pulse (thick dashed red arrow).

The results of the pump-probe experiment depicted in Fig. 7.10 indicate that the transient behavior of all species occurs on a very short timescale, which is on the order of 100 fs. This is comparable to the FWHM of the cross-correlation of the two pulses. Although some differences are present, the most pronounced being the different rise behavior of the peaks a real transient behavior can not be observed. The H_2O^+ peak for instance rises more slowly between -100 fs and -20 fs than the HCO^+ peak does, whose signal level stays almost constant between -60 fs and +60 fs. Also the dip around a time delay of 0 fs, as in the H_2O^+ peak and other product peaks is not present in all the ion signals (see e.g. the C^+ peak).

The relative ratio of the peaks does not change by a large factor for different pump-probe delay times. Consequently neither an intensity variation nor a certain time delay between two unmodulated pulses are suitable methods to drastically increase a desired signal in comparison to another.

7.5 Discussion of the reaction mechanism

For catalytic reactions on metal surfaces the revelation of the underlying reaction steps and microscopic mechanisms is not an easy task. Although numerous studies on many different systems have been performed with a multitude of experimental techniques it is still a long way to a complete understanding of surface catalysis. For instance, the actual mechanisms behind the Fischer-Tropsch synthesis, the production of liquid hydrocarbons from hydrogen and carbon monoxide are still subject to a vital discussion [271]. This is mainly due to the multitude of involved reaction stages. However it is not impossible to shed light on catalytic surface processes, as the studies by Gerhard Ertl of fundamental molecular processes at the gas-solid interface has shown for which he was awarded the Nobel Prize in chemistry in 2007 [295]. Among other important discoveries, he was able to elucidate the molecular mechanism of the catalytic reaction in the Haber-Bosch process, i.e. the production of ammonia from nitrogen and hydrogen utilizing suitable iron catalysts [296].

In the experiments presented in this chapter, the complete reaction process starting from the reactant gases in the gas phase comprises adsorption and dissociation, diffusion of the adsorbate on the surface, the actual reaction steps, desorption, ionization, possibly fragmentation, and maybe even more steps. Moreover, the influence of the metal surface, i.e. its electronic and structural properties, but also impurities and other adsorbates

which can both poison and promote [261, 297, 298] the catalytic qualities by raising or lowering energy barriers have to be taken into account. However, in our case it is hard to determine the impact of these parameters since the surface is neither sputtered nor cleansed, and the pressure is higher than in conventional surface experiments.

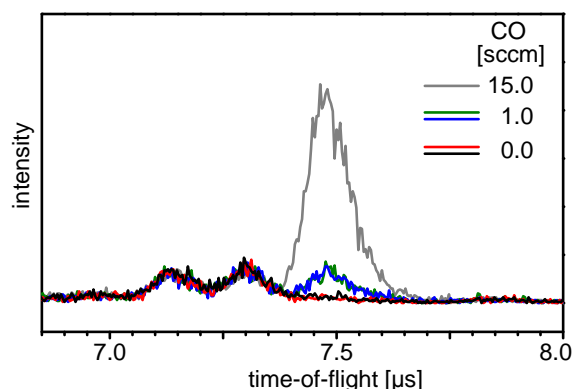
Although a detailed microscopic characterization with surface science techniques was not possible, some of our experiments can provide important insights into the laser-induced catalytic surface reactions. The experiments with the substitute gas carbon dioxide and the substitute surface platinum have revealed that the surface is important for the reaction and that carbon monoxide adsorption is a prerequisite for the reaction. Hydrogen adsorption also plays a decisive role, as is evident from the formation of H_3^+ , which may be formed in a surface reaction between different hydrogen species [283]. Also, since the mean free path of the gas particles is on the order of meters at the employed pressures [299], a pure gas phase reaction of hydrogen molecules is not very likely. However, it is very well possible that gas-phase reactants are involved in the reaction as well.

In surface chemistry, two basic reaction types can be distinguished. On the one hand a reaction can include the interaction between two species both adsorbed on the surface (Langmuir-Hinshelwood process), while on the other hand direct interactions of gas-phase particles with the adsorbate (Eley-Rideal process) [261] can be responsible for the reaction. An additional scenario, where a surface-bound species that has not yet thermally accommodated reacts with a neighboring adsorbate atom or molecule prior to thermalization what has been termed “hot-atom chemistry” [300] is also possible. Experiments where a beam of neutral hydrogen atoms, generated by dissociation of H_2 on a hot tungsten filament, is impinged on a surface with adsorbed alkenes or halogen atoms were performed. It was demonstrated that the hydrogen forms a bond with the adsorbate [300–303]. These studies indicate that both Langmuir-Hinshelwood and Eley-Rideal processes are possible and do not exclude each other [302, 303].

Under the conditions (pressure and temperature) of the experiments presented in this chapter, none of the above introduced processes occurs when no laser beam is hitting the surface. No evidence for a surface reaction of adsorbed carbon monoxide and hydrogen was found in the literature. One example is the study of Rupprechter and coworkers [277, 278], who have investigated the coadsorption of hydrogen and carbon monoxide on a palladium surface and did not detect any reaction products. When the laser beam hits the surface, however, energy is provided and non-equilibrium conditions are initiated. Probably reactive species like energetic H atoms, and also other hydrogen species like H_3^+ , are created. Thus, a similar reaction mechanism as in the experiments discussed in the previous paragraph, might play a role. The observation that for Eley-Rideal-type hydrogenation processes the surface structure may be of minor importance [261] supports this conjecture, since the experiments presented here are performed under high-vacuum conditions where the adsorbate is not a well defined monolayer.

In addition to the possibility that the reaction is induced by reactive hydrogen species, excitations of substrate electrons and phonons might also be involved. Ertl and coworkers [268] investigated the oxidation of CO to CO_2 on a ruthenium surface which is covered with oxygen and carbon monoxide with femtosecond laser pulses. Photoexcitation leads to hot substrate electrons that are initiating the oxidation reaction by electron transfer

Figure 7.11: Extract of ion spectra when only CO amounts of 0, 1, and 15 sccm are streamed onto the Pd(100) surface. The peak at $\approx 7.5 \mu\text{s}$ is attributed to the formation of CO_2 . The two peaks on the left side are due to an electronic disturb signal and do neither scale with the light intensity nor with the gas concentrations. Measurements are taken at a surface temperature of 225 K (peak is also present at room temperature) and with increased integration time.



to the adsorbed oxygen. The hot electron mediated oxidation reaction occurs on a sub-picosecond time scale, whereas desorption of carbon monoxide caused by coupling to the phonon bath of the substrate metal is happening on a slower time scale. Therefore, chemical activation of adsorbates by hot substrate electrons represents a new reaction pathway which is not accessible by heating. Thus, the pump-probe experiments of Sec. 7.4.4 indicate that a phonon-mediated heating process (lasting typically tens of ps) cannot be responsible for the observed product ions, but possibly electronic excitations of the adsorbate. The question if a photoinduced hot electron distribution in the substrate metal is part of the reaction mechanism is discussed in the following.

Evidence that this mechanism might be involved in the experiments discussed here is presented in Fig. 7.11. When only carbon monoxide is streamed onto the surface, a very weak ion peak at an ion mass of 44 amu is observed. As the peak scales with the employed CO concentrations, it is concluded that it can be assigned to the formation of CO_2 . The CO_2 may be formed by the same mechanism as in the experiments of Ertl and coworkers, with the difference that the oxygen is originating from laser-induced dissociation of CO. This peak disappears when the surface is also exposed to hydrogen or deuterium. Under these conditions hydrogenation reactions are obviously dominant.

The observation in the experiments with 400 nm pulses (Sec. 7.4.3) that no product ions are formed seems to indicate that a reaction mechanism involving hot electrons can be excluded. Usually, such a hot electron mediated mechanism is thought to be independent of the photon energy, because femtochemistry is assumed to be induced by a thermalized electron distribution [304]. Therefore, our observation could indicate the absence of such a mechanism. However, if higher lying electronic resonances of the adsorbate play an important role for the reaction there should be a dependence on the photon energy. This dependence could then arise from not yet thermalized hot electrons (thermalization usually on a 100 fs time scale [304]). But then a higher photon energy should lead to an increased product yield and not to less yield as our experiment shows. Another possibility is of course that direct optical excitation of the adsorbate is involved. Since in our experiment the formed reaction products have to be ionized in order to be detected, the already in Sec. 7.4.3 discussed importance of a resonance in the multiphoton ionization process may also play an important role. Therefore, the possible wavelength dependence due to multiphoton ionization might be dominant and mask

other wavelength dependent processes in the earlier reaction steps. As a consequence, a hot electron induced reaction cannot be absolutely excluded based on the dependence of the excitation photon energy.

In principle it is also possible that larger molecules are formed on the surface which are fragmented by the femtosecond laser pulses. Thus, they could represent a precursor for some of the product ions we observe. However, no clear evidence for or against this mechanism was found. Since the formed molecules have to be ionized in order to be detected by time-of-flight mass spectrometry, high laser intensities are necessary which could also lead to dissociation of a larger precursor. On the other hand, the laser energy is needed for the bond formation to overcome energy barriers. In our experiments we varied the laser intensity over a wide range, from low intensities (no product ions detected) to high intensities (metal ablation). At neither of the employed intensities we saw product ions arising from carbon monoxide and hydrogen larger than H_2CO^+ . In addition it is also difficult to predict if the conditions on the surface (e.g. temperature) are well suited for the formation of larger molecules. They might not be stable on the surface, like other experiments, in which molecules brought on a metal surface immediately break apart (dissociative chemisorption), are showing [305].

7.6 Towards larger molecules

The successful generation of hydrogenated species like formyl and formaldehyde from H_2 and CO on a metal surface might be a first step towards new reaction schemes leading to the production of more complex and larger molecules. The synthesis of methanol from syngas for instance is feasible by using a palladium catalyst in an appropriate temperature and pressure regime [272]. Very often in surface science decomposition reactions of larger molecules during adsorption are studied to gain insights from the "reverse reaction" about the respective product formation reactions. This has been done for instance for methanol and for aldehydes adsorbed on palladium. In contrast to carbon monoxide, where a bond between the carbon and palladium is formed, methanol adsorbs on Pd(111) with the oxygen towards the palladium surface [306–308] and decomposition leads to CH_3O surface species and subsequent formation of CH_3 , C and H_2 . Nevertheless, methanol synthesis might be possible, as with the formation of formyl and formaldehyde in our experiments it has been shown that the C-O bond is activated and the molecule still has binding points available for additional hydrogen. A problem for the detection of methanol under the current experimental conditions might be the fact that methanol on Pd(100) starts to decompose to CO and H_2 [306, 307] already at 180 K. For formaldehyde on a Pd(111) surface at 170 K several processes have been observed [309]. Decomposition to carbon monoxide and hydrogen as well as molecular adsorption occurs. In addition paraformaldehyde $((\text{H}_2\text{CO})_n)$ is formed through polymerization at the surface if the temperature stays below ≈ 250 K. An intermediate formyl species during formaldehyde decomposition possibly initiates the polymerization reaction. Since these formyl species are also present in our experiments as reaction products, a polymerization reaction could be started from syngas at lower surface temperatures.

The group of H. L. Dai showed that laser radiation can be employed to initiate poly-

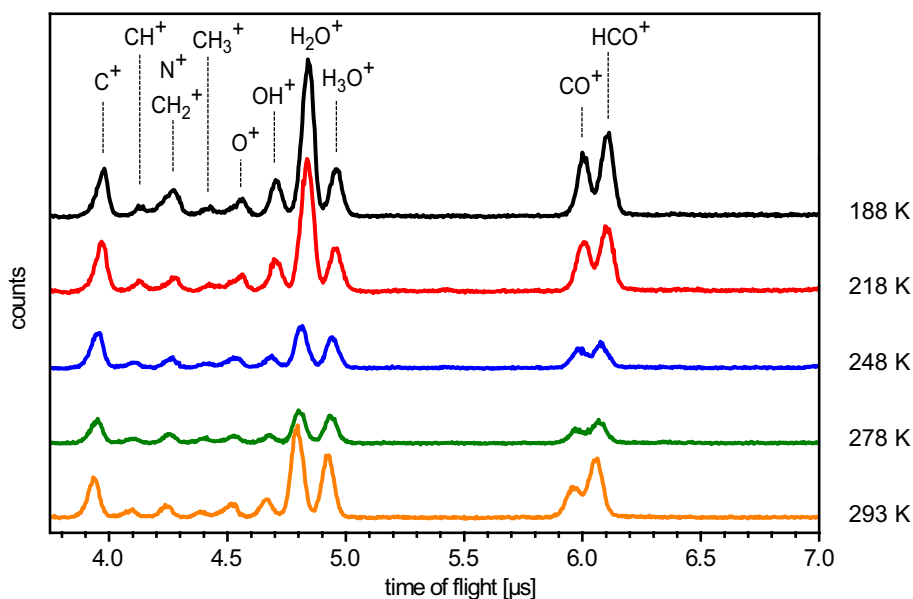
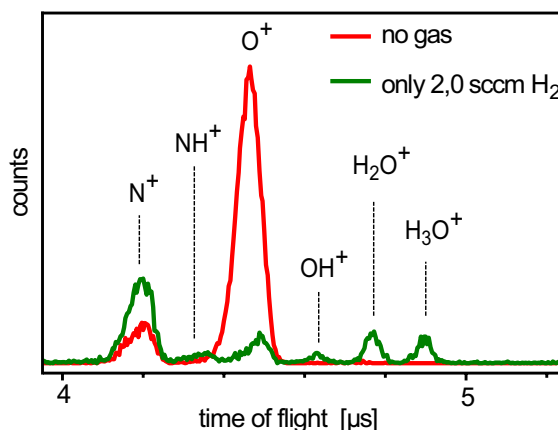


Figure 7.12: Variation of the Pd(100) surface temperature. The employed gas amounts were 4.0 sccm CO and 1.0 sccm H₂. The surface temperature was decreased from room temperature to 188 K.

merization reactions on surfaces [260, 310, 311]. When formaldehyde on Ag(111) single crystal surfaces is irradiated with UV laser light the product polyoxymethylene could only be synthesized when the temperature of the surface was chosen appropriately due to the nature of the reaction steps involved. It was found that polymerization works best in a certain temperature interval. The surface temperature must not be too low to be able to overcome thermal reaction barriers in the course of the reaction and at higher temperatures almost all species desorb (e.g. formaldehyde at 110 K, CO already at 52 K and polyoxymethylene desorbs and decomposes at 210 K) and thus no reaction occurs.

This has been the motivation for us to explore whether similar processes can also be induced by starting from syngas mixtures and applying femtosecond laser pulses at temperatures lower than room temperature. For this experiment the cryostatic cooling device (see Section 3.4.3) that is connected to the sample holder was used. The metal surface can be cooled down to about 150 K, and the surface temperature is measured by a type K thermocouple that is attached to the back side of the metal substrate. A measurement where the Pd(100) surface is exposed to 4.0 sccm CO and 1.0 sccm H₂ is depicted in Fig. 7.12. When the temperature is decreased from room temperature (293 K) down to 188 K, the ion spectra change slightly. Unfortunately, for all employed gas amounts in the entire accessible temperature range evidence of a polymerization reaction leading to larger molecules than HCO⁺ was not found. However, some changes compared to the room temperature spectra could be observed. During the decrease of the temperature the overall ion signal is decreasing and increasing again from 218 K on. At the lowest temperature (188 K) the water peak is dominating and a contribution at 14 amu from N⁺ could be identified. This is further confirmed by disconnecting the gas supply where even after very long irradiation time contributions from residual gas were

Figure 7.13: Time of flight mass spectra at 150 K on the Pd(100) surface. Without supply of gas (red curve) only contributions from N^+ and O^+ originating from adsorbed residual gas are present. The addition of hydrogen only leads to the formation of NH^+ and hydrogenated oxygen species.



still present. This is shown in Fig. 7.13 (red curve). Besides the peak at 14 amu another mass peak at 16 amu assigned to N^+ and O^+ respectively are observed. Our explanation is that residual gas adsorption must be strongly enhanced by decreasing the surface temperature. When the surface is exposed to hydrogen alone (1.0 sccm) in the presence of the residual gas adsorbate on the surface, new surface species can be synthesized as the green curve in Fig. 7.13 indicates. At 15 amu a peak is clearly showing up while the peak at 14 amu corresponding to N^+ is decreasing. Since no carbon monoxide is added it can only originate from NH^+ . In addition hydrogenated oxygen species are also observed.

7.7 Conclusion

The experiments demonstrate the feasibility of laser-induced catalytic reactions of carbon monoxide and hydrogen on a Pd single crystal surface at room temperature and under high vacuum conditions. Several product molecules have been synthesized, among them also species (e.g. CH_3^+) for whose formation three particles are involved. The results show that the interaction of the surface, its adsorbate and the femtosecond laser occurs on an ultrafast timescale and is sensitive to the incident laser polarization.

Additional experiments using different reactant gas species and concentrations, two different single-crystal surfaces, and laser beams with varying characteristics have helped to reveal certain aspects of the surface reaction and have confirmed that the properties of the metal substrate are important for an efficient reaction.

However, many other aspects have not been resolved or could not be considered. Experiments in an ultrahigh vacuum (UHV) using conventional surface spectroscopic techniques might provide additional insights. Further analysis is needed to clarify the mechanism and the intermediate steps involved in the observed reactions. Surface science offers a multitude of surface analytical techniques for this purpose [260, 261].

Another approach for further insight into the reaction is shown in the next chapter. There, femtosecond pulse shaping and quantum control techniques are used to further explore the underlying processes.

8 Adaptive quantum control of catalytic surface reactions

Adaptive femtosecond quantum control has become a very successful experimental technique in physics, chemistry and biology. It was shown that ionization and fragmentation reactions in the gas phase, and also condensed-phase processes could be manipulated by shaped femtosecond laser pulses, as was already summarized in Section 2.1.2. However, in the control experiments so far the atomic composition of the molecular system under study either did not change or it dissociated into fragments. The selective formation of molecular bonds with shaped femtosecond laser pulses has not been demonstrated up to now. The femtosecond laser-induced catalytic surface reactions introduced in the previous chapter, allow to investigate this possibility for the first time.

A first adaptive quantum control experiment, presented in Section 8.1 is performed in the absence of hydrogen, where the formation of ions from dissociated carbon monoxide is suppressed with respect to the formation of intact carbon monoxide ions. In the next step, competing bond-forming reaction channels in the catalytic reaction of carbon monoxide with hydrogen (Section 8.2) and with deuterium (Section 8.3) are successfully controlled by a closed-loop optimization. Using quantum control techniques, the surface reaction mechanism is analyzed with respect to the adsorbate composition in Section 8.4, and Section 8.5 provides a brief summary of the quantum control experiments of catalytic surface reactions.

8.1 Reduction of carbon monoxide dissociation

In order to explore if the laser-induced catalytic surface reactions of CO and H₂ can be steered in a desired direction, experiments with phase-shaped femtosecond laser pulses optimized in a closed learning loop are performed. For the experimental scheme of Fig. 7.1 this means that the computer is controlling an evolutionary algorithm (Section 3.5) to process the experimental data in order to find optimal pulse shapes for a given reaction. An SHG optimization is conducted before each of the optimizations presented in the following to make sure that an optimally compressed pulse is obtained. Thus the optimization results are compared to the impact of a transform-limited pulse. In the experiments presented in this chapter the employment of a discriminator [see Eq. (6.22)] is also necessary to avoid too small signal amplitudes in numerator and denominator in a ratio optimization (see discussion in Section 6.3). Consequently pulse shapes causing too little signal are rejected in the course of an optimization.

A first question of interest is whether the dissociation of CO on the surface due to interaction with shaped femtosecond laser pulses can be controlled. In a first optimization

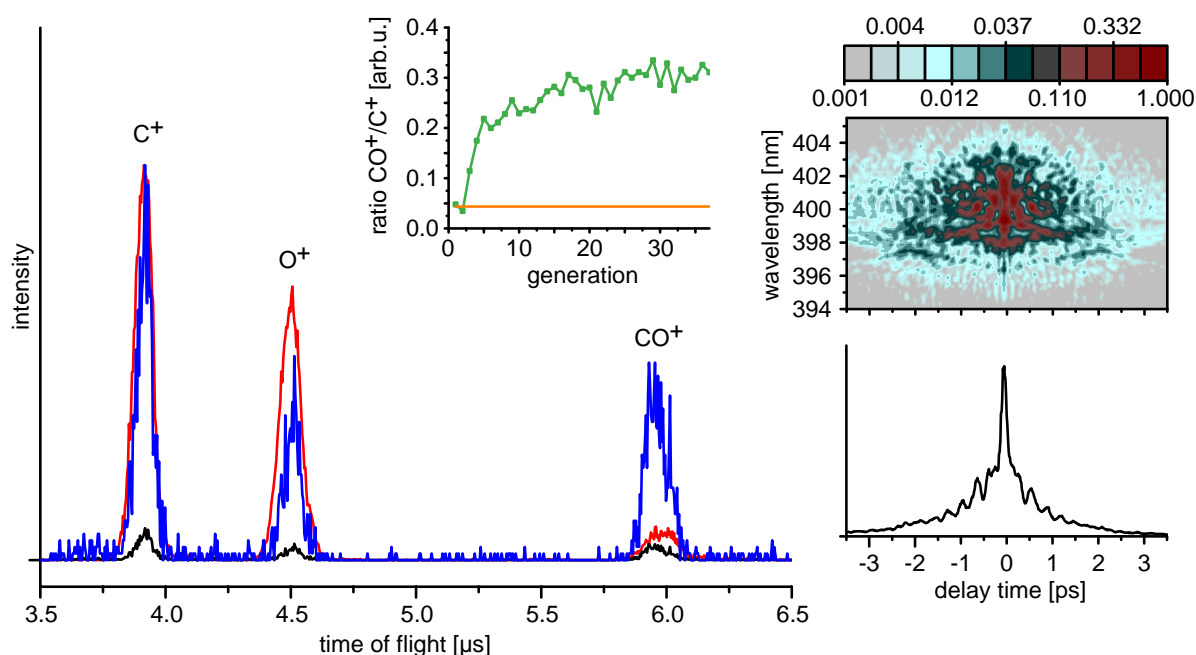


Figure 8.1: Ion spectra for the maximization of the ratio CO^+/C^+ with 4.0 sccm CO and no H_2 , obtained with the unmodulated pulse (red curve) and the optimal pulse (black curve). For comparison, the blue curve shows the latter ion spectrum rescaled by a factor such that the C^+ -peaks for unmodulated and optimal pulse match. The green curve in the inset shows the development of the fitness (the average of the ten best individuals per generation), while the signal level of the unmodulated pulse is indicated by an orange line for comparison. The two graphs on the right show the SHG-FROG trace (logarithmic color code) and autocorrelation of the optimal pulse.

experiment, the control goal (fitness function) is the maximization of the ratio CO^+/C^+ when the Pd(100) surface is exposed to CO alone. The optimization experiments clearly show that the ratio can be reproducibly enhanced by a factor of about 5 with respect to the ratio obtained with a transform-limited pulse (Fig. 8.1). However, the absolute yield for both C^+ as well as CO^+ is reduced due to the lower peak intensity of the shaped pulse. The SHG-FROG trace displayed on the right hand side of Fig. 8.1 together with the intensity autocorrelation indicates a multiple pulse structure where the central peak is dominant. Although the shape of the optimal pulse is rather complex leading to strongly reduced peak intensity, it is remarkable that ion spectra can still be recorded considering the high nonlinearity of the process.

The ionization potentials of the isolated gas-phase species do not exhibit a strong difference. While for the ionization of CO 14.0 eV are necessary, the corresponding value for C is only 11.3 eV [290]. Thus one can conclude that enhancement is not only due to an intensity effect controlling the ionization process. The optimized pulse shape must exploit a combined mechanism possibly including all involved processes, i.e.

dissociation, desorption, ionization and also the presence of the substrate might play a role. When the palladium surface is exposed to H_2 in addition to CO , the optimal pulse also leads to enhancement of the CH_2^+/C^+ and HCO^+/C^+ ratios (see Section 8.4).

8.2 Control of competing bond-forming reaction channels

In the next step the manipulation of reactions leading to hydrogenated species by suitably shaped femtosecond laser pulses was investigated. A 1:1 mixture of both gases CO and H_2 is streamed on the palladium surface to explore whether the evolutionary algorithm is able to find a pulse shape that influences the C-H bond formation. Thus, the goal of the experiment is to maximize CH^+ versus C^+ . Enhancement of about 100% compared with the unmodulated femtosecond laser pulse is achieved with the optimal pulse, as can be seen in Fig. 8.2. In addition, the CH_2^+/C^+ ratio is increased as well by about the same amount. A very surprising feature is the strong reduction of H_2O^+ formation with the optimal laser pulse. Single parameter variation however, e.g. variation of the laser intensity and recording the associated ion spectra with unshaped femtosec-

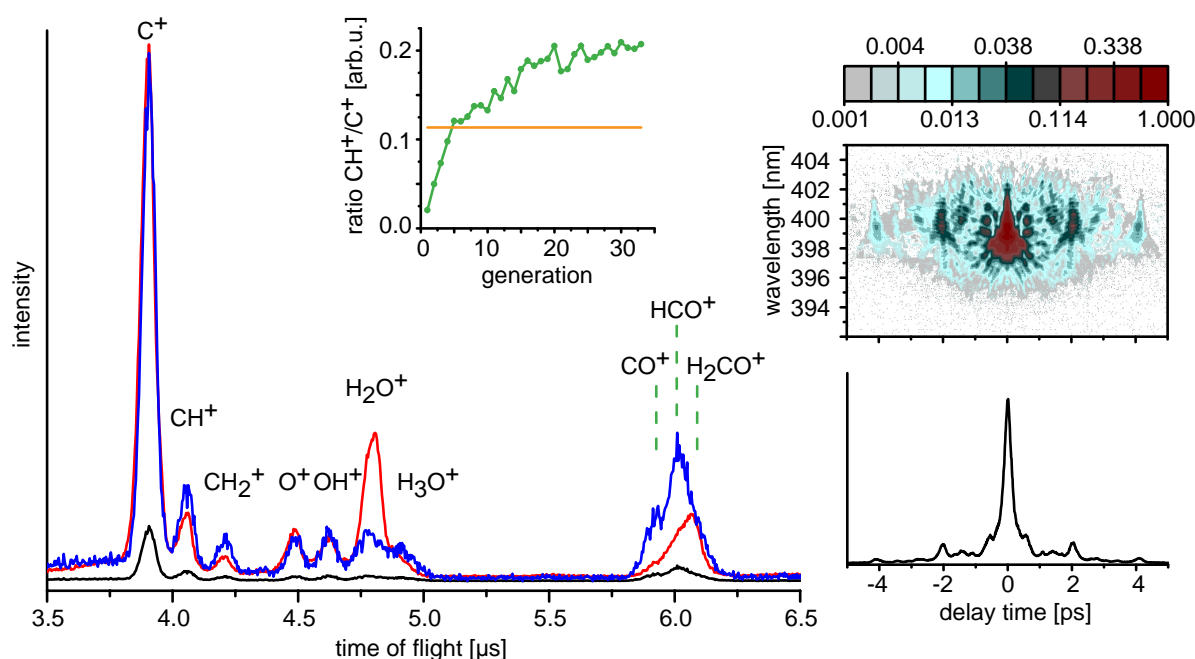


Figure 8.2: Ion spectra for the maximization of the ratio CH^+/C^+ with 4.0 sccm CO and 4.0 sccm H_2 , obtained with the unmodulated pulse (red curve) and the optimal pulse (black curve). For comparison, the blue curve shows the latter ion spectrum rescaled by a factor such that the C^+ -peaks for unmodulated and optimal pulse match. The green curve in the inset shows the development of the fitness (the average of the ten best individuals per generation), while the signal level of the unmodulated pulse is indicated by an orange line for comparison. The two graphs on the right show the SHG-FROG trace (logarithmic color code) and autocorrelation of the optimal pulse.

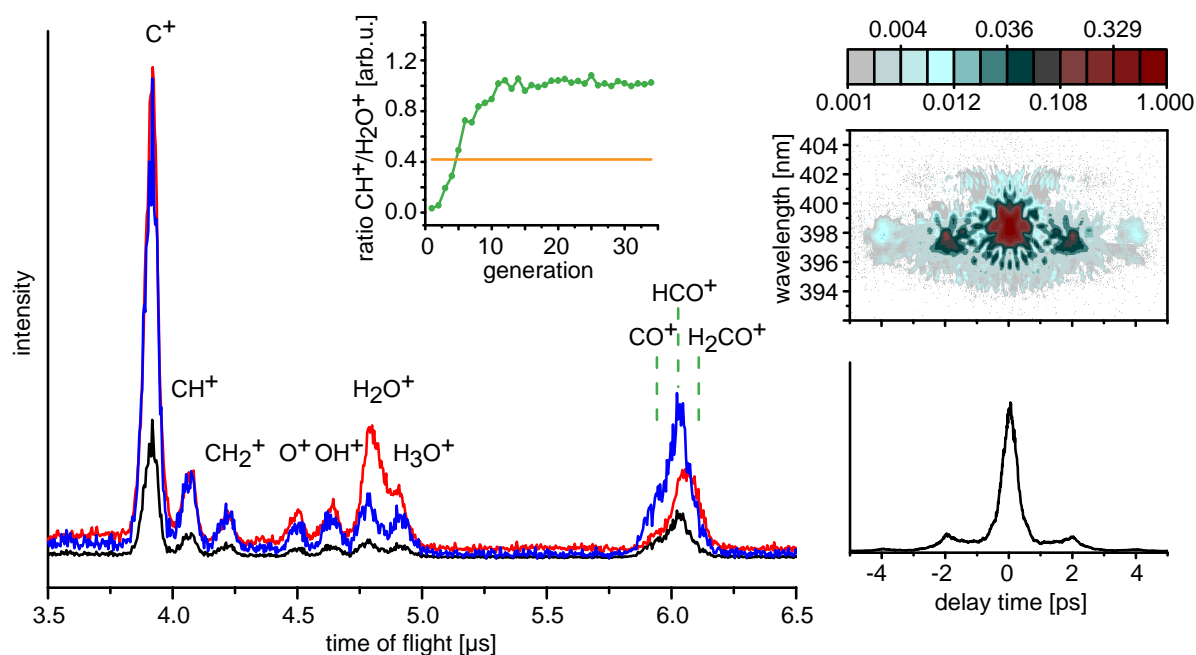


Figure 8.3: Ion spectra for the maximization of the ratio $\text{CH}^+/\text{H}_2\text{O}^+$ with 4.0 sccm CO and 4.0 sccm H_2 , obtained with the unmodulated pulse (red curve) and the optimal pulse (black curve). For comparison, the blue curve shows the latter ion spectrum rescaled by a factor such that the C^+ -peaks for unmodulated and optimal pulse match. The green curve in the inset shows the development of the fitness (the average of the ten best individuals per generation), while the signal level of the unmodulated pulse is indicated by an orange line for comparison. The two graphs on the right show the SHG-FROG trace (logarithmic color code) and autocorrelation of the optimal pulse.

ond laser pulses did not lead to a reduction of the H_2O^+ signal relative to the other peaks. From the experimental data it can be concluded that the optimal pulse favors the formation of ions having a C-H bond, while H_2O^+ formation is reduced. The yield of CO^+ and HCO^+ relative to C^+ is also greatly enhanced, while the yield of H_2CO^+ remains almost the same (see Fig. 8.2). This could be an indication for the existence of different reaction mechanisms for the formation of H_2CO^+ compared to HCO^+ .

Since water formation has been reduced even though this has not been the goal of the previous optimization, the next logical step is to include the H_2O^+ yield as a parameter in the fitness function. Another optimization experiment under virtually the same conditions is performed with the chosen control goal being the maximization of the ratio $\text{CH}^+/\text{H}_2\text{O}^+$. Although performed on another day and with a slightly different starting ratio compared to the CH^+/C^+ optimization, the control goal is achieved just as nicely. Fig. 8.3 shows that the H_2O^+ peak is reduced by about 50 percent relative to C^+ . While the H_2O^+ peak initially is larger than the CH^+ peak, this ratio is reversed with the optimal pulse. The CO^+ and HCO^+ peak intensities are increased, whereas CH^+ and CH_2^+ practically do not change relative to C^+ . The H_2CO^+ peak is even slightly reduced. Also in this experiment, the relative reduction of the water peak cannot be achieved by intensity variation of the unmodulated pulse. Surprisingly, intensity variation of the optimal pulse does not lead to a change of the ratio $\text{CH}^+/\text{H}_2\text{O}^+$, but the optimization

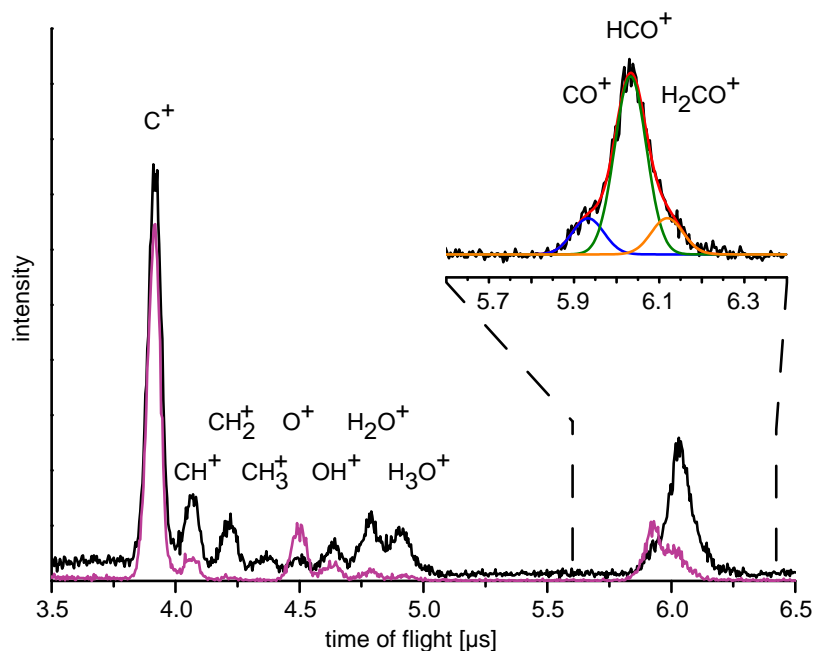


Figure 8.4: Ion spectra obtained with the optimal pulse of the CH^+/H_2O^+ optimization. While CO is set constant to 4.0 sccm, the amount of H_2 is changed to 6.0 sccm (black curve) and to 1.0 sccm (purple curve). The inset shows an extract of the black curve in the region around 6 μs , with a fit (red) and the three contributing peaks (blue, olive, orange) disclosing the formation of formaldehyde.

effect is preserved even for pulses attenuated to almost half the intensity.

In these experiments closed-loop femtosecond learning control has been successfully applied for the first time to the control of two competing reaction channels in which molecular bonds are created and not just broken. Thus, the catalytic synthesis of molecules can be selectively steered by closed-loop optimal control with shaped fs-laser pulses.

For both optimizations, the SHG-FROG trace (top right graph in Figs. 8.2 and 8.3) shows a pulse sequence with a broad main pulse and a feature after 2 ps. In the pump-probe experiments of Sec. 7.4.4, using two identical, unmodulated pulses at temporal distances longer than one pulse width has not lead to any signal at all. The intensity of the incoming laser field was comparable in all the experiments, however, while the energy in the pump-probe experiments has been distributed evenly over the two pulses, the relative position and intensity of the substructures of the optimized pulses might make the difference.

While the optimizations are performed with 4.0 sccm of both gases streaming into the vacuum chamber, ion spectra with the optimal pulse shapes are also recorded for other mixtures, as can be seen in Fig. 8.4 with the amount of hydrogen changed to 6.0 sccm (1.0 sccm) with the optimal pulse of the CH^+/H_2O^+ optimization. Two interesting aspects should be pointed out. First, despite the fact that the H_2 is much more (less) in these cases, the qualitative statement of the optimization that the water peak is suppressed so much that it is smaller than the CH^+ peak is still true. The procedure

of gas amount variation and analysis of the impact of the optimal pulse is discussed in more detail in Section 8.4. Second, even though the optimal pulse shape has a smaller peak intensity compared to the unmodulated pulse, it is still sufficient to produce all the ions also observed with the unmodulated pulse. Especially, a deconvolution of the peak resembling hydrogenated CO clearly shows that formaldehyde is also produced in this case.

8.3 Maximization of DCO^+ formation

In the ion spectra where carbon monoxide and deuterium are employed as reactant gases (Section 7.4.1) the peaks CO^+ and DCO^+ are clearly separated in contrast to the case of hydrogen where distinction of the peaks was only possible after deconvolution of the contributions from CO^+ , HCO^+ and also H_2CO^+ . Thus, when deuterium is chosen as the second reactant besides CO in an experiment the ion peaks from hydrogenated (or deuterated, to be precise) carbon monoxide can be included in the definition of the optimization goal as well. Therefore the deuteration of non-dissociated CO is maximized with respect to the hydrogenation of carbon only by choosing the ratio DCO^+/CD^+ as the fitness function. The algorithm is able to increase the fitness function by about 200%

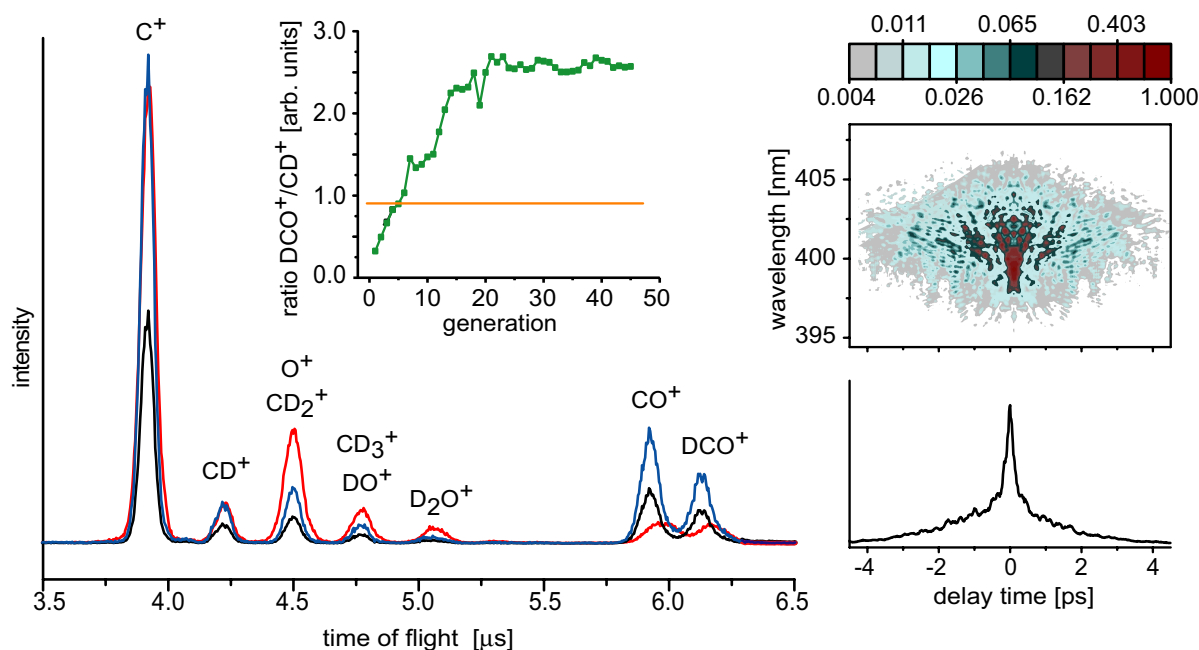
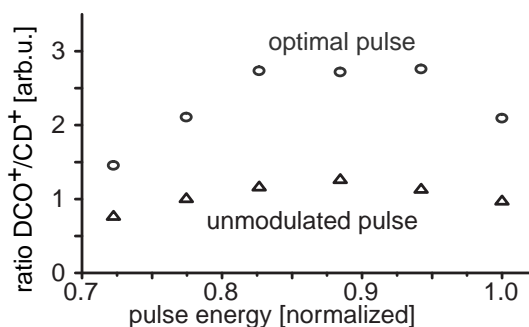


Figure 8.5: Ion spectra for the maximization of the ratio DCO^+/CD^+ with 4.0 sccm CO and 4.0 sccm D_2 , obtained with the unmodulated pulse (red curve) and the optimal pulse (black curve). For comparison, the blue curve shows the latter ion spectrum rescaled by a factor such that the CD^+ -peaks for unmodulated and optimal pulse match. The green curve in the inset shows the development of the fitness (the average of the ten best individuals per generation), while the signal level of the unmodulated pulse is indicated by an orange line for comparison. The two graphs on the right show the SHG-FROG trace (logarithmic color code) and autocorrelation of the optimal pulse.

Figure 8.6: The ratio DCO^+/CD^+ recorded with an unmodulated pulse (triangles) and with the pulse optimized for this ratio (circles) when the laser pulse energy is decreased.



after 30 generations (see Fig. 8.5).

However, as the analysis of the ion spectra shows, the CO^+ peak scales in the same way as the DCO^+ peak. One might come to the conclusion that only the dissociation or ionization of CO is optimized similar as in Section 8.1. Since the ionization potential of 8.6 eV of the isolated radical DCO (8.1 eV for HCO) in comparison to that of CD (only the ionization potential 10.6 eV of CH could be found) [290] is very low one might suggest a pure intensity effect. Additionally, this conjecture is supported by the fact that the CO^+ and HCO^+ peaks have always increased in the optimizations presented in the previous section.

In order to clarify the role of the laser pulse intensity this parameter was varied. When the laser pulse energy is reduced the optimized DCO^+/CD^+ ratio is becoming larger for the optimal pulse relative to an unmodulated laser pulse (Fig. 8.6). For even lower pulse energies, where the overall ion signal has already decreased drastically due to the high nonlinearity of the process, the fitness of the optimized pulse becomes smaller and approaches the fitness value of the unmodulated pulse. This implies that a pure intensity effect alone cannot be responsible for the achieved increase of the DCO^+/CD^+ ratio. This behavior is further investigated with the very useful procedure of gas amount variation in the next section.

8.4 Analysis of control mechanisms via variation of gas amounts

The relative proportion of the two gases can be easily changed with the employed setup, allowing an analysis of the optimization effect with respect to variations in the adsorbate composition. Specifically, it is possible to determine if the optimization is insensitive to hydrogen and if it is achieved via control of carbon monoxide dissociation only. This can be ruled out from the two exemplary measurements shown in Fig. 8.7.

First, only CO is employed and the ratio CO^+/C^+ is maximized, as in the experiment discussed in Section 8.1. Then, hydrogen is added modifying the adsorbate conditions on the surface. If the H_2 amount is small compared to CO, the optimization effect of an increased ratio CO^+/C^+ is also transferred to the hydrogenated species. Yet, a further rise of the H_2 concentration leads to alteration of, e.g. the adsorbate arrangement and electronic states and the optimization effect goes away. The ratio of hydrogenated

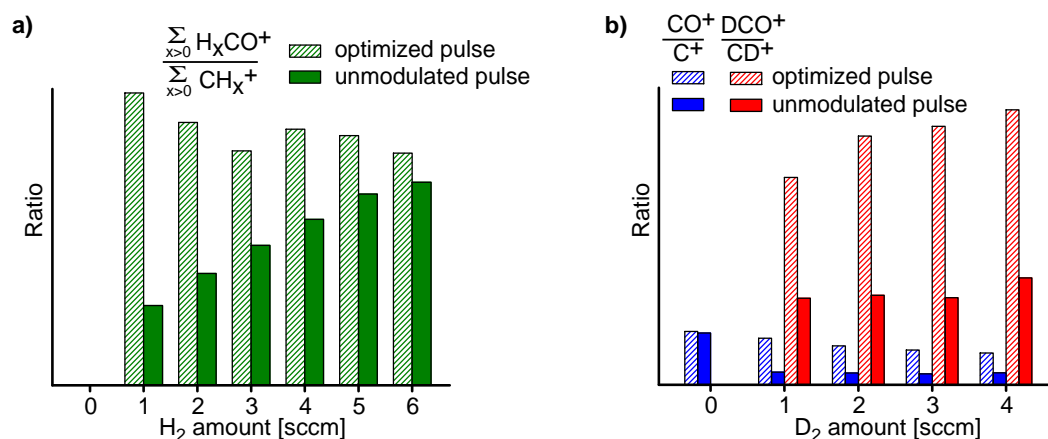


Figure 8.7: Variation of H_2 or D_2 concentrations after an optimization. a) After maximization of the ratio CO^+/C^+ with 4 sccm CO only, H_2 is streamed onto the surface. The graph shows the ratio of all species with hydrogenated CO (29-30 amu) to those with hydrogenated C (13-15 amu). The optimization effect fades away with increasing H_2 amounts. b) After maximization of the ratio DCO^+/CD^+ with 4 sccm CO and 4 sccm D_2 , the amount of D_2 is reduced. The graph shows both the fitness goal DCO^+/CD^+ (red) and the ratio CO^+/C^+ (blue). With decreasing D_2 amounts, the optimization effect diminishes, and the optimal pulse has no effect on the CO^+/C^+ ratio in the absence of D_2 .

ions with the optimal pulse approaches the ratio for an unmodulated pulse (Fig. 8.7a). Hence, the best pulse in the absence of H_2 is not special anymore if large H_2 amounts are applied, substantiating that the pulse is adapted to the specific conditions during the optimization.

This conclusion is also confirmed by the opposite procedure where an equal mixture of CO and D_2 is employed and the ratio DCO^+/CD^+ is maximized first, exactly like in the experiment of the previous section. Subsequent reduction of the D_2 amount changes the conditions on the surface and the optimization effect diminishes (red bars in Fig. 8.7b). A simultaneous analysis of the ratio CO^+/C^+ reveals the selectivity of the optimized pulse shape by showing that the optimal pulse obtained with D_2 has no effect on the CO^+/C^+ ratio anymore if D_2 is absent. Therefore, the optimal pulse does not simply control CO dissociation but again is adapted to the conditions during the optimization, i.e. this time with both CO and D_2 being present.

8.5 Conclusion

In this chapter, the catalytic surface reactions introduced in Chapter 7 have been investigated with phase-shaped femtosecond laser pulses. By applying a feedback optimal control scheme, the reaction outcome could be successfully manipulated and the ratio of different reaction channels could be selectively controlled. Evidence has been found that the underlying control mechanism is nontrivial and sensitive to the specific conditions on the surface.

The experiments shown here represent the first successful experiment on adaptive femtosecond quantum control of a chemical reaction between adsorbate molecules on a surface. In contrast to previous quantum control experiments, reaction channels comprising the formation of new molecular bonds rather than the cleavage of already existing bonds are controlled. Our results are a first step towards laser-induced catalysis of molecules, which is further improved by femtosecond quantum control, providing laser pulses that are tailored especially for the desired reaction outcome.

9 Summary

The control of quantum mechanical processes, especially the selective manipulation of photochemical reactions by shaped femtosecond laser pulses was successfully demonstrated in many experiments in the fields of physics, chemistry and biology. The difficulty that the multitude of experimentally accessible pulse shapes can not completely be tested on the quantum system studied was circumvented by the introduction of "adaptive femtosecond quantum control". Experimental feedback that is directly obtained from the quantum system itself is used by an evolutionary algorithm in a closed learning loop to adaptively find the optimal solution for a specific goal. Thus, the quantum system itself finds the optimally adapted pulse shape.

In this work, attention is directed to the control of two systems that mark a bridge to real synthetic chemistry. In a liquid phase environment, where most preparative chemistry takes place, the outcome of the photo-induced Wolff rearrangement of an industrially relevant diazonaphthoquinone compound, normally used in photoresists (e.g. Novolak) was optimized using shaped femtosecond laser pulses. In the second series of experiments chemical reactions on a catalyst metal surface which comprise laser induced molecular bond formation channels were selectively manipulated for the first time.

The control of liquid phase reactions necessitates adequate spectroscopic signals that are characteristic for the formed product species. Therefore, a pump-probe setup for transient absorption spectroscopy in the mid-infrared for the purpose of investigating ultrafast structural changes of molecules during photoreactions was constructed. It consists of an Ti:Sa pumped optical parametric amplifier with subsequent difference frequency mixing stage, where subpicosecond infrared probe pulses, tunable in the region from at least 4-7 μm are generated. The mid-infrared probe pulses exhibit excellent pulse to pulse energy stability typically of about 0.5% leading to detectable absorption changes on the order of 0.1 mOD with reasonable averaging time. With spectrally resolved detection, a wavenumber range of 80-150 cm^{-1} , depending on the spectral region can be recorded in a single measurement. The instrumental response time, and thus the time resolution of the experimental setup using pump pulses at 400 nm is 300 fs. This versatile setup enables to monitor structural changes of molecules in the liquid phase and to find appropriate feedback signals for the control of these processes.

Prior to quantum control experiments, the photoinduced Wolff-rearrangement reaction of 2-diazo-1-naphthoquinone (DNQ) dissolved in water and methanol was thoroughly investigated. Steady state absorption measurements in the mid-infrared in combination with quantum chemical density functional theory (DFT) calculations revealed the characteristic vibrational bands of DNQ. The C=N=N stretching vibration around 2116 cm^{-1} turned out to be the most prominent feature. For the expected photoproducts (e.g. ketene), the calculations predict the spectral positions of the absorption bands, that are suspected to appear. A mid-infrared transient absorption study was performed,

to illuminate the structural dynamics of the ultrafast rearrangement reaction of DNQ, i.e. to gather information about the formed photoproducts, intermediates and the characteristic time scales of the reaction steps. The experimental observations indicate, that the Wolff rearrangement reaction of DNQ proceeds very fast. The separation of the diazo-group, subsequent ring opening, rearrangement and closure of the ring to form the ketene occurs within 300 fs, which is the time resolution of our experiment. This finding showed, that no statement on the possible existence of a carbene intermediate, as proposed in recent experiments [191, 203, 204] can be given. Based on the time-resolved data a model for the relaxation dynamics of the ketene photoproduct and DNQ after photoexcitation can be deduced that fits the measured data very well. Population in the electronic excited state of DNQ can either perform the Wolff rearrangement or is returning to the ground state. From the partial recovery of the ground state bleach of DNQ the quantum yield of the reaction is determined to be about 0.32 for both solvents. The ketene right after its formation has an excess of vibrational energy and the relaxation can be monitored by the shifting absorption band of the C=C=O vibration of the ketene. The vibrational relaxation dynamics in methanol is with a time constant of about 10 ps much slower than in water (3 ps).

The object of the quantum control experiments on DNQ was the improvement of the ketene yield. It was shown that the ketene formation after Wolff rearrangement of DNQ is very sensitive to the shape of the applied excitation laser pulses. The variation of single parameters, like the linear chirp as well as the pulse separation of colored double pulses lead to the conclusion that the well known intrapulse dumping mechanism is responsible for the impact of the frequency ordering within the excitation pulse on the photoproduct yield. Due to the shrinking energy gap between the S_0 and S_1 states, down-chirped excitation pulses (decreasing momentary frequency) efficiently dump population back to the electronic ground state, while pulses with up-chirp (rising momentary frequency) reduce this effect and therefore more population remains in the excited state leading to an increased product yield. Adaptive optimizations using a closed learning loop basically lead to the same result, since the optimal pulse for the maximization of the ketene yield exhibits a similar frequency ordering, where lower frequencies precede higher frequencies.

Besides the liquid phase control experiments, adaptive femtosecond quantum control was applied to surface reactions on a catalyst metal surface for the first time. Therefore, the laser-induced catalytic reactions of carbon monoxide (CO) and hydrogen (H_2) on a Pd(100) single crystal surface were studied at room temperature and under high vacuum conditions. This photochemical reaction initiated with femtosecond laser pulses has not been observed before. Several product molecules could be synthesized, among them also species (e.g. CH_3^+) for whose formation three particles are involved. The systematic variation of different parameters showed that the reactions are sensitive to the catalyst surface, the composition of the adsorbate and to the laser properties. A pump-probe study revealed that they occur on an ultrafast time scale.

These catalytic surface reactions were then investigated and improved with phase-shaped femtosecond laser pulses. By applying a feedback optimal control scheme, the reaction outcome could be successfully manipulated and the ratio of different reaction channels could be selectively controlled. Evidence has been found that the underlying control mechanism is nontrivial and sensitive to the specific conditions on the surface.

The experiments shown here represent the first successful experiment on adaptive femtosecond quantum control of a chemical reaction between adsorbate molecules on a surface. In contrast to previous quantum control experiments, reaction channels comprising the formation of new molecular bonds rather than the cleavage of already existing bonds are controlled. These results are a first step towards laser-induced catalytic synthesis of molecules, which is further optimized by femtosecond quantum control, providing laser pulses that are tailored especially for the desired reaction outcome.

This work successfully showed that quantum control can be extended to systems closer to situations encountered in synthetic chemistry as was demonstrated in the two examples of the optimization of a complicated rearrangement reaction and the selective formation of chemical bonds with shaped femtosecond laser pulses. This opens the door for laser induced synthesis of molecules from smaller reactants and adds a new dimension to the already very versatile tool of laser radiation. The combination of shaped 400 nm pulses with the mid-infrared detection of photoproducts proved to be a very promising combination. Thus, in the near future attention should be directed to improve the pulse shaping capabilities further to the ultraviolet spectral region below 400 nm, because broadband, intense, directly shaped pulses in the ultraviolet would provide access to more classes of relevant photochemical reactions in the liquid phase.

Zusammenfassung

Die Kontrolle quantenmechanischer Prozesse, insbesondere die selektive Manipulation photochemischer Reaktionen mit Hilfe geformter Femtosekunden-Laserpulse wurde auf den Gebieten der Physik, Chemie und Biologie in vielen Experimenten erfolgreich gezeigt. Die Schwierigkeit, dass die Vielzahl der experimentell zugänglichen Pulsformen nicht alle am untersuchten Quantensystem ausprobiert werden können wurde durch die Einführung des Konzepts der "adaptiven Femtosekunden-Quantenkontrolle" umgangen. Ein experimentelles Rückkopplungssignal das vom Quantensystem selbst kommt wird von einem evolutionären Algorithmus in einer geschlossenen Lernschleife verwendet um in adaptiver Weise die optimale Lösung für eine bestimmte Zielsetzung zu finden. Auf diese Weise findet das Quantensystem selbst die optimal angepasste Pulsform.

In dieser Arbeit wird das Augenmerk auf die Kontrolle zweier Systeme gerichtet, die eine Brücke zur synthetischen Chemie darstellen. In der flüssigen Phase, wo der Großteil der präparativen Chemie stattfindet, wurde das Resultat der photoinduzierten Wolff Umlagerung einer industriell relevanten Diazonaphthoquinone Verbindung, die gewöhnlich in Photolacken (z.B. Novolak) Verwendung findet, durch geformte Femtosekunden-Laserpulse optimiert. In der zweiten Reihe von Experimenten wurden chemische Reaktionen auf einer Katalysator-Metalloberfläche, die Kanäle mit laserinduzierter molekularer Bindungsknüpfung beinhalten, zum ersten Mal selektiv beeinflusst.

Für die Kontrolle von Reaktionen in der flüssigen Phase benötigt man geeignete spektroskopische Messsignale, die charakteristisch für die gebildeten Produktspezies sind. Zu diesem Zweck wurde ein Versuchsaufbau für Anrege-Abfrage Experimente zur transienten Absorptionsspektroskopie im mittleren Infrarot aufgebaut, um ultraschnelle strukturelle Veränderungen von Molekülen während Photoreaktionen zu untersuchen. Es besteht aus einem von einem Ti:Sa Laser gepumpten optisch parametrischen Verstärker mit anschließender Differenzfrequenz-Mischungsstufe, mit der Subpikosekunden-Laserpulse zur Abfrage im Infraroten, durchstimmbare mindestens im Bereich von 4-7 μm , erzeugt werden. Die Pulse im mittleren Infrarot weisen eine hervorragende Stabilität der Pulsenergie von Puls zu Puls von typischerweise um 0.5% auf, was die Detektion von Änderungen in der optischen Dichte einer Probe im Bereich von 0.1 mOD bei annehmbarer Messdauer ermöglicht. Mit spektral aufgelöster Detektion kann, abhängig vom Spektralbereich, ein Wellenzahlbereich von 80-150 cm^{-1} mit einer einzigen Messung aufgenommen werden. Die Ansprechzeit, und damit die Zeitaufösung des Experiments mit Verwendung von 400 nm Anregepulsen ist 300 fs. Dieser vielseitige Versuchsaufbau ermöglicht die Messung struktureller Veränderungen in Molekülen in flüssiger Phase und damit das Auffinden geeigneter Rückkopplungssignale zur Kontrolle dieser Prozesse.

Vor den Quantenkontrollexperimenten wurde die photoinduzierte Wolff Umlagerung

von 2-Diazo-1-Naphthoquinone (DNQ) in den Lösungsmitteln Wasser und Methanol sorgfältig untersucht. Lineare Absorptionsmessungen im mittleren Infrarot in Verbindung mit quantenchemischen Dichtefunktionaltheorie (DFT) Rechnungen lieferten die charakteristischen Schwingungsbanden von DNQ. Die C=N=N Streckschwingung bei 2116 cm^{-1} erwies sich als die bedeutendste Signatur. Die Berechnungen sagen auch die spektralen Positionen der Absorptionsbanden der erwarteten Photoprodukte (z.B. Keten) voraus. Untersuchungen mit transientser Absorptionsspektroskopie im mittleren Infrarot wurden durchgeführt, um die strukturelle Dynamik der ultraschnellen Umlagerungsreaktion von DNQ zu beleuchten, d.h. Informationen über die entstandenen Photoprodukte, Zwischenprodukte und die charakteristischen Zeitskalen der Reaktionsschritte zu sammeln. Die experimentellen Beobachtungen deuten darauf hin, dass die Wolff Umlagerung von DNQ sehr schnell abläuft. Die Abspaltung der Diazo-Gruppe, anschließende Ringöffnung, Umlagerung und Ringschluss wobei das Keten gebildet wird verlaufen innerhalb von 300 fs, was der Zeitauflösung unseres Experiments entspricht. Dieses Ergebnis bedeutet, dass keine Aussage über die mögliche Existenz eines Carben Zwischenprodukts, wie kürzlich in Experimenten [191, 203, 204] vorgeschlagen, gemacht werden kann. Auf der Basis der zeitaufgelösten Daten wurde ein Modell für die Relaxationsdynamik des Keten Photoprodukts und DNQ abgeleitet, dass die gemessenen Daten sehr gut beschreibt. Population im elektronisch angeregten Zustand von DNQ kann entweder die Wolff Umlagerung ausführen oder in den Grundzustand zurückkehren. Aus der unvollständigen Wiederauffüllung des ausgebleichten Grundzustands von DNQ kann die Quantenausbeute der Reaktion mit etwa 0.32 in beiden Lösungsmitteln bestimmt werden. Kurz nach seiner Entstehung hat das Keten einen Überschuss an Schwingungsenergie, dessen Relaxation anhand der Verschiebung der Absorptionsbande der C=C=O Schwingung beobachtet werden kann. Die Relaxationsdynamik in Methanol ist mit 10 ps viel langsamer als in Wasser (3 ps).

Das Ziel der Quantenkontrollexperimente an DNQ war die Erhöhung der Ketenausbeute. Es wurde gezeigt, dass die Bildung des Keten nach der Wolff Umlagerung des DNQ empfindlich auf die Form der Anregungspulse reagiert. Die Variation einzelner Parameter, wie des linearen Chirps sowie des Pulsabstands von farbigen Doppelpulsen führen zu dem Schluss, dass der gut bekannte Intrapuls-Abregemechanismus verantwortlich für den Einfluss der Frequenzfolge innerhalb des Anregepulses auf die Ausbeute des Photoprodukts ist. Wegen des abnehmenden Energieabstands zwischen den Zuständen S_0 und S_1 , können Anregepulse mit Down-Chirp (fallende Momentanfrequenz) Population effizient in den elektronischen Grundzustand abregen, während Pulse mit Up-Chirp (steigende Momentanfrequenz) diesen Effekt reduzieren und demzufolge verbleibt mehr Population im angeregten Zustand was zu erhöhter Produktausbeute führt. Adaptive Optimierungen unter Verwendung einer geschlossenen Lernschleife führen zum gleichen Ergebnis, da der optimale Puls zur Maximierung der Ketenausbeute einen ähnlichen Frequenzverlauf aufweist, bei dem die niedrigeren Frequenzen vor den höheren Frequenzen kommen.

Neben Kontrollexperimenten in der flüssigen Phase wurden adaptive Quantenkontrollmethoden erstmalig auf Oberflächenreaktionen auf einer Katalysator-Metalloberfläche angewendet. Dazu wurden die laserinduzierten katalytischen Oberflächenreaktionen von Kohlenmonoxid (CO) und Wasserstoff (H_2) auf einer Pd(100) Einkristalloberfläche im

Hochvakuum untersucht. Diese photochemische Reaktion, die durch Femtosekunden-Laserpulse ausgelöst wird wurde bisher noch nicht beobachtet. Mehrere Produktmoleküle konnten synthetisiert werden, darunter auch Moleküle für deren Bildung mindestens drei Eduktmoleküle zusammenkommen und reagieren müssen. Die systematische Änderung verschiedener Parameter zeigte, dass die Reaktionen von der Katalysatoroberfläche, der Zusammensetzung des Adsorbats und den Eigenschaften der Femtosekundenlaserpulse abhängen. Eine Anrege-Abfrage Untersuchung machte deutlich, dass die Reaktionen auf einer ultrakurzen Zeitskala ablaufen.

Diese katalytischen Oberflächenreaktionen wurden im Anschluss mit Hilfe von phasen-geformten Femtosekunden-Laserpulsen weiter untersucht und gezielt gesteuert. In adaptiven Quantenkontrollexperimenten konnte das Reaktionsergebnis sowie das Verhältnis unterschiedlicher Reaktionskanäle selektiv manipuliert werden. Es wurden Hinweise gefunden, dass der zugrundeliegende Kontrollmechanismus nichttrivial ist und von den genauen Bedingungen auf der Oberfläche abhängt. Diese Experimente stellen die ersten erfolgreichen adaptiven Quantenkontrollexperimente an einer chemischen Reaktion zwischen Adsorbatmolekülen auf einer Oberfläche dar. Im Gegensatz zu bisherigen Quantenkontrollexperimenten wurden hierbei Reaktionskanäle optimiert, die die Formung und nicht den Bruch einer molekularen Bindung umfassen. Diese Ergebnisse sind ein erster Schritt in Richtung laser-induzierter katalytischer Synthese von Molekülen, zusätzlich optimiert durch Methoden der Quantenkontrolle mit maßgeschneiderten Laserpulsen um das gewünschte Reaktionsergebnis zu erzielen.

Diese Arbeit zeigt, dass die Methoden der Quantenkontrolle auf Systeme, die den Situationen in der synthetischen Chemie nahekommen, erfolgreich angewendet werden können, wie mit den zwei Beispielen, der Optimierung einer komplizierten Umlagerungsreaktion und der selektiven Bildung chemischer Bindungen mit geformten Femtosekunden-Laserpulsen demonstriert wurde. Dies ermöglicht die laserinduzierte Synthese von Molekülen aus kleineren Edukten und fügt dem ohnehin schon sehr vielseitigen Werkzeug des Lasers eine neue Dimension hinzu. Die Verbindung von geformten 400 nm Pulsen mit der Detektion von Photoprodukten im mittleren Infrarot erwies sich als vielversprechend. Deswegen sollte in Zukunft das Augenmerk darauf gelegt werden die Pulsformungsfertigkeiten weiter im Ultravioletten Spektralbereich unter 400 nm zu verbessern, da breitbandige, intensive, direkt geformte Laserpulse im Ultravioletten den Zugang zu weiteren Klassen relevanter photochemischer Reaktionen in der flüssigen Phase ermöglichen würde.

Bibliography

- [1] German Federal Ministry of Education and Research.
Optical technologies – Light is generating growth and jobs. The century of the photon.
In *The High-Tech Strategy for Germany*, pp. 91–94. Bundesministerium für Bildung und Forschung (BMBF), Berlin (Germany) (2006).
- [2] *Nobel Lectures in Chemistry 1996-2000.*
World Scientific Publishing Company, Singapore (2003).
- [3] R. S. Judson and H. Rabitz.
Teaching lasers to control molecules.
Phys. Rev. Lett. **68**, 1500–1503 (1992).
- [4] T. Brixner, N. H. Damrauer, P. Niklaus, and G. Gerber.
Photoselective adaptive femtosecond quantum control in the liquid phase.
Nature **414**, 57–60 (2001).
- [5] T. Brixner, N. H. Damrauer, B. Kiefer, and G. Gerber.
Liquid-phase adaptive femtosecond quantum control: Removing intrinsic intensity dependencies.
J. Chem. Phys. **118**, 3692 (2003).
- [6] G. Vogt, P. Nuernberger, T. Brixner, and G. Gerber.
Femtosecond pump–shaped-dump quantum control of retinal isomerization in bacteriorhodopsin.
Chem. Phys. Lett. **433**, 211–215 (2006).
- [7] G. Vogt, G. Krampert, P. Niklaus, P. Nuernberger, and G. Gerber.
Optimal control of photoisomerization.
Phys. Rev. Lett. **94**, 068305 (2005).
- [8] N. Bloembergen and E. Yablonovitch.
Infrared-laser-induced unimolecular reactions.
Phys. Today pp. 23–30 (1978).
- [9] A. H. Zewail.
Laser chemistry — Is it possible?
Phys. Today **33**, 27–33 (1980).
- [10] N. Bloembergen and A. H. Zewail.
Energy redistribution in isolated molecules and the question of mode-selective laser chemistry revisited.
J. Phys. Chem. **88**, 5459–5465 (1984).
- [11] A. H. Zewail.
Femtochemistry: Recent progress in studies of dynamics and control of reactions and their transition states.
J. Phys. Chem. **100**, 12701 (1996).

- [12] T. Elsaesser and W. Kaiser.
Vibrational and vibronic relaxation of large polyatomic molecules in liquids.
Annu. Rev. Phys. Chem. **42**, 83–107 (1991).
- [13] P. Brumer and M. Shapiro.
Control of unimolecular reactions using coherent light.
Chem. Phys. Lett. **126**, 541–546 (1986).
- [14] M. Shapiro, J. W. Hepburn, and P. Brumer.
Simplified laser control of unimolecular reactions: Simultaneous (ω_1, ω_3) excitation.
Chem. Phys. Lett. **149**, 451–454 (1988).
- [15] P. Brumer and M. Shapiro.
Laser control of molecular processes.
Annu. Rev. Phys. Chem. **43**, 257–282 (1992).
- [16] M. Shapiro and P. Brumer.
Quantum control of chemical reactions.
J. Chem. Soc., Faraday Trans., **93**, 1263–1277 (1997).
- [17] P. W. Brumer and M. Shapiro.
Principles of the Quantum Control of Molecular Processes.
Wiley-Interscience, Hoboken, NJ (USA) (2003).
- [18] S. Lee.
On the molecular phase in coherent control.
J. Chem. Phys. **107**, 2734–2737 (1997).
- [19] T. Seideman.
The role of a molecular phase in two-pathway excitation schemes.
J. Chem. Phys. **108**, 1915–1923 (1998).
- [20] S. Lee.
Phase lag near the resonances in (ω_1, ω_3) coherent control.
J. Chem. Phys. **108**, 3903–3908 (1998).
- [21] C. Chen, Y. Yin, and D. S. Elliott.
Interference between optical transitions.
Phys. Rev. Lett. **64**, 507–510 (1990).
- [22] S. M. Park, S. P. Lu, and R. J. Gordon.
Coherent laser control of the resonance-enhanced multiphoton ionization of HCl.
J. Chem. Phys. **94**, 8622–8624 (1991).
- [23] L. C. Zhu, V. D. Kleiman, X. N. Li, S. P. Lu, K. Trentelman, and R. J. Gordon.
Coherent laser control of the product distribution obtained in the photoexcitation of HI.
Science **270**, 77–80 (1995).
- [24] D. Meshulach and Y. Silberberg.
Coherent quantum control of two-photon transitions by a femtosecond laser pulse.
Nature **396**, 239–242 (1998).
- [25] D. Meshulach and Y. Silberberg.
Coherent quantum control of multiphoton transitions by shaped ultrashort optical pulses.
Phys. Rev. A **60**, 1287–1292 (1999).

- [26] D. J. Tannor and S. A. Rice.
Control of selectivity of chemical reaction via control of wavepacket evolution.
J. Chem. Phys. **83**, 5013–5018 (1985).
- [27] D. J. Tannor, R. Kosloff, and S. A. Rice.
Coherent pulse sequence induced control of selectivity of reactions: Exact quantum mechanical calculations.
J. Chem. Phys. **85**, 5805–8520 (1986).
- [28] D. J. Tannor.
Introduction to Quantum Mechanics: A Time-Dependent Perspective.
University Science Books, Sausalito, Ca (USA) (2007).
- [29] S. A. Rice and M. Zhao.
Optical Control of Molecular Dynamics.
Wiley, New York, NY (USA) (2000).
- [30] T. Baumert, M. Grosser, R. Thalweiser, and G. Gerber.
Femtosecond time-resolved molecular multiphoton ionization: The Na₂ system.
Phys. Rev. Lett. **67**, 3753–3756 (1991).
- [31] T. Baumert, B. Bühler, M. Grosser, R. Thalweiser, V. Weiss, E. Wiedenmann, and G. Gerber.
Femtosecond time-resolved wave packet motion in molecular multiphoton ionization and fragmentation.
J. Chem. Phys. **95**, 8103–8110 (1991).
- [32] E. D. Potter, J. L. Herek, S. Pedersen, O. Liu, and A. H. Zewail.
Femtosecond laser control of a chemical reaction.
Nature **355**, 66–68 (1992).
- [33] K. Bergmann, H. Theuer, and B. W. Shore.
Coherent population transfer among quantum states of atoms and molecules.
Rev. Mod. Phys. **70**, 1003–1025 (1998).
- [34] N. V. Vitanov, T. Halfmann, B. W. Shore, and K. Bergmann.
Laser-induced population transfer by adiabatic passage techniques.
Annu. Rev. Phys. Chem. **52**, 763–809 (2001).
- [35] A. Shi, A. Woody, and H. Rabitz.
Optimal control of selective vibrational excitation in harmonic linear chain molecules.
J. Chem. Phys. **88**, 6870–6883 (1988).
- [36] A. P. Peirce, M. Dahleh, and H. Rabitz.
Optimal control of quantum-mechanical systems: Existence, numerical approximation, and applications.
Phys. Rev. A **37**, 4950–4964 (1988).
- [37] R. Kosloff, S. A. Rice, P. Gaspard, S. Tersigni, and D. J. Tannor.
Wavepacket dancing: Achieving chemical selectivity by shaping light pulses.
Chem. Phys. **139**, 201–220 (1989).
- [38] W. Jakubetz, J. Manz, and H. J. Schreier.
Theory of optimal laser pulses for selective transitions between molecular eigenstates.
Chem. Phys. Lett. **165**, 100 (1990).

- [39] J. E. Combariza, B. Just, J. Manz, and G. K. Paramonov.
Isomerizations controlled by ultrashort infrared laser pulses: Model simulations for the inversion of ligands (H) in the double-well potential of an organometallic compound, $[(C_5H_5)(CO)_2FePH_2]$.
J. Phys. Chem. **95**, 10351–10359 (1990).
- [40] M. Sugawara and Y. Fujimura.
Control of quantum dynamics by a locally optimized laser field. Application to ring puckering isomerization.
J. Chem. Phys. **100**, 5646 (1994).
- [41] T. Brixner, B. Kiefer, and G. Gerber.
Problem complexity in femtosecond quantum control.
Chem. Phys. **267**, 241–246 (2001).
- [42] D. Yelin, D. Meshulach, and Y. Silberberg.
Adaptive femtosecond pulse compression.
Opt. Lett. **22**, 1793–1795 (1997).
- [43] T. Baumert, T. Brixner, V. Seyfried, M. Strehle, and G. Gerber.
Femtosecond pulse shaping by an evolutionary algorithm with feedback.
Appl. Phys. B **65**, 779–782 (1997).
- [44] T. Brixner, M. Strehle, and G. Gerber.
Feedback-controlled optimization of amplified femtosecond laser pulses.
Appl. Phys. B **68**, 281–284 (1999).
- [45] D. Zeidler, T. Hornung, D. Proch, and M. Motzkus.
Adaptive compression of tunable pulses from a non-collinear-type OPA to below 16 fs by feedback-controlled pulse shaping.
Appl. Phys. B **70**, S125–S131 (2000).
- [46] E. Zeek, R. Bartels, M. M. Murnane, H. C. Kapteyn, S. Backus, and G. Vdovin.
Adaptive pulse compression for transform-limited 15-fs high-energy pulse generation.
Opt. Lett. **25**, 587–589 (2000).
- [47] V. V. Lozovoy, I. Pastirk, and M. Dantus.
Multiphoton intrapulse interference. IV. Ultrashort laser pulse spectral phase characterization and compensation.
Opt. Lett. **29**, 775–777 (2004).
- [48] M. Aeschlimann, M. Bauer, D. Bayer, T. Brixner, F. J. de Abajo, W. Pfeiffer, M. Rohmer, C. Spindler, and F. Steeb.
Adaptive subwavelength control of nano-optical fields.
Nature **446**, 301–304 (2007).
- [49] T. Brixner, G. Krampert, P. Niklaus, and G. Gerber.
Adaptive shaping of femtosecond polarization profiles.
J. Opt. Soc. Am. B **20**, 878–881 (2003).
- [50] T. Suzuki, S. Minemoto, and H. Sakai.
Nontrivial polarization shaping of femtosecond pulses by reference to the results of dual-channel spectral interferometry.
Appl. Opt. **43**, 6047–6050 (2004).
- [51] T. Pfeifer, C. Spielmann, and G. Gerber.
Femtosecond X-ray science.
Rep. Prog. Phys. **69**, 443–505 (2006).

- [52] R. Bartels, S. Backus, E. Zeek, L. Misoguti, G. Vdovin, I. P. Christov, M. M. Murnane, and H. C. Kapteyn.
Shaped-pulse optimization of coherent emission of high-harmonic soft X-rays.
Nature **406**, 164–166 (2000).
- [53] D. H. Reitze, S. Kazamias, F. Weihe, G. Mullot, D. Douillet, F. Augé, O. Albert, V. Ramanathan, J. P. Chambaret, D. Hulin, and P. Balcou.
Enhancement of high-order harmonic generation at tuned wavelengths through adaptive control.
Opt. Lett. **29**, 86–88 (2004).
- [54] D. Yoshitomi, J. Nees, N. Miyamoto, T. Sekikawa, T. Kanai, G. Mourou, and S. Watanabe.
Phase-matched enhancements of high-harmonic soft X-rays by adaptive wave-front control with a genetic algorithm.
Appl. Phys. B **78**, 275–280 (2004).
- [55] T. Pfeifer, D. Walter, C. Winterfeldt, C. Spielmann, and G. Gerber.
Controlling the spectral shape of coherent soft X-rays.
Appl. Phys. B **80**, 277–280 (2005).
- [56] T. Pfeifer, R. Kemmer, R. Spitzenpfeil, D. Walter, C. Winterfeldt, G. Gerber, and C. Spielmann.
Spatial control of high-harmonic generation in hollow fibers.
Opt. Lett. **30**, 1497–1499 (2005).
- [57] C. Winterfeldt, T. Pfeifer, D. Walter, R. Kemmer, A. Paulus, R. Spitzenpfeil, G. Gerber, and C. Spielmann.
Adaptive temporal and spatial shaping of coherent soft x-rays.
In J. T. Sheridan and F. Wyrowski (Eds.), *Photon Management II*, volume 6187 of *Proc. SPIE*, art. no. 61870F (2006).
- [58] A. Assion, T. Baumert, M. Bergt, T. Brixner, B. Kiefer, V. Seyfried, M. Strehle, and G. Gerber.
Control of chemical reactions by feedback-optimized phase-shaped femtosecond laser pulses.
Science **282**, 919–922 (1998).
- [59] M. Bergt, T. Brixner, B. Kiefer, M. Strehle, and G. Gerber.
Controlling the femtochemistry of $\text{Fe}(\text{CO})_5$.
J. Phys. Chem. A **103**, 10381–10387 (1999).
- [60] M. Bergt, T. Brixner, B. Kiefer, M. Strehle, and G. Gerber.
Adaptive femtosecond pulse shaping and control of molecular femtochemistry.
Nonlin. Optics **24**, 181–186 (2000).
- [61] R. J. Levis, G. M. Menkir, and H. Rabitz.
Selective bond dissociation and rearrangement with optimally tailored, strong-field laser pulses.
Science **292**, 709–713 (2001).
- [62] R. J. Levis and H. Rabitz.
Closing the loop on bond selective chemistry using tailored strong field laser pulses.
J. Phys. Chem. A **106**, 6427–6444 (2002).
- [63] M. Bergt, T. Brixner, C. Dietl, B. Kiefer, and G. Gerber.
Time-resolved organometallic photochemistry: Femtosecond fragmentation and adaptive control of $\text{CpFe}(\text{CO})_2\text{X}$ ($\text{X}=\text{Cl}, \text{Br}, \text{I}$).
J. Organomet. Chem. **661**, 199–209 (2002).
- [64] N. H. Damrauer, C. Dietl, G. Krampert, S.-H. Lee, K.-H. Jung, and G. Gerber.
Control of bond-selective photochemistry in CH_2BrCl using adaptive femtosecond pulse shaping.
Eur. Phys. J. D **20**, 71–76 (2002).

- [65] C. Daniel, J. Full, L. González, C. Lupulescu, J. Manz, A. Merli, Š. Vajda, and L. Wöste. *Deciphering the reaction dynamics underlying optimal control laser fields.* *Science* **299**, 536–539 (2003).
- [66] D. Cardoza, F. Langhojer, C. Trallero-Herrero, O. L. A. Monti, and T. Weinacht. *Changing pulse-shape basis for molecular learning control.* *Phys. Rev. A* **70**, 053406 (2004).
- [67] D. Cardoza, M. Baertschy, and T. Weinacht. *Understanding learning control of molecular fragmentation.* *Chem. Phys. Lett.* **411**, 311–315 (2005).
- [68] A. Lindinger, C. Lupulescu, M. Plewicky, F. Vetter, A. Merli, S. M. Weber, and L. Wöste. *Isotope selective ionization by optimal control using shaped femtosecond laser pulses.* *Phys. Rev. Lett.* **93**, 033001 (2004).
- [69] A. Lindinger, F. Vetter, C. Lupulescu, M. Plewicky, S. M. Weber, A. Merli, and L. Wöste. *Selective ionization via different electronic pathways by optimal control demonstrated for $^{23}\text{Na}^{39}\text{K}/^{23}\text{Na}^{41}\text{K}$.* *Chem. Phys. Lett.* **397**, 123–127 (2004).
- [70] F. Vetter, M. Plewicky, A. Lindinger, A. Merli, S. M. Weber, and L. Wöste. *Optimized isotope-selective ionization of $^{23}\text{Na}^{39}\text{K}$ and $^{23}\text{Na}^{41}\text{K}$ by applying evolutionary strategies.* *Phys. Chem. Chem. Phys.* **7**, 1151–1156 (2005).
- [71] A. Lindinger, A. Merli, M. Plewicky, F. Vetter, S. M. Weber, and L. Wöste. *Optimal control of isotope selective fragmentation.* *Chem. Phys. Lett.* **413**, 315–320 (2005).
- [72] B. Schäfer-Bung, V. Bonačić-Koutecký, F. Sauer, S. M. Weber, L. Wöste, and A. Lindinger. *Isotope selective photoionization of NaK by optimal control: Theory and experiment.* *J. Chem. Phys.* **125**, 214310 (2006).
- [73] C. J. Bardeen, V. V. Yakovlev, K. R. Wilson, S. D. Carpenter, P. M. Weber, and W. S. Warren. *Feedback quantum control of molecular electronic population transfer.* *Chem. Phys. Lett.* **280**, 151–158 (1997).
- [74] S.-H. Lee, K.-H. Jung, J.-H. Sung, K.-H. Hong, and C. H. Nam. *Adaptive quantum control of DCM fluorescence in the liquid phase.* *J. Chem. Phys.* **117**, 9858–9861 (2002).
- [75] T. Okada, I. Otake, R. Mizoguchi, K. Onda, S. S. Kano, and A. Wada. *Optical control of two-photon excitation efficiency of α -perylene crystal by pulse shaping.* *J. Chem. Phys.* **121**, 6386–6391 (2004).
- [76] S. Zhang, Z. Sun, X. Zhang, Y. Xu, Z. Wang, Z. Xu, and R. Li. *Optimal feedback control of two-photon fluorescence in Coumarin 515 based on genetic algorithm.* *Chem. Phys. Lett.* **415**, 346–350 (2005).
- [77] O. Nahmias, O. Bismuth, A. Shoshana, and S. Ruhman. *Tracking excited state dynamics with coherent control: automated limiting of population transfer in LDS750.* *J. Phys. Chem. A* **109**, 8246–8253 (2005).

- [78] V. I. Prokhorenko, A. M. Nagy, and R. J. D. Miller.
Coherent control of the population transfer in complex solvated molecules at weak excitation. An experimental study.
J. Chem. Phys. **122**, 184502 (2005).
- [79] I. Otake, S. S. Kano, and A. Wada.
Pulse shaping effect on two-photon excitation efficiency of α -perylene crystals and perylene in chloroform solution.
J. Chem. Phys. **121**, 6386–6391 (2004).
- [80] E. C. Carroll, B. J. Pearson, A. C. Florean, P. H. Bucksbaum, and R. J. Sension.
Spectral phase effects on nonlinear resonant photochemistry of 1,3-cyclohexadiene in solution.
J. Chem. Phys. **124**, 114506 (2006).
- [81] G. S. Vogt.
Adaptive Femtosekunden-Quantenkontrolle komplexer Moleküle in kondensierter Phase.
Dissertation, Universität Würzburg (2006).
- [82] P. Nuernberger.
Adaptive control of quantum systems with femtosecond laser pulses.
Dissertation, Universität Würzburg (2007).
- [83] V. Prokhorenko, A. M. Nagy, S. A. Waschuk, L. S. Brown, R. R. Birge, and R. J. D. Miller.
Coherent control of retinal isomerization in bacteriorhodopsin.
Science **313**, 1257–1261 (2006).
- [84] B. Dietzek, B. Brüggemann, T. Pascher, and A. Yartsev.
Mechanisms of molecular response in the optimal control of photoisomerization.
Phys. Rev. Lett. **97**, 258301 (2006).
- [85] P. Nuernberger, G. Vogt, T. Brixner, and G. Gerber.
Femtosecond quantum control of molecular dynamics in the condensed phase.
Phys. Chem. Chem. Phys. **9**, 2470–2497 (2007).
- [86] H. Rabitz, R. de Vivie-Riedle, M. Motzkus, and K. Kompa.
Chemistry—Whither the future of controlling quantum phenomena?
Science **288**, 824–828 (2000).
- [87] T. Brixner and G. Gerber.
Quantum control of gas-phase and liquid-phase femtochemistry.
ChemPhysChem **4**, 418–438 (2003).
- [88] D. Goswami.
Optical pulse shaping approaches to coherent control.
Phys. Rep. **374**, 385–481 (2003).
- [89] T. Brixner, G. Krampert, P. Niklaus, and G. Gerber.
Femtosecond learning control of quantum dynamics in gases and liquids: Technology and applications.
J. Mod. Opt. **50**, 539–560 (2003).
- [90] M. Dantus and V. Lozovoy.
Experimental coherent laser control of physicochemical processes.
Chem. Rev. **104**, 1813–1859 (2004).

- [91] M. Wollenhaupt, V. Engel, and T. Baumert.
Femtosecond laser photoelectron spectroscopy on atoms and small molecules: Prototype studies in quantum control.
Annu. Rev. Phys. Chem. **56**, 25–56 (2005).
- [92] R. E. Carley, E. Heesel, and H. H. Fielding.
Femtosecond lasers in gas phase chemistry.
Chem. Soc. Rev. **34**, 949–969 (2005).
- [93] J.-C. Diels and W. Rudolph.
Ultrashort Laser Pulse Phenomena.
Academic Press, San Diego, Ca (USA) (1995).
- [94] T. Brixner.
Adaptive Femtosecond Quantum Control.
Dissertation, Universität Würzburg (2001).
- [95] G. Guoy.
Compt. Rendue Acad. Sci. Paris **110**, 1251–1253 (1890).
- [96] A. Siegman.
Lasers.
University Science Books, Sausalito, Ca (USA) (1986).
- [97] R. W. Boyd.
Nonlinear Optics.
Academic Press, San Diego, Ca (USA) (1991).
- [98] A. Yariv.
Quantum Electronics.
Third edition. John Wiley & Sons, New York, NY (USA) (1989).
- [99] Y. R. Shen.
The Principles of Nonlinear Optics.
A John Wiley & Sons, New York, NY (USA) (1984).
- [100] R. R. Alfano and S. L. Shapiro.
Emission in the region 4000 to 7000 Å via four-photon coupling in glass.
Phys. Rev. Lett. **24**, 584–588 (1970).
- [101] S. A. Kovalenko, A. L. Dobryakov, J. Ruthmann, and N. P. Ernsting.
Femtosecond spectroscopy of condensed phases with chirped supercontinuum probing.
Phys. Rev. A **59**, 2369–2384 (1999).
- [102] G. Cerullo and S. D. Silvestri.
Ultrafast optical parametric amplifiers.
Rev. Sci. Instr. **74**, 1–18 (2003).
- [103] G. Yang and Y. R. Shen.
Spectral broadening of ultrashort pulses in a nonlinear medium.
Opt. Lett. **9**, 510–512 (1984).
- [104] A. T. I. Buchvarov and T. Fiebig.
Toward an understanding of white-light generation in cubic media - polarization properties across the entire spectral range.
Opt. Lett. **32**, 1539–1541 (2007).

- [105] I. Golub.
Optical characteristics of supercontinuum generation.
Opt. Lett. **15**, 305–307 (1990).
- [106] C. Rullière (Ed.).
Femtosecond Laser Pulses: Principles and Experiments.
Springer, Berlin (Germany) (1998).
- [107] B. H. Bransden and C. J. Joachain.
Physics of Atoms and Molecules.
Prentice Hall, Harlow, UK (2003).
- [108] G. Herzberg.
Molecular spectra and molecular structure: II. Infrared and Raman spectra of polyatomic molecules.
Second edition. Van Nostrand Reinhold Company, New York (1945).
- [109] P. Hamm, S. M. Ohline, and W. Zinth.
Vibrational cooling after ultrafast photoisomerization of azobenzene measured by femtosecond infrared spectroscopy.
J. Chem. Phys. **106**, 519–529 (1997).
- [110] E. T. J. Nibbering and T. Elsaesser.
Ultrafast vibrational dynamics of hydrogen bonds in the condensed phase.
Chem. Rev. **104**, 1887–1914 (2004).
- [111] K. Wynne and R. M. Hochstrasser.
The theory of ultrafast vibrational spectroscopy.
Chem. Phys. **193**, 211–236 (1995).
- [112] T. Schrader, A. Sieg, F. Koller, W. Schreier, W. Z. Q. An, and P. Gilch.
Vibrational relaxation following ultrafast internal conversion: comparing IR and Raman probing.
Chem. Phys. Lett. **392**, 358–364 (2004).
- [113] Q. R. An and P. Gilch.
Cooling of hot para-nitroaniline probed by non-resonant Raman scattering.
Chem. Phys. Lett. **363**, 397–403 (2002).
- [114] M. Rini, J. Dreyer, E. T. J. Nibbering, and T. Elsaesser.
Ultrafast vibrational relaxation processes induced by intramolecular excited state hydrogen transfer.
Chem. Phys. Lett. **374**, 13–19 (2003).
- [115] E. T. J. Nibbering, H. Fidder, and E. Pines.
Ultrafast chemistry: Using time-resolved vibrational spectroscopy for interrogation of structural dynamics.
Ann. Rev. Phys. Chem. **56**, 337–367 (2005).
- [116] H. Yang, M. C. Asplund, K. T. Kotz, M. J. Wilkens, H. Frei, and C. B. Harris.
Reaction mechanism of silicon-hydrogen bond activation studied using femtosecond to nanosecond IR spectroscopy and ab initio methods.
J. Am. Chem. Soc. **120**, 10154–10165 (1998).
- [117] D. A. Steinhurst, A. P. Baronavski, and J. C. Owrutsky.
Transient infrared spectroscopy of Mn-2(CO)(10) with 400 nm excitation.
Chem. Phys. Lett. **361**, 513–519 (2002).

- [118] E. A. Glascoe, M. F. Kling, J. E. Shanoski, and C. B. Harris.
Nature and role of bridged carbonyl intermediates in the ultrafast photoinduced rearrangement of Ru-3(CO)(12).
Organometallics **25**, 775–784 (2006).
- [119] V. Lehtovuori, J. Aumanen, P. Myllyperkio, M. Rini, E. T. J. Nibbering, and J. Korppi-Tommola.
Transient midinfrared study of light induced dissociation reaction of Ru(dcbpy)(CO)(2)I-2 in solution.
J. Phys. Chem. A **108**, 1644–1649 (2004).
- [120] R. Diller, S. Maiti, G. C. Walker, B. R. Cowen, R. Pippenger, R. A. Bogomolni, and R. M. Hochstrasser.
Femtosecond time-resolved infrared laser study of the J-K transition of bacteriorhodopsin.
Chem. Phys. Lett. **241**, 109–115 (1995).
- [121] R. Diller.
Vibrational relaxation during the retinal isomerization in Bacteriorhodopsin.
Chem. Phys. Lett. **295**, 47–55 (1998).
- [122] J. Herbst, K. Heyne, and R. Diller.
Femtosecond infrared spectroscopy of bacteriorhodopsin chromophore isomerization.
Science **297**, 822–825 (2002).
- [123] F. Peters, J. Herbst, J. Tittor, D. Oesterhelt, and R. Diller.
Primary reaction dynamics of halorhodopsin, observed by sub-picosecond IR - vibrational spectroscopy.
Chem. Phys. **323**, 109–116 (2006).
- [124] R. Diller, R. Jakober, C. Schumann, F. Peters, J. P. Klare, and M. Engelhard.
The trans-cis isomerization reaction dynamics in sensory rhodopsin II by femtosecond time-resolved midinfrared spectroscopy: Chromophore and protein dynamics.
Biopolymers **82**, 358–362 (2006).
- [125] A. Usman, O. F. Mohammed, E. T. J. Nibbering, J. Dong, K. M. Solntsev, and L. M. Tolbert.
Excited-state structure determination of the green fluorescent protein chromophore.
J. Am. Chem. Soc. **127**, 11214–11215 (2005).
- [126] A. U. K. Heyne, O. F. Mohammed, E. T. J. N. J. Dreyer, and M. A. Cusanovich.
Structural evolution of the chromophore in the primary stages of trans/cis isomerization in photoactive yellow protein.
J. Am. Chem. Soc. **127**, 18100–18106 (2005).
- [127] A. Usman, O. F. Mohammed, K. Heyne, J. Dreyer, and E. T. J. Nibbering.
Excited state dynamics of a PYP chromophore model system explored with ultrafast infrared spectroscopy.
Chem. Phys. Lett. **401**, 157–163 (2005).
- [128] M. L. Groot, L. J. G. W. van Wilderen, D. S. Larsen, M. A. van der Horst, I. H. M. van Stokkum, K. J. Hellingwerf, and R. van Grondelle.
Initial steps of signal generation in photoactive yellow protein revealed with femtosecond mid-infrared spectroscopy.
Biochem. **42**, 10054–10059 (2003).
- [129] M. Lim, T. A. Jackson, and P. A. Anfinrud.
Mid-infrared vibrational spectrum of CO after photodissociation from heme: Evidence for a ligand docking site in the heme pocket of hemoglobin and myoglobin.
J. Chem. Phys. **102**, 4355–4366 (1995).

- [130] M. H. Lim, T. A. Jackson, and P. A. Anfinrud.
Ultrafast rotation and trapping of carbon monoxide dissociated from myoglobin.
Nature Structural Biology **4**, 209–214 (1997).
- [131] M. Rini, A. K. Holm, E. T. J. Nibbering, and H. Fidder.
Ultrafast UV-mid-IR investigation of the ring opening reaction of a photochromic spiropyran.
J. Am. Chem. Soc. **125**, 3028–3034 (2003).
- [132] A. K. Holm, M. Rini, E. T. J. Nibbering, and H. Fidder.
Femtosecond UV/mid-IR study of photochromism of the spiropyran 1',3'-dihydro-1',3',3'-trimethyl-6-nitrospiro-[2H-1-benzopyran-2,2'-(2H)-indole] in solution.
Chem. Phys. Lett. **376**, 214–219 (2003).
- [133] A. K. Holm, O. F. Mohammed, M. Rini, E. Mukhtar, E. T. J. Nibbering, and H. Fidder.
Sequential merocyanine product isomerization following femtosecond UV excitation of a spiropyran.
J. Phys. Chem. A **109**, 8962–8968 (2005).
- [134] S. Malkmus, F. O. Koller, B. Heinz, W. J. Schreier, T. E. Schrader, W. Zinth, C. Schulz, S. Dietrich, K. Ruck-Braun, and M. Braun.
Ultrafast ring opening reaction of a photochromic indolyl-fulgimide.
Chem. Phys. Lett. **417**, 266–271 (2006).
- [135] F. O. Koller, W. J. Schreier, T. Schrader, A. Sieg, S. Malkmus, C. Schulz, S. Dietrich, K. Rueck-Braun, W. Zinth, and M. Braun.
Ultrafast structural dynamics of photochromic indolylfulgimides studied by vibrational spectroscopy and DFT calculations.
J. Phys. Chem. A **110**, 12769–12776 (2006).
- [136] M. Rini, A. Kummrow, J. Dreyer, E. T. J. Nibbering, and T. Elsaesser.
Femtosecond mid-infrared spectroscopy of condensed phase hydrogen-bonded systems as a probe of structural dynamics.
Faraday Discussions **122**, 27–40 (2003).
- [137] M. Rini, J. Dreyer, A. Kummrow, B. Z. Magnes, E. Pines, and E. T. J. Nibbering.
Excited state proton transfer of photoacids studied with ultrafast infrared spectroscopy.
Abstr. Pap. Am. Chem. Soc. **225**, U485 (2003).
- [138] M. Rini, B. Z. Magnes, E. Pines, and E. T. J. Nibbering.
Real-time observation of bimodal proton transfer in acid-base pairs in water.
Science **301**, 349–352 (2003).
- [139] M. Rini, D. Pines, B. Z. Magnes, E. Pines, and E. T. J. Nibbering.
Bimodal proton transfer in acid-base reactions in water.
JOURNAL OF CHEMICAL PHYSICS **121**, 9593–9610 (2004).
- [140] O. F. Mohammed, D. Pines, J. Dreyer, E. Pines, and E. T. J. Nibbering.
Sequential proton transfer through water bridges in acid-base reactions.
Science **310**, 83–86 (2005).
- [141] S. Laimgruber, W. J. Schreier, T. Schrader, F. Koller, W. Zinth, and P. Gilch.
The photochemistry of o-nitrobenzaldehyde as seen by femtosecond vibrational spectroscopy.
Angew. Chem. - Int. Ed. **44**, 7901–7904 (2005).
- [142] W. J. Schreier, T. E. Schrader, F. O. Koller, P. Gilch, C. E. Crespo-Hernandez, V. N. Swaminathan, T. Carell, W. Zinth, and B. Kohler.
Thymine dimerization in DNA is an ultrafast photoreaction.
Science **315**, 625–629 (2007).

- [143] P. Maine, D. Strickland, P. Bado, M. Pessot, and G. Mourou.
Generation of ultrahigh peak power pulses by chirped pulse amplification.
IEEE J. Quantum Electron. **24**, 398–403 (1988).
- [144] S. Backus, C. G. Durfee III, M. M. Murnane, and H. C. Kapteyn.
High power ultrafast lasers.
Rev. Sci. Instrum. **69**, 1207–1223 (1998).
- [145] I. Walmsley, L. Waxer, and C. Dorrer.
The role of dispersion in ultrafast optics.
Rev. Sci. Instrum. **72**, 1–29 (2001).
- [146] G. Cheriaux, P. Rousseau, F. Salin, J. P. Chambaret, B. Walker, and L. F. DiMauro.
Aberration-free stretcher design for ultrashort-pulse amplification.
Opt. Lett. **21**, 414–416 (1996).
- [147] E. B. Treacy.
Optical pulse compression with diffraction gratings.
IEEE J. Quantum Electron. **5**, 454–458 (1969).
- [148] A. M. Weiner.
Femtosecond pulse shaping using spatial light modulators.
Rev. Sci. Instrum. **71**, 1929–1960 (2000).
- [149] O. E. Martínez.
Grating and prism compressor in the case of finite beam size.
J. Opt. Soc. Am. B **3**, 929–934 (1986).
- [150] O. E. Martínez.
Matrix formalism for pulse compressors.
IEEE J. Quantum Electron. **24**, 2530–2536 (1988).
- [151] A. M. Weiner, D. E. Leaird, J. S. Patel, and J. R. Wullert II.
Programmable femtosecond pulse shaping by use of a multielement liquid-crystal phase modulator.
Opt. Lett. **15**, 326–328 (1990).
- [152] A. M. Weiner, D. E. Leaird, A. Patel, and J. R. Wullert II.
Programmable shaping of femtosecond optical pulses by use of 128-element liquid-crystal phase modulator.
IEEE J. Quantum Electron. **28**, 908–920 (1992).
- [153] T. Brixner.
Kohärente Kontrolle von Photodissoziationsreaktionen mit optimal geformten ultrakurzen Laserpulsen.
Diplomarbeit, Universität Würzburg (1998).
- [154] M. M. Wefers and K. A. Nelson.
Analysis of programmable ultrashort waveform generation using liquid-crystal spatial light modulators.
J. Opt. Soc. Am. B **12**, 1343–1362 (1995).
- [155] J. Paye and A. Migus.
Space-time Wigner functions and their application to the analysis of a pulse shaper.
J. Opt. Soc. Am. B **12**, 1480–1490 (1995).

- [156] M. M. Wefers and K. A. Nelson.
Space-time profiles of shaped ultrafast optical waveforms.
IEEE J. Quantum Electron. **32**, 161–172 (1996).
- [157] R. Trebino.
Frequency-Resolved Optical Gating: The Measurement of Ultrashort Pulses.
Kluwer Academic Publishers, Norwell, Ma (USA) (2000).
- [158] R. Trebino, K. W. DeLong, D. N. Fittinghoff, J. N. Sweetser, M. A. Krumbügel, B. A. Richman, and D. J. Kane.
Measuring ultrashort laser pulses in the time-frequency domain using frequency-resolved optical gating.
Rev. Sci. Instrum. **68**, 3277–3295 (1997).
- [159] D. J. Kane and R. Trebino.
Characterization of arbitrary femtosecond pulses using frequency-resolved optical gating.
IEEE J. Quantum Electron. **29**, 571–579 (1993).
- [160] R. Trebino and D. J. Kane.
Using phase retrieval to measure the intensity and phase of ultrashort pulses: Frequency-resolved optical gating.
J. Opt. Soc. Am. A **10**, 1101–1111 (1993).
- [161] D. J. Kane and R. Trebino.
Single-shot measurement of the intensity and phase of an arbitrary ultrashort pulse by using frequency-resolved optical gating.
Opt. Lett. **18**, 823–825 (1993).
- [162] K. W. DeLong, R. Trebino, J. Hunter, and W. E. White.
Frequency-resolved optical gating with the use of second-harmonic generation.
J. Opt. Soc. Am. B **11**, 2206–2215 (1994).
- [163] K. W. DeLong, R. Trebino, and D. J. Kane.
Comparison of ultrashort-pulse frequency-resolved-optical-gating traces for three common beam geometries.
J. Opt. Soc. Am. B **11**, 1595–1608 (1994).
- [164] D. J. Kane, A. J. Taylor, R. Trebino, and K. W. DeLong.
Single-shot measurement of the intensity and phase of a femtosecond UV laser pulse with frequency-resolved optical gating.
Opt. Lett. **19**, 1061–1063 (1994).
- [165] S. Linden, H. Giessen, and J. Kuhl.
XFROG – a new method for amplitude and phase characterization of weak ultrashort pulses.
Phys. Stat. Sol. B **206**, 119–124 (1998).
- [166] S. Linden, J. Kuhl, and H. Giessen.
Amplitude and phase characterization of weak blue ultrashort pulses by downconversion.
Opt. Lett. **24**, 569–571 (1999).
- [167] D. Keusters, H.-S. Tan, P. O’Shea, E. Zeek, R. Trebino, and W. S. Warren.
Relative-phase ambiguities in measurements of ultrashort pulses with well-separated multiple frequency components.
J. Opt. Soc. Am. B **20**, 2226–2237 (2003).

- [168] T. Brixner, A. Oehrlein, M. Strehle, and G. Gerber.
Feedback-controlled femtosecond pulse shaping.
Appl. Phys. B **70**, S119–S124 (2000).
- [169] B. J. Pearson, J. L. White, T. C. Weinacht, and P. H. Bucksbaum.
Coherent control using adaptive learning algorithms.
Phys. Rev. A **63**, 063412 (2001).
- [170] T. C. Weinacht and P. H. Bucksbaum.
Using feedback for coherent control of quantum systems.
J. Opt. B **4**, R35–R52 (2002).
- [171] F. L. Légaré, J. M. Fraser, D. M. Villeneuve, and P. B. Corkum.
Adaptive compression of intense 250-nm-bandwidth laser pulses.
Appl. Phys. B **74**, S279–S282 (2002).
- [172] T. Pfeifer, U. Weichmann, S. Zipfel, and G. Gerber.
Compression and shaping of a self-phase-modulated laser pulse with a deformable mirror device.
J. Mod. Opt. **50**, 705–710 (2003).
- [173] K.-H. Hong and C. H. Nam.
Adaptive pulse compression of femtosecond laser pulses using a low-loss pulse shaper.
Jap. J. Appl. Phys. **43**, 5289–5293 (2004).
- [174] V. Seyfried.
Beobachtung und Kontrolle molekularer Dynamik durch Femtosekundenlaserpulse.
Dissertation, Universität Würzburg (1998).
- [175] E. Papastathopoulos.
Adaptive Control of Electronic Excitation Utilizing Ultrafast Laser Pulses.
Dissertation, Universität Würzburg (2005).
- [176] W. C. Wiley and I. H. McLaren.
Time-of-flight mass spectrometer with improved resolution.
Rev. Sci. Instrum. **26**, 1150–1157 (1955).
- [177] P. H. Nuernberger.
Design and Construction of an Apparatus for the Neutral Dissociation and Ionization of Molecules in an Intense Laser Field.
Master’s Thesis, State University of New York at Stony Brook (2003).
- [178] H.-P. Schwefel.
Evolution and Optimum Seeking.
Wiley, New York (1995).
- [179] D. E. Goldberg.
Genetic Algorithms in Search, Optimization, and Machine Learning.
Addison-Wesley, Reading (1993).
- [180] F. Seifert, V. Petrov, and M. Woerner.
Solid-state laser system for the generation of midinfrared femtosecond pulses tunable from 3.3 to 10 μm .
Opt. Lett. **19**, 2009–2011 (1994).
- [181] P. Hamm, M. Lim, and R. M. Hochstrasser.
Vibrational energy relaxation of the cyanide ion in water.
J. Chem. Phys. **107**, 10523–10531 (1997).

- [182] P. Hamm, R. A. Kaindl, and J. Stenger.
Noise suppression in femtosecond mid-infrared light sources.
Opt. Lett. **25**, 1798–1800 (2000).
- [183] O. Golonzka, M. Khalil, N. Demirdoven, and A. Tokmakoff.
Coupling and orientation between anharmonic vibrations characterized with two-dimensional infrared vibrational echo spectroscopy.
J. Chem. Phys. **115**, 10814–10828 (2001).
- [184] R. A. Kaindl, M. Wurm, K. Reimann, P. Hamm, A. M. Weiner, and M. Woerner.
Generation, shaping, and characterization of intense femtosecond pulses tunable from 3 to 20 μ m.
J. Opt. Soc. Am. B **17**, 2086–2094 (2000).
- [185] S. H. Shim, D. B. Strasfeld, E. C. Fulmer, and M. T. Zanni.
Femtosecond pulse shaping directly in the mid-IR using acousto-optic modulation.
Opt. Lett. **31**, 838–840 (2006).
- [186] S.-H. Shim, D. B. Strasfeld, and M. T. Zanni.
Generation and characterization of phase and amplitude shaped femtosecond mid-IR pulses.
Opt. Expr. **14**, 13120–13130 (2006).
- [187] T. M. Jedju and L. Rothberg.
Tunable femtosecond generation in the mid-infrared for time-resolved absorption in semiconductors.
Appl. Opt. **27**, 615–618 (1988).
- [188] K. Ekvall, P. van der Meulen, C. Dhollande, L.-E. Berg, S. Pommeret, R. Naskrecki, and J.-C. Mialocq.
Cross phase modulation artifact in liquid phase transient absorption spectroscopy.
J. Appl. Phys. **87**, 2340–2352 (2000).
- [189] M. Lorenc, M. Ziolk, R. Naskrecki, J. Karolczak, J. Kubicki, and A. Maciejewski.
Artifacts in femtosecond transient absorption spectroscopy.
Appl. Phys. B **74**, 19–27 (2002).
- [190] P. Hamm.
Coherent effects in femtosecond infrared-spectroscopy.
Chem. Phys. **200**, 415–429 (1995).
- [191] J. J. M. Vlegaar, A. H. Huizer, P. A. Kraakman, W. P. N. Nijssen, R. J. Visser, and C. A. G. O. Varma.
Photoinduced Wolff-rearrangement of 2-diazo-1-naphthoquinones - evidence for the participation of a carbene intermediate.
J. Am. Chem. Soc. **116**, 11754–11763 (1994).
- [192] A. Reiser, J. P. Huang, X. He, T. F. Yeh, S. Jha, J. Y. Shih, M. S. Kim, Y. K. Han, and K. Yan.
The molecular mechanism of novolak-diazonaphthoquinone resists.
Euro. Pol. J. **38**, 619–629 (2002).
- [193] R. R. Dammel.
Diazonaphthoquinone-based Resists, volume 11 of *SPIE Tutorial Texts Series*.
SPIE Optical Engineering Press, Bellingham WA (1993).
- [194] A. P. Goodwin, J. L. Mynar, Y. Z. Ma, G. R. Fleming, and J. M. J. Frechet.
Synthetic micelle sensitive to IR light via a two-photon process.
J. Am. Chem. Soc. **127**, 9952–9953 (2005).

- [195] J. L. Mynar, A. P. Goodwin, J. A. Cohen, Y. Z. Ma, G. R. Fleming, and J. M. J. Frechet. *Two-photon degradable supramolecular assemblies of linear-dendritic copolymers*. Chem. Comm. pp. 2081–2082 (2007).
- [196] N. K. Urdabayev and V. V. Popik. *Wolff rearrangement of 2-diazo-1(2H)-naphthalenone induced by nonresonant two-photon absorption of NIR radiation*. J. Am. Chem. Soc. **126**, 4058–4059 (2004).
- [197] H. Meier and K. P. Zeller. *Wolff rearrangement of alpha-diazo carbonyl-compounds*. Angew. Chem. - Int. Ed. **14**, 32–43 (1975).
- [198] W. Kirmse. *100 years of the Wolff rearrangement*. Euro. Journ. Org. Chem. pp. 2193–2256 (2002).
- [199] G. C. Hess, B. Kohler, I. Likhovorik, J. Peon, and M. S. Platz. *Ultrafast carbonylcarbene formation and spin-equilibration*. J. Am. Chem. Soc. **122**, 8087–8088 (2000).
- [200] N. Yamamoto, F. Bernardi, A. Bottoni, M. Olivucci, M. A. Robb, and S. Wilsey. *Ultrafast carbonylcarbene formation and spin-equilibration*. J. Am. Chem. Soc. **116**, 2064–2074 (1994).
- [201] J. Andraos, Y. Chiang, C. G. Huang, A. J. Kresge, and J. C. Scaiano. *Flash photolytic generation and study of ketene and carbocyclic-acid enol intermediates formed by the photolysis of diazonaphthoquinones in aqueous-solution*. J. Am. Chem. Soc. **115**, 10605–10610 (1993).
- [202] M. Barra, T. A. Fisher, G. J. Cernigliaro, R. Sinta, and J. C. Scaiano. *On the photodecomposition mechanism of o-diazonaphthoquinones*. J. Am. Chem. Soc. **114**, 2630–2634 (1992).
- [203] K. Tanigaki and T. W. Ebbesen. *Dynamics of the Wolff rearrangement - spectroscopic evidence of oxirene intermediate*. J. Am. Chem. Soc. **109**, 5883–5884 (1987).
- [204] K. Tanigaki and T. W. Ebbesen. *Dynamics of the Wolff rearrangement of 6-membered ring ortho-diazo ketones by laser flash photolysis*. J. Phys. Chem. **93**, 4531–4536 (1989).
- [205] J. Pacansky and J. R. Lyerla. *Photo-chemical decomposition mechanisms for AZ-type photoresists*. IBM Journal of Research and Development **23**, 42–55 (1979).
- [206] M. J. Frisch, G. W. Trucks, H. B. Schlegel, M. A. R. G. E. Scuseria, J. R. Cheeseman, J. A. Montgomery, T. V. Jr., K. N. Kudin, J. C. Burant, J. M. Millam, S. S. Iyengar, J. Tomasi, V. Barone, B. Mennucci, M. Cossi, G. Scalmani, N. Rega, G. A. Petersson, H. Nakatsuji, M. Hada, M. Ehara, K. Toyota, R. Fukuda, J. Hasegawa, M. Ishida, T. Nakajima, Y. Honda, O. Kitao, H. Nakai, M. Klene, X. Li, J. E. Knox, H. P. Hratchian, J. B. Cross, V. Bakken, C. Adamo, J. Jaramillo, R. Gomperts, R. E. Stratmann, O. Yazyev, A. J. Austin, R. Cammi, C. Pomelli, J. W. Ochterski, P. Y. Ayala, K. Morokuma, G. A. Voth, P. Salvador, J. J. Dannenberg, V. G. Zakrzewski, S. Dapprich, A. D. Daniels, M. C. Strain, O. Farkas, D. K. Malick, A. D. Rabuck, K. Raghavachari, J. B. Foresman, J. V. Ortiz, Q. Cui, A. G. Baboul,

- S. Clifford, J. Cioslowski, B. B. Stefanov, G. Liu, A. Liashenko, P. Piskorz, I. Komaromi, R. L. Martin, D. J. Fox, T. Keith, M. A. Al-Laham, C. Y. Peng, A. Nanayakkara, M. Challacombe, P. M. W. Gill, B. Johnson, W. Chen, M. W. Wong, C. Gonzalez, and J. A. Pople.
Gaussian 03.
Gaussian, Inc., Wallingford CT (2004).
- [207] A. D. Becke.
Density-functional exchange-energy approximation with correct asymptotic behavior.
Phys. Rev. A **38**, 3098–3100 (1988).
- [208] A. D. Becke.
Density-functional thermochemistry. III. The role of exact exchange.
J. Chem. Phys. **98**, 5648–5652 (1993).
- [209] C. Lee, W. Yang, and R. G. Parr.
Development of the Colle-Salvetti correlation-energy formula into the functional of the electron density.
Phys. Rev. B **37**, 785–789 (1988).
- [210] K. B. Hewett, M. Shen, C. L. Brummel, and L. A. Philips.
High resolution infrared spectroscopy of pyrazin and naphthalene in a molecular beam.
J. Chem. Phys. **100**, 4077–4086 (1994).
- [211] M. Schade.
Time-resolved IR spectroscopy and quantum control in the liquid phase.
Diplomarbeit, Universität Würzburg (2008).
- [212] D. Wolpert, M. Schade, and T. Brixner.
Femtosecond mid-infrared study of the photoinduced Wolff rearrangement of diazonaphthoquinone.
J. Chem. Phys. p. submitted (2008).
- [213] S. A. Kovalenko, R. Schanz, H. Hennig, and N. P. Ernsting.
Cooling dynamics of an optically excited molecular probe in solution from femtosecond broadband transient absorption spectroscopy.
J. Chem. Phys. **115**, 3256–3273 (2001).
- [214] A. Pigliucci, G. Duvanel, L. M. L. Daku, and E. Vauthey.
Investigation of the Influence of Solute-Solvent Interactions on the Vibrational Energy relaxation dynamics of large molecules in liquids.
J. Phys. Chem. A **111**, 6135–6145 (2007).
- [215] U. Sukowski, A. Seilmeier, T. Elsaesser, and S. F. Fischer.
Picosecond energy transfer of vibrationally hot molecules in solution: Experimental studies and theoretical analysis.
J. Chem. Phys. **93**, 4094–4101 (1990).
- [216] K. Iwata and H. Hamaguchi.
Microscopic Mechanism of Solute-Solvent Energy Dissipation Probed by Picosecond Time-Resolved Raman Spectroscopy.
J. Phys. Chem. A **101**, 632–637 (1997).
- [217] M. Hacker, R. Netz, M. Roth, G. Stobrawa, T. Feurer, and R. Sauerbrey.
Frequency-doubling of phase-modulated, ultrashort laser pulses.
Appl. Phys. B **73**, 273–277 (2001).

- [218] E. Sidick, A. Knoesen, and A. Dienes.
Ultrashort-pulse second-harmonic generation. I. Transform-limited fundamental pulses.
J. Opt. Soc. Am. B **12**, 1704–1712 (1995).
- [219] E. Sidick, A. Dienes, and A. Knoesen.
Ultrashort-pulse second-harmonic generation. II. Non-transform-limited fundamental pulses.
J. Opt. Soc. Am. B **12**, 1713–1722 (1995).
- [220] G. Cerullo, C. J. Bardeen, Q. Wang, and C. V. Shank.
High-power femtosecond chirped pulse excitation of molecules in solution.
Chem. Phys. Lett. **262**, 362–368 (1996).
- [221] C. J. Bardeen, V. V. Yakovlev, J. A. Squier, and K. R. Wilson.
Quantum control of population transfer in green fluorescent protein by using chirped femtosecond pulses.
J. Am. Chem. Soc. **120**, 13023–13027 (1998).
- [222] J. Cao, J. Che, and K. R. Wilson.
Intrapulse dynamical effects in multiphoton processes: Theoretical analysis.
J. Phys. Chem. A **102**, 4284–4290 (1998).
- [223] C. J. Bardeen, J. Cao, F. L. H. Brown, and K. R. Wilson.
Using time-dependent rate equations to describe chirped pulse excitation in condensed phases.
Chem. Phys. Lett. **302**, 405–410 (1999).
- [224] G. Vogt, P. Nuernberger, R. Selle, F. Dimler, T. Brixner, and G. Gerber.
Analysis of femtosecond quantum control mechanisms with colored double pulses.
Phys. Rev. A **74**, 033413 (2006).
- [225] N. Renard, R. Chaux, B. Lavorel, and O. Faucher.
Pulse trains produced by phase-modulation of ultrashort optical pulses: Tailoring and characterization.
Opt. Express **12**, 473–482 (2004).
- [226] D. Zeidler, T. Witte, D. Proch, and M. Motzkus.
Optical parametric amplification of a shaped white-light continuum.
Opt. Lett. **26**, 1921–1923 (2001).
- [227] P. Nuernberger, G. Vogt, R. Selle, S. Fechner, T. Brixner, and G. Gerber.
Generation of femtosecond pulse sequences in the ultraviolet by spectral phase modulation.
In J. T. Sheridan and F. Wyrowski (Eds.), *Photon Management II*, volume 6187 of *Proc. SPIE*,
art. no. 61870M (2006).
- [228] T. Binhammer, E. Rittweger, U. Morgner, R. Ell, and F. X. Kärtner.
Spectral phase control and temporal superresolution toward the single-cycle pulse.
Opt. Lett. **31**, 1552–1554 (2006).
- [229] B. von Vacano and M. Motzkus.
Time-resolved two color single-beam CARS employing supercontinuum and femtosecond pulse shaping.
Opt. Comm. **264**, 488–493 (2006).
- [230] P. Nuernberger, G. Vogt, R. Selle, S. Fechner, T. Brixner, and G. Gerber.
Generation of shaped ultraviolet pulses at the third harmonic of titanium-sapphire femtosecond laser radiation.
submitted to Appl. Phys. B (2007).

- [231] B. V. O'Grady and R. J. Donovan.
Chemiluminescent reaction between $I_2(D0_u^+)$ and Xe to yield $XeI(B^2\Sigma^{\frac{1}{2}})$.
Chem. Phys. Lett. **122**, 503–506 (1985).
- [232] R. Zadoyan and V. A. Apkarian.
Femtochemistry of the liquid phase laser-induced harpoon reaction between Cl_2 and Xe. Observation of bond formation in real time.
Chem. Phys. Lett. **206**, 475–482 (1993).
- [233] V. A. Apkarian.
Comment on "Time-resolved laser induced harpoon reactions".
J. Chem. Phys. **106**, 5298–5299 (1996).
- [234] N. F. Scherer, L. R. Khundkar, R. B. Bernstein, and A. H. Zewail.
Real-time picosecond clocking of the collision complex in a bimolecular reaction: The birth of OH from $H+CO_2$.
J. Chem. Phys. **87**, 1451–1453 (1987).
- [235] C. Wittig, S. Sharpe, and R. A. Beaudet.
Photoinitiated reactions in weakly bonded complexes.
Acc. Chem. Res. **21**, 341–347 (1988).
- [236] N. F. Scherer, C. Sipes, R. B. Bernstein, and A. H. Zewail.
Real-time clocking of bimolecular reactions: Application to $H+CO_2$.
J. Chem. Phys. **92**, 5239–5259 (1990).
- [237] S. I. Ionov, G. A. Brucker, C. Jaques, L. Valachovic, and C. Wittig.
Subpicosecond resolution studies of the $H+CO_2 \rightarrow CO+OH$ reaction photoinitiated in CO_2-HI complexes.
J. Chem. Phys. **99**, 6553–6561 (1993).
- [238] J. D. Simon and X. Xie.
Photodissociation of chromium hexacarbonyl in solution: direct observation of the formation of pentacarbonyl(methanol)chromium.
J. Phys. Chem. **90**, 6751–6753 (1986).
- [239] J. D. Simon and X. Xie.
Time-resolved studies of solvation: the photodissociation of hexacarbonylchromium in pentanol.
J. Phys. Chem. **91**, 5538–5540 (1987).
- [240] B. A. Arndtsen, R. G. Bergman, T. A. Mobley, and T. H. Peterson.
Selective intermolecular carbon-hydrogen bond activation by synthetic metal complexes in homogeneous solution.
Acc. Chem. Res. **28**, 154–162 (1995).
- [241] T. Lian, S. E. Bromberg, M. C. Asplund, H. Yang, and C. B. Harris.
Femtosecond infrared studies of the dissociation and dynamics of transition metal carbonyls in solution.
J. Phys. Chem. **100**, 11994–12001 (1996).
- [242] H. Yang, K. T. Kotz, M. Aplund, and C. B. Harris.
Femtosecond infrared studies of silane silicon-hydrogen bond activation.
J. Am. Chem. Soc. **119**, 9564–9565 (1997).

- [243] J. B. Asbury, H. N. Gosh, J. S. Yeston, R. G. Bergman, and T. Lian.
Sub-picosecond IR study of the reactive intermediate in an alkane C-H bond activation reaction by CpRh(CO)(2).
Organometallics **17**, 3417–3419 (1998).
- [244] H. Yang, P. T. Snee, K. T. Kotz, C. K. Payne, H. Frei, and C. B. Harris.
Femtosecond infrared studies of a prototypical one-electron oxidative-addition reaction: Chlorine atom abstraction by the Re(CO)(5) radical.
J. Am. Chem. Soc. **121**, 9227–9228 (1999).
- [245] P. T. Snee, A. Yang, K. T. Kotz, C. K. Payne, and C. B. Harris.
Ultrafast infrared studies of the reaction mechanism of silicon-hydrogen bond activation by eta(5)-CpV(CO)(4).
J. Phys. Chem. A **103**, 10426–10432 (1999).
- [246] P. T. Snee, C. K. Payne, S. D. Mebane, K. T. Kotz, and C. B. Harris.
Dynamics of photosubstitution reactions of Fe(CO)(5): An ultrafast infrared study of high spin reactivity.
J. Am. Chem. Soc. **123**, 6909–6915 (2001).
- [247] P. T. Snee, K. Payne, K. T. Kotz, H. Yang, and C. B. Harris.
Triplet organometallic reactivity under ambient conditions: An ultrafast UV pump/IR probe study.
J. Am. Chem. Soc. **123**, 2255–2264 (2001).
- [248] M. C. Asplund, P. T. Snee, J. S. Yeston, M. J. Wilkens, C. K. Payne, H. Yang, K. T. Kotz, H. Frei, R. G. Bergman, and C. B. Harris.
Ultrafast UV pump/IR probe studies of C-H activation in linear, cyclic, and aryl hydrocarbons.
J. Am. Chem. Soc. **124**, 10605–10612 (2002).
- [249] U. Marvet and M. Dantus.
Femtosecond photoassociation spectroscopy: Coherent bond formation.
Chem. Phys. Lett. **245**, 393–399 (1995).
- [250] P. Gross and M. Dantus.
Femtosecond photoassociation: Coherence and implications for control in bimolecular reactions.
J. Chem. Phys. **106**, 8013–8021 (1997).
- [251] P. Backhaus and B. Schmidt.
Femtosecond quantum dynamics of photoassociation reactions: the exciplex formation of mercury.
Chem. Phys. **217**, 131–143 (1997).
- [252] C. P. Koch, J. P. Palao, R. Kosloff, and F. Masnou-Seeuws.
Stabilization of ultracold molecules using optimal control theory.
Phys. Rev. A **70**, 013402 (2004).
- [253] E. Luc-Koenig, R. Kosloff, F. Masnou-Seeuws, and M. Vatasescu.
Photoassociation of cold atoms with chirped laser pulses: Time-dependent calculations and analysis of the adiabatic transfer within a two-state model.
Phys. Rev. A **70**, 033414 (2004).
- [254] E. Luc-Koenig, M. Vatasescu, and F. Masnou-Seeuws.
Optimizing the photoassociation of cold atoms by use of chirped laser pulses.
Eur. Phys. J. D **31**, 239–262 (2004).

- [255] C. P. Koch, E. Luc-Koenig, and F. Masnou-Seeuws.
Making ultracold molecules in a two-color pump-dump photoassociation scheme using chirped pulses.
Phys. Rev. A **73**, 033408 (2006).
- [256] W. Salzmann, U. Poschinger, R. Wester, M. Weidemüller, A. Merli, S. M. Weber, F. Sauer, M. Plewicky, F. Weise, A. M. Esparza, L. Wöste, and A. Lindinger.
Coherent control with shaped femtosecond laser pulses applied to ultracold molecules.
Phys. Rev. A. **73**, 023414 (2006).
- [257] B. L. Brown, A. J. Dicks, and I. A. Walmsley.
Coherent control of ultracold molecule dynamics in a magneto-optical trap by use of chirped femtosecond laser pulses.
Phys. Rev. Lett. **96**, 173002 (2006).
- [258] B. L. Brown, A. J. Dicks, and I. A. Walmsley.
The coherent effect of chirped femtosecond laser pulses on the formation of ultracold molecules in a magneto-optical trap.
Opt. Comm. **264**, 278–284 (2006).
- [259] J. A. Prybyla, T. F. Heinz, J. A. Misewich, M. M. T. Loy, and J. H. Glowia.
Desorption induced by femtosecond laser pulses.
Phys. Rev. Lett. **64**, 1537–1540 (1990).
- [260] H.-L. Dai and W. Ho (Eds.).
Laser spectroscopy and photochemistry on metal surfaces.
World Scientific, Singapore (1995).
- [261] G. Somorjai.
Introduction to surface chemistry and catalysis.
Wiley, New York (1994).
- [262] X.-Y. Zhu.
Surface photochemistry.
Annu. Rev. Phys. Chem. **45**, 113–144 (1994).
- [263] F. Budde, T. F. Heinz, M. M. T. Loy, J. A. Misewich, F. de Rougemont, and H. Zacharias.
Femtosecond Time-Resolved Measurement of Desorption.
Phys. Rev. Lett. **66**, 3024–3027 (1991).
- [264] J. A. Prybyla, H. W. K. Tom, and G. D. Aumiller.
Femtosecond time-resolved surface reaction: desorption of CO from Cu(111) in <325 fsec.
Phys. Rev. Lett. **68**, 503–506 (1992).
- [265] F.-J. Kao, D. Busch, D. Cohen, D. G. da Costa, and W. Ho.
Femtosecond laser desorption of molecularly adsorbed oxygen from Pt(111).
Phys. Rev. Lett. **71**, 2094–2097 (1993).
- [266] F.-J. Kao, D. Busch, D. G. da Costa, and W. Ho.
Femtosecond versus nanosecond surface photochemistry: O₂ + CO on Pt(111) at 80 K.
Phys. Rev. Lett. **70**, 4098–4101 (1993).
- [267] R. A. Pelak and W. Ho.
Low temperature surface photochemistry: O₂ and CO on Ag(110) at 30 K.
Surf. Sci. **321**, L233–L238 (1994).

- [268] M. Bonn, S. Funk, C. Hess, D. N. Denzler, C. Stampfl, M. Scheffler, M. Wolf, and G. Ertl.
Phonon- versus electron-mediated desorption and oxidation of CO on Ru(0001).
Science **285**, 1042–1045 (1999).
- [269] D. Denzler, C. Frischkorn, C. Hess, M. Wolf, and G. Ertl.
Electronic excitation and dynamic promotion of a surface reaction.
Phys. Rev. Lett. **91**, 226102 (2003).
- [270] B. Cornils and W. Hermann (Eds.).
Applied homogeneous catalysis with organometallic compounds.
VCH, Weinheim (1996).
- [271] P. M. Maitlis.
Fischer-Tropsch, organometallics, and other friends.
J. Organomet. Chem. **689**, 4366–4374 (2004).
- [272] M. Poutsma, L. Elek, P. Ibarbia, A. Risch, and J. Rabo.
Selective formation of methanol from synthesis gas over palladium catalysts.
J. Catal. **52**, 157–168 (1978).
- [273] C. Sudhakar and M. Vannice.
Methanol and methane formation over palladium/rare earth oxide catalysts.
J. Catal. **95**, 227–243 (1985).
- [274] C. Tracy and P. Palmberg.
Structural influences on adsorbate binding energy. I. Carbon monoxide on (100) palladium.
J. Chem. Phys. **51**, 4852–4862 (1969).
- [275] R. Behm, K. Christmann, G. Ertl, and M. V. Hove.
Adsorption of CO on Pd(100).
J. Chem. Phys. **73**, 2984–2995 (1980).
- [276] R. Behm, K. Christmann, and G. Ertl.
Adsorption of hydrogen on Pd(100).
Surf. Sci. **99**, 320–340 (1980).
- [277] G. Rupprechter.
Surface vibrational spectroscopy from ultrahigh vacuum to atmospheric pressure: Adsorption and reactions on single crystals and nanoparticle model catalysts monitored by sum frequency generation spectroscopy.
Phys. Chem. Chem. Phys. **3**, 4621–4632 (2001).
- [278] M. Morkel, G. Rupprechter, and H.-J. Freund.
Ultrahigh vacuum and high-pressure coadsorption of CO and H₂ on Pd(111): a combined SFG, TDS and LEED study.
J. Chem. Phys. **119**, 10853–10866 (2003).
- [279] H. Petek, H. Nagano, M. J. Weida, and S. Ogawa.
Quantum control of nuclear motion at a metal surface.
J. Phys. Chem. A **104**, 10234–10239 (2000).
- [280] K. Watanabe, N. Takagi, and Y. Matsumoto.
Mode-selective excitation of coherent surface phonons on alkali-covered metal surfaces.
Phys. Chem. Chem. Phys. **7**, 2697–2700 (2005).

- [281] Y. Matsumoto and K. Watanabe.
Coherent vibrations of adsorbates induced by femtosecond laser excitation.
Chem. Rev. **106**, 4234–4260 (2006).
- [282] A. Weingartshofer and E. Clarke.
Cross sections for the ion-molecule reaction $H_2^{+} + H_2 \rightarrow H_3^+ + H$ as a function of the vibration state of the H_2^+ ion.*
Phys. Rev. Lett. **12**, 591–592 (1964).
- [283] N. Papp and L. Kerwin.
Some new aston bands in hydrogen.
Phys. Rev. Lett. **22**, 1343–1346 (1969).
- [284] S. Anderson, F. Houle, D. Gerlich, and Y. Lee.
The effect of vibration and translational energy on the reaction dynamics of the $H_2^+ + H_2$ system.
J. Chem. Phys. **75**, 2153–2162 (1981).
- [285] H. Figger, M. Dixit, R. Maier, W. Schrepp, H. Walther, I. Peterkin, and J. Watson.
Spectroscopy of triatomic hydrogen molecules in a beam.
Phys. Rev. Lett. **52**, 906–909 (1984).
- [286] W. Paul, B. Lücke, S. Schlemmer, and D. Gerlich.
On the dynamics of the reaction of positive hydrogen cluster ions (H_5^+ to H_{23}^+) with para and normal hydrogen at 10 K.
Int. J. Mass Spectrom. Ion Processes **149/150**, 373–387 (1995).
- [287] T. Oka.
Observation of the infrared spectrum of H_3^+ .
Phys. Rev. Lett. **45**, 531–534 (1980).
- [288] B. McCall and T. Oka.
 H_3^+ – an ion with many talents.
Science **287**, 1941–1942 (2000).
- [289] M. Kempka, J. Sjödaahl, A. Björk, and J. Roeraade.
Improved method for peak picking in matrix-assisted laser desorption/ionization time-of-flight mass spectrometry.
Rapid Commun. Mass Spectrom. **18**, 1208–1212 (2004).
- [290] National Institute of Standards and Technology.
NIST Standard Reference Database Number 69, June 2005 Release.
<http://webbook.nist.gov/chemistry/>.
- [291] L. Cai, X. Xiao, and M. M. T. Loy.
Femtosecond laser desorption of CO from the Pt(100) surface.
Surf. Sci. **464**, L727–L731 (2000).
- [292] G. Herzberg.
Molecular spectra and molecular structure: I. Spectra of diatomic molecules.
Second edition. Van Nostrand Reinhold Company, New York (1950).
- [293] B. J. Sussman, D. Townsend, M. Y. Ivanov, and A. Stolow.
Dynamic Stark control of photochemical processes.
Science **314**, 278–281 (2006).

- [294] C. Trallero-Herrero, J. L. Cohen, and T. Weinacht.
Strong-field atomic phase matching.
Phys. Rev. Lett. **96**, 063603 (2006).
- [295] *Chemical Processes on Solid Surfaces.*
The Royal Swedish Academy of Sciences, Stockholm (Sweden) (2007).
- [296] G. Ertl.
Elementary steps in heterogeneous catalysis.
Angew. Chem. Int. Ed. **29**, 1219–1227 (1990).
- [297] S. Wilke and M. Scheffler.
Poisoning of Pd(100) for the dissociation of H₂: A theoretical study of co-adsorption of hydrogen and sulphur.
Surf. Sci. **329**, L605–L610 (1995).
- [298] A. F. Carley, P. R. Davies, R. V. Jones, K. R. Harikumar, and M. W. Roberts.
Controlling oxygen states at a Cu(110) surface: The role of coadsorbed sulfur and temperature.
Chem. Comm. pp. 185–186 (2000).
- [299] J. H. Moore, C. C. Davis, and M. A. Coplan.
Building Scientific Apparatus: A Practical Guide to Design and Construction.
Second edition. Addison-Wesley, Reading, Ma (USA) (1989).
- [300] A. V. Teplyakov and B. E. Bent.
Distinguishing direct and quasi-direct mechanisms for an Eley-Rideal gas/surface reaction.
J. Chem. Soc. Faraday Trans. **91**, 3645–3654 (1995).
- [301] M. Xi and B. E. Bent.
Evidence for an Eley-Rideal mechanism in the addition of hydrogen atoms to unsaturated hydrocarbons on Cu(111).
J. Vac. Sci. Technol. B **10**, 2440–2446 (1992).
- [302] C. T. Rettner and D. J. Auerbach.
Distinguishing the direct and indirect products of a gas-surface reaction.
Science **263**, 365–367 (1994).
- [303] C. T. Rettner.
Reaction of an H-atom beam with Cl/Au(111): Dynamics of concurrent Eley-Rideal and Langmuir-Hinshelwood mechanisms.
J. Chem. Phys. **101**, 1529–1546 (1994).
- [304] C. Frischkorn and M. Wolf.
Femtochemistry at metal surfaces: Nonadiabatic reaction dynamics.
Chem. Rev. **106**, 4207 (2006).
- [305] M. Weiss, G. Ertl, and F. Nitschke.
Adsorption and decomposition of ammonia on Fe(110).
Appl. Surf. Sci. **00**, 614–635 (1979).
- [306] K. Christmann and J. Demuth.
The adsorption and reaction of methanol on Pd(100). I. Chemisorption and condensation.
J. Chem. Phys. **76**, 6308–6317 (1982).
- [307] K. Christmann and J. Demuth.
The adsorption and reaction of methanol on Pd(100). II. Thermal desorption and decomposition.
J. Chem. Phys. **76**, 6318–6327 (1982).

- [308] R. J. Levis, J. Zhicheng, and N. Winograd.
Thermal decomposition of CH₃OH adsorbed on Pd(111): A new reaction pathway involving CH₃ formation.
J. Am. Chem. Soc. **111**, 4605–4612 (1988).
- [309] J. Davis and M. Barteau.
Polymerization and decarbonylation reactions of aldehydes on the Pd(111) surface.
J. Am. Chem. Soc. **111**, 1782–1792 (1982).
- [310] L. Fleck, W. Feehery, E. Plummer, Z. Ying, and H. Dai.
Laser-induced polymerization of submonolayer formaldehyde on Ag(111).
J. Phys. Chem. **95**, 8428–8430 (1991).
- [311] L. Fleck, Z. Ying, and H. Dai.
Temperature-controlled laser-induced polymerization of formaldehyde on Ag(111).
J. Vac. Sci. Technol. A **11**, 1942–1945 (1993).

Acknowledgements

At this point, I would like to thank many people for their continuous support in one or the other way during the last years. It goes without saying that the achievements reported in this thesis could not be realized without harmonic and effective team work and fruitful scientific collaboration. In the following, I would like to thank the people who have directly and indirectly contributed to the success of this work.

I really appreciated the friendly and cooperative atmosphere created by all members of “Experimentelle Physik I” at the University of Würzburg. I felt very comfortable and enjoyed working here even in difficult situations when experiments weren’t going that well and progress was not in sight.



I would like to thank explicitly:

- Prof. Dr. Gustav Gerber for giving me the opportunity to work in this exciting research field, for his helpful advice and enthusiasm to discuss new experimental results, for his belief in my abilities and for giving me the chance to visit conferences and provide own contributions
- Prof. Dr. Tobias Brixner for his steady encouragement and sharing his expertise and experience, for supervising the mid-infrared project and for coordinating the numerous projects in “Labor B” in a way that everybody was satisfied
- Dr. Patrick Nürnberger for the fantastic cooperation in the surface experiments, for his initiative and endurance during long lab nights and for letting me benefit from his wide knowledge and experience
- Marco Schade for his brilliant support in the mid-infrared experiments, for his diligent work and virtually contagious positive attitude throughout his diploma thesis
- Florian Langhojer for spending so much time on optimizing the laser system and for his important contributions to the DNQ control paper
- Frank Dimler, Dr. Reimer Selle and Susanne Fechner for their support in different issues, and their contribution to an excellent atmosphere in the group

- Jochen Aulbach for his restless research for new interesting molecular systems to be studied with the mid-infrared setup and for continuing the work on the mid-infrared project
- Mareike Koch for her help in the early stages of the mid-infrared project
- Dr. Evangelos Papastathopoulos for his help in the early conception of the surface experiments
- the complete “Labor B” team for the steady support, valuable discussions and the many activities after work ranging from theater to the participation in sporting competitions. Not yet mentioned are: Johannes Buback, Stefanie Karg, Dr. Gerhard Krampert, Eliza-Beth Lerch, Tatjana Löhrig, Kate Moore, Alexander Rodenberg, Christoph Schwarz, Ulrike Selig, Christian Spindler, Philip Tuchscherer, Dr. Gerhard Vogt and Dr. Dmitri Voronine,
- Robert Spitzenfeil for his competence and restless efforts as network administrator,
- the guys from the lab next door for sharing their laser in the beginning of the surface experiments in 2005 and their readiness to help in many situations: Dr. Carsten Winterfeldt, Dr. Dominik Walter, Alexander Paulus, Ron Kemmer, Nico Franke, and Sebastian Jung,
- Prof. Dr. Christian Spielmann and Prof. Dr. Walter Pfeiffer and all of their group members for contributing to the unique atmosphere in “Experimentelle Physik I”,
- the technical assistants Helga Schwark, Monika Seifer, and Valentin Bajanov, as well as the secretary Diep Phan for their helpful efforts in different situations,
- the staff of the machine shop and the electronics shop for building many parts of the experimental apparatus that was required for this work
- Dr. Horst Weiß, Dr. Wendel Wohlleben, Dr. Simon Nord, and Dr. Peter Deglmann for countless stimulating discussions and for providing new insights and approaches for inducing and studying a catalytic reaction with a femtosecond laser, and particularly Dr. Horst Weiß for his belief in and enthusiasm about the project and interest in new experimental results,
- Prof. Dr. Jürgen Gauß and Michael Harding for valuable discussions on possible reaction mechanisms related to our observations in the surface reactions,
- my parents Adalbert and Adelgunde for their continuing support, their love and for setting a high value on a good education



-
- my brother Christian for his interest in and for numerous discussions about my work and the physics behind it
 - and the rest of my family, especially my grand parents Lothar and Juliane and my aunt Eugenie for always encouraging me

Lebenslauf

Persönliche Daten

Name: Daniel Stephan Wolpert
Wohnort: Spessartstraße 29, 97249 Eisingen
geboren am: 24. April 1978 in Würzburg
Staatsangehörigkeit: deutsch
Familienstand: ledig

Schulbildung

09/1984 – 07/1988 Volksschule Dürrbachgrund - Würzburg
09/1988 – 06/1997 Deutschhaus Gymnasium - Würzburg
27. Juni 1997 Allgemeine Hochschulreife

Zivildienst

09/1997 – 10/1998 Leonhard-Frank-Haus in Würzburg

Studium der Physik

11/1998 – 10/2004 Julius-Maximilians-Universität Würzburg
Diplomarbeit bei Prof. Dr. W. Pfeiffer:
Optische Spektroskopie an Nanokontakten
20. Oktober 2004 Abschluss: Diplom-Physiker
08/2001 – 10/2002 State University of New York at Buffalo (USA)
Master's Thesis bei Prof. Dr. A. Markelz:
*Ferroelectric Nanosystems studied by Terahertz
Time Domain Spectroscopy with Electrooptic Detection*
1. Februar 2003 Abschluss: Master of Science in Physics
seit 12/2004 Julius-Maximilians-Universität Würzburg
Promotion bei Prof. Dr. G. Gerber

Berufsweg

seit 12/2004 wissenschaftlicher Mitarbeiter der Universität Würzburg

Würzburg, den 08.02.2008

Daniel Wolpert